



HAL
open science

Path instabilities of spheres, spheroids and bubbles

Wei Zhou

► **To cite this version:**

Wei Zhou. Path instabilities of spheres, spheroids and bubbles. Fluid Dynamics [physics.flu-dyn].
Université de Strasbourg, 2016. English. NNT : 2016STRAD038 . tel-01549537

HAL Id: tel-01549537

<https://theses.hal.science/tel-01549537>

Submitted on 28 Jun 2017

HAL is a multi-disciplinary open access archive for the deposit and dissemination of scientific research documents, whether they are published or not. The documents may come from teaching and research institutions in France or abroad, or from public or private research centers.

L'archive ouverte pluridisciplinaire **HAL**, est destinée au dépôt et à la diffusion de documents scientifiques de niveau recherche, publiés ou non, émanant des établissements d'enseignement et de recherche français ou étrangers, des laboratoires publics ou privés.



UNIVERSITÉ DE STRASBOURG



ÉCOLE DOCTORALE MATHÉMATIQUES,
SCIENCES DE L'INFORMATION ET DE L'INGÉNIEUR
ICUBE

THÈSE présentée par :

Wei ZHOU

soutenue le : **29 septembre 2016**

pour obtenir le grade de : **Docteur de l'université de Strasbourg**

Discipline/ Spécialité : Mécanique des Fluides

**Instabilités de trajectoires de sphères,
ellipsoïdes et bulles**

THÈSE dirigée par :

M DUŠEK Jan

Professeur, Université de Strasbourg

RAPPORTEURS :

M BOURGOIN Mickaël

Directeur de Recherche CNRS, Laboratoire de
Physique, ENS Lyon

M FABRE David

Maître de Conférence Université Paul Sabatier, HDR,
IMFT, Toulouse

EXAMINATEURS :

M JENNY Mathieu

Maître de Conférence Université de Lorraine, HDR,
LEMTA, Nancy

Wei ZHOU



Instabilités de trajectoires de sphères, ellipsoïdes et bulles



La thèse présente une étude numérique des instabilités de trajectoires de sphères, d'ellipsoïdes aplatis et de bulles en mouvement libre sous l'action de la gravité, de la poussée d'Archimède et des forces hydrodynamiques.

Le chapitre sur les sphères reprend, complète et étend l'étude numérique de Jenny et al. (2004) en se concentrant sur la transition au chaos et sur les trajectoires chaotiques. Les résultats montrent la différence entre le scénario de transition au chaos de sphères de faible et de grand rapport de densité. Plusieurs grandeurs statistiques sont proposées afin de fournir une caractérisation quantitative des états chaotiques. Elle permettent de mettre en relation les états ordonnés et chaotiques et offrent une possibilité de comparaison objective de données aléatoires d'origine numérique ou expérimentale.

L'étude, très extensive, du comportement d'ellipsoïdes aplatis établit le lien entre les disques et les sphères en faisant varier l'aplatissement des objets depuis infiniment plat jusqu'à presque sphérique. Les huit diagrammes d'état présentés permettent de comprendre l'effet de la forme des ellipsoïdes sur le scénario de transition. Le cas d'ellipsoïdes presque sphériques montre que de faibles imperfections de la forme peuvent avoir un impact significatif sur les trajectoires de sphères de très faible rapport de densité.

Pour les bulles considérées dans la limite de rapport de densité et viscosité gaz/liquide nul, l'étude se concentre sur l'analyse de stabilité linéaire et aboutit à la courbe de stabilité marginale dans le plan des paramètres nombre de Bond – nombre de Galilée en tenant compte de la déformation des bulles au moment de la perte de leur axisymétrie. Plus deux décades de nombres de Bond, entre 0,1 et 20, sont couvertes. Les résultats montrent clairement l'effet de la déformation de la bulle sur le seuil de l'instabilité.

Mots clé : chute ou ascension libre, instabilités de trajectoires, sphère, ellipsoïdes aplatis, bulle déformable

The thesis presents a numerical study of path instabilities for spheres, oblate spheroids and bubbles moving freely under the effect of the gravity, buoyancy and hydrodynamic forces.

For spheres, the parametric study of Jenny et al. (2004) is revisited, improved and extended with a special focus on the chaotic states. The results reveal that the effect of density ratio responsible for different oblique oscillating states of low and high frequencies has a significant impact both on the onset of chaos and on the behavior of fully chaotic states. Several quantitative statistical quantities are proposed and shown to be relevant for establishing the relation between chaotic and ordered states and for an objective comparison of random data of numerical or experimental origin.

The extensive study on freely moving spheroids establishes the link between disks and spheres by varying the aspect ratio of spheroids from infinitely flat to almost spherical. The state diagrams provided for eight different aspect ratios of spheroid show in detail how the transition scenario varies depending of the body shape. The investigation of almost spherical spheroids reveals the specificities of the dynamics of light imperfect spheres.

For the deformable gas bubble in the limit of zero gas/liquid density and viscosity ratio, a marginal stability curve is given in the two-parameter plane of the Galileo and the Bond number indicating the critical Galileo numbers for the loss of stability of vertical trajectories. The numerical investigation covers more than two decades of Bond number going from 0.1 to 20. The results clearly show the crucial role of the surface deformation.

Keywords: free fall or ascension, path instability, transition scenario, sphere, oblate spheroids, deformable bubble

Acknowledgment

By finishing this thesis and the study of three years, I would like to express my immense thanks and gratitude briefly.

I would like to thank, first of all, the department of mechanics of the Institute ICUBE and its directors Yves Rémond and Robert Mosé to give me a chance of experiencing three wonderful years of learning knowledge and enriching myself.

I would like to thank my supervisor Jan Dušek who is a good mentor presenting the wealth of knowledge and the technique of efficiency. This thesis would have never been accomplished without him. I enjoyed the moments working with him trying to figure out different ideas and receiving satisfactory results, even in the most tedious procedure of revise and correction.

I would like to thank Professor Yannick Hoarau who has opened the door of the fluid mechanics for me, his passion in work and enthusiastic attitude inspire me a great deal.

I would like to thank our group of “Instabilités, Turbulences, Diphasique” including Ph.D. students: Daniel Durrenberger, Anthony Ponce, Vincent Léautaud, Chao-Kun Huang and Dorian Pena, you are very helpful.

Last and the most important, I would like to thank my parents, and everyone of the “Guoxue Finance” team in China. Thank you all, for my existence stems from you all.

Résumé

Le comportement de particules individuelles peut avoir une grande influence sur celui des systèmes d'un grand nombre de particules intervenant dans de nombreuses applications du domaine de l'environnement (sédimentation) ou de l'industrie (lits fluidisés, écoulements à bulles). Il apparaît que la trajectoire d'une particule individuelle, sphérique ou axisymétrique, ou celle d'une bulle isolée, tombant ou montant dans un fluide newtonien, devient sous certaines conditions non-verticale, instationnaire, voire chaotique. Ce phénomène s'explique par des instabilités intervenant dans un système combinant les degrés de liberté du fluide avec ceux de l'objet solide ou avec ceux de la surface libre de la bulle. L'apparition des instabilités de trajectoire se répercutent à leur tour sur un système de grand nombre de particules en changeant brutalement ses propriétés statistiques Uhlmann & Doychev (2014).

La thématique des instabilités de trajectoire fait l'objet d'une série de travaux réalisés au sein de l'équipe Mécanique des Fluides de l'ICube. La thèse de Mathieu Jenny (cf. les articles Jenny *et al.* (2003, 2004); Jenny & Dušek (2004)) était le premier travail numérique présentant le scénario de transition d'une sphère en mouvement libre dans un fluide newtonien sous l'action de la gravité. Le diagramme d'état qui y est présenté a été plusieurs fois reproduit dans des travaux postérieurs (ex. Veldhuis *et al.* (2008)). La richesse du comportement d'objets plats (disques, cartes) intriguait pendant de nombreuses années les expérimentateurs Willmarth *et al.* (1964); Field *et al.* (1997) sans qu'on arrive à simuler numériquement le système d'une manière fiable et précise. Les premiers résultats numériques ont été obtenus par F. Auguste à l'IMF de Toulouse Auguste (2010) et une étude paramétrique exhaustive a été effectuée dans le cadre de la thèse de M. Chrust (cf. articles Chrust *et al.* (2013, 2014)). La volonté d'expliquer les résultats expérimentaux publiés après la thèse de M. Jenny a motivé des simulations complémentaires. Une motivation supplémentaire venait de la nécessité de fournir une base de données complète des trajectoires d'une sphère dès que les résultats de l'équipe ont commencé à servir de benchmarks pour des méthodes numériques visant des simulations de systèmes à grand nombre de particules Uhlmann & Dušek (2014). Il s'est avéré nécessaire d'avoir des résultats plus précis, plus complets. En ce qui concerne la thèse de M. Chrust, la méthode numérique développée dans son cadre a montré un potentiel permettant d'envisager une étude multiparamétrique et a ouvert la question du lien entre le scénario d'objets plats (disques) et celui de la sphère.

Les instabilités de trajectoires des bulles n'ont été abordées numériquement et théoriquement jusqu'alors que sous des hypothèses simplificatrices Magnaudet & Mougin (2007a); Tchoufag *et al.* (2013); Cano-Lozano *et al.* (2013) supposant une forme fixe de la bulle à l'apparition des instabilités. Le récent article de Nature Communications Tripathi *et al.* (2015) est le

premier à donner des résultats numériques pleinement tridimensionnels tenant compte de la déformation de la surface de la bulle. L'ambition de l'article allant au delà de l'apparition de l'instabilité, les informations portant sur son seuil et ses caractéristiques restent, cependant, trop sommaires.

La présente thèse aborde les sujets mentionnés ci-dessus.

Sphère

Le problème de la particule sphérique est numériquement le plus aisé et une version légèrement améliorée du code développé pendant la thèse de M. Kotouc (cf. e.g. Kotouc *et al.* (2009)) s'est avéré très efficace pour l'aborder. Le résultat de plusieurs centaines de simulations peut être résumé sous la forme du diagramme d'état de la figure 1. Comme expliqué dans les articles précédents (ex. Jenny *et al.* (2003)), tous les systèmes comportant une sphère homogène de masse volumique ρ_s et de diamètre d en chute ou en ascension libre sous l'action de la gravité (d'accélération g), de la poussée d'Archimède et des forces hydrodynamiques dans un fluide newtonien (de masse volumique ρ et de viscosité cinématique ν) asymptotiquement au repos et non confiné, peuvent être caractérisés par seulement deux paramètres. Nous choisissons, à cet effet, le nombre de Galilée $G = \sqrt{\left| \frac{\rho_s}{\rho} - 1 \right| g d^3 / \nu}$ et le rapport des densités ρ_s / ρ . Pour chaque couple de paramètres nous résolvons numériquement les équations de Navier-Stokes et représentons les états asymptotiques obtenus (c'est à dire, pour une sphère lâchée au repos, bien après la phase d'accélération initiale) sur le diagramme de la figure 1. Dans certains cas, en fonction des conditions initiales, deux états asymptotiques différents ont été mis en évidence (bi-stabilité). C'est le cas d'une superposition partielle de la zone chaotique et de la zone de trajectoires périodiques verticales. Hormis la délimitation exacte de cette zone d'ordre dans le chaos (au centre de la figure), nous avons répondu à la question de l'origine de deux fréquences des trajectoires obliques et oscillantes. La zone de basse fréquence correspond aux systèmes où l'inertie des particules reste suffisamment faible pour permettre à la particule d'effectuer des oscillations de grande amplitude et d'interagir fortement avec le sillage. En revanche, dans la zone de haute fréquence, l'amplitude des oscillations de la sphère est faible et le système possède essentiellement la dynamique du sillage d'une sphère fixe. Finalement, nous avons essayé de fournir une quantification statistique des états chaotiques afin de faciliter des comparaisons avec des expériences effectuées en général pour des nombres de Galilée élevés. L'utilité d'une telle approche est illustrée par la figure 2 mettant en évidence une zone de grandes fluctuations de la vitesse horizontale (grands G , faible rapport de densités) correspondant à des trajectoires presque hélicoïdales ayant des fréquences proches des trajectoires observées expérimentalement Horowitz & Williamson (2010). Ce volet de travail a été publié dans l'International Journal of Multiphase Flow Zhou & Dušek (2015).

Ellipsoïdes de révolution (sphéroïdes)

Le code servant à simuler les trajectoires des ellipsoïdes de rotation avait été développé dans le cadre de la thèse de M. Chrust mais la dynamique des ellipsoïdes restait à explorer. Le problème a été paramétrisé par trois paramètres, le rapport d'aspect $\chi = d/a$, d étant le diamètre et a la longueur de l'axe de révolution, la masse adimensionnée $m^* = m / (\rho d^3)$

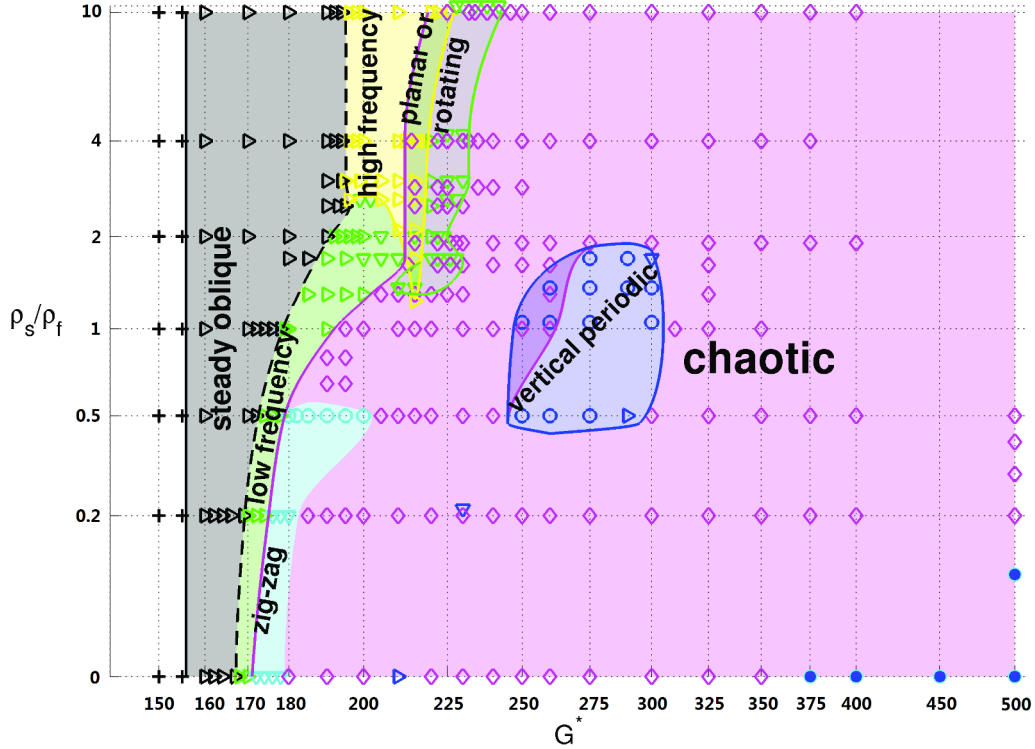


FIGURE 1 – Diagramme d'états dans le plan des paramètres G^* - ρ_s/ρ_f pour les trajectoires d'une sphere. Les seuils des bifurcations sont représentés par des lignes, les couleurs marquent les régimes indiqués dans la figure. Les symboles représentent les trajectoires effectivement simulées. Pour la description détaillée des symboles : cf. l'article Zhou & Dušek (2015).

(mesurant l'inertie du solide), m étant la masse de l'ellipsoïde et ρ la masse volumique, et $G = \sqrt{|m^* - V^*|gd^3/\nu}$ le nombre de Galilée faisant intervenir l'accélération gravitationnelle g , la viscosité cinématique du fluide ν et le volume adimensionné $V^* = V/d^3$. L'étude s'est limitée aux ellipsoïdes aplatis ($\chi \geq 1$), $\chi = 1$ correspondant à la forme sphérique et $\chi = \infty$ à un disque infiniment plat (avec la masse distribuée légèrement non-uniformément). L'étude a ainsi permis d'établir le lien entre le scénario de la sphere et celui du disque. Plusieurs milliers de simulations ont été effectuées pour balayer les plans $\chi = \infty, 10, 6, 5, 4, 3, 2$ et 1.1 . Les figures 3 et 4 représentent les exemples des plans $\chi = 6$ et $\chi = 1.1$. La forme de l'ellipsoïde est schématisée en bas à gauche des figures. Le scénario sur la figure 3 est très proche de celui d'un disque plat Chrust *et al.* (2013). Il est caractérisé par trois régimes dominants : des trajectoires en zig-zag le long desquelles l'axe de l'ellipsoïde s'incline fortement par rapport à la verticale (zone bleue de la figure 3), des trajectoires obliques avec l'ellipsoïde effectuant périodiquement des culbutes (zone rouge) et une zone de transition (zone verte) d'intermittence entre les deux régimes. L'article Chrust *et al.* (2013) a mis en évidence des régimes de

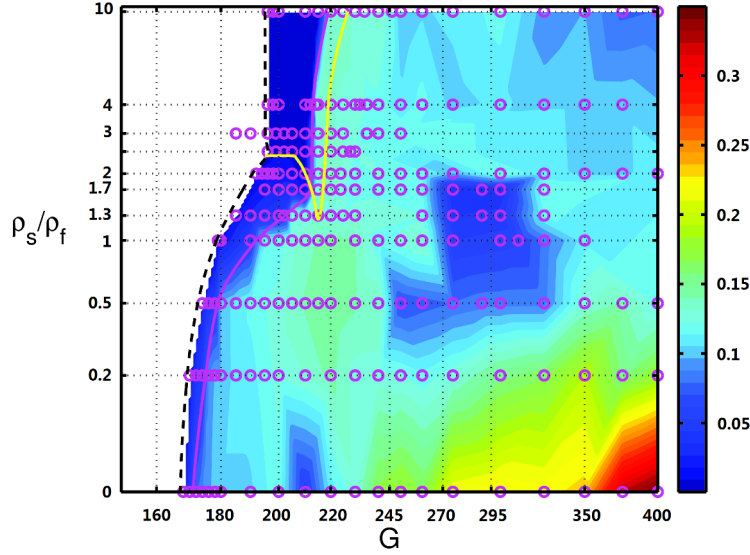


FIGURE 2 – Moyenne quadratique des fluctuations de la vitesse horizontale de la sphère $\langle\langle(\mathbf{u}_h - \langle\mathbf{u}_h\rangle)^2\rangle\rangle^{1/2}$.

faibles oscillations qui peuvent passer inaperçues dans les expériences. Ces régimes existent également pour les ellipsoïdes aplatis (zones magenta). Déjà pour les disques, plusieurs domaines de co-existence de régimes avait été mis en évidence. Ces zones de bi-stabilité sont encore plus développées dans le cas d’ellipsoïdes de rapport d’aspect 6. En particulier on remarque que les trois régimes caractérisés par de fortes amplitudes d’oscillations débordent dans la zone de trajectoires verticales ce qui s’explique par l’inertie de l’objet solide. Sur la figure 4 on reconnaît les régimes du scénario de la sphère (figure 1). La seule différence consiste dans le fait que dans les régimes obliques (régime stationnaire et régime oscillant - zones grise, verte et jaune) l’ellipsoïde ne peut pas tourner sur lui même car même le faible aplatissement l’en empêche. En revanche, ce même aplatissement permet la co-existence des régimes typiques pour la sphère avec le régime d’oscillations en zig-zag qui apparaît même à des nombres de Galilée inférieurs au seuil du régime oblique stationnaire suite à une bifurcation de Hopf précédant (pour de faibles inerties) la bifurcation régulière intervenant au $G \approx 110$. Une fois la figure 4 commentée, il est intéressant de revenir à la figure 3. On peut y remarquer le scénario de la sphère sous une forme embryonnaire. En effet, la ligne verticale noire marquant l’instabilité primaire pour des masses adimensionnées inférieures à 0.25 correspond au seuil du régime oblique stationnaire qui se distingue par son indépendance de l’inertie. On a pu également mettre en évidence plusieurs cas de régime oblique stationnaire (triangles bleus près de la ligne ligne verticale) ainsi que de régime oblique oscillant (triangles verts).

Bulle

L’étude de la bulle a été précédée par une étape d’adaptation extensif du code numérique.

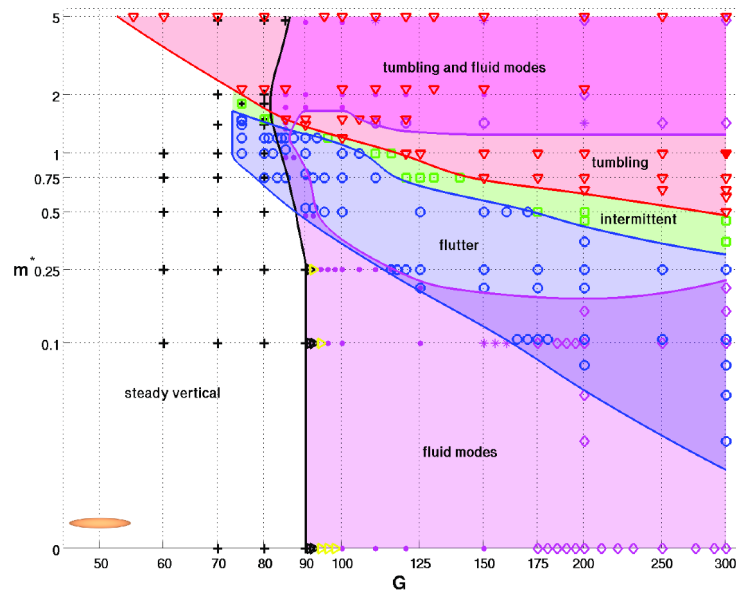


FIGURE 3 – Diagramme d’état pour des ellipsoïdes très aplatis ($\chi = 6$). Signification des couleurs : blanche : trajectoires verticales, rouge - régime périodique de chute accompagnée de culbutes (“tumbling”), bleue - oscillations périodiques de grande amplitude d’inclinaison de l’axe (régime “zig-zag”), verte - régime intermittent entre culbutes et oscillations, magenta - modes périodiques, quasi-périodiques ou chaotiques avec faible amplitude d’inclinaison.

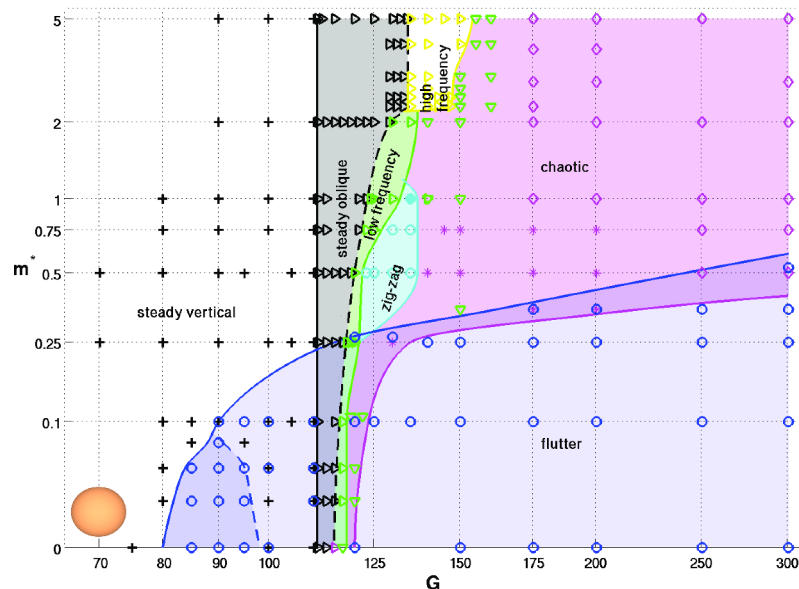


FIGURE 4 – Diagramme d’état pour des ellipsoïdes de forme presque sphérique ($\chi = 1.1$). Même signification de couleurs que figure 1 sauf la couleur bleue qui représente le régime “zig-zag” comme sur la figure 3. 1.

L'approche comportant un maillage 3D déformable a été retenue (méthode ALE). La description de la géométrie du maillage se fait, néanmoins, toujours par décomposition azimutale spectrale ce qui permet au code de garder sa précision et son efficacité lorsque la perte de l'axisymétrie du maillage accompagne celle de l'ensemble de l'écoulement. La bulle est traitée comme un espace vide de volume constant délimité par une surface libre. Afin de tenir compte de la condition de surface libre, la formulation faisant intervenir le tenseur de contrainte dans les équation de Navier-Stokes (stress formulation) a dû être implémentée. La discrétisation assure la stabilité numérique de l'algorithme malgré la présence des ondes de surface.

Dans le cadre des hypothèses retenues, le problème ne comporte que deux paramètres, le nombre de Bond $Bo = \rho g d^2 / \sigma$, caractérisant les effets de tension superficielle, combinant la gravité g , le diamètre de la bulle au repos (lorsqu'elle est sphérique) et la tension superficielle σ , et le nombre de Galilée, défini, cette fois-ci comme $G = \sqrt{g d^3} / \nu$, avec ν la viscosité cinématique du liquide ambiant. En absence de connaissances préliminaires fiables (les études numériques précédentes ayant été effectuées sous hypothèses de bulles 'rigides'), sans parler des difficultés numériques impliquées par la nouveauté du sujet, nous avons décidé de limiter l'étude essentiellement à l'analyse de stabilité linéaire de la montée verticale. La nécessité de prendre en compte la déformation de la surface comme facteur essentiel de l'instabilité apparaît clairement sur la figure 5 montrant la forme de la bulle pour une instabilité développée. Une forme légèrement triangulaire a été également obtenue dans quelques travaux numériques où les bulles ont pu être simulées pleinement en 3D dans des régimes supercritiques.

L'analyse de stabilité linéaire a été menée dans l'intervalle $Bo \in [0.1, 10]$. Dans l'ensemble de cet intervalle, la bifurcation est du type de Hopf et son seuil (nombre de Galilée critique) varie relativement peu en fonction du nombre de Bond. La bifurcation donne clairement naissance à des trajectoires planes oscillantes dont la fréquence d'oscillation varie d'une manière assez significative en fonction du nombre de Bond. Nous avons obtenu les seuils, les fréquences au seuil et les modes linéaires au seuil pour 11 valeurs différentes du nombre Bond ce qui nous a permis d'obtenir une courbe de stabilité relativement détaillée sur l'intervalle considéré (figure 6).

Conclusion

Alors que l'étude des trajectoires des objets solides est à présent relativement complète, les travaux portant sur le problème de la bulle devront être poursuivis après l'achèvement de la présente thèse. Malgré l'impossibilité de capturer les phénomènes accompagnés de changements topologiques (extraction de bulles secondaires) l'étude pleinement non-linéaire apportera certainement de nombreuses informations intéressantes. On peut également s'attendre à ce que les problèmes de stabilité numériques soient moindres pour des gouttes et inclusions fluides qui pourront également être simulées par le code obtenu.

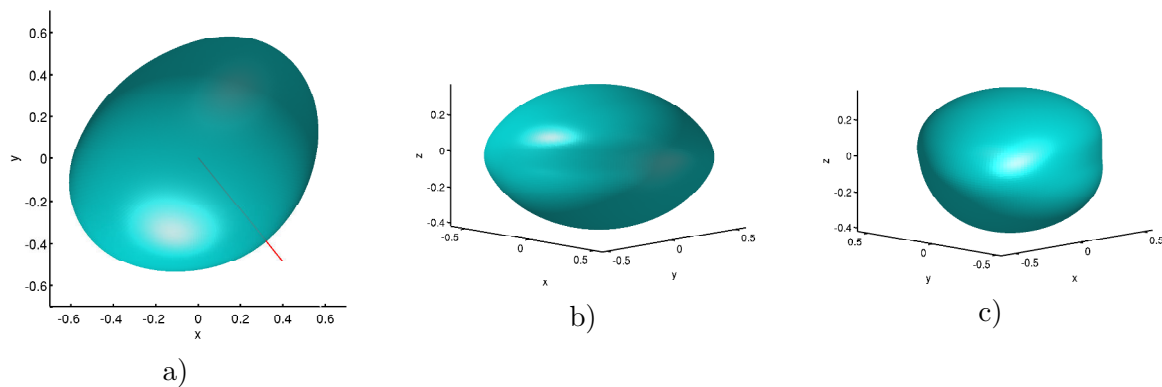


FIGURE 5 – Bulle déformée dans le régime saturé non-linéaire pour $Bo = 1$ et $G = 100$. a) Vue du haut. La direction du déplacement vertical est indiquée par la ligne rouge. b) Vue (presque) horizontale dans le plan de la trajectoire. La bulle s’approche du lecteur. c) Vue (presque) horizontale perpendiculairement au plan de la trajectoire. La bulle se déplace vers la droite.

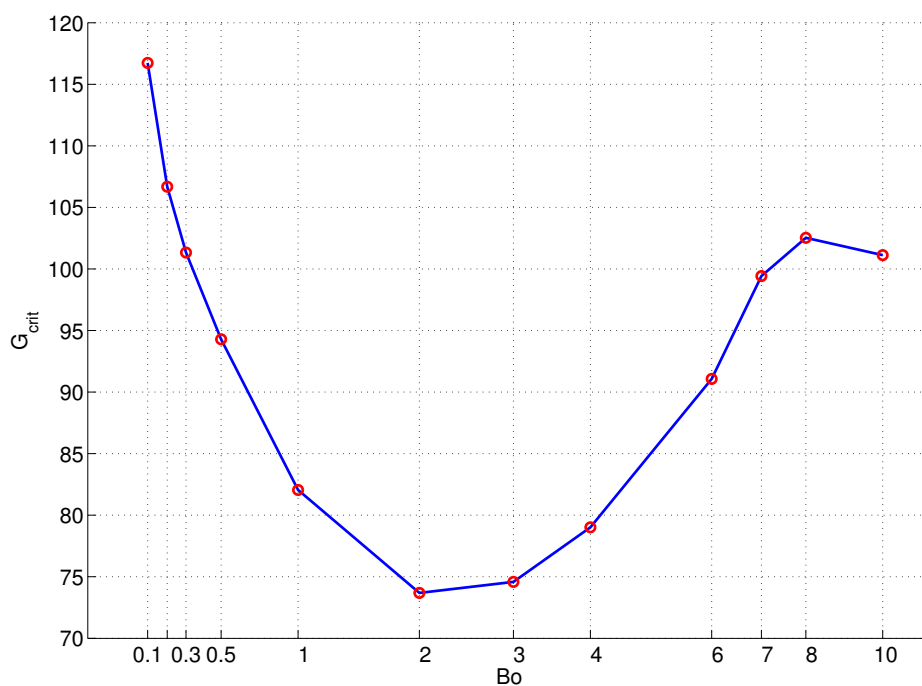


FIGURE 6 – Nombre de Galilée critique G_{crit} de l’instabilité linéaire de l’ascension d’une bulle en fonction du nombre de Bond

References

- AUGUSTE, F. 2010 Instabilités de sillage générées derrière un corps solide cylindrique, fixe ou mobile dans un fluide visqueux. PhD thesis, Université Paul Sabatier, Toulouse.
- CANO-LOZANO, J. C., BOHORQUEZ, P. & MARTÍNEZ-BAZÁN, C. 2013 Wake instability of a fixed axisymmetric bubble of realistic shape. *Int. J. Multiphase Flow* **51**, 11–21.
- CHRUST, M., BOUCHET, G. & DUŠEK, J. 2013 Numerical simulation of the dynamics of freely falling discs. *Physics of Fluids* **25**, 044102.
- CHRUST, M., BOUCHET, G. & DUŠEK, J. 2014 Effect of solid body degrees of freedom on the path instabilities of freely falling or rising flat cylinders. *J. Fluids and Structures* **47**, 55–70.
- FIELD, S. B., KLAUS, M. & MOORE, M. G. 1997 Chaotic dynamics of falling disks. *Nature* **388**, 252–254.
- HOROWITZ, M. & WILLIAMSON, C. H. K. 2010 The effect of reynolds number on the dynamics and wakes of freely rising and falling spheres. *Journal of Fluid Mechanics* **651**, 251–294.
- JENNY, M., BOUCHET, G. & DUŠEK, J. 2003 Nonvertical ascension or fall of a free sphere in a Newtonian fluid. *Physics of Fluids* **15**, L9–L12.
- JENNY, M. & DUŠEK, J. 2004 Efficient numerical method for the direct numerical simulation of the flow past a single light moving spherical body in transitional regimes. *Journal of Computational Physics* **194**, 215–232.
- JENNY, M., DUŠEK, J. & BOUCHET, G. 2004 Instabilities and transition of a sphere falling or ascending freely in a Newtonian fluid. *J. Fluid Mech.* **508**, 201–239.
- KOTOUČ, M., BOUCHET, G. & DUŠEK, J. 2009 Transition to turbulence in the wake of a fixed sphere in mixed convection. *J. Fluid Mech.* **625**, 205–248.
- MAGNAUDET, J. & MOUGIN, G. 2007 Wake instability of a fixed spheroidal bubble. *J. Fluid Mech.* **572**, 311–337.
- TCHOUFAG, J., MAGNAUDET, J. & FABRE, D. 2013 Linear stability and sensitivity of the flow past a fixed oblate spheroidal bubble. *Physics of Fluids* **25**, 054108.
- TRIPATHI, M. K., SAHU, K. C. & GOVINDARAJAN, R. 2015 Dynamics of an initially spherical bubble rising in quiescent liquid. *Nature Communications* **6:6268**.
- UHLMANN, M. & DOYCHEV, T. 2014 Sedimentation of a dilute suspension of rigid spheres at intermediate galileo numbers: the effect of clustering upon the particle motion. *J. Fluid Mech.* **752**, 310–348.
- UHLMANN, M. & DUŠEK, J. 2014 The motion of a single heavy sphere in ambient fluid: A benchmark for interface-resolved particulate flow simulations with significant relative velocities. *Int. J. Multiphase Flow* **59**, 221–243.
- VELDHUIS, C., BISHEUVEL, A. & VAN WIJNGAARDEN, L. 2008 Shape oscillations on bubbles rising in clean and tap water. *Physics of Fluids* **20**, 040705.
- WILLMARTH, W. W., HAWK, N. E. & HARVEY, R. L. 1964 Steady and unsteady motions and wakes of freely falling disks. *Physics of Fluids* **7**, 197–208.
- ZHOU, W. & DUŠEK, J. 2015 Chaotic states and order in the chaos of the paths of freely falling and ascending spheres. *Int. J. Multiphase Flow* **75**, 205–223.

Contents

Acknowledgment	i
Résumé	iii
1 Introduction	1
1.1 Two phase flows of solid particles bubbles and drops	1
1.2 Phenomenological models	5
1.3 Non-straight-trajectories and path instabilities	8
1.3.1 Path instabilities of non-deformable bodies	8
1.3.2 Path instabilities of deformable bubbles	11
1.4 Theory of the loss of axisymmetry in flows	13
1.5 Wake of a bluff body	17
1.5.1 Wake of a fixed cylinder	18
1.5.2 Wake of a fixed sphere	18
1.5.3 Wake of a fixed disk	21
1.6 Freely falling or rising spheres	25
1.7 Axisymmetric but aspherical bodies	27
1.8 Bubbles and drops	30
1.9 Aims of this thesis	33
2 Freely falling or ascending spheres	35
2.1 Introduction	35
2.2 Mathematical formulation and numerical implementation	36
2.3 Primary and secondary instabilities	37
2.4 Low and high frequencies	39
2.5 Various imperfect zigzagging trajectories	48
2.6 Transition to chaos	58
2.6.1 Light sphere	58
2.6.2 Dense sphere	58
2.7 Vertical oscillating regime in the chaotic domain	65
2.8 Helical regime	72
2.9 Chaotic states	75

3	Freely falling or ascending spheroids	87
3.1	Introduction	87
3.2	Mathematical formulation and numerical method	89
3.3	Results	91
3.3.1	$\chi = \infty$	93
3.3.2	$\chi = 10$	97
3.3.3	$\chi = 6$	108
3.3.4	$\chi = 5$	113
3.3.5	$\chi = 4$	115
3.3.6	$\chi = 3$	115
3.3.7	$\chi = 2$	118
3.3.8	$\chi = 1.1$	121
3.3.9	Conclusion	125
4	Bubble rising in a quiescent liquid	127
4.1	Introduction	127
4.2	Mathematical formulation and numerical method	129
4.2.1	Governing equations	129
4.2.2	Numerical method	130
4.3	Numerical validation	132
4.3.1	Mesh refinement	132
4.3.2	Time step	133
4.3.3	Validation	133
4.4	Linearly unstable mode	134
4.5	Marginal stability curve	138
4.6	Some preliminary non-linear results	138
4.7	Conclusions	140
5	Conclusions and perspectives	145
6	Appendix	147
6.1	Bubble: mathematical formulation	147
6.1.1	Freely moving fluid inclusion	147
6.1.2	Semi-discrete equations and weak formulation	151
6.1.3	Time splitting formulation	155
6.2	Bubble: numerical method of solution	157
6.2.1	Storage of variables	159
6.2.2	Differential operators on undeformed mesh	160
6.2.3	Description of bubble surface and domain deformation	163
6.3	Capillarity waves on a spherical free surface	166
6.4	Divergence of transposed velocity gradient	168
6.5	Stress formulation in spectral representation	168
6.6	Stress formulation on the deformed mesh	169

CONTENTS

xiii

Bibliography

171

Chapter 1

Introduction

1.1 Two phase flows of solid particles bubbles and drops

The intriguing phenomena of multiphase flows have been challenging human understanding and imagination since the beginning of the world. In ancient times, far before the invention of writing, people saw materials of the physical world as different forms of energies flowing freely in space, which may be the origin of the famous “panta rei” of Heraclitus, a pre-Socratic Greek philosopher, having inspired not only rheologists (Beris & Giacomin, 2014) but also, more broadly, hinting to fluid flows. In the sky of deep quiet starry nights through the unlimited extending space, we see stars traveling in the ambient interstellar gases through varying states over large time scale during the formation of galaxies, which can be compared to transitions of multiparticle flows and sedimentation processes within the human life cycle. Bathing in the solar wind, our planet Earth keeps moving and rotating under the effect of electromagnetic field of the Sun, giving the impression of similarities to the well studied problem of flow past cylinders (Figure 1.1).

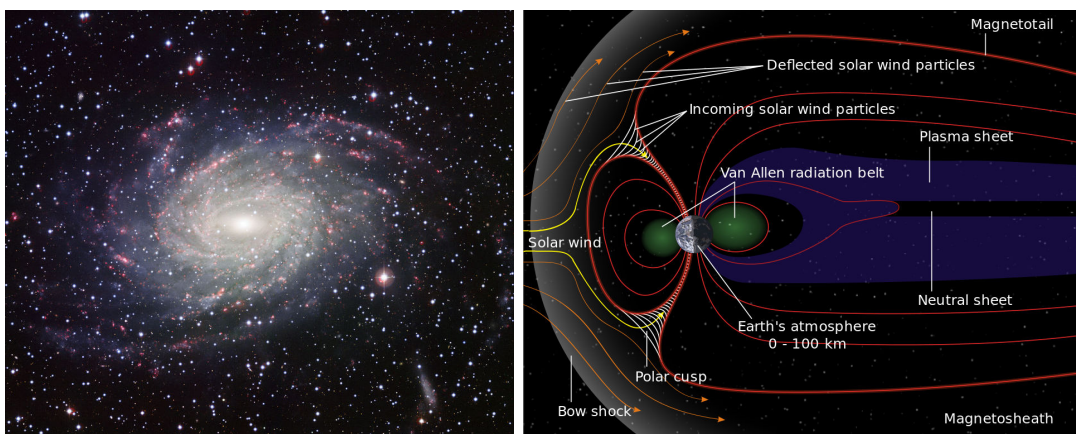


Figure 1.1: left: Milky Way, right: Earth's magnetosphere, the solar wind flows from left to right.

Beside the interaction between cosmological bodies and interstellar environment, large amount of particles under gravity-driven motion in a viscous flow is a phenomenon frequently observed in nature and encountered in geology, life sciences and industries, such as cloud formations, fall of rain, sedimentation, saltation and red blood cell aggregation. Sandstorm, or saltation, is a process of particle transportation through which the particles vibrate, leap, strike the ground, break up into smaller particles. As the wind goes beyond the critical speed, mechanisms of suspension, saltation and creep occur (Squires (2007)). In the ocean-atmosphere environment, fluxes of heat, moisture and momentum are exchanged at the ocean-atmosphere interface, consequently ocean surface waves are generated which eventually changes the wind speed near the surface. Under certain circumstances a tropical cyclone, or violent hurricane, forms.



Figure 1.2: Yueya Quan (Crescent Lake) in the Gobi Desert, Dunhuang, China.

Given large scales of temporal and spatial evolution, a good understanding of these complex systems is yet far from being fulfilled, though, experiments and simulations still provide qualitative characteristics by simplifying the physical models. In sedimentation, earlier experiments and simulations (Nguyen & Ladd (2005); Mucha *et al.* (2004)) for dilute systems of suspensions at low Reynolds numbers, in a macroscopic view, focused on the effect of confinement on hydrodynamic interactions in the bulk suspensions and stratification. Nguyen & Ladd (2005) suggested the crucial role of the container in determining the distribution of suspensions, although the reason why macroscopic boundary conditions played a key component of the dynamics was unclear. Mucha *et al.* (2004) used numerical simulations and experiments showing “a critical stratification above which the characteristics of the density and velocity fluctuations change significantly.”

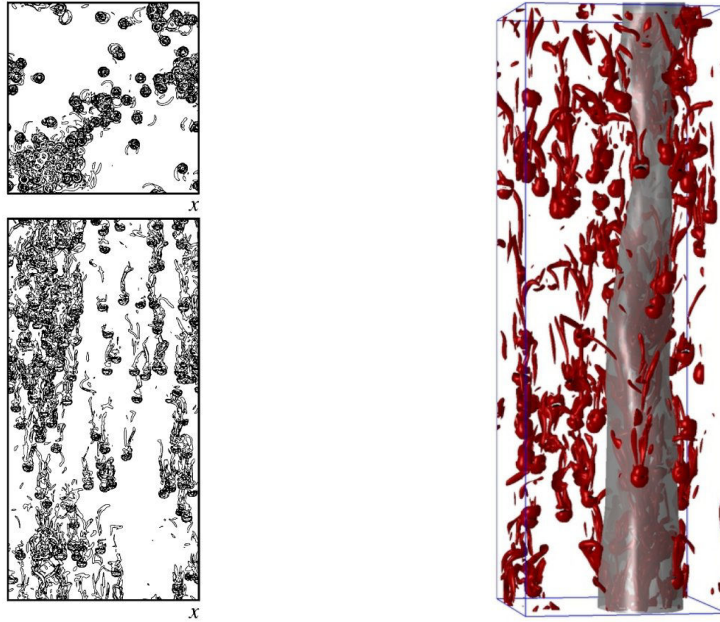


Figure 1.3: Left figure: top and side view of instantaneous flow field including 128 falling particles at Reynolds number $Re = 400$ (reproduced from Kajishima & Takiguchi (2002)). Right figure: simulation of a flow induced by clustering of spheres falling at Galileo number $Ga = 178$. The grey tube-like structure shows a significantly downward accelerated flow, the individual particles are visualized by the vorticity of their wakes (reproduced from Uhlmann & Doychev (2014)).

Particle clustering at moderate Reynolds number ($Re < 400$) has been discussed by Kajishima & Takiguchi (2002) showing the phenomenon of wake-induced clustering for higher Reynolds numbers. They explained the formation of clustering as “the drag on particles trapped in the wake of upstream ones is likely to be small than those falling individually” and “approach ones present in lower position” (left Figure 1.3). Recently, Uhlmann & Doychev (2014) provided the evidence of a significant change of the collective motion due to onset of path instabilities of individual particles by in a massively parallel numerical simulation involving 12 000 fully resolved spheres: “... it appears tempting to relate the onset of clustering to the bifurcation point (from axisymmetric to planar oblique) of the wake of an isolated sphere...”, and pointed out the effect of the settling velocity of a single sphere: “it may be possible to approximate the particle settling velocity as the sum of two contributions, adding the characteristic meso-scale velocity of the surrounding fluid to the settling velocity value of an isolated sphere”. The quantitative knowledge of the behavior of a single sphere helped not only to the understanding of the physics of the multiparticle flow but also served as a useful benchmark to optimize numerical parameters for aforementioned massive multiparticle simulation (Uhlmann & Dušek, 2014).

On the other hand, bubbly flows, frequently encountered in daily life as well as in industry, have been receiving much attention. They play an important role in processes, for instance,

of cavitation, two-phase heat transfer, nuclear and chemical reaction, smelting of metals. Compared with the particle-laden flows, the small size, fast times scales and deformation of rising bubbles makes the problem of gas-liquid interaction more difficult to investigate experimentally and simulate numerically. Neglecting the bubble deformation, Esmaceli & Tryggvason (1998) carried out direct numerical simulations of rising bubbles at low Reynolds number ($Re = 1 - 2$) in a periodic box, including up to 324 two-dimensional bubbles and 8 three-dimensional bubbles. They found that the original regular array of bubbles was unstable and broke quickly in a “drafting, kissing and tumbling” (Fortes *et al.* (1987)) fashion. Bubbly flows are also common issue in the study of cavitation similarly to the process of boiling. The primary difference of both is that boiling occurs when the local vapor pressure of the liquid rises above its local ambient pressure and increasing energy generate the phase change to a gas, whereas in the case of cavitation, local pressure falls sufficiently far below the saturated vapor pressure (Brennen (1995)).

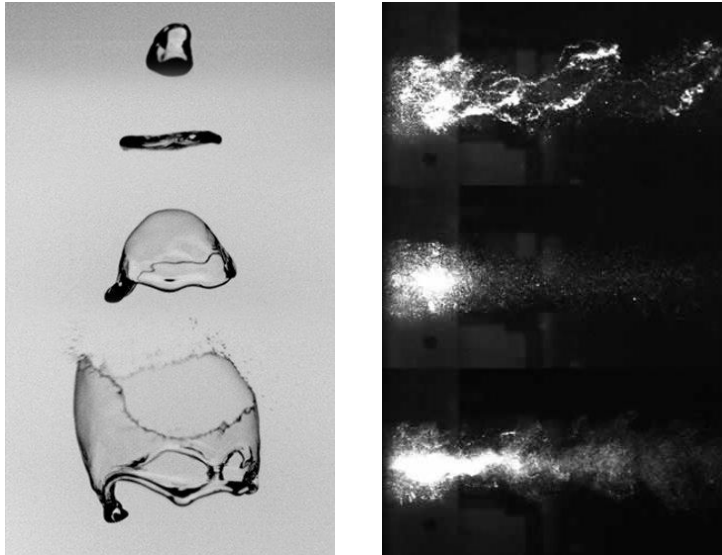


Figure 1.4: Left: a falling water drop breaking (Villermaux & Bossa (2009)), right: cavitation in the wake of a water jet at St. Anthony Falls Laboratory, University of Minnesota.

Other deformable bodies, drops and droplets, differentiate generally from bubbles by the mechanisms of transition, coalescence and breakup. Besides the dependence on inertia and surface tension, the size of bubbles and drops has been well discussed. In the case of raindrops, Villermaux & Bossa (2009) have shown that the larger drops deform as they interact with their surroundings during the fall and fragment into smaller drops, which affect the distribution of sizes and limit the largest raindrops. Another important issue is the vorticity induced by the bubble(drop) motion. In a recent paper, Tripathi *et al.* (2014) compared similarities and differences between rising bubbles and falling drops and showed that residual vorticity tends to lie in the lighter fluid, that is, to concentrate within a bubble and outside of a drop.

Despite the strong motivation given by the fact that multiparticle and bubbly flows play a very important role in industrial and geophysical processes and that the motion of single particles is essential for their understanding, the problem of a single particle moving freely in a fluid is, to some extent, still an open topic, especially in the case of a bubble where numerical parametric work is still scarce.

1.2 Phenomenological models

The essential for the understanding the dynamics of multiphase flows is to know how particles move within the surrounding fluid and how their interfaces evolve under the mechanism of fluid–particle interaction. To illustrate the mutual interactions of the fluid and solid phases, consider the motion of a single particle immersed in a fluid. Fluid exerts a hydrodynamic force on a particle at the same time when a particle disturbs the flow. In what follows, the density and kinematic viscosity of the continuous phase are considered constant and the fluid is assumed to be incompressible. The flow is then governed by the Navier–Stokes equations:

$$\frac{\partial \mathbf{v}}{\partial t} + (\mathbf{v} \cdot \nabla) \mathbf{v} = -\nabla p + \frac{1}{Re} \nabla^2 \mathbf{v} \quad (1.1)$$

and the continuity equations describing the conservation of mass

$$\nabla \cdot \mathbf{v} = 0 \quad (1.2)$$

where $Re = U_\infty d / \nu$ is the Reynolds number representing an inverse of the non-dimensionalized kinematic viscosity (ν). These equations have to be completed by the initial and boundary conditions. The domain is considered to be infinite with the fluid being at rest on its limits. In practice the domain is finite. However, its size should be sufficiently large so that the flow is not altered due to the introduced confinement. The interaction between the solid and the fluid is due to the no-slip boundary condition on its surface S , which moves with a velocity \mathbf{u} . This boundary condition is expressed by:

$$\mathbf{v}|_S = \mathbf{u} + \boldsymbol{\Omega} \times \mathbf{r}|_S \quad (1.3)$$

where $\mathbf{v}|_S$ is a velocity of the fluid, that is in contact with the solid, $\boldsymbol{\Omega}$ is the angular velocity of the solid and \mathbf{r} is the position vector of a point on its surface.

The difficulty of solving the coupled solid–fluid problem consists in resolving all the scales present in the problem. Moving particle introduces the energy to the surrounding fluid, that in turn governs the evolution of large scale flow structures. The two-way coupling between a particle and continuous phase is non-trivial and requires careful treatment.

Theoretical approaches to the modeling of multiparticle flows can be challenging since they can additionally account for the interactions between particles. An approach consists in considering both the fluid and solid phases as distinct media. The continuous phase is resolved using Eulerian approach through the solution of the Navier Stokes equations possibly augmented by a source term modeling the action of the solid phase on the fluid one to account for a two way coupling. The solid phase is resolved using the Lagrangian approach consisting in integration of Eq. (1.4). The forces \mathbf{F} acting on a single particle listed

in Eq. (1.6) are modeled phenomenologically (see Tanabe & Kaneko (1994); Mahadevan *et al.* (1999); Caballina (2002)).

The three translational degrees of freedom of a particle obey the motion equation:

$$m \frac{d\mathbf{u}}{dt} = (m - m_f)\mathbf{g} + \mathbf{F} \quad (1.4)$$

where m and m_f is the mass of a particle and that of a volume of the displaced fluid respectively, \mathbf{u} is the velocity of the center of mass of the particle and \mathbf{g} represents the vector of gravitational acceleration. In a sub-critical regime, a particle placed in a steady homogeneous flow follows a vertical path. The driving force (resulting from gravity and buoyancy) is counterbalanced by the hydrodynamic drag $\mathbf{F} = \mathbf{F}_D$. The derivative on the left hand side of Eq. (1.4) is equal to zero in this case. Non-dimensionalization of the drag force yields the drag coefficient:

$$C_D = \frac{F_D}{\frac{1}{2}\rho u^2 S} \quad (1.5)$$

where C_D being the drag coefficient, ρ density of the fluid, u velocity of the body and S the reference area.

As soon as the velocity of a particle starts to vary, the acceleration effects appear. Moreover, the shear of the flow must often be accounted for. The instantaneous force acting on a particle contains, along with the drag force \mathbf{F}_D present before, supplementary terms:

$$\mathbf{F} = \mathbf{F}_D + \mathbf{F}_{ma} + \mathbf{F}_h + \mathbf{F}_L, \quad (1.6)$$

where \mathbf{F}_{ma} , \mathbf{F}_h and \mathbf{F}_L are the added mass, history and lift forces respectively. The added mass force accounts for the inertial effects. It is a force exerted by a particle to accelerate the surrounding fluid. It is expressed by:

$$\mathbf{F}_{ma} = C_{ma} m_f \left(\frac{d\mathbf{v}}{dt} - \frac{d\mathbf{u}}{dt} \right), \quad (1.7)$$

with C_{ma} being the added mass coefficient equal to $C_{ma} = 1/2$ for a sphere (Magnaudet *et al.*, 1995). The history force, proposed independently by Boussinesq (1885) and Basset (1888), represents the delay necessary for the flow to adapt to the boundary conditions imposed by the motion of a particle. It can be expressed using the integral formulation (see e.g. Magnaudet (1997)):

$$\mathbf{F}_h = \int_0^t K(t - \tau) \left(\frac{\partial \mathbf{v}}{\partial \tau} - \frac{\partial \mathbf{u}}{\partial \tau} \right) d\tau, \quad (1.8)$$

where the kernel $K(t - \tau)$ depends on the process of the diffusion of the vorticity. Calculation of the history force is computationally expensive, however, especially for bubbles, it cannot be neglected, when fluctuations of the relative velocities between phases become important (Rivero *et al.* (1991)). If the vorticity is present in the flow, the lift force must be also considered. It is expressed by:

$$\mathbf{F}_L = -C_L m_f (\mathbf{u} - \mathbf{v}) \times \boldsymbol{\omega}, \quad (1.9)$$

where the vorticity in the absence of the rotation of a particle is given by $\boldsymbol{\omega} = \nabla \times \mathbf{v}$ and the lift coefficient is defined as:

$$C_L = \frac{F_L}{\frac{1}{2} \rho u^2 S} \quad (1.10)$$

The problem consists then in the modeling of the drag and lift forces. There exist various expressions of both dated from early in the last century. The well known drag coefficient for a classical Stokes flow past a solid sphere is expressed as:

$$C_D = \frac{24}{Re}. \quad (1.11)$$

For a bubble the factor 24 is to be replaced by 18. For Reynolds numbers larger than one and in more complicated configuration, the drag law obeys various empirical formulas of increasing complexity. E.g. Moore (1963) provided a description of the flow in the asymptotic limit of high Reynolds number for the regions of a thin boundary layer and a narrow wake where the vorticity produced by the shear-free condition is confined resulting in the law

$$C_D = \frac{48}{Re} \left(1 - \frac{2.21}{Re^{1/2}} \right) + O\left(Re^{-11/6}\right) \quad (1.12)$$

for $Re \geq 50$. Mei *et al.* (1994) proposed an empirical drag law for clean spherical bubbles:

$$C_D = \frac{16}{Re} \left\{ 1 + \left[\frac{8}{Re} + \frac{1}{2} \left(1 + 3.315 Re^{-1/2} \right) \right]^{-1} \right\}. \quad (1.13)$$

Due to the inertial effect of a three-dimensional motion the lift force is more difficult to model. For an inviscid fluid and a spherical particle $C_L = 0.5$ according to Auton (1983). For moderate Reynolds numbers, C_L is a function of shear present in the flow $A_\omega = d|\boldsymbol{\omega}|/|\mathbf{u} - \mathbf{v}|$ and tends to the asymptotic value as $C_L = 0.5 - 4.0 Re^{-1}$ (Komori & Kurose (1996)). The numerical results of Legendre & Magnaudet (1998) found that the empirical law in the range of Reynolds number and shear rate $1 \leq Re \leq 500, 0 \leq Sr \leq 200$, respectively, follows as

$$C_L(Re) = \frac{1}{2} \left(\frac{1 + 16 Re^{-1}}{1 + 29 Re^{-1}} \right). \quad (1.14)$$

The above mentioned approaches are often used in industry to save the computational costs. Many studies of last decades cited in the previous section lead to the conclusion that in sedimenting flows reliable predictions can be obtained only if all the involved scales are taken into account. This requires to resolve the boundary layers of the particles in the system which can be achieved by direct numerical simulations, though it is still expensive within the technology of today's computing capacities. As emphasized in the previous section, changes of behavior of individual particles may affect a complicated system of large amount of particles. Transition scenarios of a single particle must thus be well elucidated first.

Many experimental studies were motivated by the unavailability of accurate theoretical models in the transitional regimes. The free fall of solids was intensively investigated. The development of sophisticated optical techniques, namely of high-speed imaging, particle image velocimetry (PIV) and of visualization methods and post-processing tools allowed for a precise tracking of all 6 degrees of freedom of the body as well as for the measurement of the velocity field (with the 3D PIV it is now possible to obtain velocity field in a volume). Researchers focused their attention mainly on the prototypical bodies possessing an axis of symmetry, namely on a sphere and on a disk. The advantage of considering these geometries is that path instabilities are easy to recognize as deviation from vertical fall. Nonetheless, the experimental approach also presents certain drawbacks for theoretical interpretations. Namely, it is difficult to control precisely physical parameters of the system and the boundary conditions, as well as to access in a non-intrusive manner all the relevant physical quantities. Another issue is the high cost of experimental equipment.

It was shown that standard particle models do not predict the trajectories of a spherical particle that moves with a speed corresponding to transitional regimes (Karamanev & Nikolov (1992)). At Reynolds numbers characteristic of the transition to turbulence in a sphere wake ($Re_\infty \geq 135$), experimental investigations (Karamanev *et al.* (1996)) give evidence that free light spheres ascend following oblique or spiral trajectories and the mean drag measured on the basis of the mean ascension velocity is greater than expected. The effect appears to be the stronger the lighter the particles.

1.3 Non-straight-trajectories and path instabilities

One of the most impressive features of a freely falling or rising object in a fluid is its non-straight trajectory, which seems a fundamental phenomenon for all bodies of any form starting from a moderately large scale. The old wisdom of I Ching (易经, in Chinese, or Classic of Changes) considers the world including Heaven, Earth, and living things as an indivisible whole where any tiny variation in one scale will have effect on any other scales. By taking extremely sophisticated law of changes, one can predict man's destiny or the state of any object in a given time. Very surprisingly, the incredible accuracy of these complicated theories of changes is based on one simple concept that everything is created by the interaction of Yin and Yang, without being confused by apparently complicated features.

The research on non-straight-trajectories of falling objects can be of great interest in scientific domains such as meteorology, biology, botany, especially in the study of seed dispersal, where falling seeds exhibit falling styles resembling that of disks. It focuses on the mechanism of the vortices generated in the wake of the objects and its dynamic effect on the body trajectories and shape oscillations (for deformable objects).

1.3.1 Path instabilities of non-deformable bodies

For objects falling or rising freely in a fluid it is known that, generally, as the Reynolds number increases, the body can experience eventually, after the first bifurcation sets in, various transition from steady oblique, steady oscillating, intermittent, tumbling, spiral to chaotic. Figure 1.5 lists the falling styles of disks, paper cards and maple seeds reported

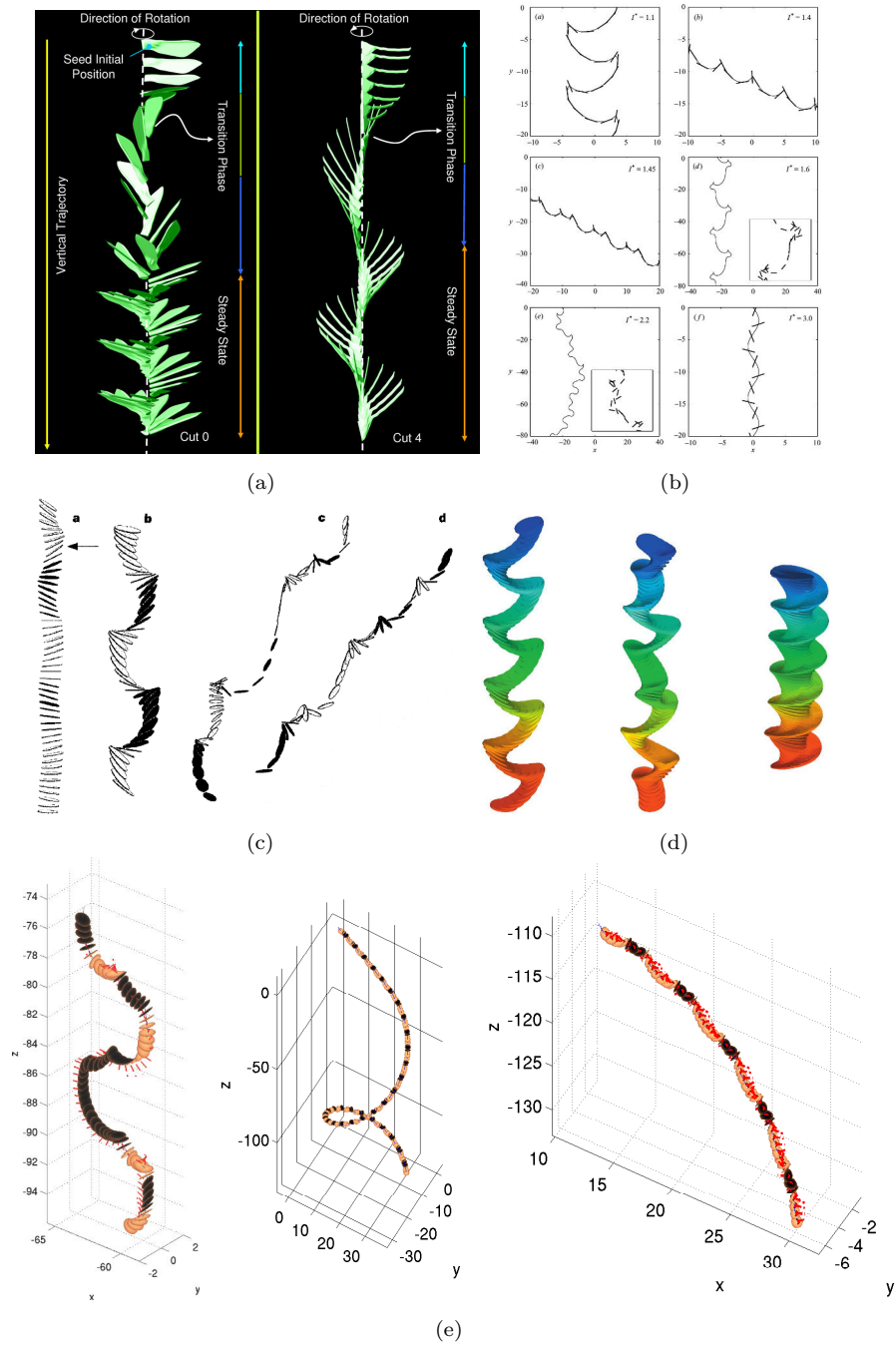


Figure 1.5: Numerical and experimental observations of falling styles: (a) auto-rotation of maple seeds (Varshney *et al.* (2012)); (b) tumbling with various periodicity of paper cards (Anderson *et al.* (2005)) and fluttering, intermittent, tumbling, spiral trajectories of thin disks ((c) Field *et al.* (1997); (d) Zhong *et al.* (2011); and (e) Chrust *et al.* (2013)).

in literature. The most directly observed characteristics may be the deviation of the path, direction of the rotation and the variation of the inclination angle for a non-spherical object. However, rich amount of information retrieved from the numerical and experimental data allows deeper understanding of the mechanism of the fluid-solid interaction.

The experiment of steel and lead disks falling in water and water/glycerol mixture performed by Field *et al.* (1997) motivated further studies on the intriguing transition scenarios of freely moving objects. Apart from the four classical falling states reported: steady vertical fall, fluttering (zigzagging), intermittent and tumbling, additional helical and transitional states for disks having small moments of inertia I^* have been observed by Zhong *et al.* (2011) experimentally (Figure 1.5(d)). After the primary bifurcation, vertically moving disks switch directly to a planar zigzag motion, this motion is further destabilized by the growth of a secondary oscillation in the normal direction, as this direction of oscillation rotates in the meantime, the disk starts to spin around the revolution axis.

Direct numerical simulations predict even more subtle trajectories. Chrust *et al.* (2013) evidenced, for light disks at higher Galileo numbers ($m^* = 0.25, G = 300$), a periodic version of the intermittent state between the regions of periodic fluttering and tumbling states (Figure 1.5, bottom left). The switching of the sign of the angular and horizontal velocity occurs periodically. A simulation starting from a tumbling state shows an angular velocity of positive sign with oscillations be perturbed by a rapidly growing “sub-harmonic modulation” resulting eventually in a change of the tumbling direction occurring, itself, periodically. The resulting trajectory becomes vertical in the average but is more complicated than the simple flutter. They also found a spiral tumbling motion for light disks at sufficient high Galileo number (for instance, $m^* = 0.5, G = 400$) where the tumbling state has its spiral counter-part (Figure 1.5, bottom middle and right) making the projection of its trajectories on the horizontal plane to be a large circle.

Periodically changing tumbling direction was evidenced also by Anderson *et al.* (2005) who explored the path instabilities for thin paper cards with more attention concentrated on the transition between fluttering to tumbling. By increasing the moment of inertia (I^*) they observed that the paper cards experienced normal periodic fluttering ($I^* = 1.1$), period-one tumbling ($I^* = 1.4$), period-two tumbling ($I^* = 1.45$), periodic mixture of fluttering and tumbling ($I^* = 1.6$), chaotic dynamics ($I^* = 2.2$) and small-amplitude broadside-on fluttering ($I^* = 3.0$) (Figure 1.5(b), from top to bottom, left to right for corresponding states). They suggested that the bifurcation between broadside-on descent and oscillatory motion is of supercritical Hopf type while that between fluttering and tumbling is a “heteroclinic” one which leads to a logarithmic divergence of the period of oscillation.

For objects with asymmetric mass distribution, the situation becomes different. Varshney *et al.* (2012) studied the trajectories of a falling maple seed using a high-speed camera (Figure 1.5(a)). They found that after releasing, the transition from rest goes through three stages: a tumble about the span-wise direction, followed by a tilt towards the vertical axis, leading to the gyration about the vertical axis and an opening of the cone angle before settling to the asymptotic state with a constant angular velocity. An unexpected observation of the same auto-gyration on a cut off wing of a maple seed made them measure carefully the kinematics of falling seeds with intact and cut wings, and point out three essential ingredients of observed helical motion, which are center of mass far away from the centroid of the seed,

a tilt initiated by aerodynamic damping and, in the asymptotic state, the balance between aerodynamic force and the gravity and centrifugal force exerted on the seed. Another study was also carried out (Varshney *et al.* (2013)) on falling parallelograms. Unlike maple seeds which auto-rotate but do not tumble, or rectangular cards which tumble but do not rotate, falling parallelograms exhibit coupled motion of auto-rotation and tumbling, similar to that of above mentioned falling disks of small m^* and high G .

1.3.2 Path instabilities of deformable bubbles

The fascinating phenomenon of zigzagging and spiraling rising bubbles have been attracting scientists and artists over centuries. The circling vortices generated in the wake remind us of the starry night of Van Gogh and even of a spiral galaxy. Studies on the characteristics of freely rising bubbles were investigated both experimentally and numerically (Mougin & Magnaudet (2002*b*); de Vries *et al.* (2002*b*); Ellingsen & Risso (2001); Zenit & Magnaudet (2008); Veldhuis *et al.* (2008)) for the last decade. It is known that small bubbles of diameter less than 1.5 mm rise in water vertically keeping their shape almost spherical by surface tension, while larger bubbles exhibit oscillating trajectories of zigzag and helical forms.

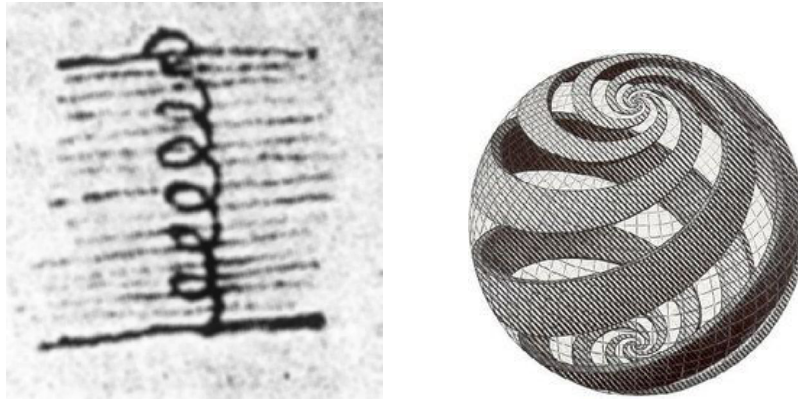


Figure 1.6: Left: Leonardo's sketch of the spiraling motion of a rising bubble (Prosperetti (2004)); right: "Sphere spirals" by M.C. Escher.

Most preliminary studies focused mainly on profiles of non-deformable axisymmetric bubbles. By considering the bubble shape as a non-deformable ellipsoid and varying the value of aspect ratio (χ) which characterizes the shape, Mougin & Magnaudet (2002*b*) performed numerical simulations showing the strong coupling between bubble rotation and two counter-rotating vortices in its wake, which are believed as the primary cause of the path instability. They found that beyond certain aspect ratio ($\chi = 2.2$, below which the loss of vertical motion can not occur) of bubble shape, the axisymmetric wake breaks into double-threaded with much vorticity being generated at the bubble surface. In zigzagging regime the double-threaded wake structure vanishes twice in one period making the bubble moving sideways in opposite directions periodically under the wake-induced lift forces. Further explorations (Magnaudet & Mougin (2007*b*); Zenit & Magnaudet (2008)) emphasized their suggestion of

direct link of the primary path instability with the wake instability due to sufficient vorticity generated by the oblate shape of the bubble. The instability results in a sideways motion and a zigzagging path.

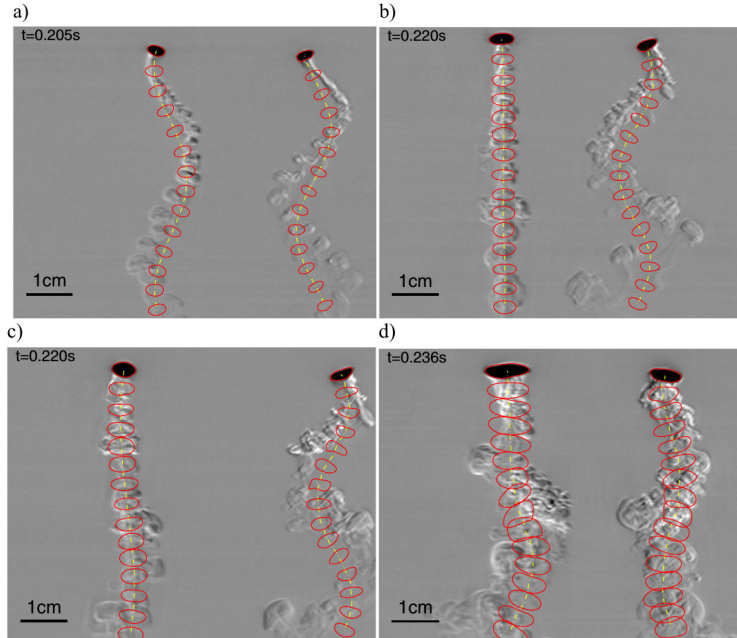


Figure 1.7: Experimental observations of two mutually perpendicular images of bubbles rising in purified water with the bubble path indicated by the dot-dashed line and the bubble shape indicated by the closed contours with an interval of 0.016 s, for Reynolds number equal to a) 1062, b) 1197, c) 1289, d) 1674 (Veldhuis *et al.* (2008)).

Similarly, Tchoufag *et al.* (2013) carried out linear stability analysis of the flow past a fixed spheroidal bubble to determine the regions of the flow most sensitive to perturbations. They found that for two perturbation modes of different forms of streamwise vortices corresponding to zigzag and helical motions, the sensitivity reaches the maximum in the core of the standing eddy and near the separation line, respectively. Moreover, as long as the condition of aspect ratio is fulfilled ($\chi \geq 2.2$ for zigzag and $\chi \geq 2.41$ for helical modes), the wake is found to be unstable only within a finite range of Reynolds number. However, the absence of instability for $\chi \leq 2.2$ for their spheroidal bubbles is in contrast with other results such as that of Cano-Lozano *et al.* (2013) assuming also a fixed but a more realistic bubble shape.

It is obvious that if we address the problem of the path instability of a deformable body, it is inevitable to discuss the effect of shape asymmetry and of shape variation resulting from the inertia of the fluid and the effect of surface tension. Unlike rigid bodies, loss of vertical motion can be caused either by unsteady vortices or shape asymmetry. Due to the fact that they are closely correlated in the process, the effect of these two phenomena is difficult to separate. The vortices can also be affected by shape asymmetry and vice versa as has been discussed by Tripathi *et al.* (2015). In a recent numerical work accounting for real

bubble deformation, they found that the path instability and shape asymmetry go hand in hand and the onset of primary instability is directly related to switching between axisymmetric and asymmetric shapes. Similarly, the numerical results of Gaudlitz & Adams (2009) focusing on the bubble shape variations during zigzagging rise showed that the main cause of the non-straight trajectories and periodic vortex shedding, is accompanied with the shape oscillation and results in a periodic asymmetric deformation.

1.4 Theory of the loss of axisymmetry in flows

Axisymmetric bodies fall (or rise) vertically if they are sufficiently small and their path instabilities are accompanied by axisymmetry breaking of the surrounding flow. All flows considered in this thesis are axisymmetric at low Reynolds numbers. This section is a brief summary of the theory of axisymmetry breaking in flows presented in Ghidersa & Dušek (2000), Jenny & Dušek (2004) and Chrust (2012). This theory is also the basis of the code used in the thesis.

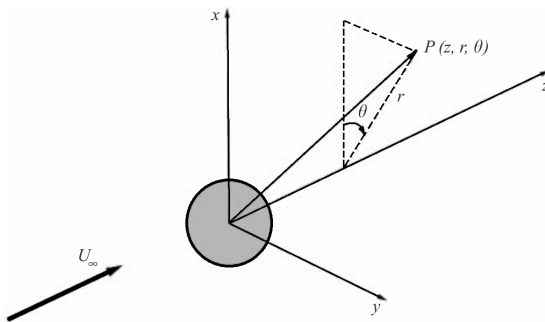


Figure 1.8: Problem geometry. U_∞ is the inflow velocity and the z -axis points in the flow direction.

The onset of the primary bifurcation making a particle losing its straight trajectories is often preceded by a detachment of the boundary layer and a build up of a recirculation zone. The linear stability analysis decomposes the problem of instability by considering an axisymmetric base flow plus a perturbation term. It can be extended to a weakly non-linear theory as was done for a jet by Danaila *et al.* (1998) or to describe the interplay of two unstable eigenvalues as done by Meliga *et al.* (2009). Linear stability analysis was also used to investigate the local sensitivity of the wake of a sphere, a disk and a spheroidal bubble by Tchoufag *et al.* (2013).

It has been shown by Ghidersa & Dušek (2000) that the axisymmetry of the base flow, equivalent to the fact that the linearized, fully three-dimensional, Navier–Stokes operator commutes with the operator of rotation $\partial/\partial\theta$ around the flow axis, implies that the linear stability problem can be split up by projection onto subspaces characterized by a specific azimuthal wavenumber m .

For axisymmetric flows the flow field is independent of θ , moreover, for non-swirling flows,

there is no azimuthal velocity. The linear stability of an axisymmetric solution (\mathbf{V}, P) , $\mathbf{V} \equiv (V_z, V_r, V_\theta)^T$ being the axisymmetric velocity field and P the pressure, consists in studying a perturbed flow field

$$\mathbf{v} = \mathbf{V} + \mathbf{v}', \quad p = P + p', \quad (1.15)$$

with an infinitesimal perturbation \mathbf{v}', p' expressed via complex eigenmodes Φ, Π associated with the eigenvalue λ :

$$\mathbf{v}' = \alpha e^{\lambda t} \Phi + c.c., \quad p' = \alpha e^{\lambda t} \Pi + c.c., \quad (1.16)$$

α being a small, but arbitrary, complex constant (c.c. standing for complex conjugate). The perturbation is amplified or dampened depending on the solution of the eigenvalue problem:

$$\lambda \Phi + \mathcal{L}[\mathbf{V}] \Phi + \nabla \Pi = 0, \quad (1.17a)$$

$$\nabla \cdot \Phi = 0, \quad (1.17b)$$

obtained by the linearization of the Navier Stokes equations around the axisymmetric solution (\mathbf{V}, P) . \mathcal{L} is a linear operator that commutes with the rotation operator $\partial/\partial\theta$, since the base flow is independent of θ . Hence, both operators have common eigenfunctions which can be expressed in the following form:

$$\Phi(z, r, \theta) = \sigma(m) \phi_m(z, r) e^{-im\theta}, \quad (1.18a)$$

$$\Pi(z, r, \theta) = \pi_m(z, r) e^{-im\theta} \quad (1.18b)$$

where $\sigma(m) = \text{diag}(1, 1, -i \text{sgn}(m))$, m stands for the azimuthal wavenumber, $m = 0, \pm 1, \pm 2, \dots$ and the array $\phi_m(z, r) \equiv (\phi_{m,z}, \phi_{m,r}, \phi_{m,\theta})$ represents, respectively, the azimuthal modes of the axial, radial and azimuthal velocity. The sign function $\text{sgn}(m)$ is zero for $m = 0$. The imaginary factor $-i \text{sgn}(m)$ is related to the complex representation of plane rotations discussed by Jenny & Dušek (2004) which is better suited than the usual polar coordinates in the plane normal to the symmetry axis.

In the general case of rotationally invariant swirling flows ($V_\theta(z, r) \neq 0$) the eigenvalue problem (Eqs. 1.17) breaks up into a sequence of independent eigenvalue problems in m -subspaces:

$$\lambda \phi_m + \Lambda_m[\mathbf{V}] \phi + \nabla_{|m|} \pi_m = 0, \quad (1.19a)$$

$$\nabla_{|m|} \pi_m \cdot \phi_m = 0, \quad (1.19b)$$

The eigenvalues $\lambda = \lambda_m$ depend obviously on m . The primary instability corresponds to the first eigenvalue λ_m crossing the imaginary axis. In the absence of swirl $V_\theta = 0$, the linear operator of Eqs. (1.19) is, moreover, independent of the sign of m so that

$$\Lambda_m[\mathbf{V}] = \Lambda_{|m|}[\mathbf{V}], \quad \lambda_m = \lambda_{|m|}, \quad \phi_m = \phi_{|m|}, \quad \pi_m = \pi_{|m|}. \quad (1.20)$$

	$m = 0$	$m \neq 0$
$Im(\lambda) = 0$	Steady axisymmetric	Steady non-axisymmetric
$Im(\lambda) \neq 0$	Unsteady axisymmetric	Unsteady non-axisymmetric

Table 1.1: Characteristics of the perturbed flow depending on the azimuthal wavenumber and on the imaginary part of the first eigenvalue to become unstable.

Depending on the azimuthal wavenumber and on the imaginary part of the first eigenvalue to become unstable, four scenarios summed up in Table 1.1 can be expected. Natarajan & Acrivos (1993) showed that it is the steady non-axisymmetric case with $m = \pm 1$ that applies to the sphere wake at the primary instability. For λ real, the corresponding eigensolution of Eq. (1.19b) can be taken real ($\phi_{-m} = \bar{\phi}_m$). Let us denote β the argument of the complex number α representing the amplitude of the initial perturbation amplitude. The flow perturbation that arises then has the form

$$\mathbf{v}' = 2 |\alpha| e^{\lambda_1 t} [\phi_{1,z}(r, z) \cos(\theta - \beta), \phi_{1,r}(r, z) \cos(\theta - \beta), \phi_{1,\theta}(r, z) \sin(\theta - \beta)]^T, \quad (1.21a)$$

$$p' = 2 |\alpha| e^{\lambda_1 t} \pi_1(r, z) \cos(\theta - \beta). \quad (1.21b)$$

Eqs. (1.21) together with (1.18a) show that the perturbation is symmetric with respect to the plane $\theta = \beta$ chosen arbitrarily by the initial conditions (by the initial perturbation of the flow).

The nonlinear terms of the Navier–Stokes equations will generate higher-order harmonics to the fundamental azimuthal mode Φ_1 . The perturbation will then be expanded into a full Fourier series:

$$\mathbf{v}'(z, r, \theta) = \sum_{m=-\infty}^{\infty} \sigma(m) \mathbf{v}'_m(z, r) e^{-im\theta}, \quad (1.22a)$$

$$p'(z, r, \theta) = \sum_{m=-\infty}^{\infty} p'_m(z, r) e^{-im\theta}. \quad (1.22b)$$

Note that $m = 0$ does not correspond to the whole axisymmetric mode but only to the axisymmetric nonlinear correction of the base flow \mathbf{V} . To describe the amplification of an infinitesimal perturbation proportional to the real linear mode the following initial condition can be assumed

$$\mathbf{v}'_1|_{t=0} = \alpha \phi_1, \quad p'_1|_{t=0} = \alpha \pi_1 \quad (1.23)$$

with a very small complex constant $\alpha = a e^{i\beta}$.

Being closely linked to the nonlinear theory of axisymmetry breaking in wakes of axisymmetric bodies, the azimuthal Fourier expansion can thus be considered as an optimal discretization for physical reasons. The axisymmetry gets broken if $m > 0$ (negative values are equivalent if no swirl is present). The most unstable eigenvalue is mostly in the $m = 1$ sub-space, however, Kotouč *et al.* (2009) have evidenced regular bifurcations in $m = 2$ and

$m = 3$ subspaces in the opposing flow past a heated sphere. The weakly non-linear effects at a regular axisymmetry breaking bifurcation were described to the third order of the instability amplitude A by Ghidersa & Dušek (2000) by a real Landau model:

$$\frac{dA}{dt} = (\lambda - C|A|^2)A, \quad (1.24)$$

where λ is the real positive eigenvalue and C a real constant (as opposed to the Landau model relevant to the Hopf bifurcation where the constants are complex). The amplitude A is, however, complex. The bifurcation is supercritical if $C > 0$. The growth rate λ of the instability is proportional to the parameter $\varepsilon = (Re - Re_{crit})/Re_{crit}$ close to the threshold and the saturation amplitude $|A|$ is proportional to $\sqrt{\varepsilon}$. The third order model makes it clear that the phase of the amplitude is arbitrary. A real amplitude A corresponds to a flow having a planar symmetry with respect to the plane defined by the real axis chosen in the complex perpendicular plane. The arbitrary phase accounts for the arbitrary orientation of the symmetry plane.

A weakly non-linear theory of the Hopf bifurcation was presented by Danaila *et al.* (1998). The cited paper suggests a 5-th order model required for explaining a relatively complex dynamics of a jet. A third order model is, however, sufficient to explain the existence of helical and planar zigzagging trajectories arising at a Hopf bifurcation. A third order model generalized to a simultaneous onset of a regular and a Hopf bifurcation was developed by Fabre *et al.* (2008) and Meliga *et al.* (2009). If the unstable eigenvalue in the problem (1.19) has a non zero imaginary part the instability generates two helical modes of opposite helicity corresponding to the unstable ($\gamma > 0$) complex eigenpair $\gamma \pm i\omega$. The helical modes are characterized by complex amplitudes A_+ and A_- . Any two-dimensional vectorial quantity in the plane normal to the base flow direction, say yOz plane, (e.g. the lift) is representable as a complex function of time $u_+ = u_y + iu_z$ expressed as:

$$u_+ = A_+(t)e^{i\omega t} + A_-(t)e^{-i\omega t}. \quad (1.25)$$

A weakly non-linear third order approximation of the dynamics of the axisymmetry breaking by a Hopf bifurcation yields the following two coupled equations for the amplitudes A_{\pm} (Danaila *et al.* (1998))

$$\frac{dA_{\pm}}{dt} = [\gamma - (C|A_{\pm}|^2 + D|A_{\mp}|^2)] A_{\pm}. \quad (1.26)$$

where C and D are complex constants, the same in both equations with upper and lower sign to account for the symmetry with respect to the change of the sign of helicity. A simple calculation shows that Eqs. (1.26) have two types of asymptotic solutions:

- a) one of $|A_+|$ or $|A_-|$ zero, the other equal to $(\gamma/C_r)^{-1/2}$,
- b) both modules equal and $|A_+| = |A_-| = [\gamma/(C_r + D_r)]^{-1/2}$.

(C_r and D_r stand for real parts of C and D . Both C_r and D_r are assumed to be positive.) For $C_r < D_r$ the solution a) is stable and b) is unstable. The converse is true for $D_r < C_r$.

The imaginary parts of C and D yield a non-linear shift of angular frequency. As a result, Eq. (1.25) yields asymptotic states:

$$u_{+, \infty} = \left[|A_{+, \infty}| e^{i(\omega' t - \varphi_+)} + |A_{-, \infty}| e^{-i(\omega' t - \varphi_-)} \right] \quad (1.27)$$

where $\omega' = \omega + \Delta\omega$ is the angular frequency of the limit cycle and φ_{\pm} phase shifts determined by the initial perturbation. The trajectory in the complex plane in the case a) is a circle and in the case b) a straight line the inclination of which is given by the phase shifts, i.e. by initial conditions. Danaïla *et al.* (1998) show that higher order non-linear effects may result in states with unequal amplitudes $|A_{+, \infty}| \neq |A_{-, \infty}|$ yielding a flattened ellipse instead of a straight line or a circle. (See Figure 1.9.)

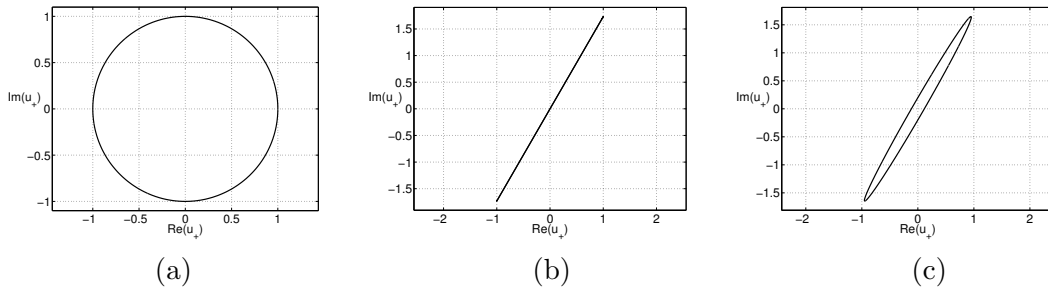


Figure 1.9: (Reproduced from Chrust (2012)) Paths in the complex plane of the modeled complex velocity of Eq. (1.27) for (a) a single non zero amplitude, $A_{-, \infty} = 0$, (b) two equal amplitudes $|A_{+, \infty}| = |A_{-, \infty}|$ and (c) for $|A_{-, \infty}| = 0.9|A_{+, \infty}|$.

In regimes where the modulus of the amplitude of both helical modes is the same we find a planar symmetry where the net helicity is zero. In the case of the wake of a thin disk at sufficiently high Reynolds number, the lift oscillates with a zero mean value in the same way as Figure 1.9(b). Similarly, the “zigzagging” trajectories, vertical in the average, correspond to this case. Purely helical trajectories of Figure 1.9(a) and “flattened” helical trajectories of Figure 1.9(c) correspond to a non zero helicity.

1.5 Wake of a bluff body

The instabilities in the wakes of fixed bluff body have been the first to be fully understood. The rise to the von Kármán vortex street in the wake of a cylinder placed perpendicularly to the flow has become a prototypical example of Hopf bifurcation, the latter having inspired the first speculative scenario of transition to turbulence suggested by Landau & Lipschitz (1959). Oscillations in wakes receive, however, also much attention from industry. For axisymmetric bodies, like spheres, spheroids and cylinders, they help in the understanding of oscillating paths of free particles.

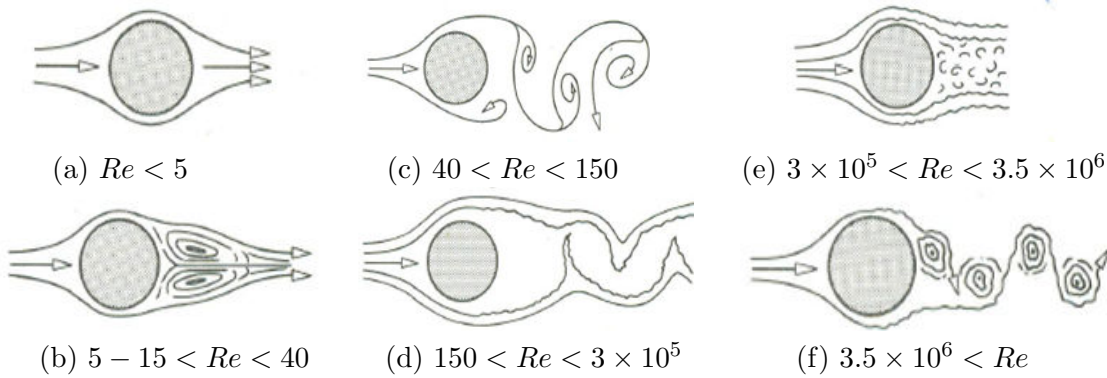


Figure 1.10: Sketch of transition of the vortical structures for an increasing Reynolds number in the wake of a cylinder. (a) unseparated streaming flow; (b) a pair of fixed vortices; (c) a laminar vortex street; (d) a turbulent vortex street; (e) narrowed and disorganized wake; (f) a narrower reestablished turbulent vortex street (Lienhard (1966)).

1.5.1 Wake of a fixed cylinder

Motivated by various applications of cylinders in industry, the transition scenario of flow past a fixed cylinder was well studied in the past. Fig. 1.10 illustrates the overall picture of regimes of flow past a circular cylinder in which an unseparated streaming flow becomes turbulent with increasing Reynolds number passing through stages of fixed vortices, laminar vortex street until becoming turbulent with laminar and turbulent boundary layer. When the Reynolds number is sufficiently small, the streaming flow keeps its unseparated characteristic while as Re slightly increases, a pair of vortices arises in the wake. It is not until $Re = 150$ that an established two dimensional laminar vortex street gives way to fully three-dimensional flow. Numerical linear analysis showed that the 2D flow becomes linearly unstable at $Re = 188.5$ (Henderson & Barkley (1996)). Up to $Re = 3 \times 10^5$ the previously laminar boundary layer in front of the separation point undergoes transition to turbulent boundary layer and the wake becomes narrow and disorganized. Beyond $Re = 3 \times 10^6$ a turbulent vortex street is reestablished but is narrower than for $150 < Re < 3 \times 10^5$.

1.5.2 Wake of a fixed sphere

For the problem of an unconfined sphere, experimental studies date back to the middle of last century (Taneda (1956), Magarvey & Bishop (1961)). Further investigation (Nakamura (1976), Sakamoto & Haniu (1990), Tomboulides *et al.* (1993), Sakamoto & Haniu (1995), Ormières & Provansal (1999), Johnson & Patel (1999), Ghidersa & Dušek (2000), Gumowski *et al.* (2008), Pier (2008)) focus on the range of moderate Reynolds numbers where the wake of the sphere experiences bifurcations before settling to a chaotic state. Some of their results are listed in Table 1.2 for the primary and secondary bifurcations and Table 1.3 for the onset of quasi-periodicity and of chaos. Unlike the flow past a fixed cylinder which becomes unsteady and loses its symmetry at a considerably lower Reynolds number $Re = 46$, the

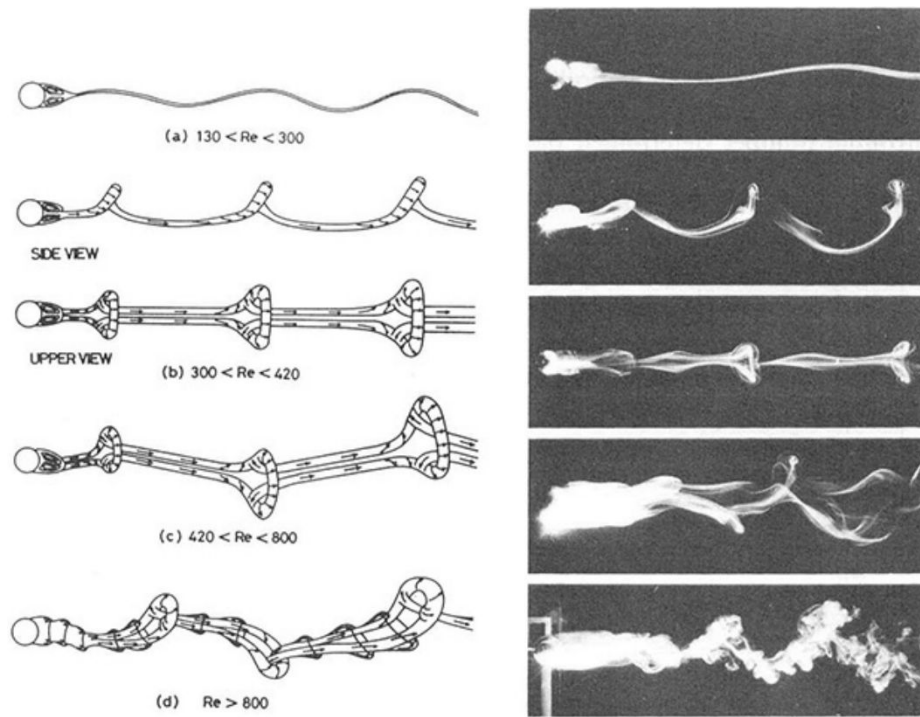


Figure 1.11: Patterns of vortex shedding in the wake of a sphere by Sakamoto & Haniu (1990).

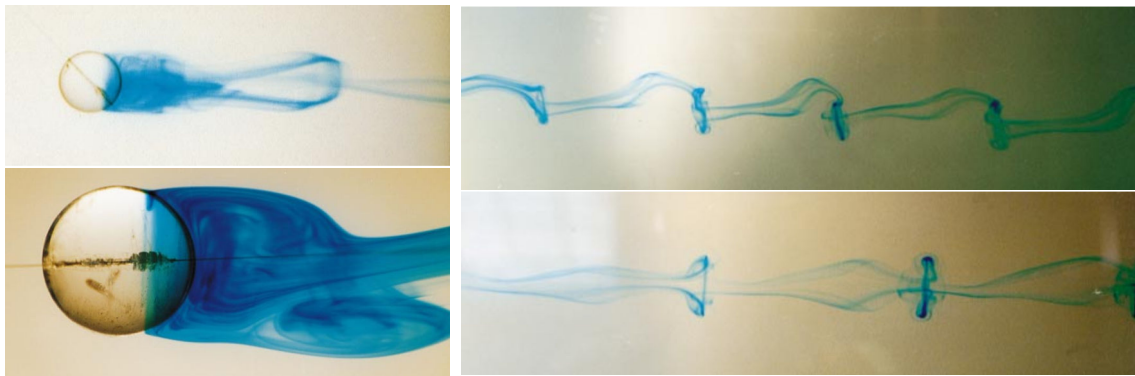


Figure 1.12: Dye visualization of the hairpin vortices at $Re = 300$. Near wake (bottom-left), (x, y) -plane (top-right) and (x, z) -plane (bottom-right) by Johnson & Patel (1999).

primary bifurcation yields a steady state with a non-axisymmetric wake consisting of two counter-rotating vorticity threads at $Re_1 = 212$. The secondary Hopf bifurcation which makes the double-thread becoming unsteady and triggers shedding of hairpin vortices from the sphere is not observed until Reynolds numbers larger than $Re_2 = 270$. The impressive ladder-like chain of hairpin vortices oriented in one direction inspires Johnson & Patel (1999)

to seek the forming mechanism. They conclude that, during the process, one loop of the wake vortex is shed downstream while the other loop moves under its self-induced velocity field across the wake to cut the next vortex loop free.

Authors	Re_1	Re_2	St
Taneda (1956)	130		
Magarvey & Bishop (1961)	210	270	0.1 ($Re = 300$)
Nakamura (1976)	190		
Natarajan & Acrivos (1993)	210	277.5	0.113 ($Re = 270$)
Tomboulides <i>et al.</i> (1993)	210-212	250-285	0.136 ($Re = 300$)
Sakamoto & Haniu (1995)		300	0.15-0.165 ($Re = 300$)
Ormières & Provansal (1999)	180-200	275-280	
Johnson & Patel (1999)	211	270-280	0.137 ($Re = 300$)
Ghidersa & Dušek (2000)	212	272.3	0.127 (Re_{crit})
			0.135 ($Re = 300$)
Pier (2008)	210-220	270-280	0.135 ($Re = 300$)

Table 1.2: Published results in literature concerning the critical Reynolds number of primary (Re_1) and secondary (Re_2) bifurcations and the Strouhal number (St) at the secondary bifurcation.

Authors	Re_3	St_{crit}	St_{500}	St_{1000}^l	St_{1000}^h
Achenbach (1974)	500		0.163-0.174		0.39
Kim & Durbin (1988)	360-375		0.171	0.187-0.202	0.33-0.37
Sakamoto & Haniu (1995)	420		0.175-0.18	0.195-0.205	0.29-0.34
Tomboulides & Orszag (2000)	300-500	0.045 0.136	0.167	0.195	0.35
Mittal (1999)	350-375		0.05 0.17-0.19	0.05 0.17-0.19	
Ormières (1999)	390	0.12-0.13			
Bouchet <i>et al.</i> (2006)	325	0.137			

Table 1.3: Critical Reynolds number (Re_3) for the third (chaotic) bifurcation and the Strouhal number for $Re = Re_3$, $Re = 500$ and $Re = 1000$, note that different frequencies coexist.

The third bifurcation is of Hopf type and leads to quasi-periodicity (Bouchet *et al.* (2006)). At Reynolds number $Re = 500$, Tomboulides & Orszag (2000) report one dominant Strouhal number 0.167 with an existing lower frequency 0.045 which has been confirmed by Bouchet *et al.* (2006) at the onset of the second Hopf bifurcation for $Re = 325$. This, about 3 times smaller ratio, “appears to vary smoothly with the Reynolds number” which characterizes quasi-periodicity. The same lower frequency is found (Mittal & Wilson (1999)) to be present at even higher Reynolds number for $Re = 500, 650, 1000$. At Reynolds number

$Re = 1000$, about twice higher frequencies are observed (Achenbach (1974), Kim & Durbin (1988), Sakamoto & Haniu (1995), Tomboulides & Orszag (2000)). When the Reynolds number exceeds 800, they report the appearance of small scales in the sphere wake due to a Kelvin–Helmholtz instability of the separated shear layer.

The shape, size and corresponding variation of the cores of vortices have been examined experimentally by Przada *et al.* (2008) for $250 < Re < 310$. They found that vortices are elliptical and comparably as large as the sphere. Concerning the size of the recirculation zone, by using the nonlinear dynamical systems theory Ghidersa & Dušek (2000) showed that the recirculation zone of the axisymmetric average of the non-axisymmetric flow ($m = 0$ mode) must be shallower and shorter compared to the base flow, which is also the case for the time averaged wake of a cylinder as pointed out by Zielinska *et al.* (1997): the onset of the bifurcation reverses the trend of growth of the recirculation zone: while in the subcritical and steady base flow the recirculation length grows with increasing Reynolds number, the time, or azimuthal, average of the unsteady or non-axisymmetric, supercritical flow has a decreasing recirculation length.

Considering the fact that the global dynamics of shear flow depends closely on the local instability characteristics, Pier (2008) carried out the local linear stability analysis for both the axisymmetric and asymmetric base flows by the frequency damping method of Åkervik *et al.* (2006). His results evidenced an absolutely unstable region (a “wave-maker”) in the near wake which sustains fluctuations that develop *in situ* and feed waves into the downstream connectively unstable domain. He found that the absolutely unstable regions appear for $Re > Re_a \simeq 130$ (which may correspond to the threshold of Taneda (1956) of a faint periodic motion “with a very long period”, listed in the first line of Table 1.2) and keep being unstable beyond the primary bifurcation for $Re > Re_1 \simeq 212$.

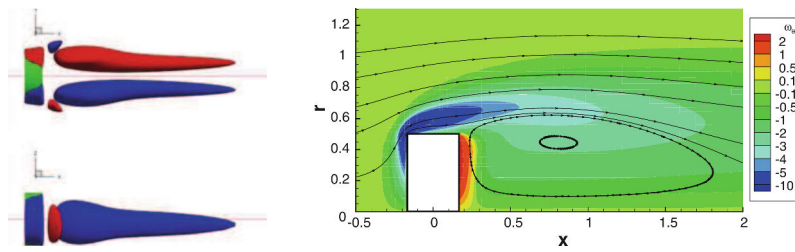
1.5.3 Wake of a fixed disk

Imagine that the cylinder present in the previous section has an axial length smaller than its diameter and we turn it by 90 degrees letting its circular cross-section perpendicular to the flow direction. We directly find that the flattened shape makes the observation of primary bifurcation occur considerably earlier (at $Re \approx 160$ for disk of aspect ratio $\chi = d/h = 3$, d being the diameter of the cross-section and h its axial length) than that of a sphere, moreover, the transition process consists in several new regimes which do not exist for a sphere. Figure 1.13 illustrates newly found regimes, named “Knit-Knot” (Figure 1.13(c)) and “Yin-Yang” (Figure 1.13(d)) modes by Auguste *et al.* (2010), for disk of $\chi = 3$. The “Zig-Zig” mode is that of a sphere above the secondary bifurcation. It does not exist for an infinitely flat disk, where it is replaced by specific “Yin-Yang” (RSB -reflectional symmetry breaking, i.e. periodic without planar symmetry) and “Zig-Zag” (unsteady symmetry preserving, standing wave or planar periodic with zero mean lift) modes.

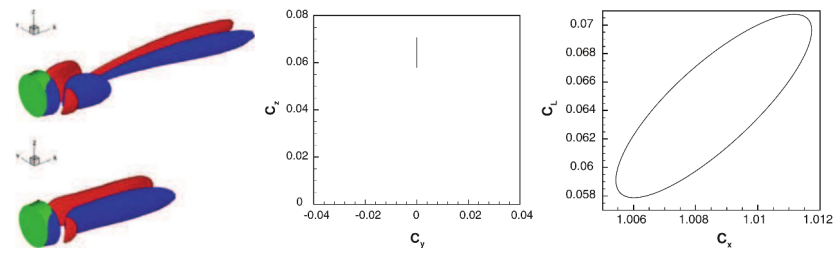
Some reported critical Reynolds numbers and the corresponding Strouhal numbers for different aspect ratio listed in Table 1.4 show quite small discrepancies between numerical results (except for $\chi = 10$) in Table 1.4). Experiments face the difficulty of setting the cross-section of a disk exactly perpendicular to the flow direction in experiments and the effect of slightly imperfect axisymmetry in axial direction results in significant change concerning the

selection of symmetry plane as already noted by Meliga *et al.* (2009). The effect of inclination angle on the onset of instability is further explored by Chrust *et al.* (2015) numerically with joint experiments. They concluded that the vortex shedding is promoted (the critical Reynolds number decreases) at inclination angles smaller than 20° while restrained for larger inclinations (see Table 1.5). Non-negligible discrepancies between numerical and experimental results however subsist even if the inclination is accounted for. They are suggested to be due to the confinement of the water tunnel and the presence of cylinder support in the experimental set up.

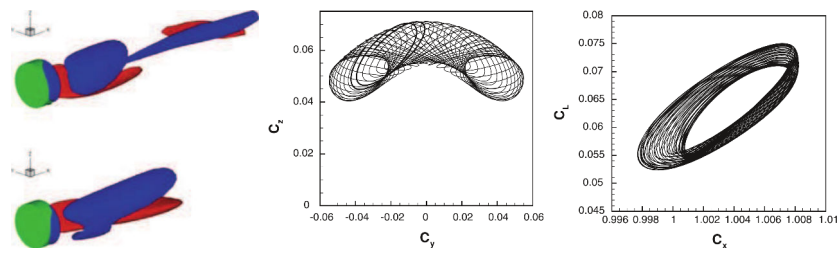
The numerically computed Strouhal numbers reported in all oscillatory regimes for a certain aspect ratio are also in a good mutual agreement (see Table 1.4). They are smaller than that of a sphere. Co-existing frequency of about 3 times smaller than the leading one is found in the transition to chaos similarly as for spheres.



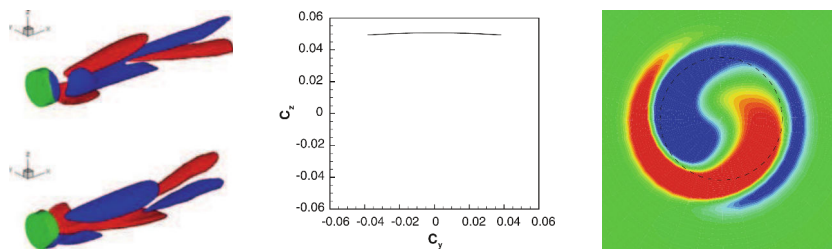
(a) Left: iso-surfaces of the streamwise vorticity of non-axisymmetric steady state ($Re = 165$); right: azimuthal vorticity for axisymmetric flow ($Re = 150$).



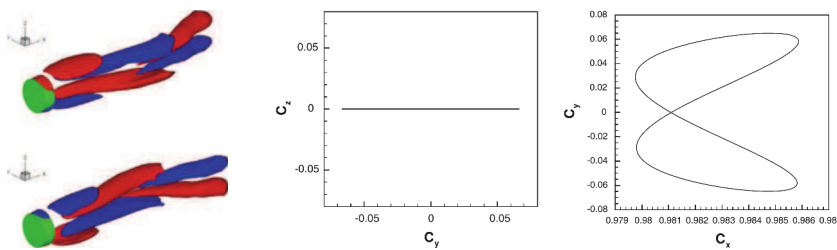
(b) Periodic, reflectional-symmetry-preserving (or “Zig-Zig” mode) at $Re = 182$.



(c) Quasi-periodic pulsating (or “Knut-Knot” mode) at $Re = 187$.



(d) Periodic, reflectional-symmetry-breaking (or “Yin-Yang” mode) at $Re = 195$.



(e) Periodic mode with reflectional symmetry and zero mean lift (or “Zig-Zag” mode) at $Re = 216$.

Figure 1.13: Bifurcations in the wake of a flat cylinder ($\chi = 3$) by Auguste *et al.* (2010).

Shenoy & Kleinstreuer (2008)¹, Chrust <i>et al.</i> (2010)², $\chi = 10$						
state	I	II	III	IV	V	
Re_{crit}^1	< 135	135	155	172	280	
Re_{crit}^2	< 129.6	129.6	136.6-138.7	154.4	188.8	
St^1			0.113			
St^2			0.115	0.114		
Auguste <i>et al.</i> (2010)¹, Chrust <i>et al.</i> (2010)², $\chi = 3$						
state	SS	'Zig-Zig'	'Knit-Knot'	'Yin-Yang'	'Zig-Zag'	Chaotic
Re_{crit}^1	159.8	179.9	184.7	190.4	215.2	240
Re_{crit}^2	159.65	181-182	185-190	195-198	220-230	235-240
St^1		0.109				
St^2		0.112	0.112	0.112	0.111	
Fabre <i>et al.</i> (2008)¹, Meliga <i>et al.</i> (2009)², Chrust <i>et al.</i> (2010)³, $\chi = \infty$						
state	SS	RSB	SW	QSP		
Re_{crit}^1	115	121.5	139.6			
Re_{crit}^2	116.92	124-125.2	142-143	165-170		
St^2		0.120	0.118			
Re_{crit}^3	116.9	125.3	143.7			
St^3		0.121	0.118			

Table 1.4: Published studies on bifurcations of fixed disks with various aspect ratio (χ). The table recalls the original terminology of various papers.

State: I: steady axisymmetric, II: steady asymmetric, III: 3D, periodic, regularly rotating separation region, IV: unsteady planar symmetric, V: unsteady, loss of planar symmetry, SS: steady non-axisymmetric, RSB: reflectional symmetry breaking, SW: standing wave, QSP: quasi-periodic.

Chrust <i>et al.</i> (2015), inclined disk ($\chi = \infty, 6$)									
ϕ	0	5	10	15	20	30	40	50	60
$Re_{\chi=\infty}^{num}$	125.2		116.1		102.6	110.0	136.9	205.4	
$Re_{\chi=6}^{num}$	150.0		145.3		136.5	140.0	158.9	200.0	266.8
$Re_{\chi=6}^{exp}$	166	164	162	154	145	163		212	280
$St_{\chi=\infty}^{num}$	0.120		0.113		0.132	0.171	0.239	0.352	
$St_{\chi=6}^{num}$	0.120		0.117		0.130	0.154	0.205	0.254	0.321
$St_{\chi=6}^{exp}$	0.158	0.147	0.143	0.156	0.158	0.170		0.212	0.226

Table 1.5: Numerical and experimental results on the onset of the Hopf bifurcation for inclined disks of aspect ratio $\chi = \infty$ and $\chi = 6$.

The effect of variation of aspect ratios has been studied experimentally by Bobinski *et al.*

(2014). The observation confirms the increasing trend of the threshold of instability for decreasing aspect ratio. For objects of other geometries, similar transition scenario in the wake of cubes was evidenced (Saha (2004); Klotz *et al.* (2014)). By linear analysis of the Fourier decomposition on streamwise vorticity, Klotz *et al.* (2014) suggest that the observed irregular amplitudes of mode $m = 4$ are due to the characteristics of the body geometry rather than instability effects connected with other modes, as the mode $m = 4$ contributes most energy to the base flow whereas in cases of spheres and disks it is the mode $m = 0$.

1.6 Freely falling or rising spheres

As we have gained a global picture of how it looks like generally in the wake of a fixed sphere from the previous section, let us now set the body free. From this moment on, we find that it rises or falls because it is light or dense, i.e. its solid/fluid density ratio is smaller or larger than one. We are very curious to know how much the transition scenario becomes different and, more accurately, how much the values of bifurcation thresholds vary, if the scenario remains close to that of a fixed sphere. The scenario turns out to be very different if we compare the motion of a rising sphere to that of a falling one.

Early experiments of Magarvey & Bishop (1961) and Magarvey & MacLachy (1965) show vortex shedding very similar to that observed in the wake of a solid fixed sphere. At density ratio $1 < \rho_s/\rho < 1.6$ (ρ_s being the density of the body and ρ that of the fluid) and Galileo number $G \approx 250$ ($G = \sqrt{|\frac{\rho_s}{\rho} - 1|gd^3/\nu}$ where g is the acceleration due to gravity, d the diameter of the sphere and ν the kinematic viscosity) the observed Strouhal number is 0.12. Another much smaller frequency $St \approx 0.07$ is reported by Goldburg & Florsheim (1966) at $Re = 300$ ($G \approx 220$) and $\rho_s/\rho = 1.12$.

A globally clear diagram of the transition scenario of freely moving spheres did not exist until the paper by Jenny *et al.* (2004) which provided a parametric numerical study in the two-parameter plane of density ratios and Galileo numbers accompanied with joint preliminary experiments. In the paper, the significant difference of the transition to a full spatio-temporal chaos between rising and falling spheres is well demonstrated. For very dense spheres, the results obtained are in agreement with the results of simulation of the fixed sphere wake. The threshold of the primary (regular, axisymmetry breaking) bifurcation is independent of the density ratio and lies only a little lower than that of a fixed sphere. The difference between light and dense spheres appears at the onset of the secondary instability yielding the oblique oscillating state. Jenny *et al.* (2004) found that the density ratio $\rho_s/\rho = 2.5$ seems to be the threshold delimiting the high and low frequencies at the onset of the oblique oscillating state. Below this value spheres rise or fall with a low frequency whereas denser spheres fall with an approximately 2.5 times larger frequency. The further transition to chaos was also found significantly different for light and dense spheres. For light spheres the trajectories tend to become zigzagging with low and high frequency (the latter appearing inside the chaotic region of the parameter space). Irregular but close to helical trajectory were evidenced for early chaotic regimes of dense spheres. The paper focuses also on differences between experimental observations and the numerical results. For the two primary states, the steady oblique and oblique oscillating ones, the agreement between numerics and experiment

was found very good. However, the low-frequency periodic zigzagging state failed to be observed experimentally. Jenny *et al.* (2004) provide an explanation in terms of a non-uniform mass distribution of the spheres in the experiment.

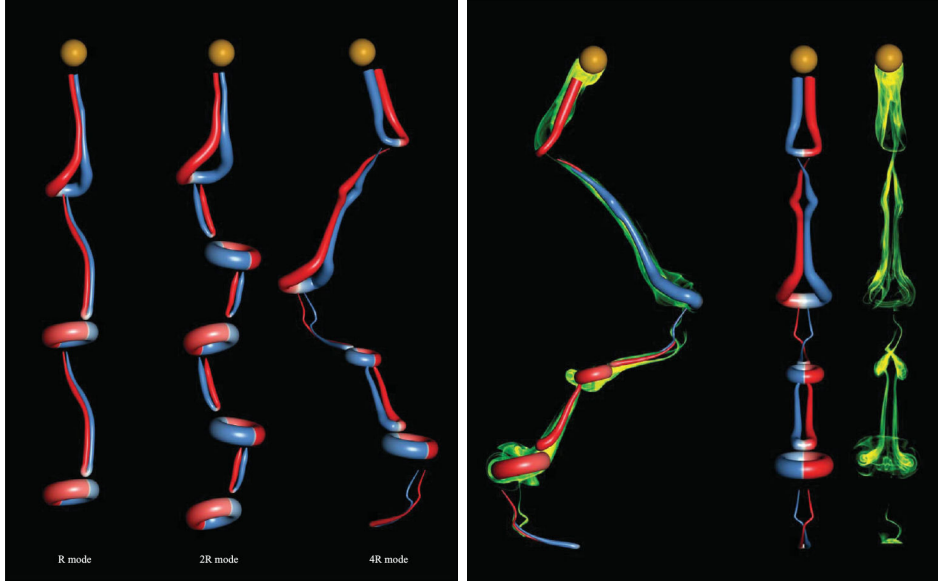


Figure 1.14: Left: the family of periodic wake modes for rising and falling spheres. R mode: steady oblique state ($m^* > m_{crit}^*$, $270 < Re < 600$, m^* being the mass ratio of sphere and fluid), 2R mode: vertical state comprising a double-sided chain of vortex rings ($m^* > m_{crit}^*$, $Re > 600$); right: creation of a three-dimensional rendering of the 4R mode in the periodic zigzagging states ($m^* < 0.4$, $260 < Re < 1550$ and $m^* < 0.6$, $Re > 1550$). The color corresponds to the initial sign of the streamwise vorticity component: positive in red, negative in blue (Horowitz & Williamson (2010)).

Further experimental work by Veldhuis & Biesheuvel (2007) confirmed the conservation of the two earliest transitional states but did not evidence the the periodic zigzagging state. In contrast, focusing on the problem of the occurrence of vortex induced vibration, Horowitz & Williamson (2010) found that in a wide range of considered Reynolds number between 100 and 15000, there exists a critical mass ratio ($m_{crit}^* \equiv \rho_s/\rho$) below which the trajectories of the spheres are planar, periodic and vertical in the mean. Their frequency is situated between the numerically obtained high and low frequency zigzagging states. The value of m_{crit}^* is nearly constant over two decades of Reynolds number ($m_{crit}^* \approx 0.4$ for $260 < Re < 1550$ and $m_{crit}^* \approx 0.6$ for $Re > 1550$). Two modes of single- and double-sided vortex and a new mode consisting in four vortex rings per cycle in the regime of zigzagging oscillation are observed (Figure 1.14). The problem of vortex induced vibration (VIV) for moving spheres was studied already by Govardhan & Williamson (2005) and their groups. In the experiment they compared the cases of a (very light) tethered sphere and an elastically mounted (of higher mass) one induced to vibrate under the action of their own vortical

wake, respectively, in a transverse motion and both streamwise and transverse. They found that when the oscillation frequency (f) is of the order of the static-body vortex shedding frequency (f_{vo}) two modes of periodic large-amplitude oscillation arise and are separated by a non-periodic transition regime. The different responses to this regime between light tethered and heavier mounted spheres are consistent with the large difference in the phase of the vortex force between both, which is also consistent with the aforementioned, stronger fluid – solid interaction. The question whether the behavior of tethered spheres is relevant for the understanding of path oscillation of totally free spheres is, however, open.

1.7 Axisymmetric but aspherical bodies (disks, flat cylinders, spheroids)

Spheres are of course not the only prototypical body considered concerning the path instabilities. In this section we discuss mainly the motions of bodies having an axisymmetric but aspherical shape.

Earlier experimental studies (Willmarth *et al.* (1964); Field *et al.* (1997)) brought the fall of disks and of flat axisymmetric bodies to the spotlight. The visualizations of the wake behind the disks and of intriguing non-straight paths motivated further investigations. Using the particle–image–velocimetry (PIV) technique, Fernandes *et al.* (2007) found a good agreement between the flow field of a freely rising disk of aspect ratio $\chi = 10$ with that of a fixed body obtained by DNS. They remark, however, a significant disagreement between the predictions of the onset of oscillation by numerical simulations of the wake of a fixed cylinder and their experimental observations for very flat cylinders of aspect ratio larger than 8. Ern *et al.* (2011) suggest that small amplitude states precede the onset of flutter. They were described as “possibly irregular or even chaotic”, which was further confirmed by numerical simulations of Auguste (2010). The variety of observed trajectories was completed by Zhong *et al.* (2011) who report a destabilization of the planar zigzagging yielding spiral trajectories for disks having a small moment of inertia.

With their numerical simulations, Auguste *et al.* (2013) and Chrust *et al.* (2013) provide each a state diagram of transition scenario for infinitely thin disk in $Ar - I^*$ and $G - m^*$ parameter planes, respectively. Ar is the Archimedes number $Ar = \sqrt{3/32}U_g d/\nu$ where $U_g = \sqrt{2|\rho_s/\rho - 1|gh}$ is the gravitational velocity and $I_* = (\pi/64)\rho_s/\rho\chi$ the dimensionless moment of inertia. $m^* = m/\rho d^3$ is the dimensionless mass and G stands for the Galileo number defined for infinitely flat disks as $G = \sqrt{m^*gd^3}/\nu$. The transition scenario is quite different from that observed in the wake of a fixed disk.

According to Chrust *et al.* (2013), the transition to chaos for a disk initially at rest in a fluid can be generally characterized by four stages (vertical, flutter, intermittent and tumbling) plus three additional distinct styles (spiral, quasi-vertical periodic and chaotic) for very light disks and another two three-dimensional trajectories (tumbling-zigzagging and spiral tumbling) for more massive disks. At sufficiently low Galileo number, disks follow a vertical path, as soon as the primary bifurcation sets in, which occurs at a larger Galileo number for lighter disks, they start to flutter and exhibit zigzagging states. The Strouhal number in this regime can be as high as 0.6 for an infinitely light disk ($m^* = 0$). In a

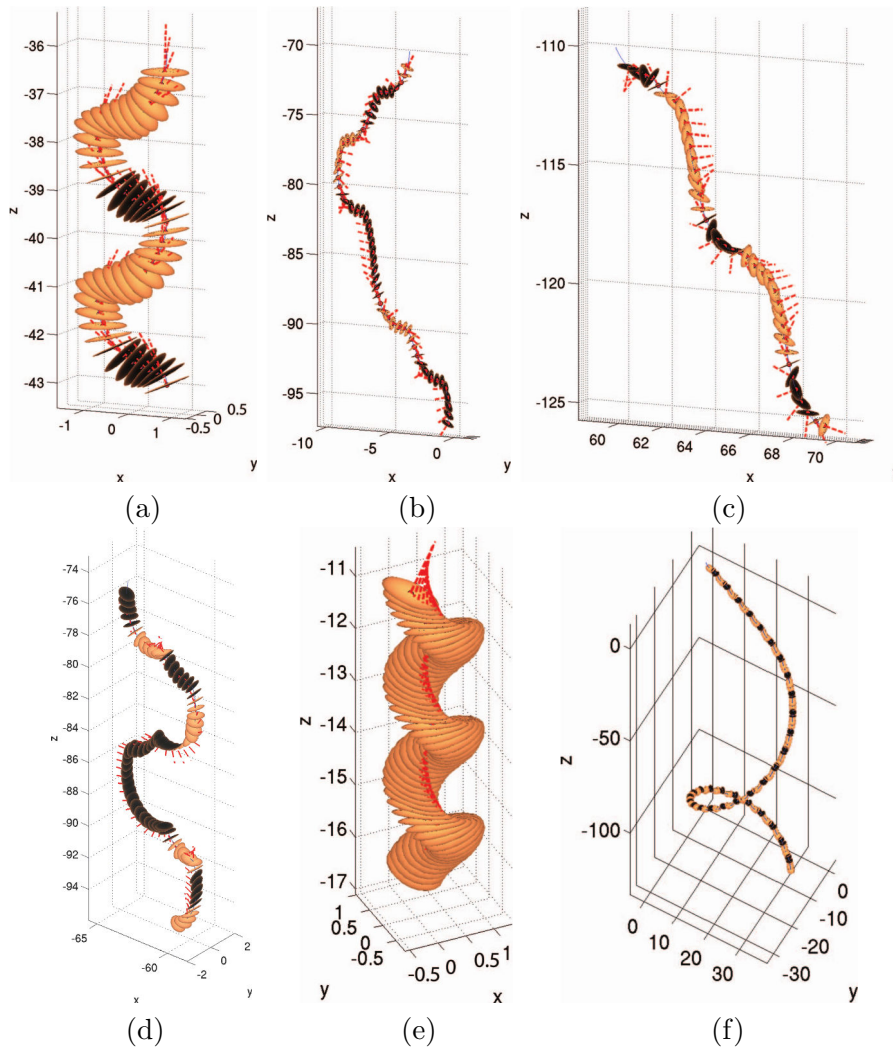


Figure 1.15: Distinct moving styles of infinitely thin disks by Chrust *et al.* (2013), (a) fluttering periodic state ($m^* = 0.1$, $G = 200$); (b) intermittent ($m^* = 0.25$, $G = 110$); (c) tumbling ($m^* = 0.5$, $G = 160$); (d) tumbling-zigzagging ($m^* = 0.25$, $G = 300$); (e) spiral ($m^* = 0.05$, $G = 300$); (f) spiral tumbling ($m^* = 0.5$, $G = 400$).

region of the parameter space delimited by $0.25 < m^* < 2$ and $G > 50$, the inclination angle of fluttering disks exceeds 90 degrees but the tumbling is not yet stable enough to persist in a periodic regime which results in an intermittent rotation with irregular interval and changes of direction (green symbols in Figure 1.16). For more massive disks ($m^* > 0.5$), as the Galileo number further increases, periodic tumbling and tumbling-zigzagging trajectories are evidenced. For very light disks ($m^* \leq 0.05$), quasi-vertical periodic (QVP) and chaotic (QVC) states are found. They are characterized by a very small amplitude of the horizontal velocity component. The Strouhal numbers of the QVP are approximately equal to 1/3 that

of the flutter states. At higher Galileo numbers a non zero helicity systematically sets in. The most beautiful spiral paths are evidenced at high Galileo numbers. The disk keeps a constant inclination angle and a constant angular velocity along this trajectory (E.g. angle of 25° and $\omega_z = 0.635$ at $m^* = 0.25$ and $G = 400$). Special and intriguing spiral tumbling trajectories are found to exist at sufficiently high Galileo numbers for all disks of any value of dimensionless mass. The projection of the trajectory on the horizontal plane describes a large circle and the pitch angle of the spiral is equal to 42.5° . In figure 1.16, the trajectories losing their planarity due to non zero helicity are represented by filled symbols (red triangles, green squares and blue circles).

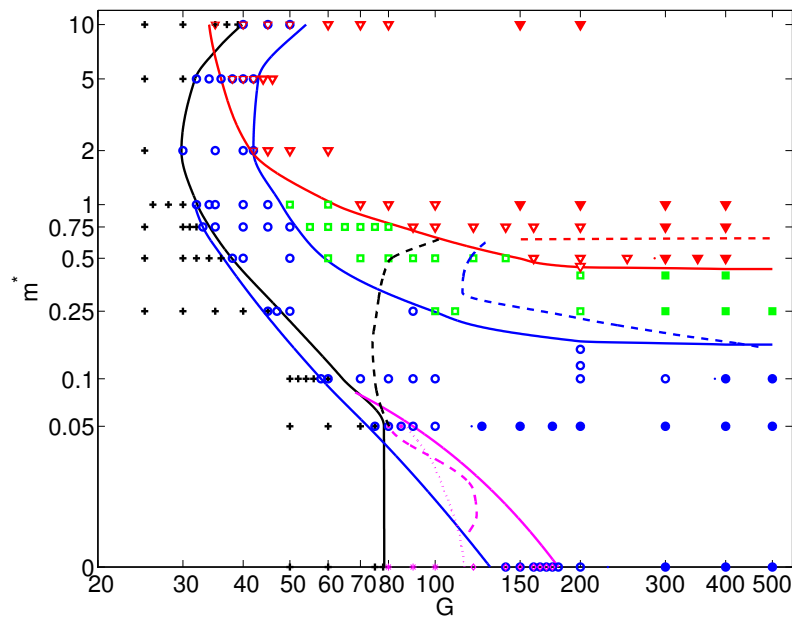


Figure 1.16: The state diagram of an infinitely thin ($\chi = \infty$) disk by Chrust *et al.* (2013). Red triangles: tumbling; black squares: intermittent; blue circles: flutter; black crosses: vertical. Small region of the coexistence of the vertical and oscillating states due to the sub-critical effect is depicted by the left-most blue line. Dashed lines correspond to the experimental results of Field *et al.* (1997) and Willmarth *et al.* (1964).

However, in the real world, disks are not “infinitely” thin. The issue to what extent a disk can be considered “thin” and whether all characteristic values have a limit as the disk becomes thinner and thinner is discussed in detail by Auguste *et al.* (2013) who compared the thresholds of zigzagging state for flat cylinders of aspect ratio $\chi > 10$ and found that for a given I^* , the characteristics of zigzagging motion are still significantly different between disks of $\chi = 25$ and $\chi = 50$. Considering the preliminary numerical results of freely moving spheroids of large aspect ratios by Chrust (2012), presenting no such significant difference between spheroids of aspect ratio ten end infinity, this sensitivity may be due to the sharp corners in the geometry.

As remarked by Chrust (2012), the interesting issue of the link between the characteristics of infinitely thin disks and of spheres can be addressed by investigating spheroids of variable aspect ratio. A fine numerical investigation of the variation of the scenario with the aspect ratio of spheroids will be carried out in this thesis.

1.8 Bubbles and drops

The most important characteristic of bubbles and drops is their deformable shape. Depending on the values of the Galileo number G (or the Reynolds number Re) and the Bond number Bo (same as the Eötvös number Eo), the shapes of bubbles and drops in unhindered gravitational motion in liquid before the breakup are classified into three categories: spherical, ellipsoidal and spherical-cap. In general, bubbles and drops can be approximately considered as spheres when their size is tiny since the inertia forces are much smaller than surface tension and viscous forces. Ellipsoidal bubbles and drops are oblate and convex when viewed from inside, though in reality the shapes may be far from an axisymmetric ellipsoid. This is the most often assumed shape in today’s numerical studies. Spherical-cap or ellipsoidal-cap often correspond to large bubbles and drops which look similar to segments cut from spheres or spheroids. They can be “dimpled” if the rear of the shape has an indentation, or “skirted” if the indentation is large enough to form a thin envelop of dispersed fluid (Figure 1.17).

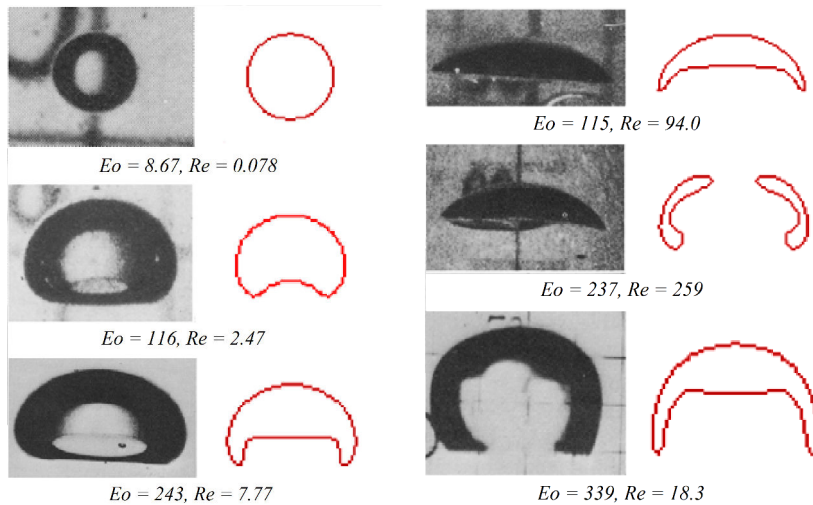


Figure 1.17: Simulated bubbles (red) by Hua & Lou (2007) compared to experimentally observed shapes by Bhaga & Weber (1981).

The second important feature is that under certain conditions bubbles and drops break up. The different corresponding regimes of breakup can be already noticed earlier from their different trends to deformation. According to the studies reported in literature, bubbles often dimple from the center (Bhaga & Weber (1981)) while drops possess a spherical-cap (Han & Tryggvason (1999)). As a consequence, doughnut shaped bubbles are created by successively

deeper dimpling until the pinch-off, whereas flattened drops break up into smaller fragments under several modes including shear, bag and catastrophic breakup.

Figure 1.18 demonstrates a sequential picture of droplet deformation and fragmentation by Jalaal & Mehravaran (2012). As the droplet falls, the deformation from the initial spherical shape to an oblate ellipsoid is followed by bag formation at the preliminary stages (figure (a) to (c)). When the surface tension is not sufficient to hold the droplet in a stable shape, the bag-like shape grows and breaks up, forming ligaments, liquid bridges and even smaller droplets. A very thin disk-like core is left during the bag breakup. This core breaks up in a short lapse of time. The process continues and fragments in each stage break up further until all fragments reach a stable condition. Three modes of breakup evidenced in numerical simulations by Tripathi *et al.* (2015) represented in Figure 1.19 suggest that bubble breakup occurs at both moderate and high Galileo and for high Bond numbers. They also found a new mode of breakup at high Galileo number and significant surface tension where even smaller bubbles are ejected from the rim of the original one during when it recovers from an initially elongated to a spherical cap shape. The strong vertical stretching gives rise to a narrower skirt which results in an ellipsoidal rather than a cap-like bubble and a small tail of satellite bubbles (Figure 1.19(c)).

Prior to the breakup, the kinematics and shape oscillations of bubbles and drops are still only very partially understood. To determine the effect of rising on the dynamics of inertial shape oscillations, axisymmetric numerical simulations were performed by Lalanne *et al.* (2013) and the results were analyzed by spherical harmonic decomposition. Two major differences between bubbles and drops were observed. Bubbles experience larger acceleration and deform more and faster than drops due to the negligible mass, the shape oscillations of bubbles cause much stronger velocity oscillations than those of drops.

As shown by experimental studies (Mougin & Magnaudet (2002*b*); Wu & Gharib (2002); de Vries *et al.* (2002*b*); Shew *et al.* (2006); Veldhuis *et al.* (2008)), bubbles rising in a vertical path develop a zigzagging motion in a plane which subsequently evolves into a spiraling motion after a certain number of periods. The wake behind is found quite similar to that of a fixed or moving solid body both in the zigzagging (characteristic by a regular generation and shedding of alternate oppositely oriented hairpin vortices) and spiraling states (with a twisted pair of streamwise vortex filaments).

An important issue consists in setting the stability limit of the vertical rise of bubbles. This loss of stability assumed to be directly related to the onset of the experimentally observed non-vertical trajectories. Traditionally, this theoretical problem was addressed assuming a fixed spheroidal shape of the bubble (Mougin & Magnaudet, 2002*b*; Tchoufag *et al.*, 2013, see e.g.). Recently, Cano-Lozano *et al.* (2013) analyzed numerically the path instability of axisymmetric bubbles of realistic shapes obtained by axisymmetric simulations for a set of combinations of the Bond and Galileo numbers. The numerical results showed that, in contrast to what was suggested by assuming a fixed ellipsoidal shape, the onset of zigzagging motion is not limited to bubbles with high aspect ratios of deformation. The bubble deformation can, however, be expected to play a direct role in the loss of axisymmetry of the flow. Except for the coarse parametric investigation by Tripathi *et al.* (2015) a more accurate study is still missing. This issue is addressed in this thesis where we provide a precisely evaluated marginal stability curve of the onset of zigzagging state.

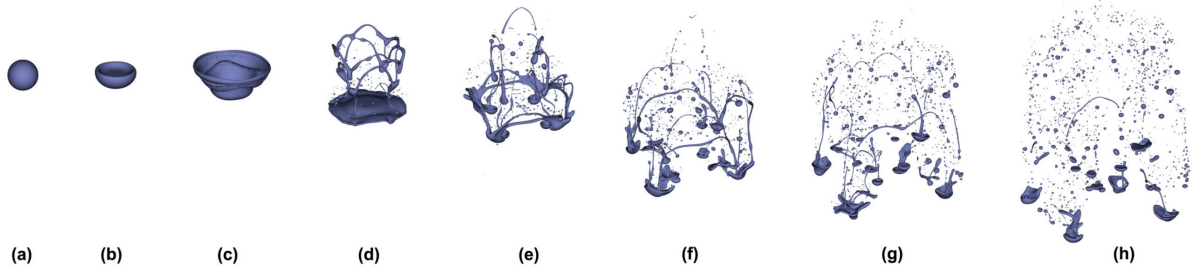


Figure 1.18: Deformation and fragmentation of a liquid drop for: $Eo = 288$, $Oh_d = 0.05$, $Oh_c = 0.05$ and $\rho^* = 10$ (Eo being the Eötvös number, Oh_d and Oh_c both Ohnesorge number based on droplet properties and continuous phase properties respectively **find out and mention the definitions!!!!**, ρ^* the density ratio between droplet and continuous phase). Evolution in terms of non-dimensional time τ : (a) $\tau = 0.0$, (b) $\tau = 0.1647$, (c) $\tau = 0.2642$, (d) $\tau = 0.3574$, (e) $\tau = 0.4434$, (f) $\tau = 0.5183$, (g) $\tau = 0.5924$, (h) $\tau = 0.6728$. (Reproduced from Jalaal & Mehrvaran (2012))

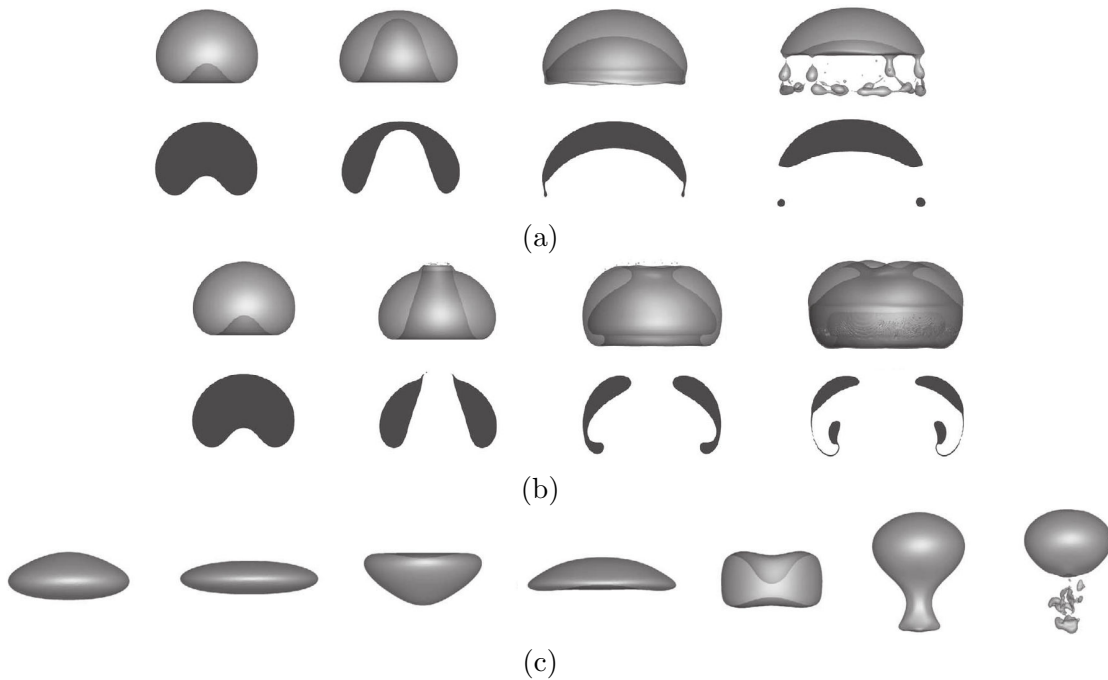


Figure 1.19: Time evolution of bubble breakup (dimensionless time from left to right $t = 1, 2, 4$ and 5 for figures (a) and (b), $t = 2, 4, 6, 7, 8, 9$ and 9.1 for figures (c)). (a) Bubble breaking into a spherical cap and several small satellite bubbles, $G = 70.7$, $Bo = 20$, (b) bubble changing in topology from dimpled ellipsoidal to toroidal, $G = 70.7$, $Bo = 200$, (c) A new breakup mode for $G = 500$, $Bo = 1$ (Tripathi *et al.* (2015)). (Here G and Bo are based on the equivalent bubble radius $G = \sqrt{gr_{eq}^3/\nu}$ and $Bo = \rho gr_{eq}^2/\sigma$)

1.9 Aims of this thesis

1. Extension of the study of freely moving spheres by Jenny *et al.* (2004) with special focus on the onset of chaos and on the characterization of chaotic states.
2. Refinement of the parametric study on freely moving spheroids of various aspect ratios ranging from 10 to 1.1 to establish a link between infinitely thin disks and spheres by providing state diagrams in the $G - m^*$ parameters plane.
3. Establishment of the marginal instability curve determining the onset of zigzagging motion of a deformable bubble.

Chapter 2

Freely falling or ascending spheres

2.1 Introduction

The main issue in the investigation of the motion of a single sphere is the understanding of the transition scenario. The state diagram appearing in the paper by Jenny *et al.* (2004) (called JDB, in what follows) has been recognized as a useful tool of summarizing the existing knowledge. Several points not fully explained in the paper combined with the new findings reported in literature motivate an extension and improvement of the parametric study of the JDB paper.

In the present chapter we address the following topics.

1. The threshold of the primary instability reported by the JDB paper has a progressive growing trend as the solid/fluid density ratio (ρ_s/ρ) increases. The critical Galileo numbers varies from $G = 155.8$ (corresponding asymptotic Reynolds number $Re_\infty \approx 205$) for an infinitely light sphere ($\rho_s/\rho = 0$) to $G = 160$ ($Re_\infty \approx 212$) for a dense sphere of $\rho_s/\rho = 10$, which obeys the intuition of considering dense spheres as fixed whose primary instability occurs at $Re \approx 212$. In contrast, the study on the steady oblique state of moving spheres by Fabre *et al.* (2012) remarks the independence of this threshold on the density ratio since the latter disappears in Eqs. (2.4,2.5) when the time derivative vanishes. A set of more precise calculations need to be carried out to verify that the thresholds are density independent.
2. In the oblique oscillating regime, the roughly estimated critical density ratio ($\rho_s/\rho = 2.5$) separating the low and high frequencies by the JDB paper needs to be examined rigorously. It is also interesting to know more about the different characteristics of the two frequencies to understand the mechanism of their formation.
3. For rising spheres, the JDB paper reported the existence of two zigzagging regimes distinguished by significantly different frequencies. A closer examination of the experimental results by Veldhuis & Biesheuvel (2007) and Horowitz & Williamson (2010), seemingly confirming the existence of a zigzagging state, do not quantitatively agree with numerical predictions. The low frequency, exactly periodic, zigzagging regime

described and analyzed in much detail in the JDB paper was, actually, not evidenced and Veldhuis & Biesheuvel (2007) raised the question whether the experimental observation did not correspond to the high frequency zigzagging regime. Neither of the two corresponds to the extremely robust vibrating state of Horowitz & Williamson (2010). The domain of strictly periodic zigzagging states is thus to be re-examined.

4. The transition to chaos after the loss of vertical trajectories is determined by the existence of the two aforementioned regions of oblique oscillating states characterized by low and high frequencies and an apparently questionable domain of perfect zigzagging regime. A more precise state diagram delimiting each state in the two-parameter ($G - \rho_s/\rho$) plane is needed.
5. A bi-stability between chaotic and a rapidly oscillating zigzagging trajectories was evidenced in the JDB paper. A large region in the $G - \rho_s/\rho$ parameter plane at $\rho_s/\rho < 1$ was suggested as an estimation of this coexistence. To get a more precise conclusion, it is worth exploring the rapidly oscillating periodic state inside the chaotic domain.
6. The intriguing robust “vibrating” trajectories reported by Horowitz & Williamson (2010) (see Figure 1.14, Chapter 1) can be expected to be confirmed by simulations. This issue should be raised.
7. The extension of the investigation far into the chaotic domain makes it necessary to distinguish differences in the chaotic states by providing a quantitative characterization of random data.
8. As mentioned in Chapter 1, the motion of a single sphere has been used for benchmarking of a multi-particle code. Should it be further used for benchmarking of more complicated simulations, more accurate and more quantitative data is needed.

2.2 Mathematical formulation and numerical implementation

As described in previous papers (Jenny *et al.* (2004); Uhlmann & Dušek (2014)), the mathematical formulation consists of Navier-Stokes equations

$$\frac{\partial \mathbf{v}}{\partial t} + [(\mathbf{v} - \mathbf{u}) \cdot \nabla] \mathbf{v} + \nabla p = \frac{1}{G} \nabla^2 \mathbf{v}, \quad (2.1)$$

$$\nabla \cdot \mathbf{v} = 0, \quad (2.2)$$

non-dimensionalized with respect to the sphere diameter d and to the reference velocity

$$U_{ref} = \sqrt{\left| \frac{\rho_s}{\rho} - 1 \right| gd} \quad (2.3)$$

coupled with motion equations

$$\frac{\rho_s}{\rho} \frac{d\mathbf{u}}{dt} = \frac{6}{\pi} \int_S (\boldsymbol{\tau} \cdot \mathbf{n} - p\mathbf{n}) dS - \mathbf{k}, \quad (2.4)$$

$$\frac{\rho_s}{\rho} \frac{d\boldsymbol{\omega}}{dt} = \frac{60}{\pi} \int_S \mathbf{r}_S \times (\boldsymbol{\tau} \cdot \mathbf{n} - p\mathbf{n}) dS, \quad (2.5)$$

by the no slip boundary condition at the sphere surface S

$$\mathbf{v}|_S = \mathbf{u} + \boldsymbol{\Omega} \times \mathbf{r}|_S. \quad (2.6)$$

In the above equations, \mathbf{v} and \mathbf{u} stand for the flow field and the translation velocity of the sphere, respectively, both considered with respect to a fixed frame. ρ and ρ_s are the fluid and solid densities. \mathbf{k} is the vertical unit vector in the direction of effective gravity:

$$\mathbf{k} = \text{sign}(\rho_s/\rho - 1)\mathbf{g}/g \quad (2.7)$$

$\boldsymbol{\tau}$ denotes the viscous stress tensor $\frac{1}{G}(\nabla\mathbf{v} + \nabla\mathbf{v}^T)$. \mathbf{r}_S is the position vector on the sphere surface and $\boldsymbol{\omega}$ the angular velocity, both with respect to the sphere center, and \mathbf{n} denotes the normal vector to the sphere surface. The non-dimensionalization reduces the problem parameters to the Galileo number

$$G = \frac{\sqrt{\left| \frac{\rho_s}{\rho} - 1 \right| g d^3}}{\nu} \quad (2.8)$$

and the density ratio ρ_s/ρ . Though an exactly unit density ratio implies, physically, an infinitely large sphere diameter, this limit represents no singularity for the simulations. As the result, it makes sense to speak about the density ratio 1. It is to be understood as the case of a large sphere immersed in fluid of almost the same density. Such experimental conditions are, indeed, often selected to increase the size of the immersed body. The physical interpretation of the case $\rho_s/\rho = 1$ is such that if the real density ratio differs, e.g. by 2% from 1 as it is the case in the paper by Fernandes *et al.* (2007), then the results given here for exactly unit density ratio apply with a very good accuracy.

A cylindrical numerical domain accompanies the translational motion of the sphere, the latter being allowed to rotate freely inside this domain. The numerical discretization is based on a Fourier azimuthal decomposition combined with a spectral element discretization of the radial-axial plane. The azimuthal decomposition is truncated at the mode $m = 7$ and the radial-axial plane is decomposed into 245 elements containing 6 times 6 collocation points distributed similarly as in previous papers. The domain radius and height are those of Jenny *et al.* (2004). The previously published results (e.g. Uhlmann & Dušek, 2014) prove the accuracy and adequacy of the so defined numerical configuration for the considered transitional regimes.

2.3 Primary and secondary instabilities

Since the publication of the first numerical papers (Jenny *et al.* (2003, 2004)), the primary bifurcation state - the steady oblique regime - has been evidenced experimentally in the

predicted parameter domain (Veldhuis & Biesheuvel (2007)) and its onset has been analyzed theoretically (Fabre *et al.* (2012)). Fabre *et al.* (2012) remark that the threshold of the primary, regular bifurcation is independent of the density ratio (since the latter disappears in Eqs. (2.4,2.5) when the time derivative vanishes). They report a critical Archimedes number $Ar = 55.00$. The relation to the Galileo number (Eqs. 2.8) being $G = \sqrt{8}Ar$, this corresponds to $G_{crit} = 155.6$. We find $G_{crit} = 155.8$ (the corresponding asymptotic Reynolds number $Re_\infty = 205.3$). The time derivative vanishes for all steady oblique regimes so that the latter depend only on the Galileo number and not on the density ratio. This new finding reconciles the contradiction between the results of JBD paper and that of Fabre *et al.* (2012) but raises another problem if, by intuition, we consider a highly dense sphere as fixed whose critical Reynolds number at the primary instability is $Re_{crit} \approx 212$. The explanation consists in noting that even a very dense sphere ends up by moving along an oblique trajectory and by rotating. The difference consists only in the time scale of the transients.

Of course, the threshold of the secondary bifurcation leading to unsteadiness is no longer independent of the density ratio. Its characteristics in terms of the critical values of velocities and of oscillation frequency are given in Table 2.1. The velocities can be converted to dimensional units using U_{ref} of Eq. 2.3. The time unit is d/U_{ref} . The provided values of the vertical velocity make it possible to convert the Galileo to Reynolds number ($Re = u_z G$) and non-dimensionalized frequencies to Strouhal numbers ($St = f/u_z$). The horizontal velocity is roughly equal to 8 to 10% of the vertical one which yields an angle of about 4 to 6 degrees with respect to the vertical direction.

ρ_s/ρ	G_{crit}	u_h	u_z	ω_h	f
0	167.18	0.0969	1.3355	0.0149	0.0701
0.2	169.23	0.1031	1.3388	0.0151	0.0667
0.5	172.52	0.1108	1.3443	0.015	0.0644
1	178.55	0.1224	1.3544	0.0139	0.0672
1.3	182.5	0.1275	1.3622	0.0129	0.0677
1.7	187.35	0.1327	1.3704	0.0112	0.0711
2	190.69	0.1356	1.3763	0.0099	0.0729
2.5	196.08	0.1387	1.3859	0.0077	0.076/0.175*
3	195.19	0.1383	1.3843	0.0081	0.1741
4	195.18	0.1383	1.3842	0.0081	0.1751
10	195.06	0.1384	1.3838	0.0082	0.1771

Table 2.1: Critical Galileo number G_{crit} , horizontal velocity u_h , vertical velocity u_z , angular velocity of rotation ω_h and frequency f at the onset of oblique oscillating regime. (* For the density ratio of 2.5 both frequencies are present even at the threshold of unsteadiness. Note that the critical Galileo number, terminal horizontal and vertical velocities are larger while the angular velocity is smaller at the onset of the high frequency regime.)

The values of the critical Galileo numbers of the primary and secondary instabilities were found by cubic interpolation of three smallest amplification rates as a function of the

corresponding Galileo numbers. Two simulations for each Galileo number restarted from previously obtained results below and above the secondary instability threshold (namely, from the steady oblique and oblique oscillating states close to the threshold) prove that the bifurcation is super-critical. Figure 2.1 shows an example of determination of the critical Galileo number of the secondary instability for $\rho_s/\rho = 0.2$. The values of amplification rates are directly extracted by examining the decreasing or increasing trend of the amplitude of oscillations of horizontal velocity. The time dependence being very accurately exponential it appears as a straight line in the logarithmic scale. The slope is equal to the amplification rate γ .

2.4 Low and high frequencies

As can be seen in the following section 2.6, the type of oblique oscillating regime is determinant for the transition to chaos. A contrasting behavior of “dense” and “light” spheres was already evidenced in the JDB paper. The frequency of oscillation of spheres of density ratio 3 and more was found almost three times higher than for spheres of density ratio 2 and less. The results of Table 2.1 confirm this result. Both frequencies are marginally unstable at $\rho_s/\rho = 2.5$ which results in a quasi-periodic behavior at the very threshold of the Hopf bifurcation showing that the limit between the low and high frequency oblique oscillating regime is quite accurately situated at $\rho_s/\rho = 2.5$ at their onset.

To understand the difference between the physical origin of the high and low frequency oblique oscillating regimes, let us recall the recent paper by Tchoufag *et al.* (2014) showing that two types of modes exist in systems involving a fluid - solid interaction: fluid and solid modes. The former are characterized by dominant fluid oscillation while the latter are typical for a strong fluid - solid interaction. This is what we observe in Figures 2.2 and 2.3. Figures 2.2 (a) and (b) compare the vortical structures of the fluid mode at $G = 199$ and for the density ratio of 3 with those of the wake of a fixed sphere obtained by freezing the translation velocity and setting the rotation velocity to zero. There is virtually no difference between both. Indeed, the frequency of the fluid mode is in agreement with values reported for the fixed sphere wake. At $Re = 300$, the Strouhal number of the periodic regime of the sphere wake was found between 0.135 and 0.137 (see Johnson & Patel (1999); Tomboulides & Orszag (2000)). At the threshold ($Re_{crit} = 275$) the Strouhal number given by Ghidersa & Dušek (2000) is 0.127. Using the vertical velocity of Table 2.1, we obtain specifically for $\rho_s/\rho = 3$ and $G = 199$ a Strouhal number of 0.129 and an average Reynolds number of 274.6. The fixed sphere wake with frozen velocity 1.396 at $G = 199$ corresponds to the Reynolds number $Re = 277.9$ and the Strouhal number of vortex shedding is 0.130. The increase of frequency due to fixing the sphere velocity is thus negligible. The oscillations of the free sphere reflect only a very limited reaction of the body to the oscillations of the wake. The amplitude of velocity oscillations of the sphere is thus very small as can be seen in Figure 2.5.

In contrast, Figure 2.3 (a) shows a much longer wavelength in agreement with the smaller frequency of the solid mode. Moreover, the vorticity is concentrated in the neighborhood of the sphere. Note that the vorticity level in this figure had to be taken three times lower

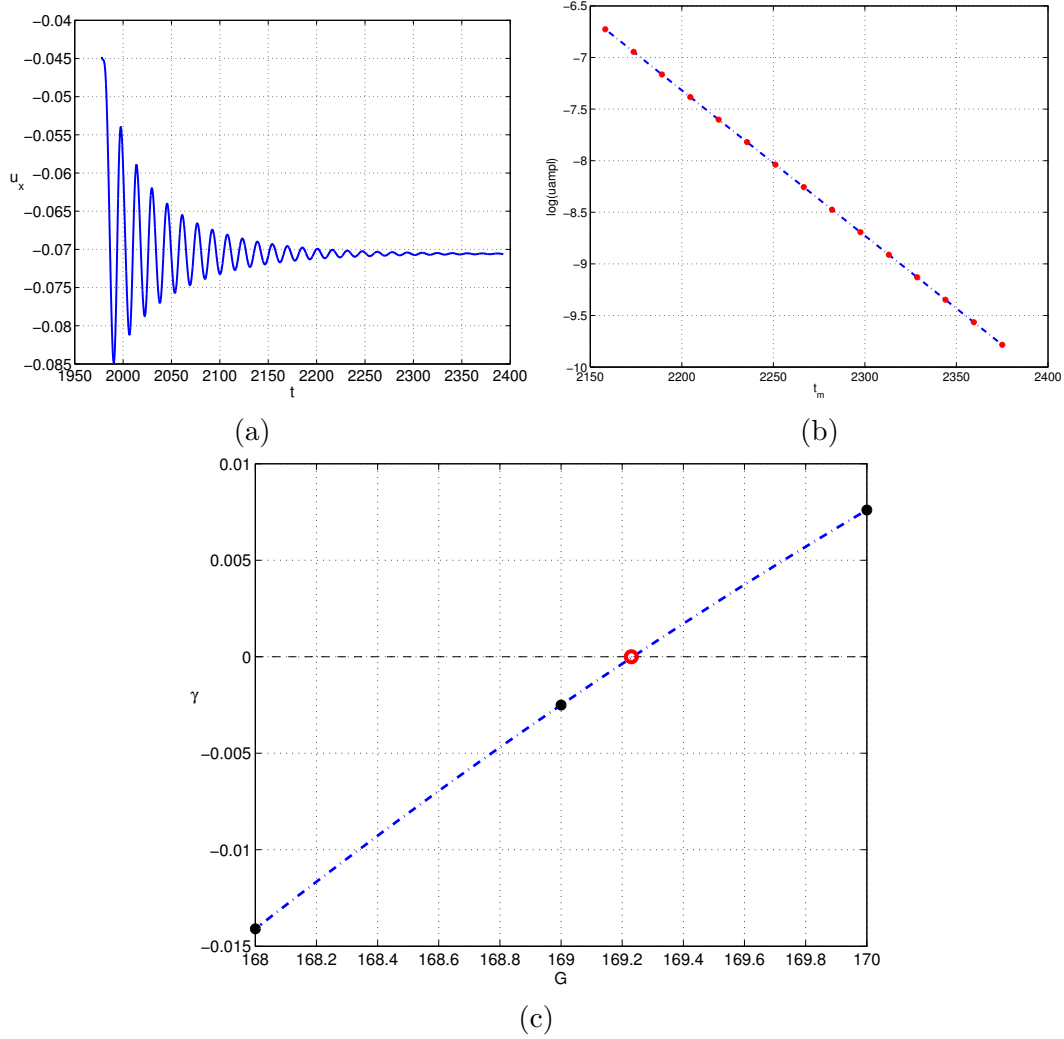


Figure 2.1: Calculation of the critical Galileo number at the secondary instabilities for $\rho_s/\rho = 0.2$. (a) Horizontal velocity as a function of time at $G = 168$, (b) the amplification rate is the slope of the dotted dashed line established by plotting the amplitude (red points) in (a) in the logarithmic scale, (c) calculation of the critical Galileo number. Black points represent the extracted values the amplification rates $\gamma = -0.0141, -0.0025$ and 0.0076 at $G = 168, 169$ and 170 , respectively, the red circle corresponds to the critical Galileo number $G_{crit} = 169.23$ found by cubic interpolation (blue dotted dashed line).

than in Figures 2.3(b) and 2.2 to capture visible structures in the whole represented domain. As compared to the fluid mode, the oscillation of the horizontal velocity of the sphere has a more than ten times higher amplitude (see Figure 2.5).

The transition to chaos of the fluid mode is characterized by a quasi-periodicity given by the simultaneous presence of both the low and high frequency. They are, in general,

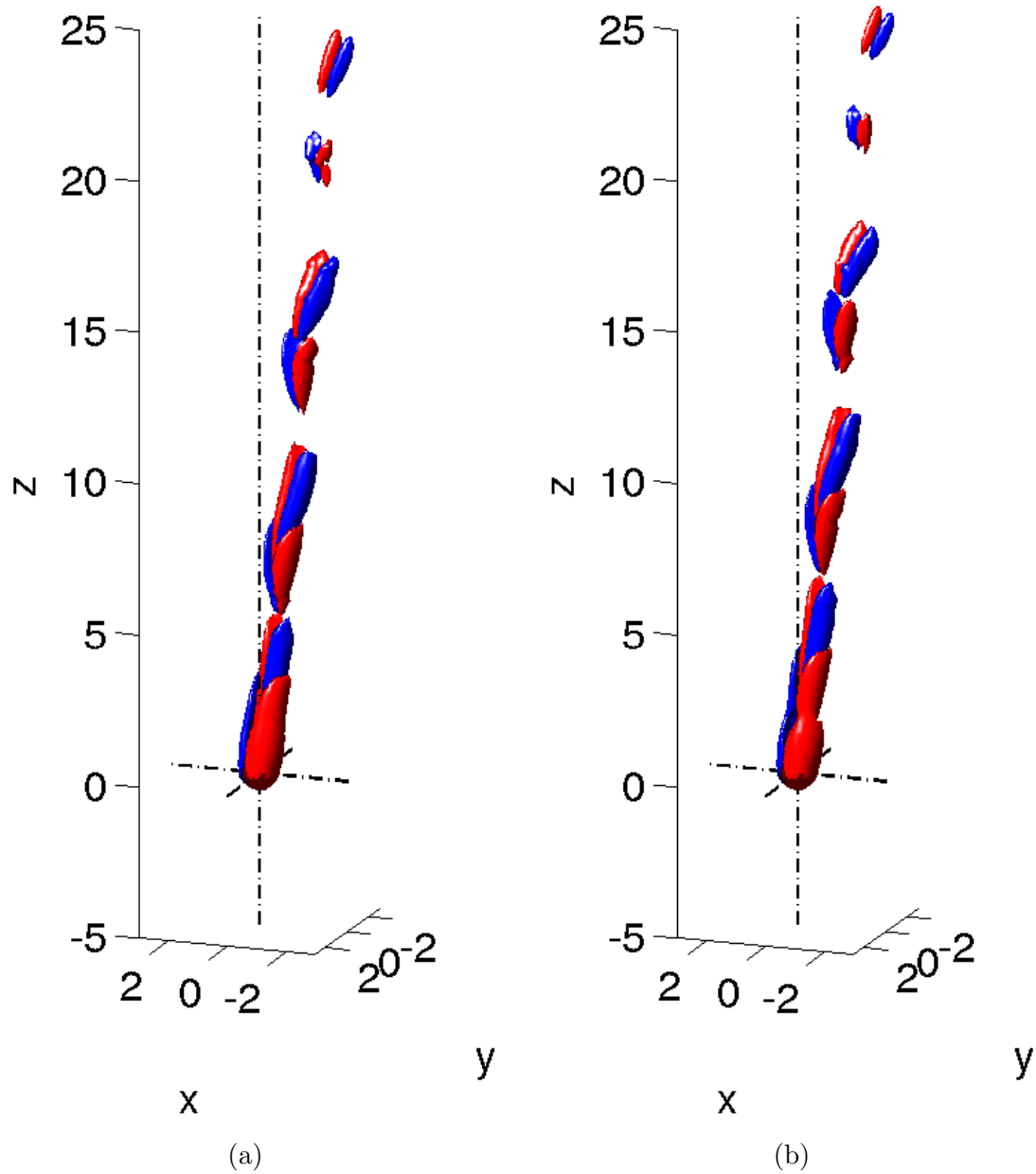


Figure 2.2: (a) High frequency (fluid) mode ($G = 199, \rho_s/\rho = 3$, stream-wise vorticity levels: ± 0.15). (b) Fixed sphere wake (frozen translation velocity of figure (a), no rotation, $Re = 277.9$, same vorticity levels: ± 0.15 as in (a)).

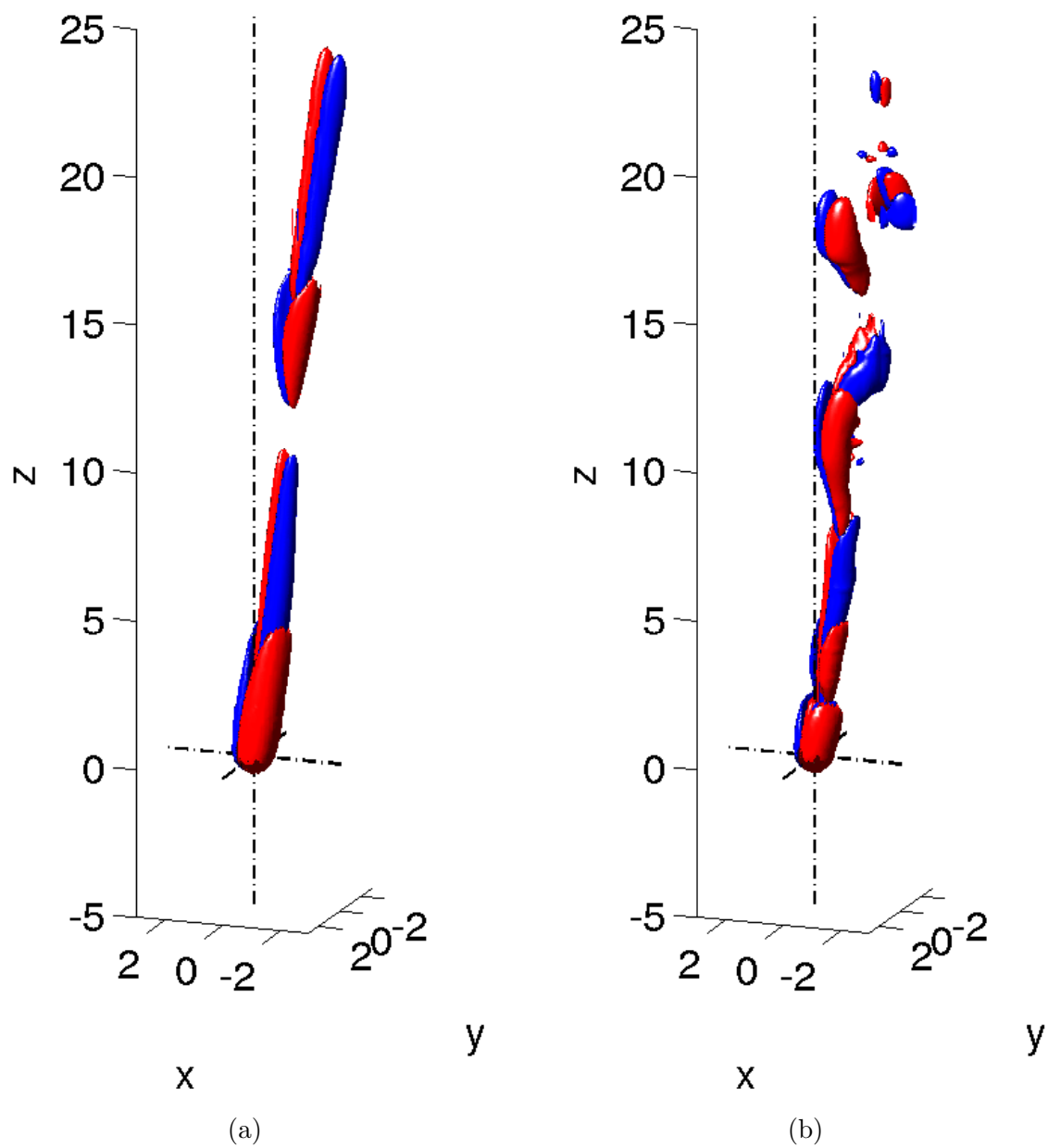


Figure 2.3: (a) Low frequency (solid) mode ($G = 196, \rho_s/\rho = 2$, vorticity levels: ± 0.05). (b) Locked in, low and high frequency, periodic mode ($G = 220, \rho_s/\rho = 3$, vorticity levels: ± 0.15).

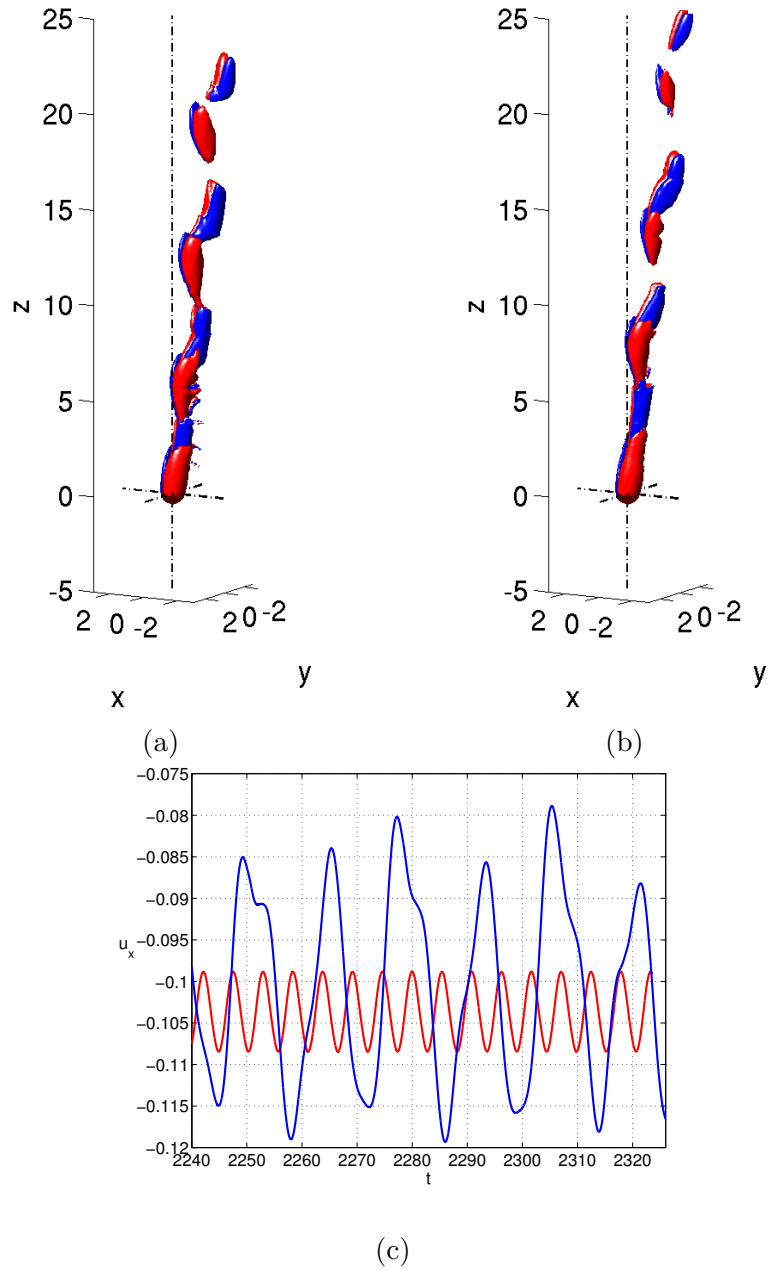


Figure 2.4: Co-existence of two frequencies at $G = 215$, $\rho_s/\rho = 2$, (a) high frequency (vorticity levels: ± 0.15), (b) low frequency (vorticity levels: ± 0.15). (c) Comparison between velocities of high (red) and low (blue) frequency modes. Note that the large difference of motion of the sphere is not visible on the vorticity structures.

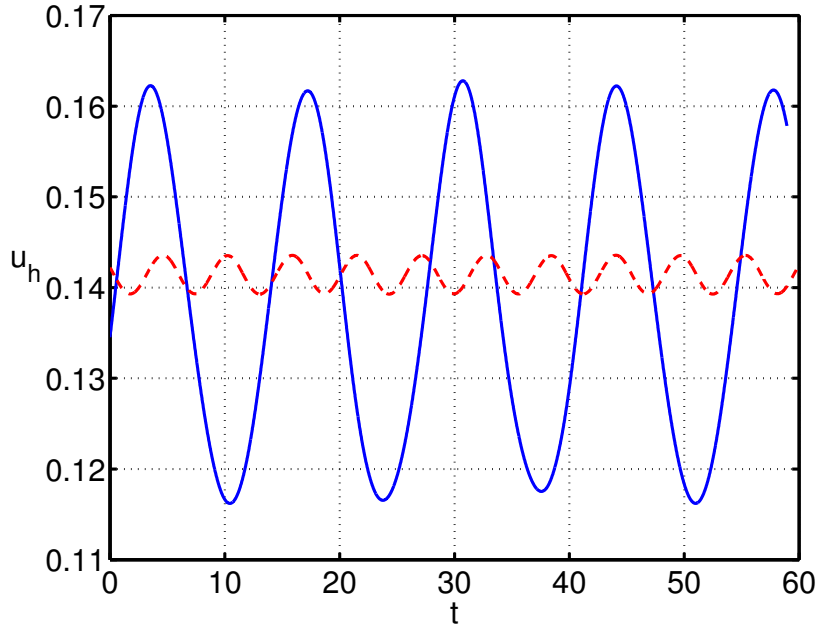


Figure 2.5: Comparison of amplitudes of oscillations of the low frequency regime $\rho_s/\rho = 2$, $G = 196$ (full blue line) and high frequency regime $\rho_s/\rho = 3$, $G = 199$ (dashed red line). Note that the mean values are comparable.

incommensurable except when they lock in at the ratio of 3:1 and a periodic low frequency regime reappears around $G = 220$. In this case, the solid mode dominates only in the close wake whereas more downstream the vortical structures of short wave-length and high intensity are seen in Figure 2.3 (b). Special cases of coexistence of both low and high frequency regime have been found. The vorticity structures illustrated in Figure 2.4 for both frequencies have practically the same shape yet the motion of the sphere is different.

The fact that the degrees of freedom of the sphere have little effect on the fluid mode explains why the horizontal velocity is virtually independent of the density ratio at its onset (see Figure 2.6(a)) while it grows with growing density ratio for the solid mode. The strong oscillations of the solid mode have also a significant effect on the mean value of the horizontal velocity which starts to decrease as soon as the oblique oscillating regime sets in. This is not the case for the small oscillations of the fluid mode. (see Figure 2.6(b)).

The simulated regimes are represented in the state diagram of Figure 2.7. The high frequency regime was evidenced at as low density ratio as 1.3 at Galileo number 215. At this point of the state diagram it co-exists with a low frequency and a chaotic state. The transition between low and high frequency regime at density ratio between 1.5 and 2.5 is always progressive. As the Galileo number increases from the threshold of the low frequency oblique oscillating regime the high frequency appears before the low frequency disappears which yields a quasi-periodic oscillation. The low frequency reappears at the transition to chaos. At first both, the high and low, frequencies are locked in at a ratio of 3 (at density

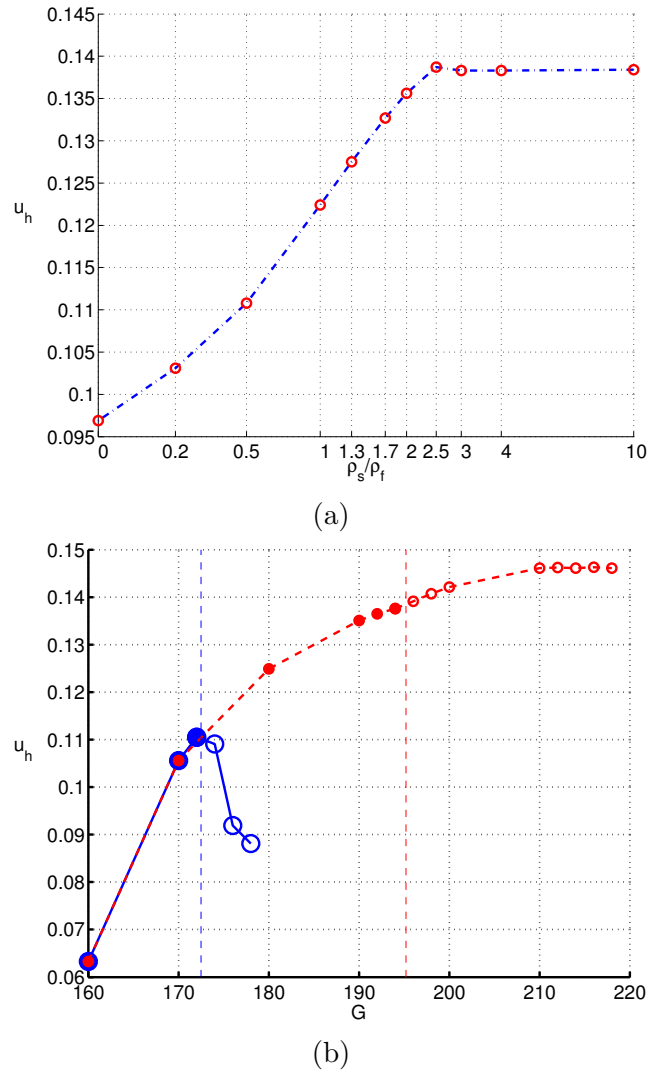


Figure 2.6: (a) Horizontal velocity at the threshold of the oblique oscillating regime as a function of the density ratio. (b) Horizontal velocity as a function of Galileo number for a low density ratio ($\rho_s/\rho = 0.5$ - blue solid line) and a high density ratio ($\rho_s/\rho = 4$ - dotted red line). The filled markers correspond to steady oblique regimes, the empty markers represent the mean values. The thresholds of oblique oscillating regimes are given by dashed vertical lines.

ratios from 2 to 4 and $G = 220$) then they become incommensurate and yield a quasi-periodic regime with planar symmetry (see Figure 2.8) before the symmetry plane loses its stability and the chaos sets in. The co-existence of both frequencies was remarked already by Veldhuis & Biesheuvel (2007).

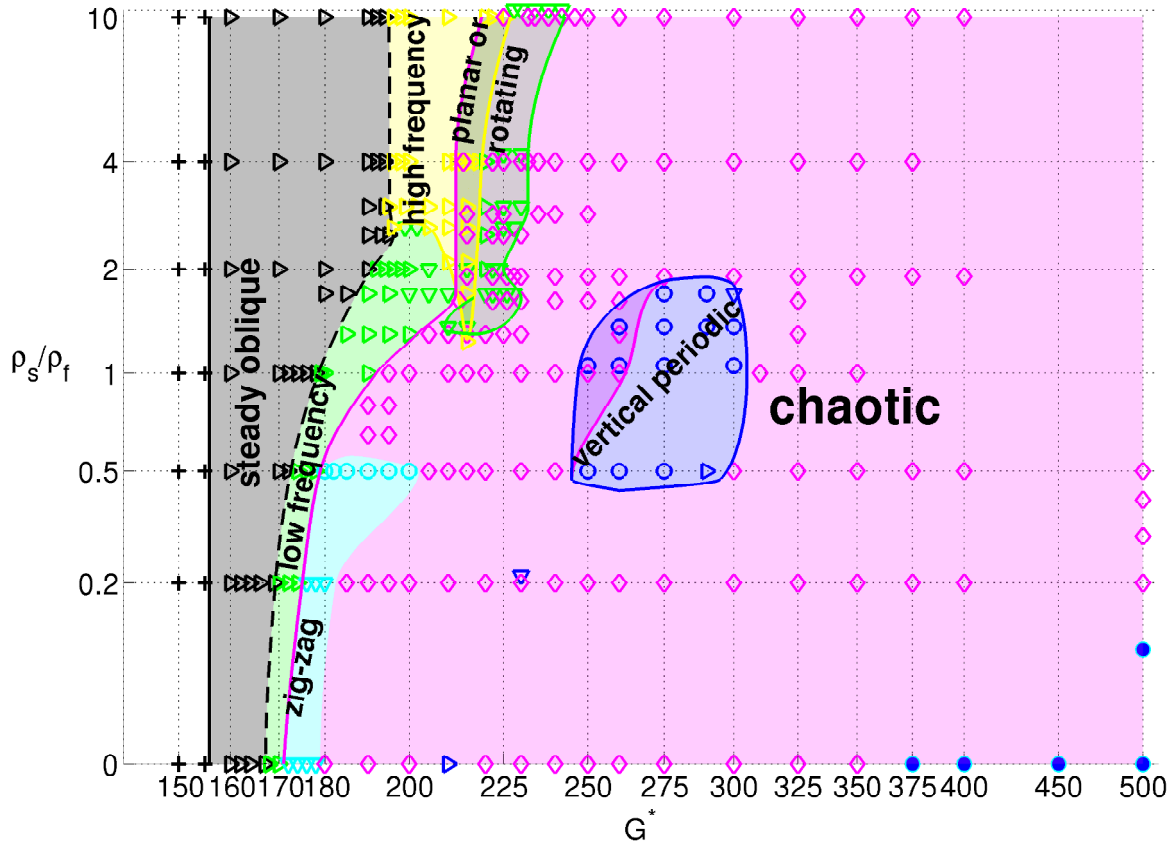
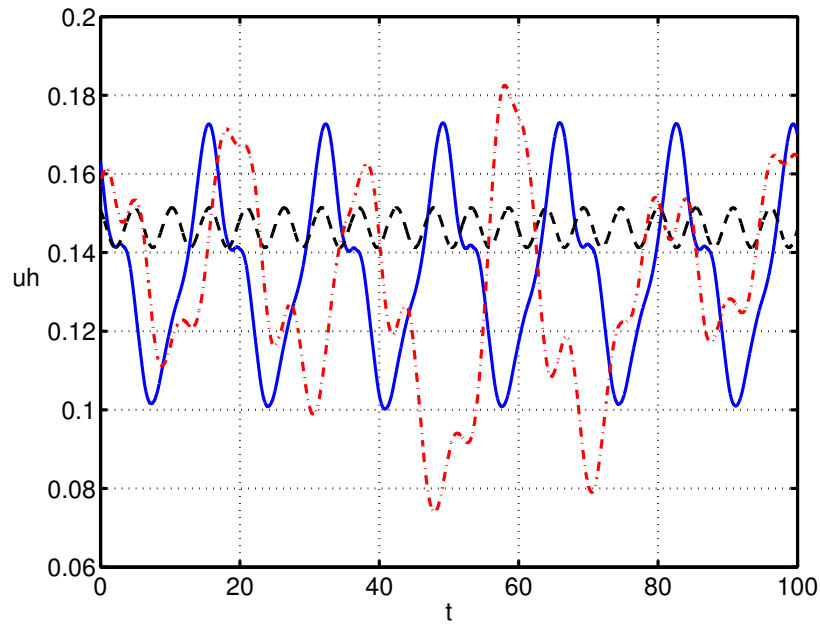
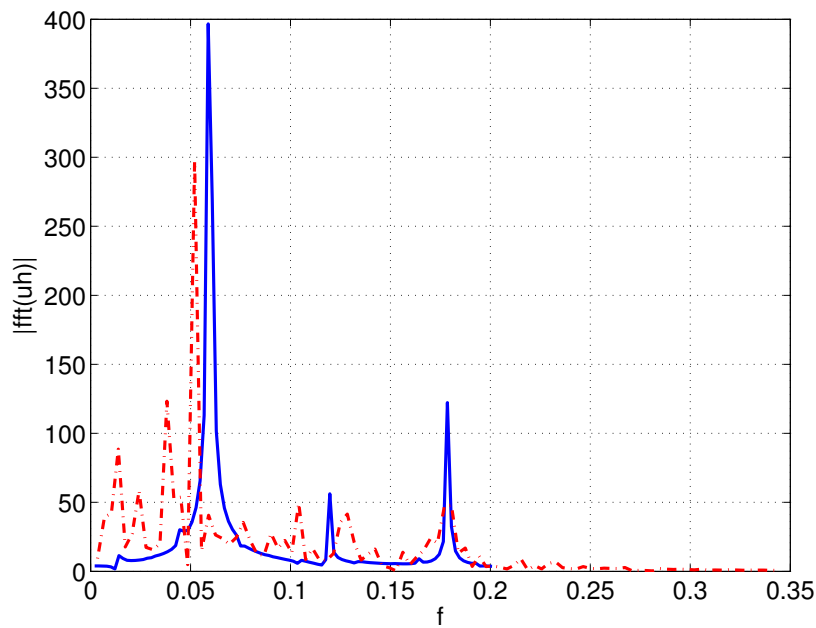


Figure 2.7: State diagram in the $G - \rho_s/\rho$ parameter space. Thresholds of bifurcations are represented by lines, different colors represent regimes indicated in the figure. Overlapping areas mean bi-stability. The overlapping of the chaotic area with zones of high and low frequency oblique oscillating regimes (labeled as “planar or rotating”) is an area of bi-stability of states with fixed and slowly rotating symmetry axis. The symbols represent the simulated trajectories (in cases of coexistence of two or three regimes the symbols are artificially shifted)

Meaning of symbols. $+$: vertical regime, $>$: steady oblique, $>$: low frequency oblique oscillating, $>$: low frequency quasi-periodic oblique oscillating, $>$: high frequency oblique oscillating, $<$: perfect or slightly oblique zig-zag, $<$: intermittent zig-zag, $<$: vertical oscillating planar, $<$: vertical quasi-periodic, $<$: periodic planar slightly inclined, $<$: helical, $<$: chaotic (or rotating plane in the bi-stability domain).



(a)



(b)

Figure 2.8: (a) Horizontal velocity for the density ratio $\rho_s/\rho = 3$. Solid blue line: periodic low frequency oscillations at $G = 220$; dashed black line: high frequency oblique oscillating state at $G = 215$ (frequency: 0.186); dash-dotted red line: quasi-periodic state at $G = 225$. (b) Power spectrum of horizontal velocity for $G = 220$ (solid blue line) and $G = 225$ (dash-dotted line).

2.5 Various imperfect zigzagging trajectories

To our knowledge, the “low frequency” zigzagging state reported in the JDB paper corresponds to no experimental evidence. In fact, the perfect periodicity and planarity of the trajectory found in the cited paper for the low frequency zigzagging regime at $\rho_s/\rho = 0.5$ and $G = 180$ is rather an exception (see Figure 2.9). As the Galileo number further increases, this perfect planarity gives way to a progressively slightly increasing inclination (shown in Figure 2.10(d)). As a result, a great variety of regimes arises (see Figure 2.11 to 2.17), most of them presenting trajectories having not much resemblance with the “perfect” zigzagging regime on a large scale. At very small density ratios (0 and 0.2) the symmetry plane is at first (with increasing Galileo number) conserved. The randomness is due to the intermittency of switching of the sign of the horizontal velocity resulting in imperfect zigzagging (see Figures 2.11 and 2.12). At higher Galileo numbers, the memory of the symmetry plane is no longer perfect, which results in a non planar trajectory. The projection of the velocity vector onto the horizontal plane describes a curve (see Figure 2.13 (c)), resulting in a non zero mean horizontal velocity, not repeating with exact periodicity (Figure 2.13 (a)). On a short time scale, the trajectory drifts sideways so that its plane appears inclined (Figure 2.13 (d)). On a large time scale the trajectory has an aperiodic wavy shape (Figure 2.13 (b)). Attention must be paid to very weakly unstable trajectories such as that represented in Figure 2.14. It appeared as planar and periodic (albeit with a very small sub-harmonic modulation, however, after a small perturbation it developed into a similar state as that represented in Figure 2.13).

The density ratio of 0.5 is somewhat exceptional because of several periodic regimes extending from the onset of zigzagging at $G = 180$ (the case of perfect planar zigzagging trajectory reported in JDB) to about 200. However, except for $G = 180$, the trajectory is not vertical on average but drifts sideways (its plane is oblique - see Figure 2.15 (a),(b)). The reason is obvious from Figure 2.15 (a) showing that the sphere does not choose the same vertical plane after the stage of vertical ascension which results in a non zero average horizontal velocity.

A similar oscillation is visible in Figure 2.15 (c) for the density ratio $\rho_s/\rho = 0.65$ and $G = 195$. On the scale of the trajectory represented in Figure 2.15 (d) only the variation of the mean value has a visible impact and results in intermittent changes of the inclination of the trajectory plane. At the density ratio 0.5, a sub-harmonic (double) period sets in (see Figure 2.16) before an aperiodic oscillation of the shape of the path of the horizontal velocity vector appears at $G = 205$.

For marginally buoyant spheres, the angle between the old and new plane selected after the vertical ascension stage exceeds 90 degrees. At the scale of one oscillation period, the shape of the path of the velocity vector in the horizontal plane assumes a “V” form. The angle of “V” varies randomly and even changes sign (see Figure 2.17 (a)). As a result, on a short time scale, the trajectory is oblique oscillating (albeit non planar) whereas on a large time scale, at which the oscillations are not visible, it presents a random waviness similar to that of trajectories of dense, falling spheres (see Figure 2.18).

To sum up, the zigzagging trajectories are rarely perfect and the transition to fully random ones is progressive. There is no clear cut domain of zigzagging trajectories. What is

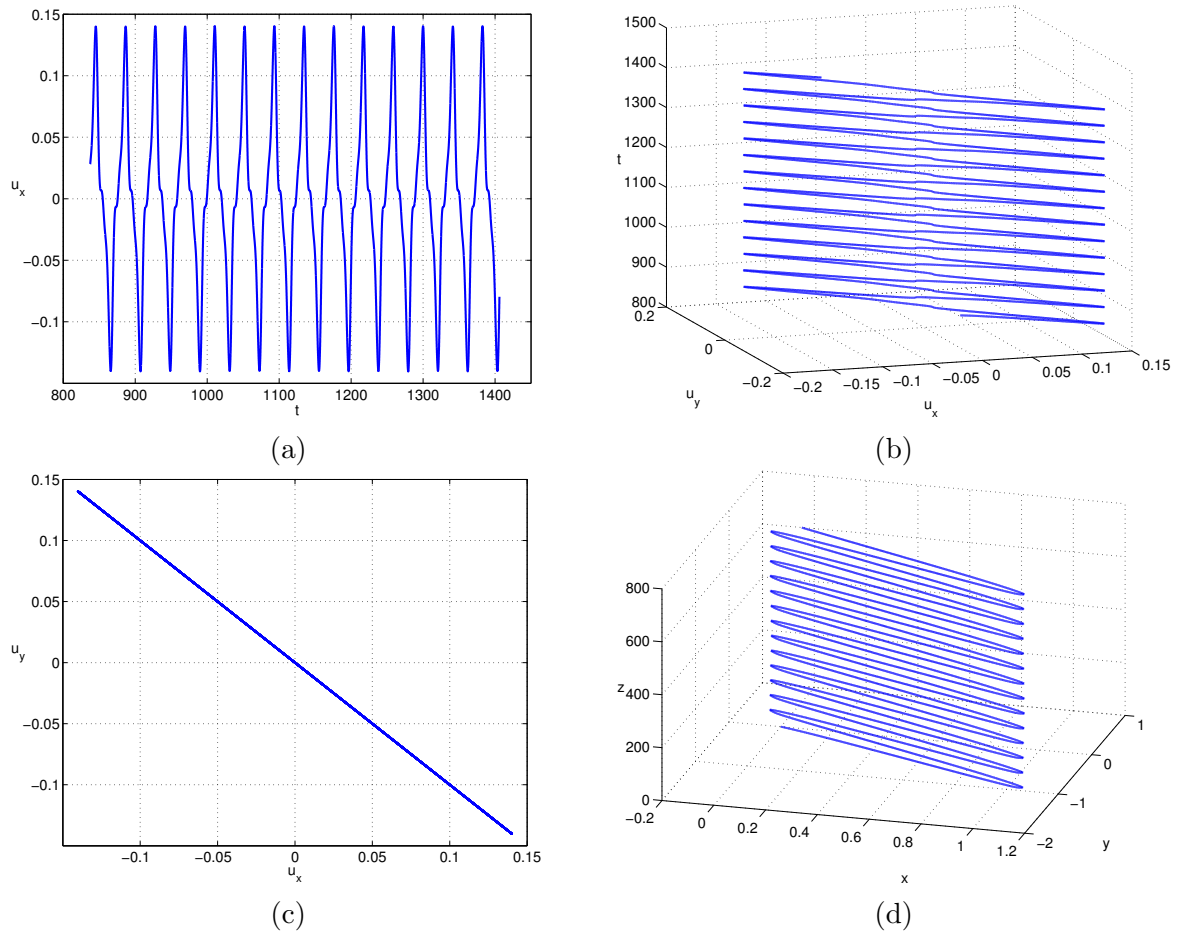


Figure 2.9: Perfect zigzagging trajectories of spheres $\rho_s/\rho = 0.5$, $G = 180$. (a),(b) Horizontal velocities as a function of time, (c) projection of the velocity vectors onto the horizontal plane, (d) trajectory.

reported in the state diagram is a domain of almost planar trajectories delimited using the criterion of isotropy described in Sec. 2.9.

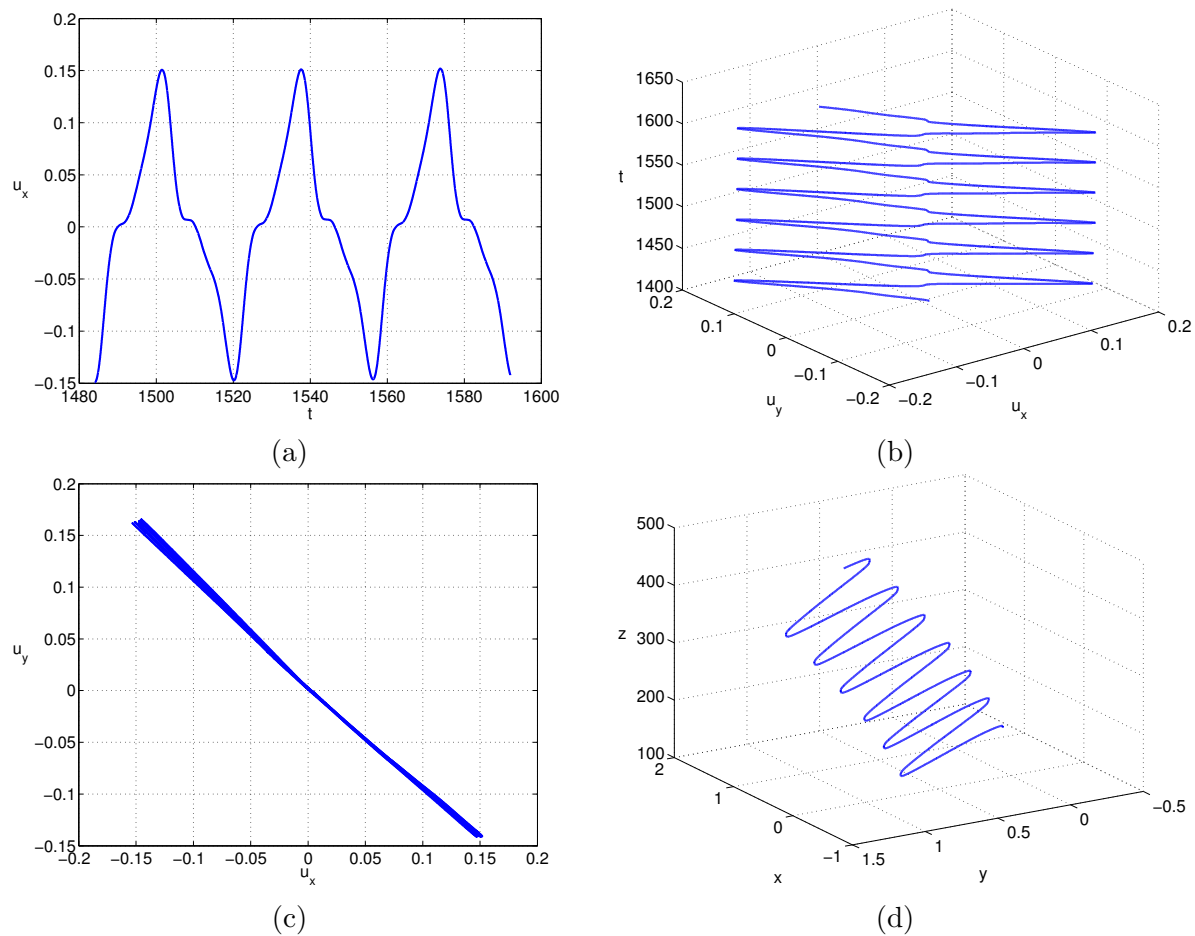
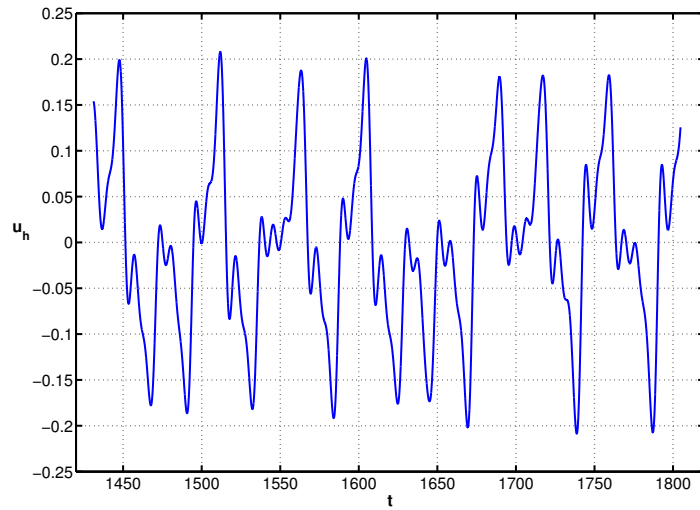
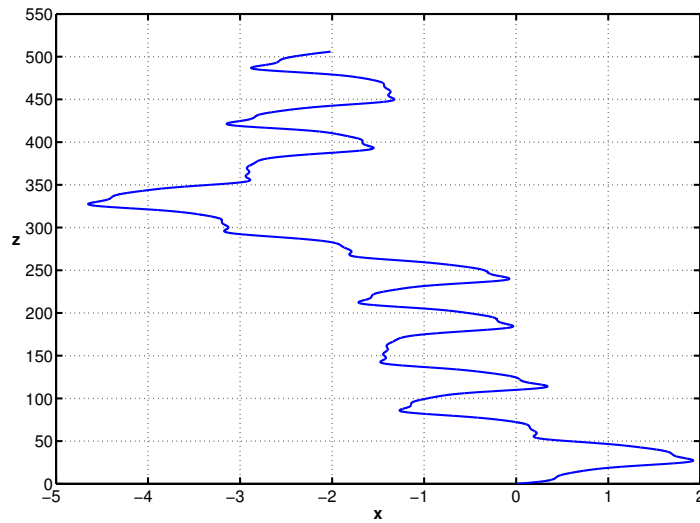


Figure 2.10: Almost perfect zigzagging trajectories of spheres $\rho_s/\rho = 0.5$, $G = 185$. (a),(b) Horizontal velocities as a function of time, (c) projection of the velocity vectors onto the horizontal plane, (d) trajectory.

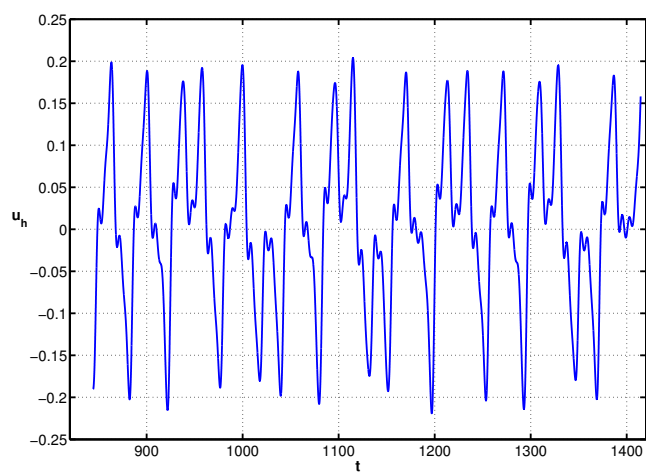


(a)

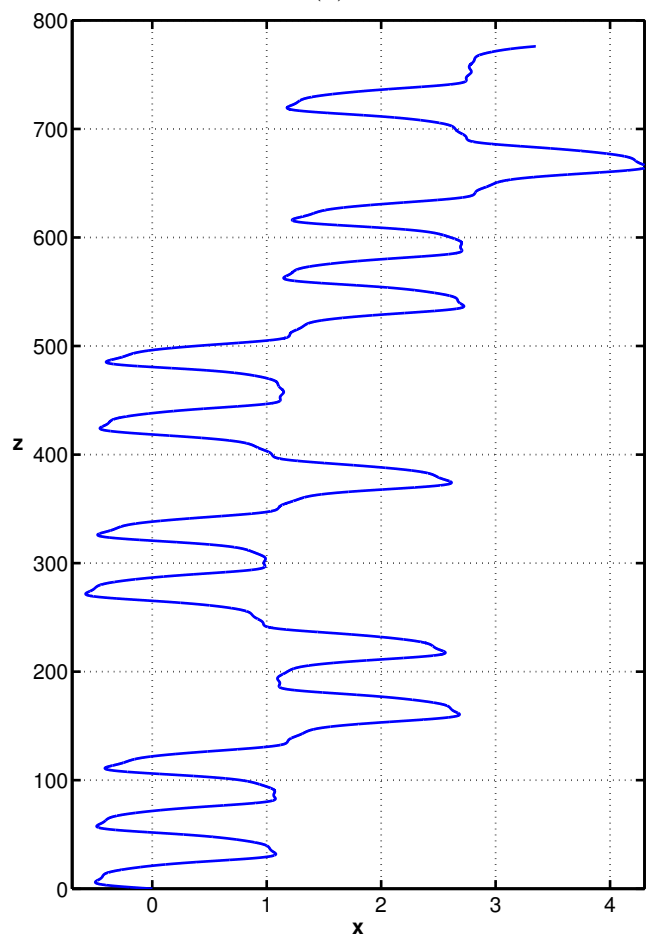


(b)

Figure 2.11: Horizontal velocities and trajectories of very light spheres. (a),(b): $\rho_s/\rho = 0$, $G = 176$ (planar trajectory).



(a)



(b)

Figure 2.12: Horizontal velocity and trajectory of very light spheres at $\rho_s/\rho = 0.2$, $G = 180$.

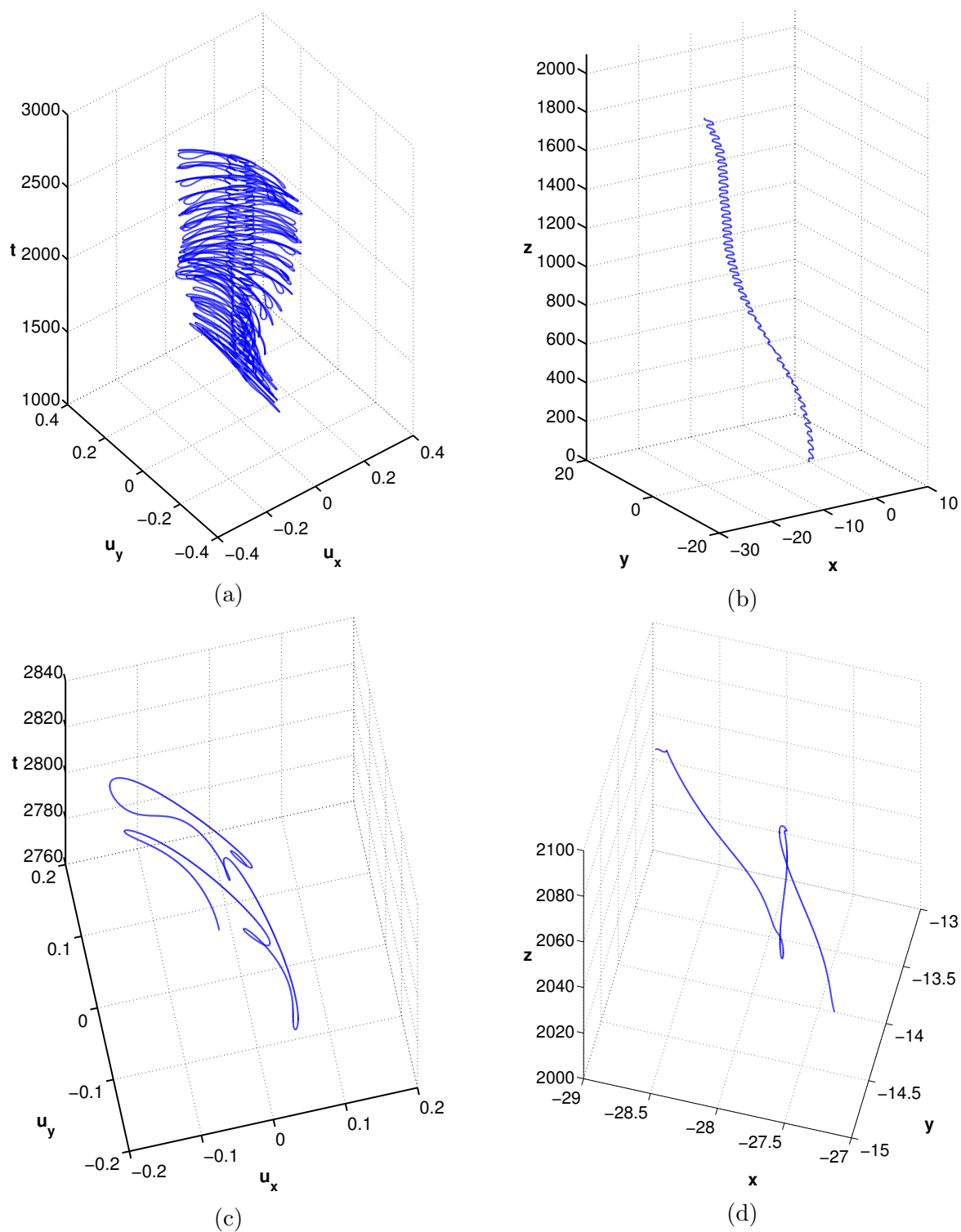


Figure 2.13: Velocities and trajectories of very light spheres at $\rho_s/\rho = 0.2$, $G = 190$, (a) horizontal velocities as function of time (vertical axis), (b) trajectory, (c),(d) zoom on last 50 time units of figures (a) and (b).

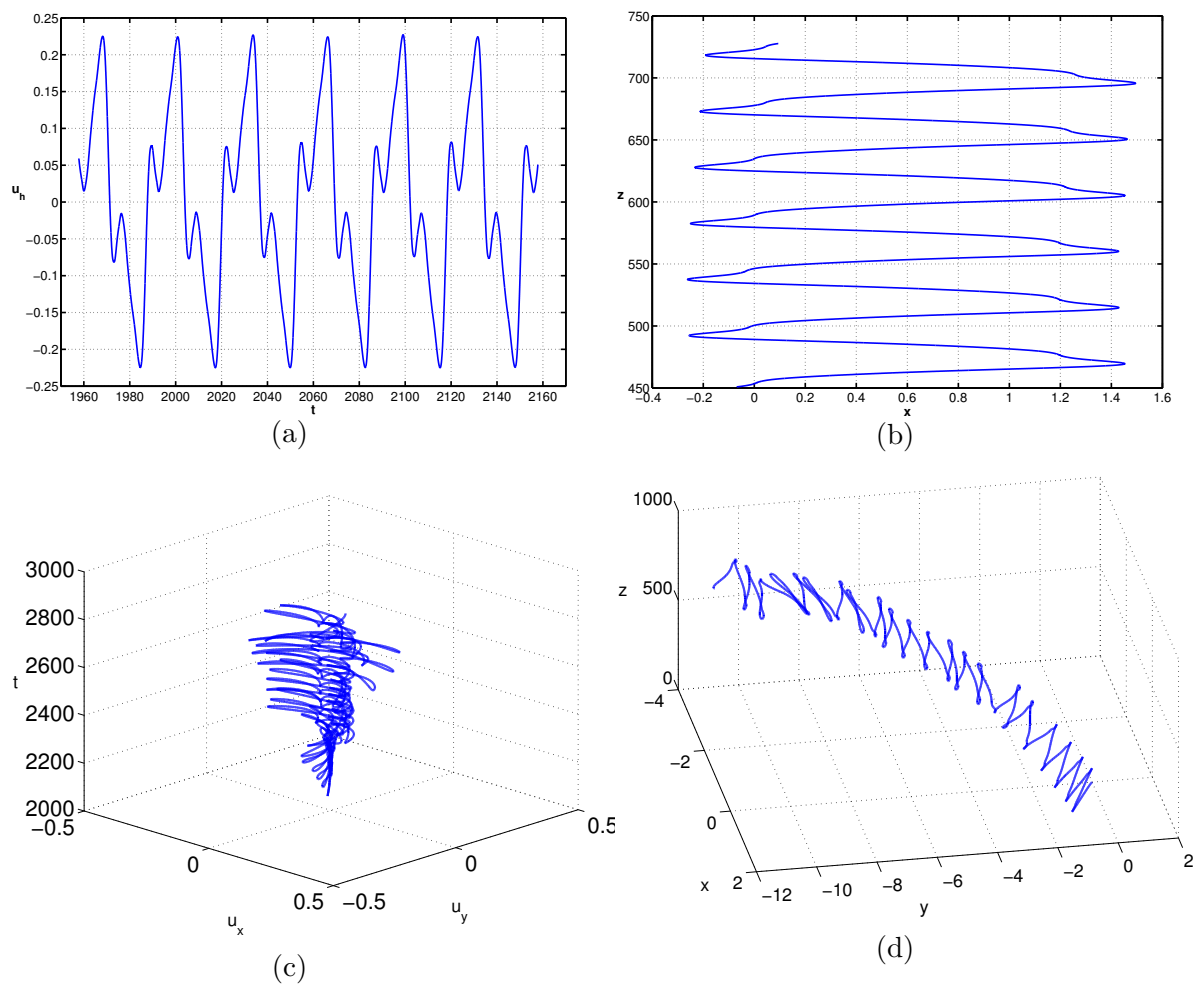


Figure 2.14: Velocities and trajectories of very light spheres at $\rho_s/\rho = 0.2$, $G = 200$. (a),(c) Horizontal velocities as a function of time, (b),(d) trajectory. Note that the temperately appeared planar trajectory (b) is soon replaced by a three dimensional motion (d) whose horizontal velocities behave similarly as the case in Figure 2.13(a).

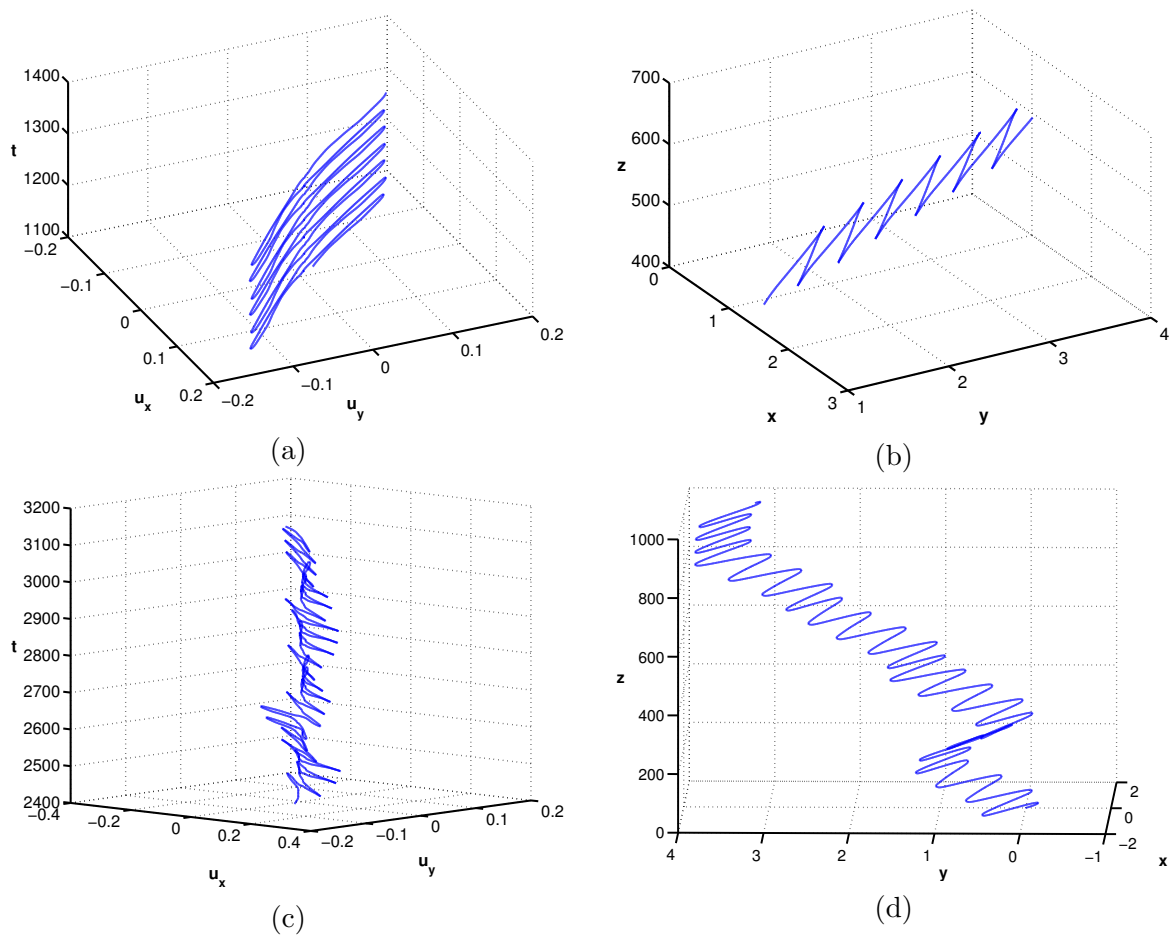


Figure 2.15: Velocities and trajectories of heavier but still buoyant spheres. Left column: horizontal velocities as a function of time, right column: trajectory. (a),(b) $\rho_s/\rho = 0.5$, $G = 190$ (last 6 periods), (c),(d) $\rho_s/\rho = 0.65$, $G = 195$.

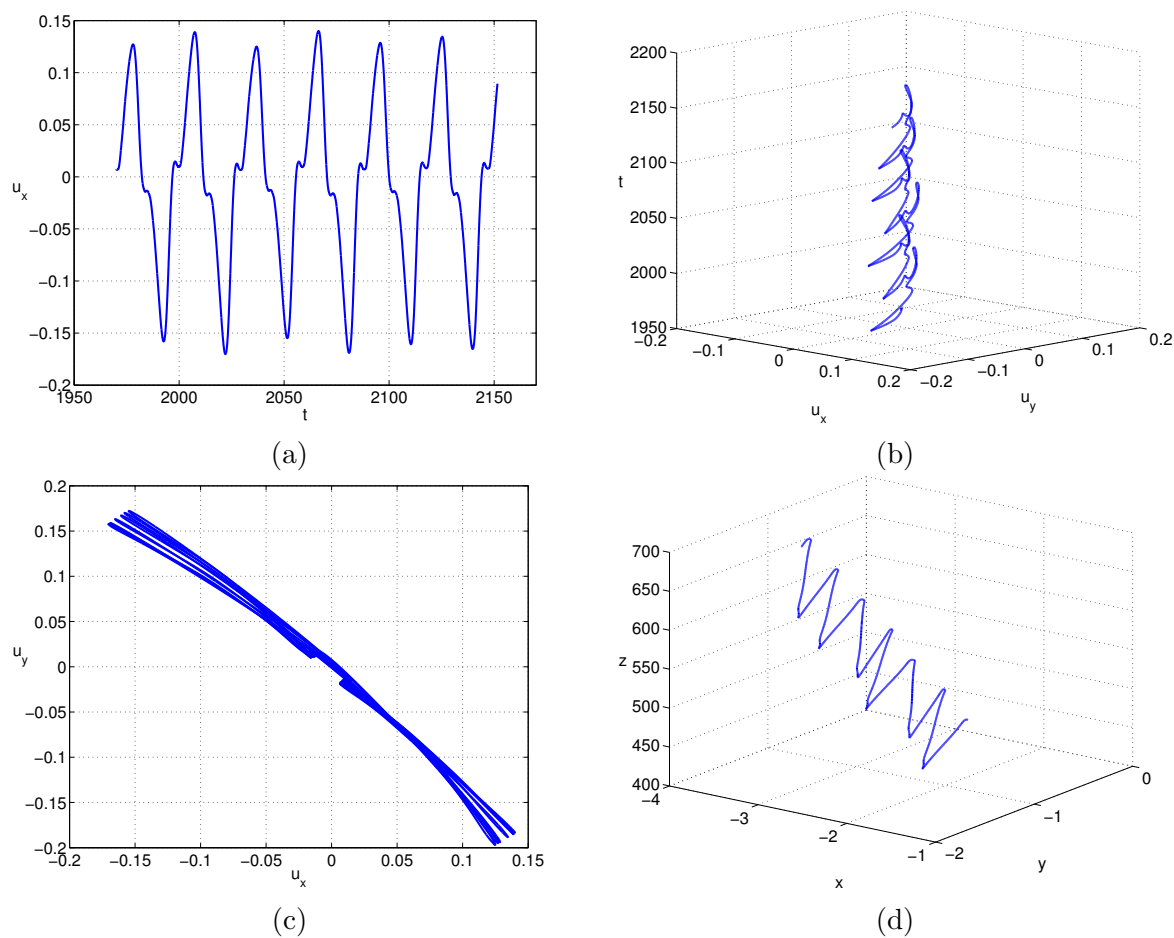
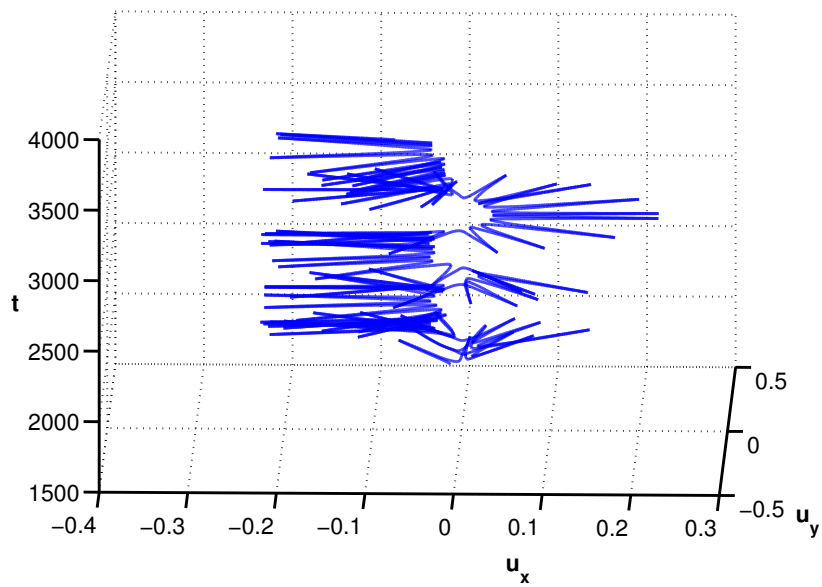
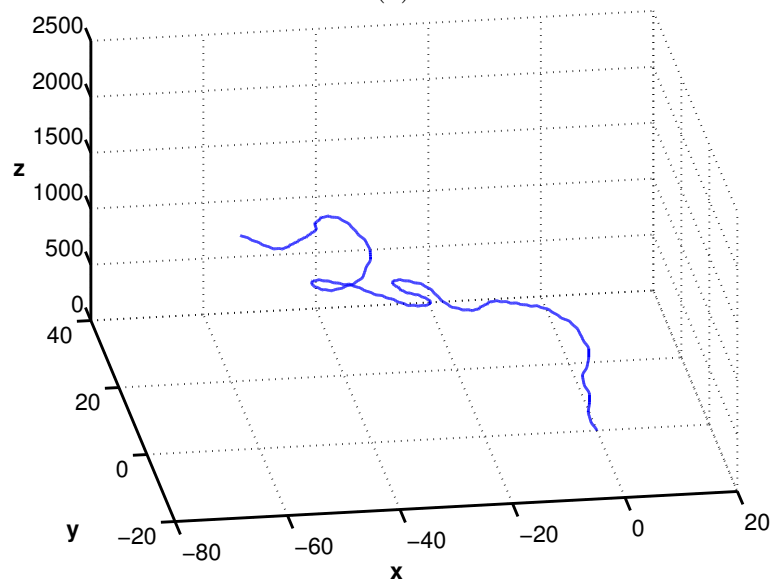


Figure 2.16: Quasi-periodic zigzagging trajectories of heavier spheres at $\rho_s/\rho = 0.5$, $G = 200$ (last 6 periods). (a),(b) Horizontal velocities as a function of time, (c) projection of the velocity vectors onto the horizontal plane, (d) trajectory.



(a)



(b)

Figure 2.17: Horizontal velocities and trajectory of heavier but still marginally buoyant spheres at $\rho_s/\rho = 1$, $G = 195$.

2.6 Transition to chaos

2.6.1 Light sphere

As shown in the previous section, for buoyant spheres ($\rho_s/\rho \leq 1$) the oblique oscillating regime was found to disappear due to vanishing horizontal velocity in the JDB paper. A more thorough investigation of this process shows that, in general, a chaotic behavior sets in already at this stage and that the density ratio of 1 is not a relevant distinction between light and dense spheres. At moments when the horizontal velocity of the sphere vanishes, the flow close to the sphere becomes temporarily axisymmetric which is accompanied with some, albeit, limited freedom of selection of a new symmetry plane of the wake. As a consequence, various imperfect zigzagging states exist before being replaced by fully three-dimensional and chaotic one.

Considering the lower limit of the chaotic domain (in terms of the Galileo number) to be given by the loss of stability of oblique oscillating states, the zigzagging regime described in the JDB paper represents an exception. The existence of genuinely periodic zigzagging states was confirmed only in cases summed up in Table 2.2 and represented in the state diagram (Figure 2.7). The regimes described as “zig-zag, oblique” correspond to imperfect but still periodic zigzagging, an example of which is already represented in Figure 2.15 (a,b). They can be considered as a periodic case standing between the intermittent planar zigzagging (Figure 2.11 (a,b) and 2.12) and slightly oblique, not exactly planar, intermittent zigzagging regimes of Figure 2.15 (c,d). A quasi-periodic regime was evidenced at the density ratio 0.5 and $G = 200$ (see Figure 2.16) before the onset of a fully chaotic one of the type of Figure 2.17. In spite of a relatively detailed sweep of the parameter plane, the perfect vertical zigzagging regime was found only for $\rho_s/\rho = 0.5$, $G = 180$ (see Figure 2.9).

description	$(\rho_s/\rho, G)$
zig-zag, oblique	(0,178); (0.2,185); (0.5,185); (0.5,190); (0.5,195)
zig-zag, oblique, quasi-periodic	(0.5,200)
zig-zag, vertical, periodic	(0.5,180)
fast ZZ oblique	(0,210); (0.2,230)

Table 2.2: Exceptional ordered regimes for light spheres in the chaotic domain.

The critical Galileo numbers of the onset of chaos, identified as the loss of stability of the oblique oscillating regime, is reported in Table 2.3.

2.6.2 Dense sphere

For density ratios $\rho_s/\rho \geq 1.7$ the transition to chaos is subcritical with a region of co-existence of states with a fixed symmetry plane and states in which the symmetry plane slowly rotates. In both cases, the same periodic and quasi-periodic oscillations with a main frequency corresponding to the high frequency oblique oscillating regime are present. The quasi-periodic oscillations contain the roughly three times slower frequency characteristic

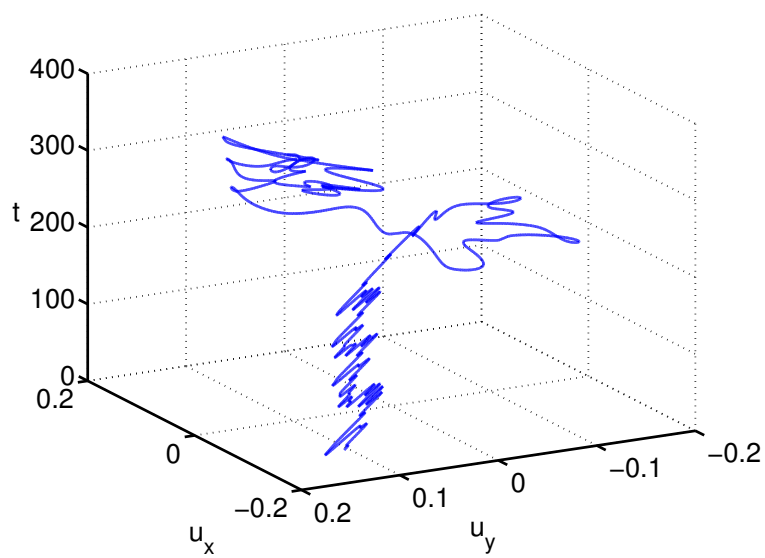
ρ_s/ρ	0	0.2	0.5	1	1.3	
G_{crit1}	171	175	179	192	202	
u_{z1}	1.350	1.356	1.361	1.381	1.392	
ρ_s/ρ	1.7	2	2.5	3	4	10
G_{crit1}	228	224	228	230	234	240
G_{crit2}	212	216	215	215	213	219
u_{z1}	1.429	1.424	1.430	1.436	1.439	1.447
u_{z2}	1.409	1.410	1.413	1.413	1.412	1.417

Table 2.3: Estimates of critical Galileo numbers G_{crit} and corresponding mean vertical velocities at the onset of chaos. For subcritical transition two values (upper and lower limit of bi-stability) are provided.

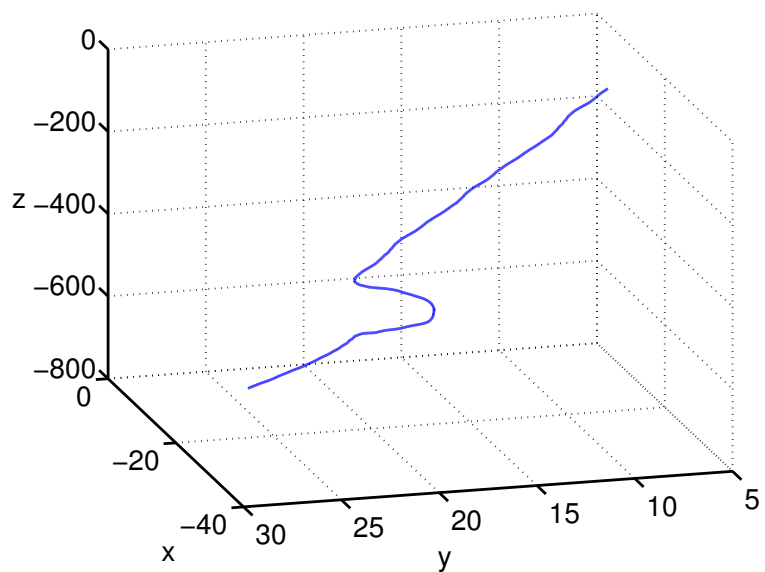
for the low frequency oblique oscillating regime. It is, however, interesting to note that a similar frequency was also reported in the fixed sphere wake by G. Bouchet & Dušek (2006) at $Re = 325$ where no fluid-solid interaction was present. ($Re = 325$ is close to the Reynolds number 330 based on the average vertical velocity at $G = 230$ and $\rho_s/\rho = 10$.) The overlapping extends over an interval of Galileo numbers having widths of 10 to 20 (see Table 2.3). The three-dimensional trajectories arising at the upper limit of the bi-stability domain can be considered as fully chaotic (see Figure 2.18).

The almost helical chaotic trajectories of dense spheres were already reported in the JDB paper. A detailed investigation of the non planar branch of the bi-stability shows, however, really perfect spiral trajectories. The latter are, strictly speaking, quasi-periodic with fast oscillation superimposed on the much slower rotation. The small amplitude of oscillation is invisible on the scale of the pitch of the trajectory. To investigate this branch of bistability we used a chaotic regime as an initial condition and we progressively lowered the Galileo number until the branch lost its stability i.e. when the rotation stopped. Figure 2.19 and 2.20 represent rotating regimes for the density ratio of 4 and 10, respectively. Table 2.4 provides some quantitative data. It shows that frequency, amplitude of oscillations and inclination/pitch angle given by the ratio of mean values of horizontal and vertical velocity remain, in general, the same whether the symmetry plane rotates or not. The slow rotation of the symmetry plane of the wake has little effect on the wake itself and on the frequencies generated by fluid-solid interaction. It is to be noted that the period of rotation is extremely long which may result in a pitch exceeding $1000d$ and very small curvature of the spirals.

Figure 2.21 shows how the lower limits of stability of supercritical states denoted G_{crit2} in Table 2.3 were determined.



(a)



(b)

Figure 2.18: Loss of stability of the symmetry plane at $\rho_s/\rho = 2$ and $G = 230$. (a) Horizontal velocity components as a function of time in a false 3D plot, (b) trajectory.

ρ_s/ρ	G	f_1	f_2	$\Delta u_h $	T_{rot}	$\langle u_h \rangle$	R	$\langle u_h \rangle/\langle u_z\rangle$
2.5	215	0.059	0.178	0.025	135	0.1343	2.88	0.095
		–	0.186	0.0041		0.1466		0.1040
3.0	215	0.060	0.178	0.022	167	0.135	3.59	0.096
		–	0.186	0.0036		0.146		0.104
3.0	220	0.060	0.181	0.023	133	0.1335	2.82	0.094
		0.060	0.179	0.0214		0.1351		0.095
4.0	214	0.060	0.179	0.017	403	0.137	8.80	0.097
		–	0.187	0.0027		0.146		0.104
4.0	220	0.060	0.182	0.018	174	0.135	3.72	0.095
		0.061	0.182	0.016		0.137		0.097
4.0	225	0.061	0.185	0.018	143	0.132	2.99	0.092
		0.051	0.179	0.023		0.131		0.091
10.0	220	0.055	0.191	0.0015	1115	0.145	25.8	0.102
		–	0.191	0.0015		0.145		0.103
10.0	225	0.056	0.190	0.0028	337	0.139	7.44	0.097
	224	0.055	0.191	0.0016		0.144		0.101
10.0	230	0.054	0.186	0.0085	354	0.134	7.53	0.093
		0.053	0.186	0.0089		0.138		0.096

Table 2.4: Quantitative characteristics of the bi-stability domain of dense spheres. Upper lines: rotating symmetry plane, lower lines: fixed symmetry plane. f_1 : low oscillation frequency, f_2 : high frequency, $\Delta|u_h|$: r.m.s. of fluctuations of the norm of the horizontal velocity, T_{rot} : period of rotation of the symmetry plane, $\langle|u_h|\rangle$: mean value of the the norm of the horizontal velocity, R : radius of the horizontal projection of the trajectory, $\langle u_z\rangle$: mean vertical velocity.

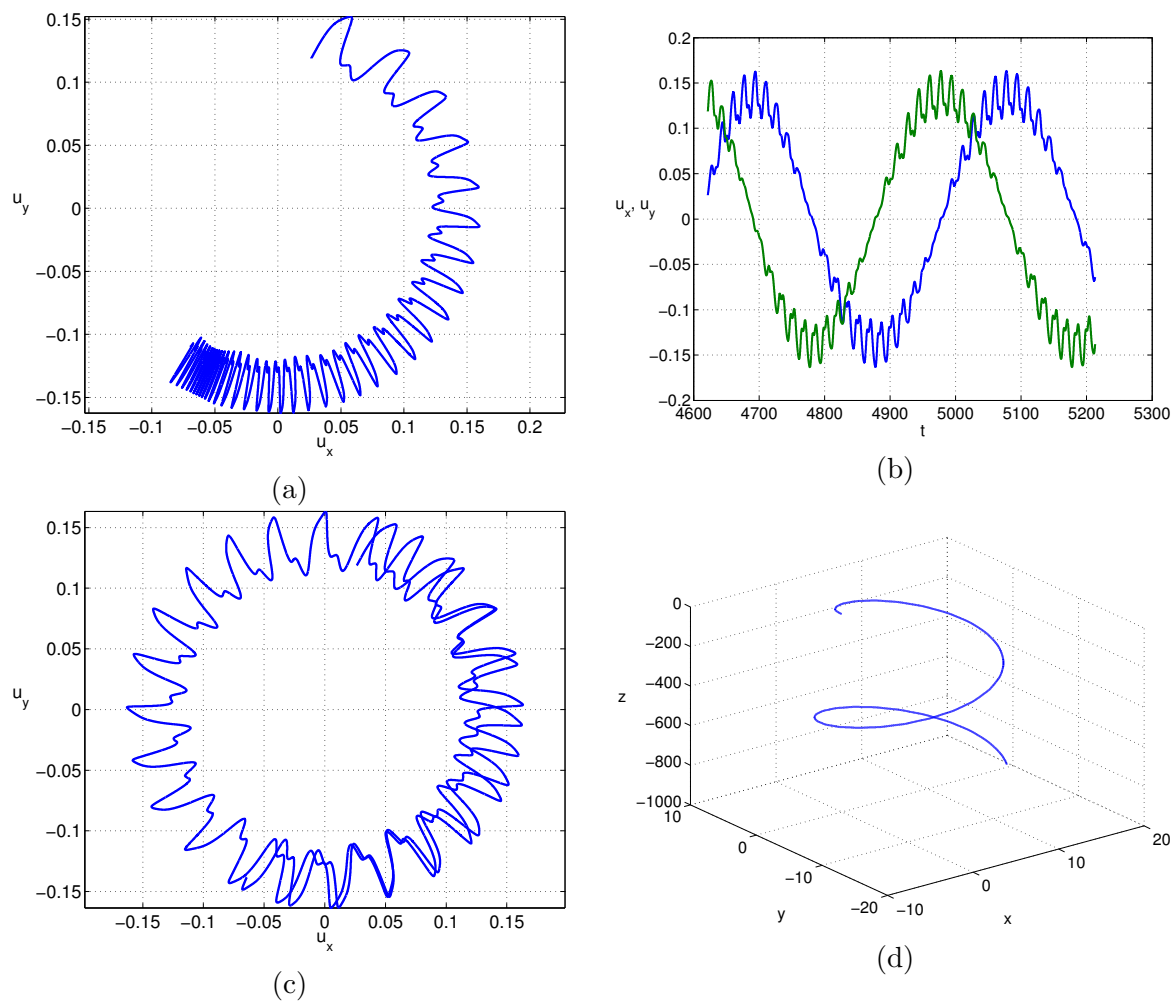


Figure 2.19: Velocities and trajectories of spheres of density ratio $\rho_s/\rho = 4$ on the rotating bi-stability branch. (a) $G = 212$: Settling to oblique oscillating state. (b,c,d) $G = 214$: slowly rotating symmetry plane and periodic low frequency oscillations, (b) horizontal velocity components as a function of time, (c) projection of the velocity vectors onto a horizontal plane, (d) trajectory.

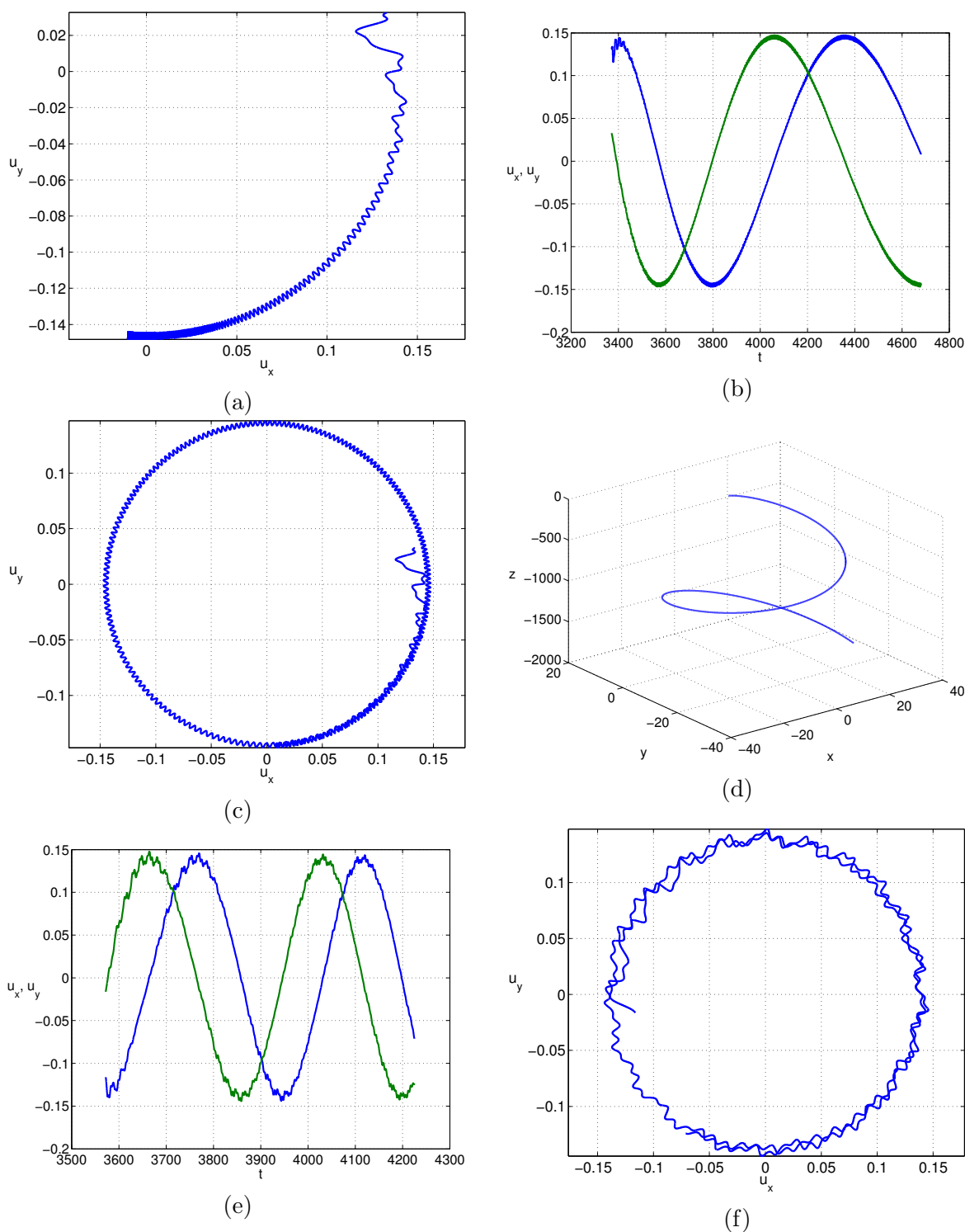


Figure 2.20: Velocities and trajectories of spheres of density ratio $\rho_s/\rho = 10$ on the rotating bi-stability branch. (a) Settling to oblique oscillating state at $G = 215$, (b,c,d) slowly rotating symmetry plane and periodic high frequency oscillation at $G = 220$ (same types of figures as 2.19 (b,c,d)), (e) horizontal velocity components as a function of time, (f) projection of the velocity vectors onto a horizontal plane in the case of quasi-periodic oscillation at $G = 225$.

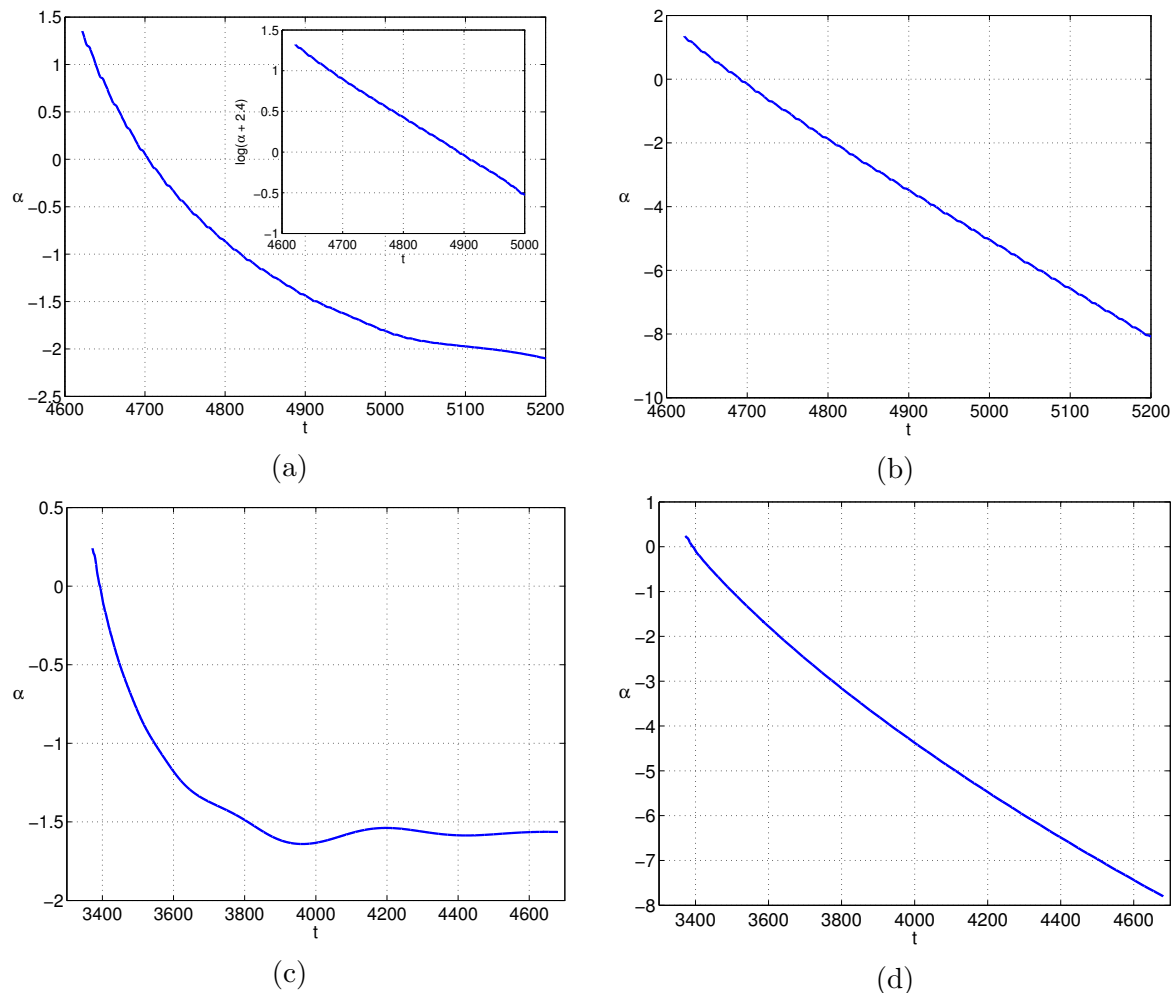


Figure 2.21: Angle of the (almost) symmetry plane represented by the argument α of $u_x + iu_y$ as a function of time for spheres of Figures 2.19 and 2.20. (a) $\rho_s/\rho = 4, G = 212$, (b) $\rho_s/\rho = 4, G = 214$, (c) $\rho_s/\rho = 10, G = 215$, (d) $\rho_s/\rho = 10, G = 220$. Note that the angle of trajectory plane tends to a constant value in (a) (see the inset in logarithmic scale) and (c) for oscillations tending to a fixed symmetry plane while it reaches a constant slope in (b) and (d) for the symmetry plane tending to rotate with constant angular velocity.

2.7 Vertical oscillating regime in the chaotic domain

In this section we focus on the “periodic windows” known to be “interspersed between chaotic clouds” in many dynamical systems such as the logistic map (see e.g. Strogatz (1994)). The JDB paper reported the existence of a vertical periodically oscillating regime at density ratios 0.5 and 0. The most striking feature of this periodic regime is its frequency, roughly equal to 0.14 in the units introduced in Sec. 2.2. It was shown to be associated to the least stable complex eigenpair of the linear operator describing the linear stability of the axisymmetric fluid - solid system. At the secondary bifurcation giving rise to the oblique oscillating regime, this eigenpair has no relevance because the primary instability considerably modifies the flow from which this bifurcation arises. In the case of vertical paths with rapid periodic oscillations the sphere motion remains essentially vertical because (see below) the amplitude of oscillation appears to be very small. The present data show that there exists a domain of parameters in which this regime appears as the only stable one. The domain of stability and the characteristics of the vertical periodic trajectories were investigated in detail. Some other ordered states were evidenced but the latter appear as isolated particular cases, except, possibly, the helical regime described in Sec. 2.8.

The vertical trajectories presenting fast transverse oscillations are qualitatively very similar to those of the high-frequency oblique oscillating regime. The trajectory is planar, i.e. the wake has a fixed symmetry plane, its oscillations have a high frequency, small wavelength and small amplitude similarly as in the oblique oscillating regime (see Figure 2.22). The main difference consists in a zero mean value of horizontal velocity. Instead of oblique oscillating, this regime can be called vertical oscillating. In the JDB paper, two different simulations at $\rho_s/\rho = 0.5$ and $G = 240$ lead to the conjecture that the vertical oscillating regime co-exists systematically with the chaotic one. This is not the case and Figure 2.23 representing a simulation over a much longer time interval (about 1000 time units) explains the why. It can be seen that the mean value of velocity deviates, initially only very slowly, from zero leading to a progressively more and more inclined plane of the trajectory. The amplification of mean horizontal velocity finally leads to chaos. The state considered in JDB as coexisting with a chaotic regime is thus unstable and appears to be either chaotic or intermittently switching from vertical oscillating to chaotic on a very large time scale. In the same manner, all vertical oscillating regimes represented in the state diagram of Figure 2.7 have been tested for bi-stability by running sufficiently long simulations starting each time from at least two different initial conditions. With three exceptions $\rho_s/\rho = 1$, $G = 250, 260$, and $\rho_s/\rho = 1.3$, $G = 260$, bi-stability could be excluded.

At density ratios smaller than 0.5 all trajectories resembling vertical oscillating ones appeared to be intermittent except for two cases reported in Table 2.2 ($\rho_s/\rho = 0$, $G = 210$ and $\rho_s/\rho = 0.2$, $G = 230$). They are closely related to vertical oscillating regimes due to their frequency, 0.134 and 0.145, respectively. Their specificity consists in a significantly non zero mean horizontal velocity. The trajectory is not very far from planar (note the different scales of horizontal axes in Figure 2.25 (a) used to make the three-dimensionality apparent). The average horizontal velocity is close to 0.1 and is thus close to that of oblique oscillating regimes. The main difference consists in the fact that the oscillations are perpendicular to the mean value shift. This could be described as an RSB mode in terms of Fabre *et al.* (2008) or

MM_π according to Meliga *et al.* (2009). The resulting trajectory is thus, practically, planar in a plane inclined by 3.7° with respect to the vertical direction. The trajectory obtained at $\rho_s/\rho = 0.2$ and $G = 230$ (Figure 2.25 (d)) is very similar. The mean value of the velocity is offset perpendicularly to the mean direction of the velocity oscillations. The dynamics is now significantly quasi-periodic. This might cast a doubt on the stability of this regime but, in the case represented in Figure 2.25 (c), there is no trend to change over more than 500 time units. The state is found to co-exist with a chaotic one which might also indicate intermittence on an extremely large time scale. Figure 2.26 shows that regimes lying below the subdomain of vertical oscillating states of the parameter plane are intermittent with very long characteristic times.

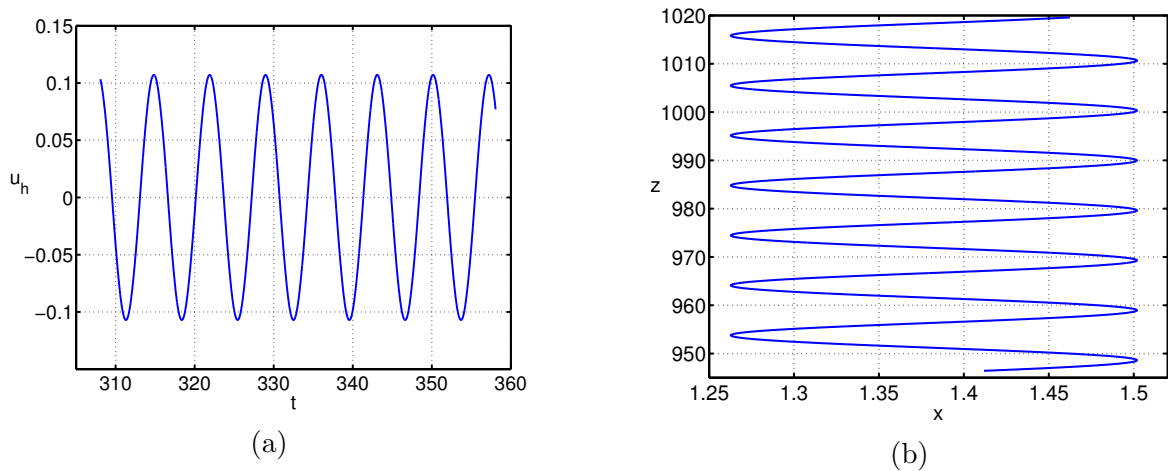


Figure 2.22: Vertical oscillating regime at $\rho_s/\rho = 0.5$, $G = 260$. (a) Horizontal velocity in the trajectory plane as a function of time, (b) trajectory in its plane.

The typical vertical oscillating trajectory represented in Figure 2.22 at $\rho_s/\rho = 0.5$ and $G = 260$ is very accurately vertical. Figure 2.22 (a) shows that the oscillation amplitude of the velocity barely exceeds 0.1 (0.105), the period of oscillation is about 7, more accurately, the frequency is 0.1416. The high frequency (not much lower than the frequency of the high frequency oblique oscillating regime - 0.18) and the relatively small horizontal velocity amplitude (as compared to chaotic fluctuations of neighboring chaotic states) yields a small amplitude of oscillations of the trajectory with respect to the vertical direction (see Figure 2.22 (b)): 0.12 of the sphere diameter.

The domain of stability of the vertical oscillating regime is limited to spheres of intermediate density $0.2 < \rho_s/\rho < 2$. The frequency of oscillations slightly grows (with increasing density ratio and with growing Galileo number) from 0.141 at $\rho_s/\rho = 0.5$ and $G = 250$ to 0.150 at $\rho_s/\rho = 1.7$ and $G = 290$. In contrast, the amplitude (both of horizontal velocity and of the trajectory oscillation) decreases quite significantly: by a factor of 1/2. The amplitude of the vertical velocity never exceeds 0.001, i.e., given the vertical velocity varying only very slightly around 1.5, it is less than 0.07 %. All vertical oscillating regimes have been found very accurately planar and having an average horizontal velocity of less than 10^{-6} . The

loss of verticality and planarity is probably not completely abrupt at higher Galileo number limit. At $\rho_s/\rho = 0.5$ and $G = 290$ we evidenced a slightly oblique trajectory plane inclined by 0.55° with respect to the vertical direction (similarly as in Figure 2.15 (b)) but with smaller inclination and much smaller amplitude of oscillations). At $\rho_s/\rho = 1.7$ and $G = 300$ the trajectory was no longer found planar and the periodicity was found to have given way to quasi-periodicity. The intriguing pattern of oscillations is represented in Figure 2.24. The fall of the sphere remains vertical in the average and the oscillation amplitude of both of the horizontal velocity and of the trajectory is similar as for the perfectly planar and periodic trajectory we evidenced at $\rho_s/\rho = 1.7$ and $G = 290$.

To sum up, the vertical oscillating regime is characterized by very small and fast oscillations and its planarity and verticality are remarkably accurate. This behavior is due to a symmetric vortex shedding described elsewhere as SW mode (Fabre *et al.* (2008); Meliga *et al.* (2009)) resulting in a zero mean lift (Kotouč *et al.* (2009)) for a fixed body. The typical wake structure is represented in Figure 2.27.

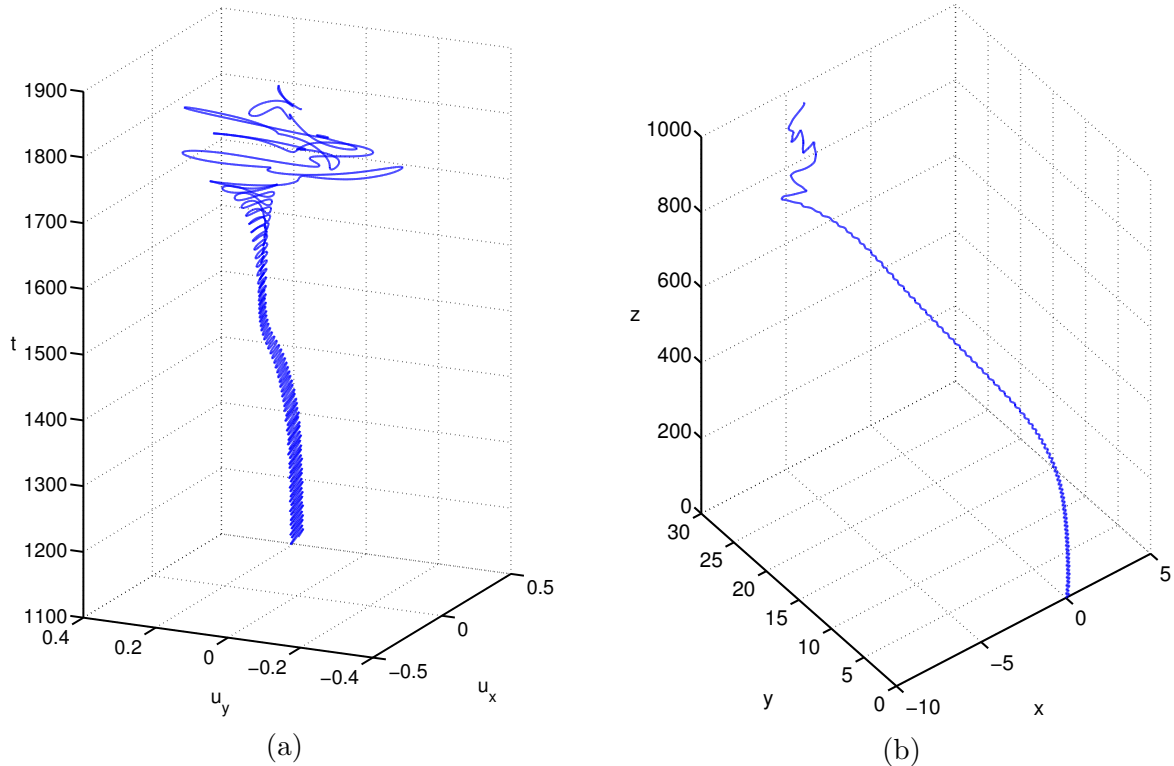
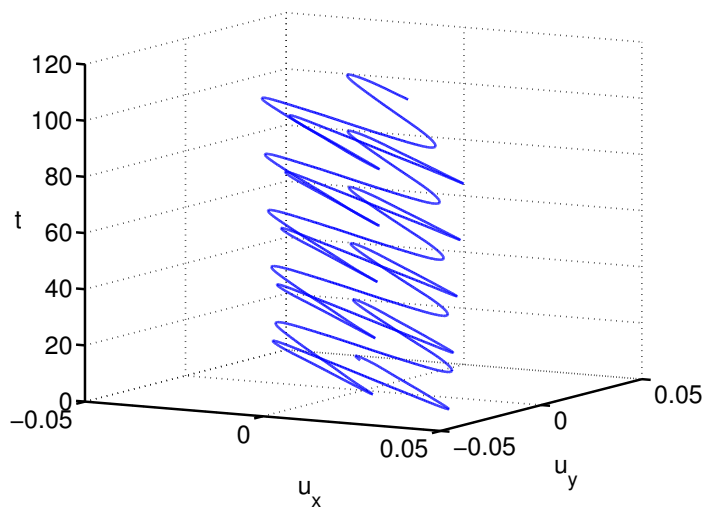
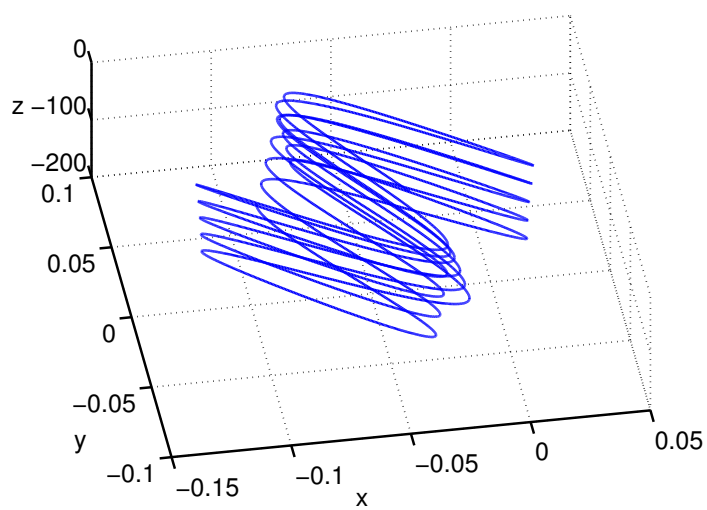


Figure 2.23: Simulation of an initially vertical oscillating regime at $\rho_s/\rho = 0.5$, $G = 240$. (a) Horizontal velocity vector as a function of time, (b) trajectory.



(a)



(b)

Figure 2.24: Non planar vertical oscillating regime at $\rho_s/\rho = 1.7$, $G = 300$. (a) Horizontal velocity vectors as a function of time, (b) trajectory. The figures are truncated to the last 100 time units of simulation.

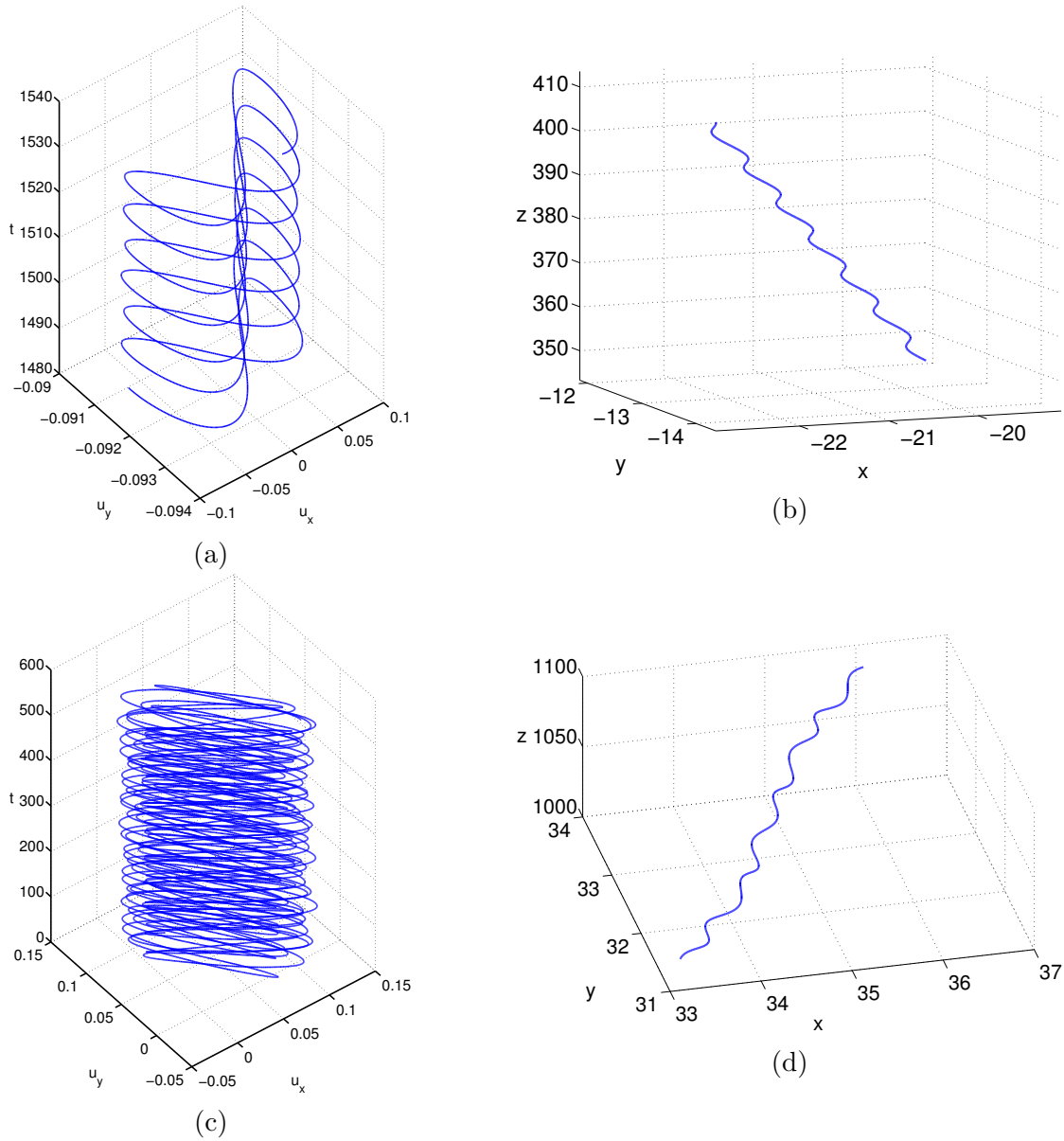


Figure 2.25: Trajectories oscillating in oblique plane. Left column: horizontal velocity vectors as a function of time, right column: trajectory. (a,b): $\rho_s/\rho = 0$, $G = 210$ (only the last 50 time units are plotted), (c,d): $\rho_s/\rho = 0.2$, $G = 230$.

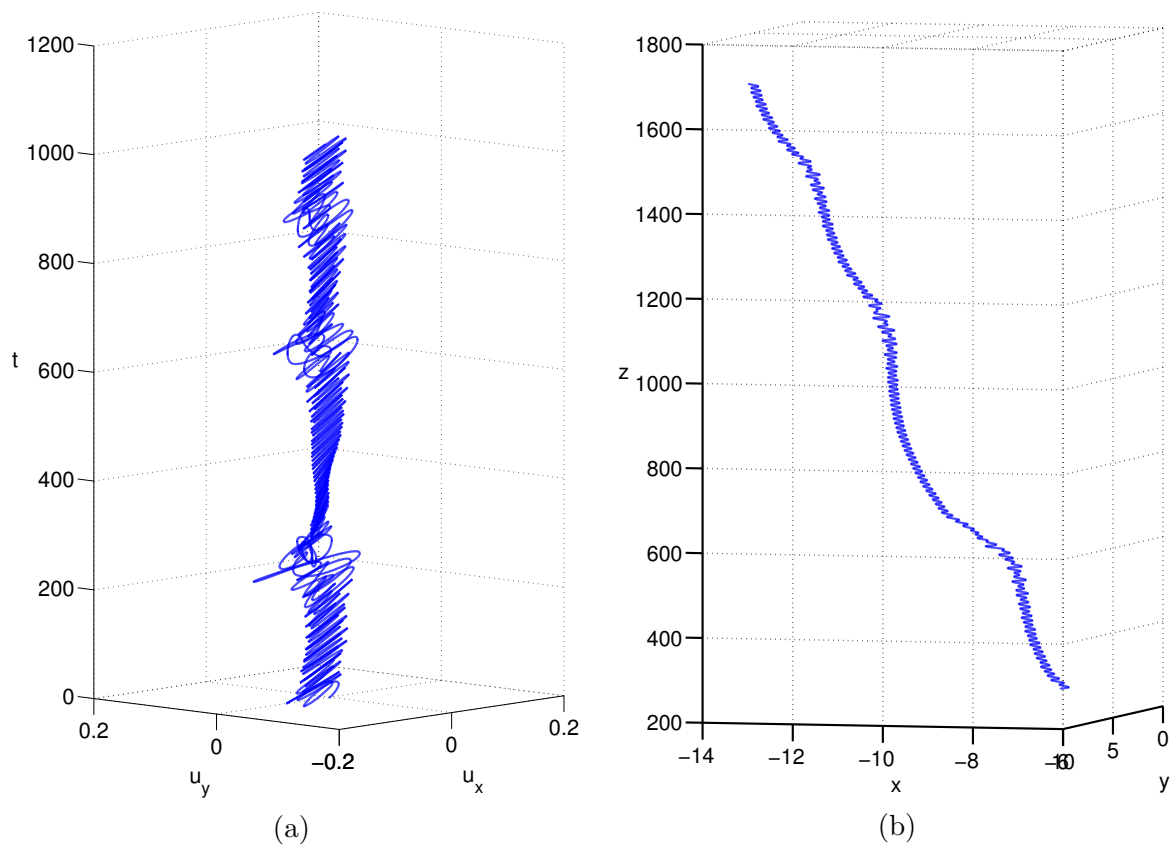


Figure 2.26: Intermittent state at $\rho_s/\rho = 0.2$, $G = 240$. (a) Horizontal velocity vectors as a function of time, (b) trajectory.

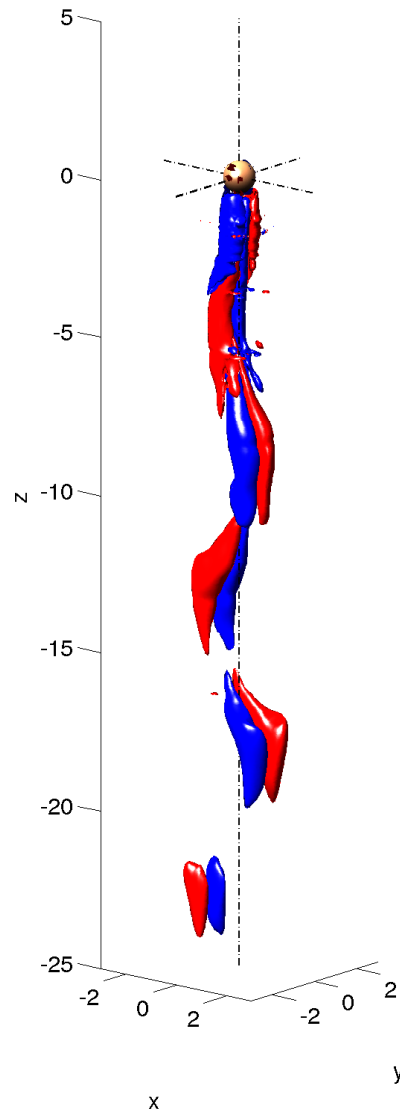


Figure 2.27: Vortical structure of the wake of the vertical oscillating regime at $\rho_s/\rho = 0.5$ and $G = 250$. The represented levels of vorticity are ± 0.25 .

2.8 Helical regime

For infinitely light spheres and at the upper limit of the considered Galileo number interval we evidenced states promising to provide a link with the “vibrating” states observed by Horowitz & Williamson (2010) for a very large variety of parameters corresponding to light spheres. For this reason we put a special focus on these intriguing, very regular states far above the onset of chaos. The trajectories are perfectly spiral, projecting like circles onto a horizontal plane. The rotation periods are approximately 10 (in time units d/U_{ref}) which results (with account of the average vertical velocity of about 1.4) in wavelengths close to 15 observed by Horowitz & Williamson (2010). However, the trajectories are not planar and the domain of their existence was found to be very restricted (see Figure 2.7.) For massless spheres ($\rho_s/\rho = 0$) we started to observe the spiral trajectory at $G = 375$. The vertical velocity being 1.408, this corresponds to the Reynolds number $Re = 530$, which is already significantly above the experimentally evidenced threshold of vibrating states of Horowitz & Williamson (2010) (reported to be about 260). Moreover, though the upper limit of density ratio (critical mass) found in experiment was close to 0.4, we did not find any regular spiral (let alone zigzagging planar) trajectory at the density ratio as low as 0.2. For this reason, we decided to reverify the numerical accuracy of the simulation by doubling the number of azimuthal modes of the azimuthal Fourier expansion (by truncating at the mode $m = 15$ instead of 7), by doubling also the number of collocation points of the spectral element discretization (switching from 6×6 to 8×8 collocation points per spectral element) and by increasing the number of spectral elements from 245 to 335. This increase of numerical accuracy did not bring about any significant quantitative change of results. At $\rho_s/\rho = 0.1$ and $G = 500$ we found a rotation period of 9.2, a horizontal velocity of 0.30 and a vertical velocity of 1.506 (both velocities are practically constant in the helical regime) for the “low” resolution and 9.2, 0.32 and 1.501, respectively, for the higher resolution. (The investigation was continued with the higher resolution.) We evidenced the perfectly spiral trajectory for the density ratio of 0.1 (as already mentioned) but no longer for 0.2 where the ordered trajectories gave way to a chaotic behavior.

The most striking feature of the helical regime is the high regularity of the trajectory despite the high Galileo number, i.e. also the Reynolds number (750 for $\rho_s/\rho = 0.1$ and $G = 500$). The characteristics of a typical trajectory ($\rho_s/\rho = 0.1$ and $G = 500$) are represented in Figures 2.29 (a,b,c), quantitative data for three helical regimes are reported in Table 2.5. Figure 2.29 (d) shows the typical twisted wake. The helical regime stands out for an exceptionally large horizontal velocity. While the typical horizontal velocity represents less than 10% of the vertical one in oblique regimes (see Table 2.1), the same ratio amounts to 30% for the massless sphere and 20% for the sphere of density ratio 0.1. The helical shape of the trajectory is not very far from an ideal spiral having a circular horizontal projection (Figure 2.29 (b)). The norm of the velocity vector is practically constant (within about 1%). The horizontal projection turns regularly with less than 2% r.m.s. fluctuations, the vertical component is constant with about a half percent accuracy. The large horizontal velocity is correlated with a drop of vertical velocity. The common features with the vibrating states of Horowitz & Williamson (2010) are the perfect average verticality of the trajectories, the pitch (very similar to their wavelength), the radius (in qualitative correspondence with the

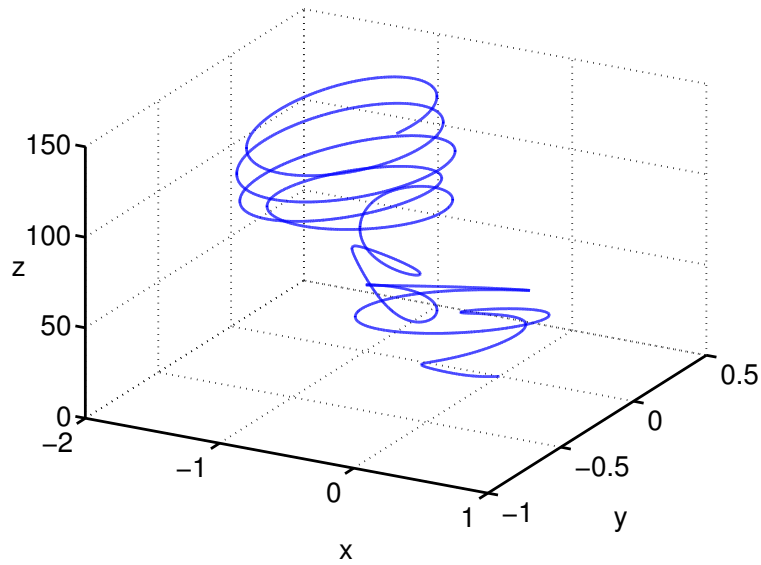


Figure 2.28: $\rho_s/\rho = 0.1, G = 500$: An initially planar trajectory resuming the helical shape.

r.m.s. of the horizontal projection of the vibrating trajectories) and the extreme regularity of the trajectories. However, the drop of vertical velocity is insufficient to account for the experimentally observed increase of drag coefficient. As for the difference of the shape of trajectories, we attempted to test the stability of the planarity by simulating trajectories starting from vertical rise (forced for the same parameters $\rho_s/\rho = 0.1$ and $G = 500$) perturbed by an imposed horizontal velocity of 0.01 (0.6% of the vertical velocity). The trajectory left the initially imposed plane already during the stage of amplification of axisymmetry breaking without presenting any transient zigzagging character (see Figure 2.28) and settled very rapidly to the helical shape.

$(\rho_s/\rho, G)$	period	$\ \mathbf{u}_h\ $	$\Delta\ \mathbf{u}_h\ $	u_z	Δu_z	pitch	radius	C_D
(0,400)	9.12	0.384	0.005	1.382	0.009	12.6	0.56	0.70
(0,500)	8.96	0.422	0.008	1.406	0.006	12.6	0.60	0.67
(0.1,500)	9.22	0.326	0.006	1.501	0.003	13.8	0.48	0.59

Table 2.5: Characteristics of three helical regimes. For the modulus of horizontal velocity $\|\mathbf{u}_h\|$ and for the vertical velocity u_z , the mean values over 5 periods are reported. The corresponding root mean square deviations are denoted Δ . “Pitch” and “radius” refer to the trajectory.

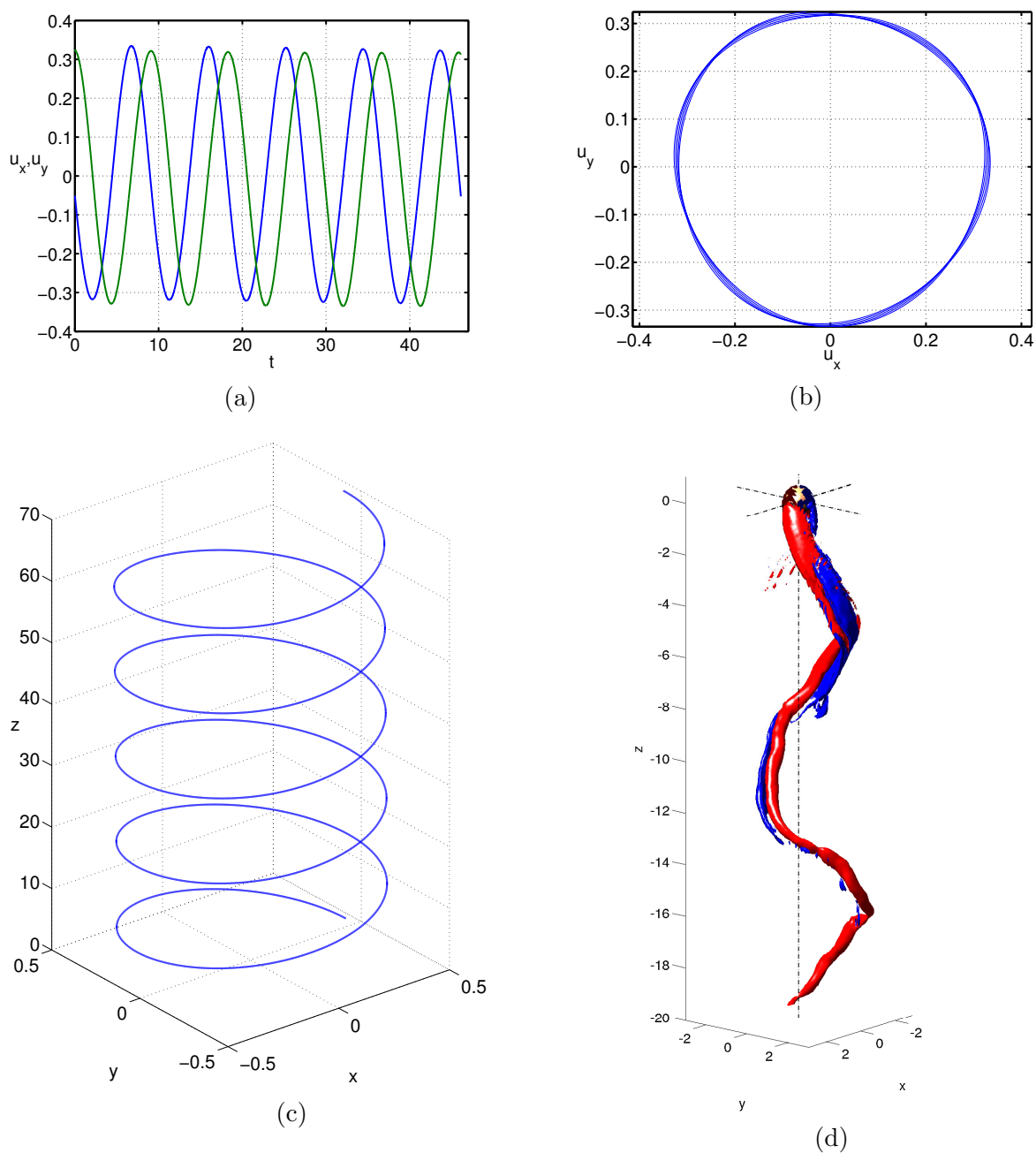


Figure 2.29: Five periods of helical trajectory for $\rho_s/\rho = 0.1$ and $G = 500$. (a) horizontal velocity components as functions of time, (b) path of the horizontal velocity vector, (c) trajectory. Figure (b) shows the very small deviations from periodicity and from circular form. Figure (d) represents iso-surfaces of stream-wise vorticity at levels ± 1 at the end of the time interval of figure (a).

2.9 Chaotic states

The randomness of chaotic states limits the interest of graphic representations because each sample is different. Nonetheless, the chaotic trajectories present features reminiscent of neighboring ordered regimes. In Figure 2.30, three very different chaotic states are represented in terms of the time evolution of the horizontal velocity vector and as three-dimensional paths. There are clear qualitative differences. The first represented state ($\rho_s/\rho = 0.5, G = 230$) carries a fingerprint of intermittent oblique zigzagging of Figure 2.15 and 2.17, the second one ($\rho_s/\rho = 0.5, G = 500$) is intermittently helical (with turning horizontal velocity vector of large magnitude), the last one ($\rho_s/\rho = 2, G = 400$) presents features described in Sec. 2.6.2. A statistical approach is necessary to quantify the differences independently of the random details. Moreover, in view of the presence of ordered states within the chaotic domain, the quantitative characterization must apply both to ordered and chaotic states. In what follows we evaluate the following statistical quantities in the entire domain of unsteady (both ordered and chaotic) regimes:

- mean value of the horizontal velocity vector $\mathbf{u}_h = (u_x, u_y)^T$:

$$\langle \mathbf{u}_h \rangle \equiv (\langle u_x \rangle, \langle u_y \rangle)^T = \lim_{T \rightarrow \infty} \frac{1}{T} \int_{t_0}^{t_0+T} \mathbf{u}_h(t) dt; \quad (2.9)$$

- root mean square of the horizontal velocity fluctuations $\mathbf{u}'_h = \mathbf{u}_h - \langle \mathbf{u}_h \rangle$:

$$\left(\langle \mathbf{u}'_h{}^2 \rangle \right)^{1/2} = \left[\lim_{T \rightarrow \infty} \frac{1}{T} \int_{t_0}^{t_0+T} (\mathbf{u}'_h)^2 dt \right]^{1/2}; \quad (2.10)$$

- correlation time T_{corr} defined by the autocorrelation function

$$R(\tau) = \lim_{T \rightarrow \infty} \frac{1}{T} \int_{t_0}^{t_0+T} (u'_x(t+\tau)u'_x(t) + u'_y(t+\tau)u'_y(t)) dt \quad (2.11)$$

as the first time shift τ at which R vanishes:

$$T_{corr} = \min \{ \tau; R(\tau) = 0 \}. \quad (2.12)$$

The time averages are, actually, computed over finite time intervals but the statistical convergence is checked by monitoring the decrease of fluctuations of the averages with increasing size of the time series.

The plotting of the computed values faces the problem of bi-stability. We make the choice of plotting chaotic states whenever they are found to co-exist with ordered ones. In the domain of bi-stability of the fixed and rotating symmetry plane (see sec. 2.6.2) we plot the states with rotating symmetry plane representing a natural (albeit ordered) continuation of chaotic regimes.

The plot of the norm of the mean value of the horizontal velocity vector (Figure 2.31) lets the oblique oscillating states stand out. The quantitative evolution toward larger horizontal

velocity when the density ratio increases, evidenced in Table 2.1, is also reflected in the figure. The “exceptional” oblique oscillating state $\rho_s/\rho = 0, G = 210$, for which we did not find a co-existence with a chaotic regime, also emerges. For the chaotic states, a theoretically zero mean value is expected as expression of randomness.

In Figure 2.32, representing the r.m.s. of horizontal velocity fluctuations, the helical regime strongly emerges in the right lower corner of the plot. This corresponds to the exceptionally large value of the horizontal velocity oscillations in this regime. It is, however, to be noted that all chaotic regimes of light spheres at high Galileo numbers present above average horizontal velocity fluctuations. In contrast, the domain of oblique oscillating states stands out for below average fluctuations. This is due to the fact that what appears as dominant fluctuations in the chaotic domain of falling spheres are randomized oblique trajectories. This can be seen when the sum of the norm of the mean value and of the r.m.s. of fluctuations of horizontal velocity is represented (Figure 2.33). The sharp distinction between oblique oscillating and chaotic states disappears which means that the mean horizontal velocity of oblique oscillating regimes is roughly the same as the amplitude of the horizontal velocity fluctuations in the chaotic states. Since these fluctuations are, for dense spheres, related to the slow rotation of the symmetry plane of the sphere wake, the chaotic trajectories appear as oblique oscillating on short scale (see Figure 2.30 (f)). Figure 2.33 shows that only zigzagging and vertical oscillating regime present relatively small horizontal velocity. In contrast, chaotic states of light spheres have an above average horizontal velocity even in spite of the fact that their trajectories are not helical. The island of vertical oscillating regimes in the center of the graph represents an extreme case of very accurately vertical trajectories with very small oscillations.

It may also be useful to quantify the planarity of the trajectories, especially for light spheres for which the transition to chaos only partly destroys the planarity of trajectories. For this purpose we computed the eigenvalues $\lambda_1 \geq \lambda_2$ of the correlation matrix

$$\langle \mathbf{u}_h \mathbf{u}_h^T \rangle = \begin{bmatrix} \langle u_x^2 \rangle & \langle u_x u_y \rangle \\ \langle u_x u_y \rangle & \langle u_y^2 \rangle \end{bmatrix}. \quad (2.13)$$

For exactly planar trajectories $\lambda_2 = 0$. In the case of perfect planar isotropy (helical or completely random trajectories) $\lambda_2 = \lambda_1$. The ratio $0 \leq \sqrt{\lambda_2/\lambda_1} \leq 1$ measures the intermediate cases. The use of this ratio allows us to redefine the zone of zigzagging states as chaotic state with close to planar trajectories (see Figure 2.34). The zone was approximately reported in the state diagram Figure 2.7 to show the link with the JDB paper.

To quantify the frequencies of aperiodic regimes we used the correlation time defined by Eqs. (2.11) and (2.12). For a periodic and harmonic function and $T \rightarrow \infty$ the time T_{corr} is exactly equal to a quarter of the period. We verified that $1/(4T_{corr})$ does not significantly differ from the frequencies that can be directly obtained from the data of periodic regimes. For aperiodic regimes the so defined frequency often corresponds to the highest peak of the power spectrum density but it can rather be interpreted as the smallest significant frequency. The correlation approach is more robust to the truncation of the analyzed time series than the search of the highest peak of the power spectrum. Apart from the trivial confirmation of the frequencies of strictly periodic regimes, Figure 2.35 shows that a significant subset of chaotic regimes is dominated by fast oscillations connected to the vertical oscillating regime.

For slowly rotating regimes the correlation time detects the frequency of the slow rotation which is of the order of 0.01 or less.

There exists a significant amount of experimental data (e.g. Karamanev *et al.* (1996); Horowitz & Williamson (2010)) showing a significant increase of the drag coefficient at the transition to turbulence for light spheres. This effect is related to a significant reduction of the vertical velocity taken as the basis for the computation of the drag coefficient. As already mentioned in the JDB paper and in Sec. 2.8, numerical simulations failed, so far, to confirm this observation quantitatively. A qualitative trend can, nonetheless, be seen in Figure 2.36. The non-dimensionalized vertical velocity increases mainly in the diagonal direction of the graph, i.e. both for increasing density ratio and Galileo number. In the lower right corner of the plot, the helical regime significantly lowers the vertical velocity, but the drop is insufficient to bring a quantitative agreement with experimental data (see Figure 12 of Horowitz & Williamson (2010) and Table 2.5). The r.m.s. of fluctuations of the vertical velocity is generally very small, which gives a good sense to the Reynolds number based on its average value. It is, however, interesting to note that for regimes presenting intermittent switching between helical and vertical rise non negligible fluctuations of vertical velocity may arise (see Figure 2.37).

In spite of some residual noise due to sometimes insufficient length of time series used in the statistical post-treatment, the global characteristics provide physically relevant information.

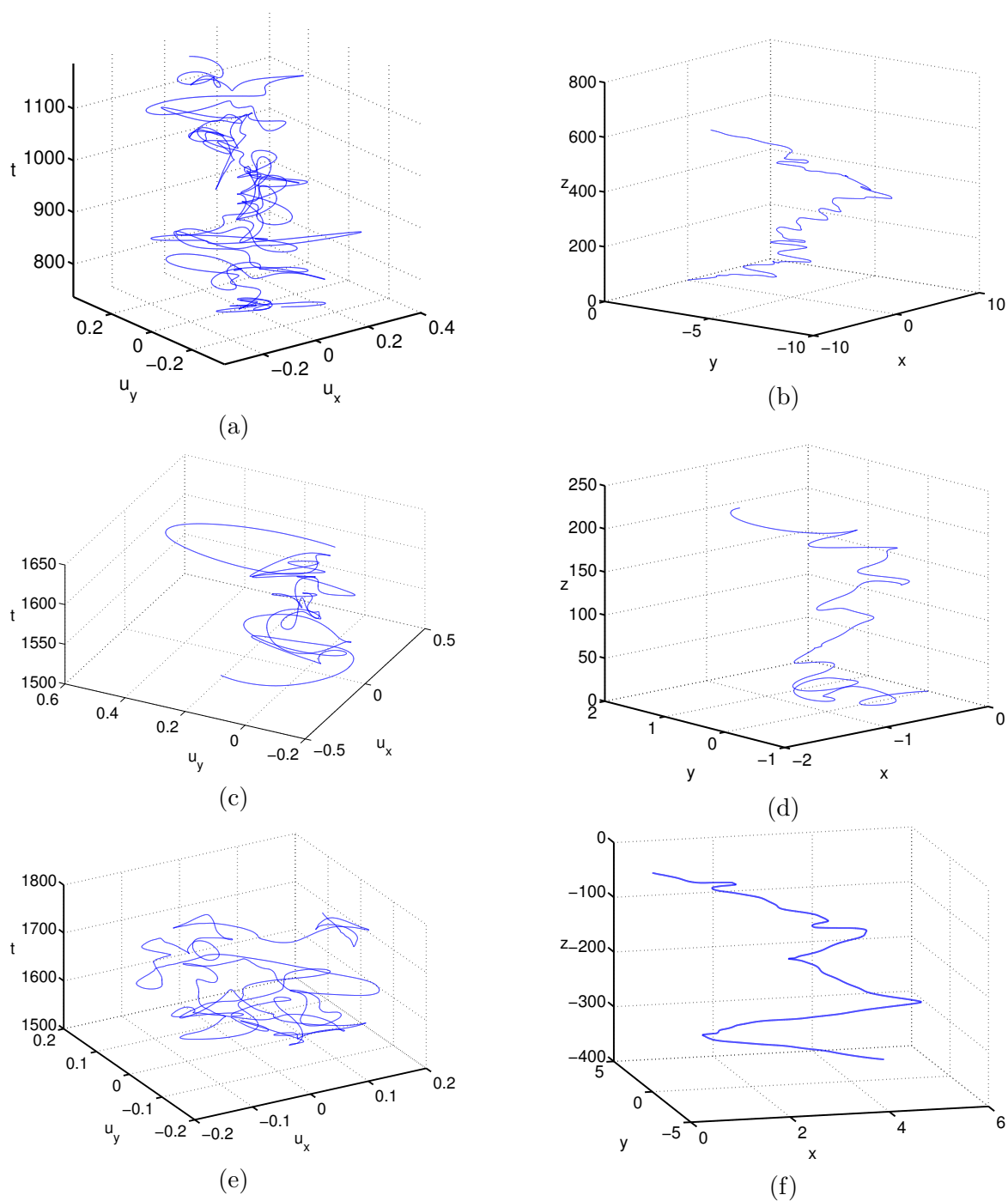


Figure 2.30: Three examples of chaotic trajectories. Left column (a,c,e): horizontal velocity vector as a function of time, right column (b,d,f): trajectories. (a,b) $\rho_s/\rho = 0.5, G = 230$, (c,d) $\rho_s/\rho = 0.5, G = 500$, (e,f) $\rho_s/\rho = 2, G = 400$.

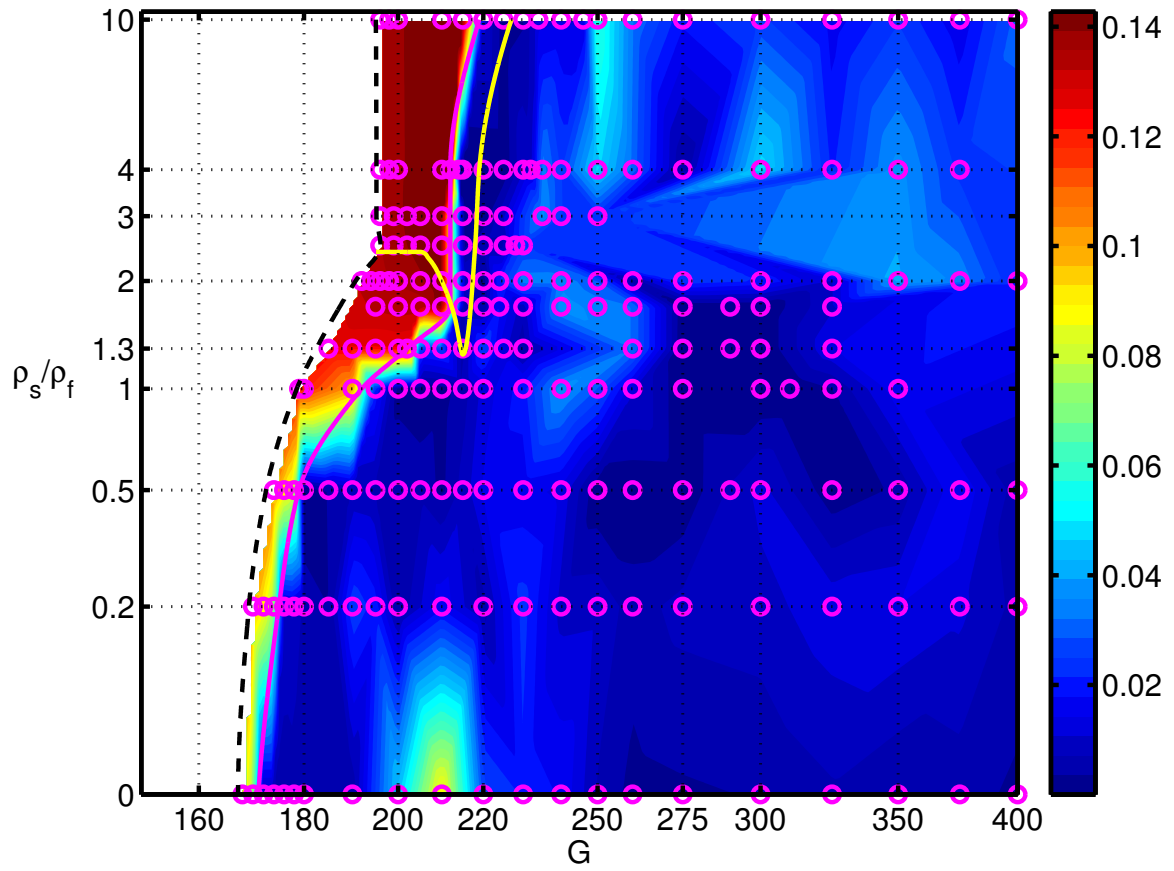


Figure 2.31: Statistical characteristics of mean value of horizontal velocity vector $\|\langle \mathbf{u}_h \rangle\|$. Markers represent the interpolated points.

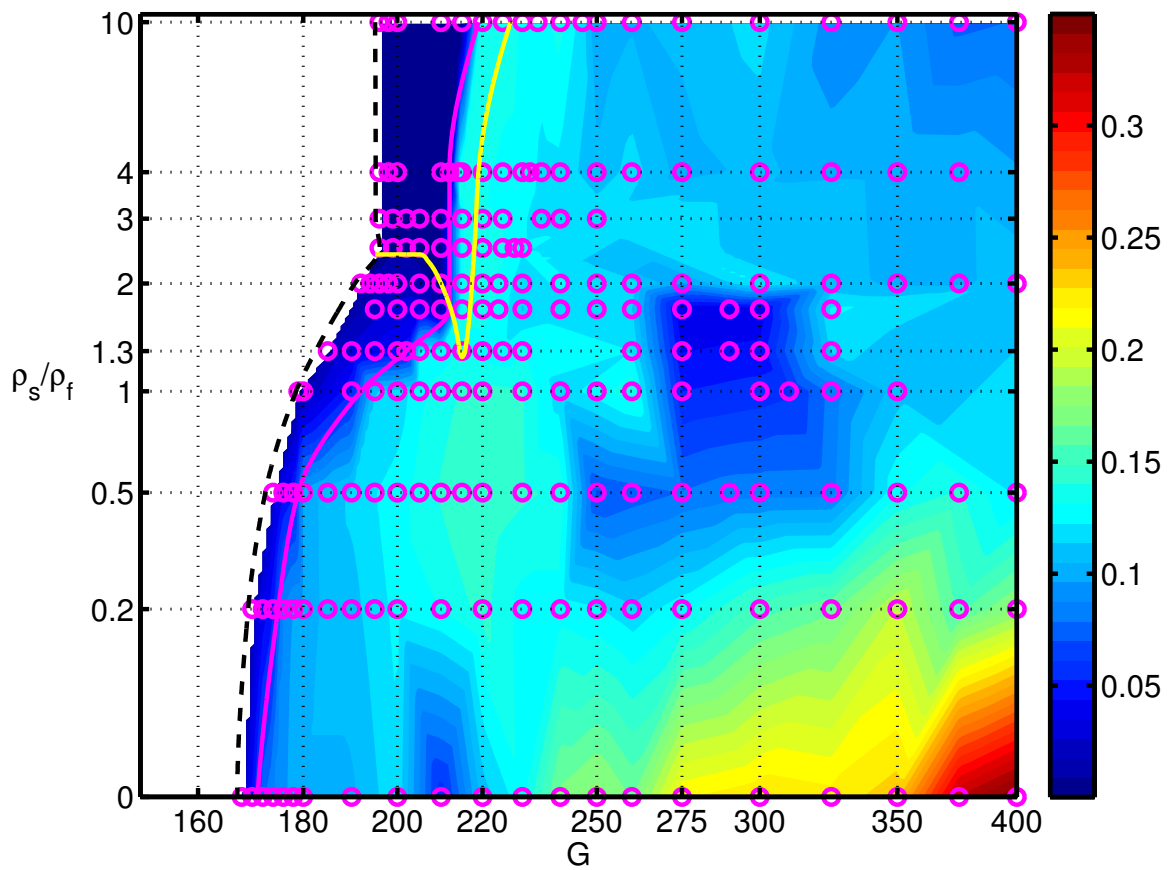


Figure 2.32: Statistical characteristics of unsteady regimes of the r.m.s. of horizontal velocity fluctuation $\langle (\mathbf{u}_h - \langle \mathbf{u}_h \rangle)^2 \rangle^{1/2}$. Markers represent the interpolated points.

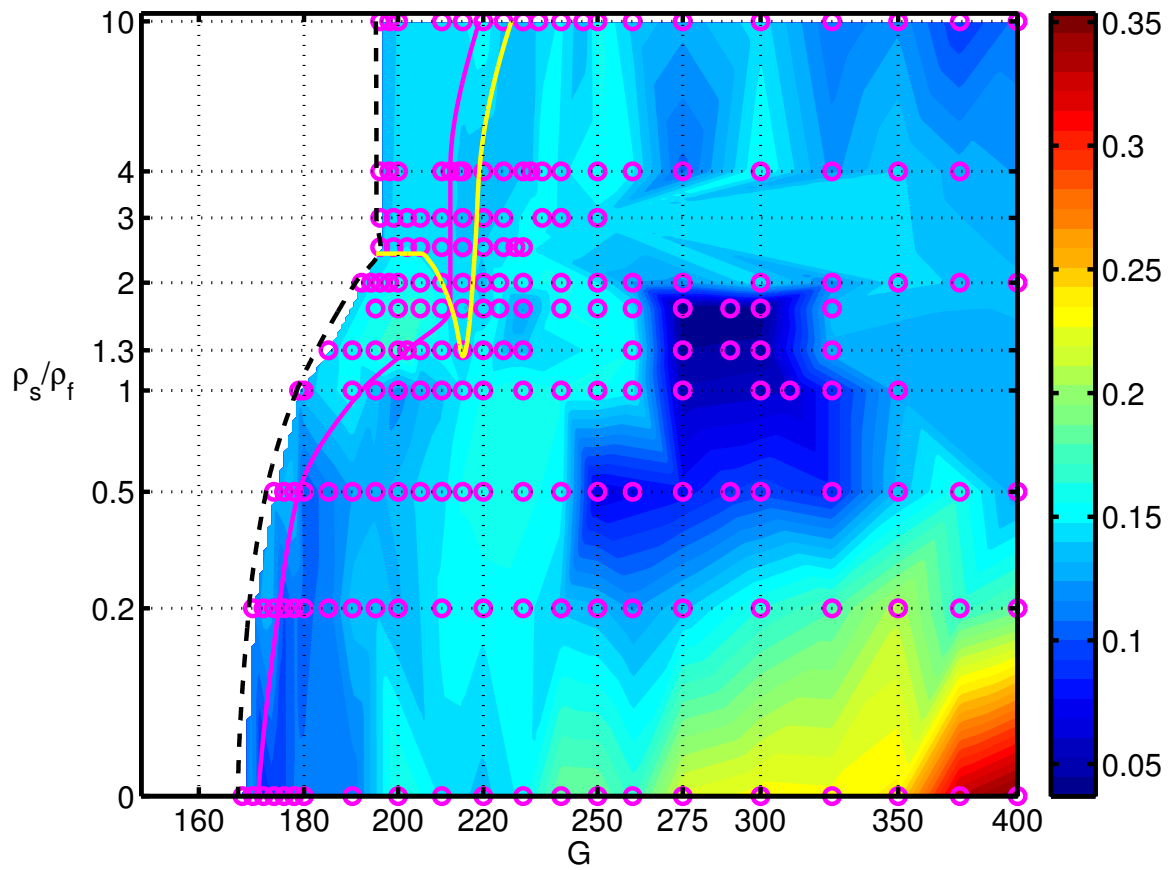


Figure 2.33: Sum of the mean value of horizontal velocity vector (Figure 2.31) and the r.m.s. of horizontal velocity fluctuation (Figure 2.32) $\|\langle \mathbf{u}_h \rangle\| + (\langle (\mathbf{u}_h - \langle \mathbf{u}_h \rangle)^2 \rangle)^{1/2}$.

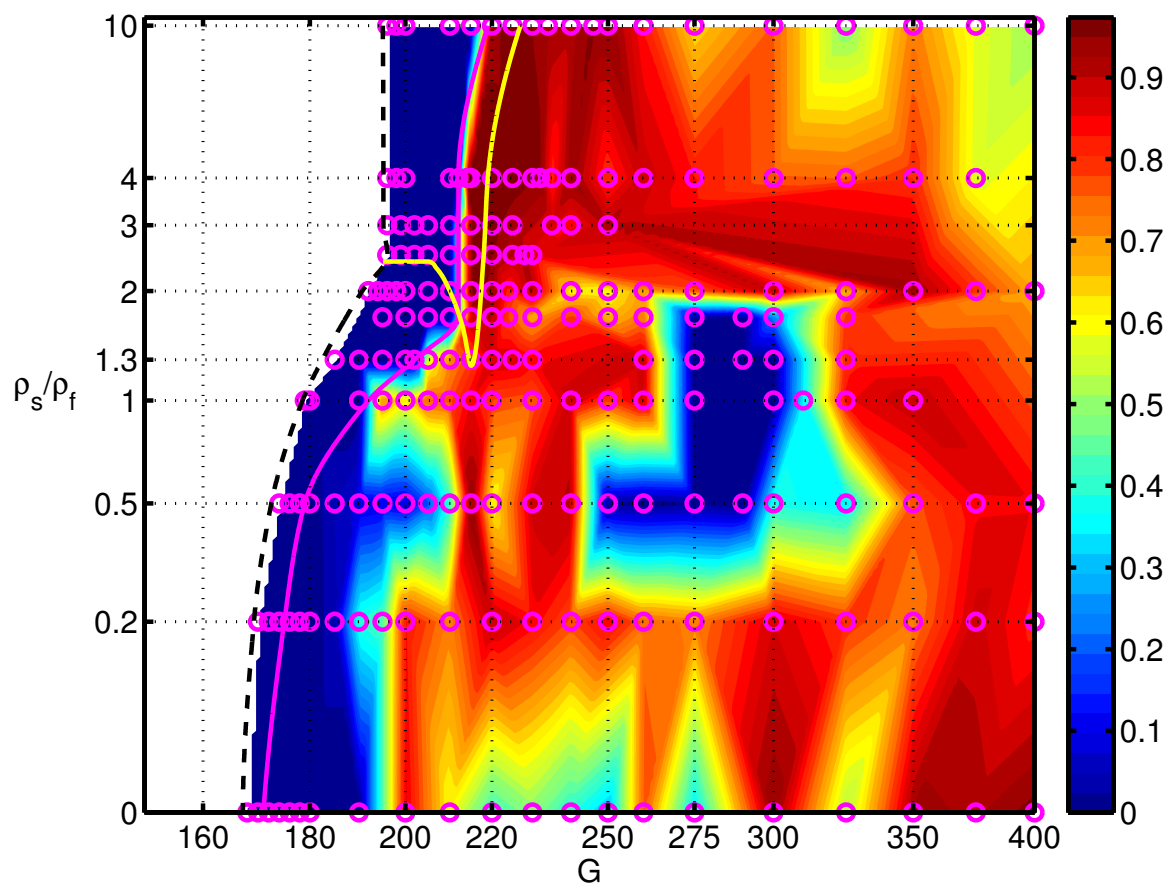


Figure 2.34: Planar isotropy of horizontal velocity fluctuations in the horizontal plane (square root of ratio smaller/larger eigenvalue of $\langle \mathbf{u}_h \mathbf{u}_h^T \rangle$).

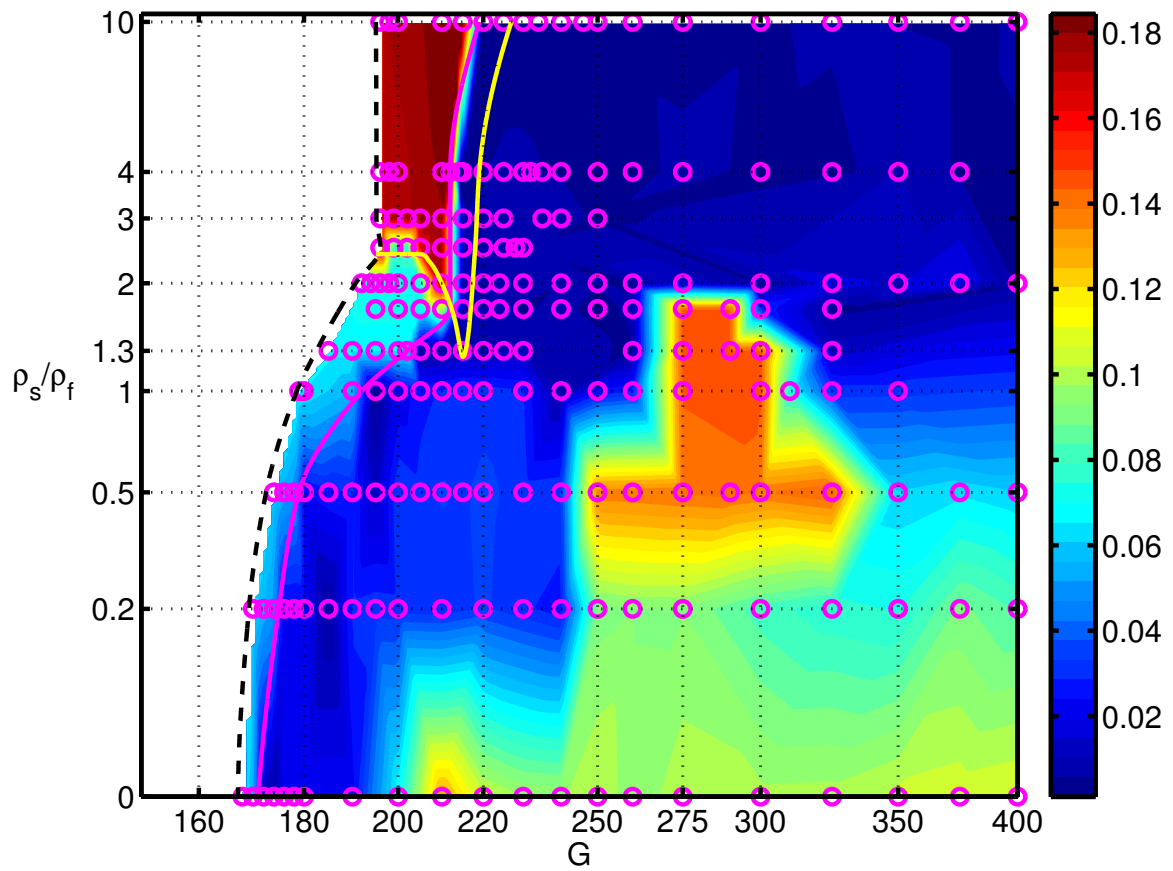


Figure 2.35: Frequency $1/(4T_{corr})$ (see Eqs. (2.11) and (2.12)).

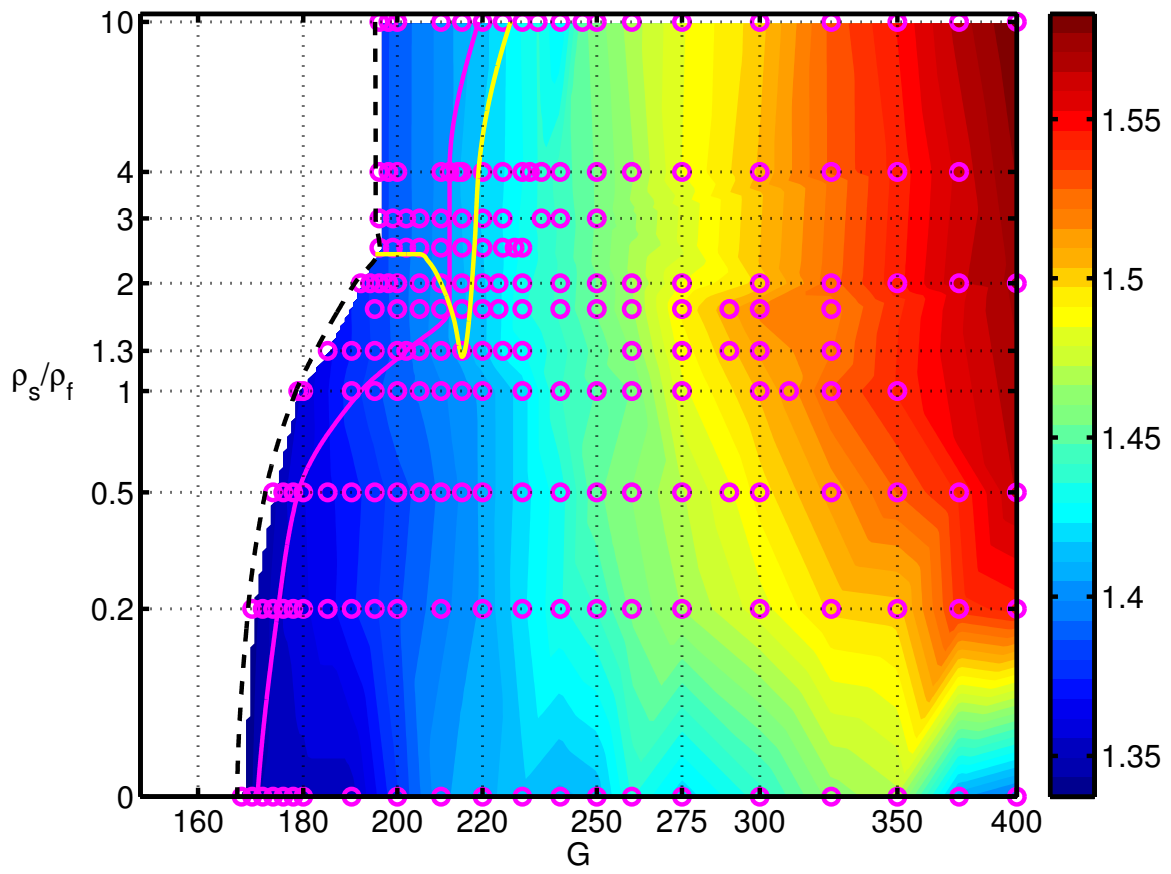


Figure 2.36: Mean value of vertical velocity $\|\langle \mathbf{u}_z \rangle\|$.

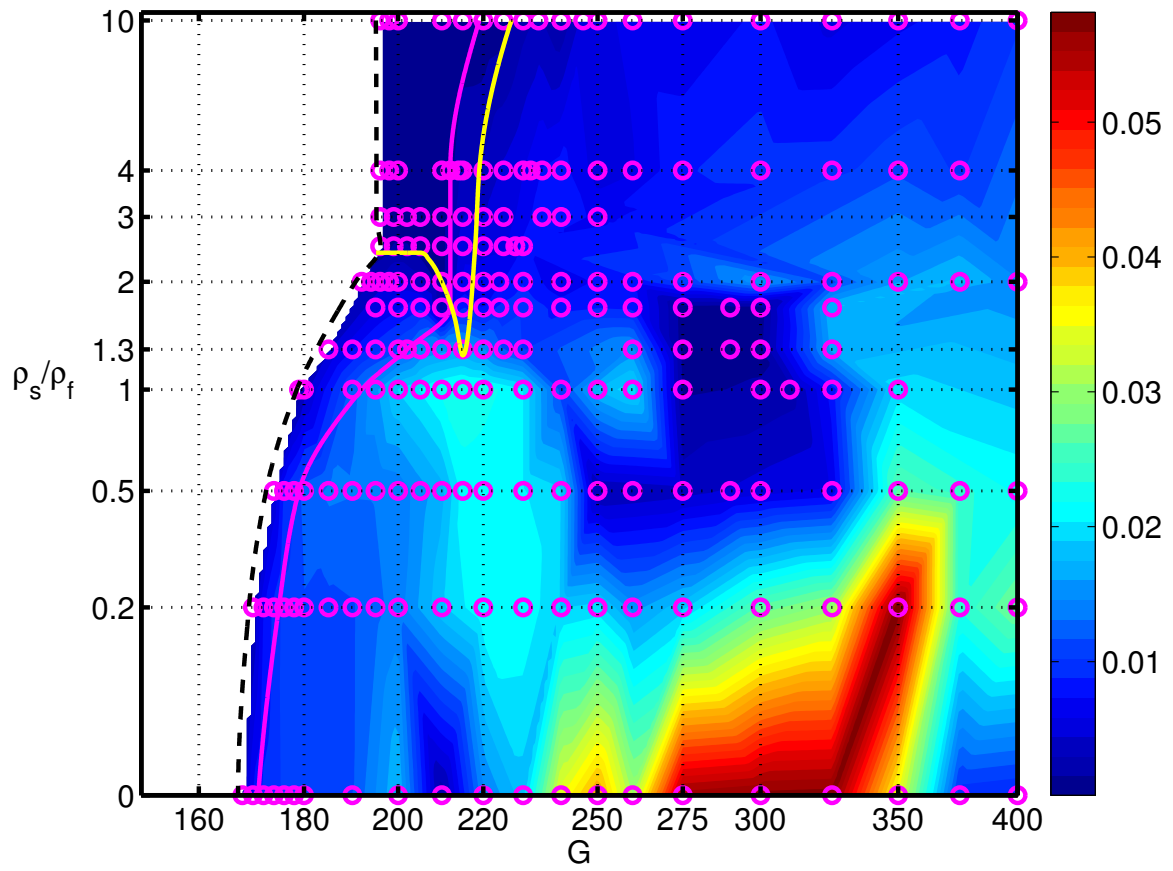


Figure 2.37: The r.m.s. of vertical velocity fluctuations $(\langle(\mathbf{u}_z - \langle\mathbf{u}_z\rangle)^2\rangle)^{1/2}$.

Chapter 3

Freely falling or ascending spheroids

3.1 Introduction

The motion of two prototypical bodies: a sphere and a disk have been studied in the literature both numerically and experimentally. In the present thesis, we devoted the previous chapter to provide additional information on the motion of a sphere. The PhD thesis by Chrust (2012) focused on disks and flat cylinders. A brief summary of the underlying bibliography was presented in section 1.7. Here, we recall some additional facts.

The study of Chrust (2012) had been largely motivated by existing, challenging and sometimes controversial, experimental results. The experimental paper of Field *et al.* (1997) (comprising the results of their own and earlier experiments: Willmarth *et al.* (1964), Stringham *et al.* (1969)) demonstrated a variety of motion regimes of falling disks and interpreted them from the viewpoint of the theory of deterministic chaos (Strogatz (1994)). They identified four distinct states depending on two dimensionless parameters: the non-dimensionalized moment of inertia $I^* = I/(\rho d^5)$ (I being the moment of inertia with respect to an axis lying in the plane of the disk) and the Reynolds number based on the mean vertical velocity u_m . For low Reynolds numbers the fall was found to be steady and vertical almost independently of I^* . At higher Reynolds number, a periodic regime consisting in a flutter of the disks and a zigzagging trajectory was observed for small values of moment of inertia I^* . For values of I^* exceeding 0.04 the disks were observed to tumble over edge, again in a perfectly periodic manner. This resulted in oblique trajectories. The fluttering state was characterized by the authors as periodic oscillations with inclination angle ϕ smaller than $\pi/2$. The tumbling motion was described as a side-wise drifting of a disk rotating in a given direction. The authors stressed the true periodicity of this regime. The regions of the parameter plane corresponding to purely tumbling and purely fluttering trajectories were found to be separated by a “chaotic” sub-domain. The chaos was identified as intermittence due to irregular switching between the flutter and the tumbling.

Flat, marginally buoyant (of density ratio 0.99) cylinders of aspect ratio $\chi = d/h$, where d is the cylinder diameter and h its height, were investigated more recently by Fernandes *et al.*

(2007)). While, in agreement with expectations, the vertical rise of cylinders of aspect ratio smaller or equal than 6 was found to lose its stability and give way to oscillations at smaller Reynolds numbers than predicted by numerical simulation of the wake of a fixed cylinder of the same aspect ratio, the experiments showed a very significant rise of the critical Reynolds number for aspect ratios 10, 15 and 20. Given the relatively small non-dimensionalized moment of inertia of flat cylinders, the observed non vertical regime was always fluttering.

The experiments of Field *et al.* (1997) stimulated a significant effort (Bönisch & Heuveline, 2007) to develop an appropriate simulation method capable to reproduce the observations with sufficient accuracy at acceptable costs to allow a parametric study. The challenge of reproducing the experiments was raised by two recent theses: that by Auguste (2010) and by Chrust (2012). Auguste (2010) showed the existence of small amplitude non-vertical regimes preceding the appearance of large planar oscillations of very flat cylinders. These trajectories, experimentally hard to be distinguished from vertical ones, were conjectured to explain the surprising observation of Fernandes *et al.* (2007). A recent paper by Chrust *et al.* (2014) confirmed this conjecture quantitatively.

The numerical method developed in the framework of the PhD thesis of Chrust (2012) proved to be especially well suited for parametric investigations. In the paper by Chrust *et al.* (2013) it was used to present a numerical counterpart of the experiments by Field *et al.* (1997) by investigating the transition scenario of thin disks of infinite nominal aspect ratio χ and of variable inertia. Instead of I^* , they characterize, equivalently, the disk inertia by the non-dimensionalized mass $m^* = m/(\rho d^3)$, where ρ is the fluid density, d the disk diameter and m its mass. The Reynolds number being based on an *a priori* unknown vertical velocity, they introduce the Galileo number defined as

$$G = \sqrt{|m^* - V^*|gd^3}/\nu \quad (3.1)$$

where $V^* = V/d^3$ is the non-dimensionalized volume (accounting for buoyancy) and ν the kinematic viscosity of the fluid. A good agreement with experiments was obtained and, moreover, many additional facts were revealed. Most notable were the strong subcritical effects leading to coexistence of stable states and a substantially different scenario for light ($m^* < 1$) and massive ($m^* > 1$) disks. In particular, for disks characterized by non-dimensionalized mass $m^* < 0.1$ they evidenced weakly oscillating periodic and chaotic states filling a gap between the loss of stability of the vertical fall and the onset of instability of a strong flutter in the same manner as for flat cylinders. At $m^* = 0$ the critical Galileo number of loss of stability of the vertical fall was found to be 78 and the strong flutter was evidenced starting only from $G = 130$. Moreover, again at $m^* = 0$, the chaotic weakly oscillating state was found to coexist with the strong periodic flutter in the wide interval $130 \leq G \leq 180$. The virtually experimentally unobservable, weakly oscillating states were shown to explain the shape of the critical curve of Willmarth *et al.* (1964) characterized by a strong upward shift of the observed onset of oscillations (flutter) of very light disks. The spiral trajectories of Zhong *et al.* (2011) were also evidenced. The different trajectories evidenced in the Physics of Fluids paper by Chrust *et al.* (2013) are reproduced in Figure 1.15. The names referring to the styles will also be used in the present chapter.

There is no obvious analogy between the scenario of spheres and disks. For this reason, Chrust (2012) states the interest of investigating intermediate particle shapes represented by

oblate spheroids of aspect ratios (defined as $\chi = d/a$) where d is the diameter and a the length of the axisymmetry axis of the spheroid) going from infinity to 1. A preliminary attempt to provide information on the scenario of spheroids of intermediate aspect ratios showed that the investigation of the three parameter space is a significant numerical challenge. In the present chapter this challenge is raised. We aim to establish an understandable link between the transition scenario of a thin disk and that of a sphere. The limit cases are represented by a spheroid of infinite aspect ratio, which is not exactly equivalent to the homogeneous disk of Chrust *et al.* (2013). Due to a non uniform mass distribution, its non-dimensional moment of inertia is $m^*/20$ instead of $m^*/16$. This does not radically change the scenario but the quantitative differences require a specific investigation of this case. At the opposite limit of the aspect ratio interval, we face the qualitative difference between a perfect sphere which can “roll” and a slightly oblate body. For this reason we consider the aspect ratio $\chi = 1.1$ as the limit case. Between these two extreme values we consider aspect ratios 10,6,5,4,3 and 2. In each considered plane of $\chi = const.$, the scenario presents significant particularities. The whole study is illustrated by eight state diagrams which demonstrate the transition scenario in the three-parameter space.

3.2 Mathematical formulation and numerical method

In order to obtain a body fitted mesh close to the moving body and cylindrical mesh translated along with the wake, the computational domain is decomposed into a relatively small spherical sub-domain rotating with the body, connected to the remaining cylindrical sub-domain by a spherical function expansion at the common interface (see Figure 3.1). We adapt the fully implicit fluid-solid coupling described earlier (Jenny & Dušek (2004)) to the configuration of spheroids. The resulting numerical code remains both accurate and efficient in the same way as the version used for the simulation of a freely moving sphere.

We assume the fluid to be incompressible and Newtonian with constant kinematic viscosity ν . The motion of a homogeneous rigid spheroid, of diameter d and the length of the polar axis a , is driven by gravity and buoyancy. A very thin spheroid of finite mass m can be considered to be made of an infinitely dense material and to have a zero volume. From this viewpoint the buoyancy effects would be negligible as it is the case for experiments in the air. In water, however, the solid/fluid density ratio (ρ_s/ρ) remains small and buoyancy combined with gravity results in an effective gravitational acceleration $\mathbf{g}_{eff} = (1 - \rho/\rho_s) \mathbf{g}$, where \mathbf{g} is the gravitational acceleration. The definition of \mathbf{g}_{eff} covers both falling and ascending spheroids. Note that the present definition differs by the factor ρ/ρ_s from that used for the simulation of freely moving spheres focusing mostly on the case of light spheres, i.e., $\rho_s/\rho < 1$. Flat ascending spheroids have small inertia and, from the viewpoint of parametric investigation, are equivalent to “infinitely light spheroids”. The mathematical limit of spheroids of infinite aspect ratio $a \ll d$ requires, strictly speaking, $\rho_s/\rho \rightarrow \infty$. In experimental configurations this limit is often hard to achieve (e.g., in water) but, virtually in all cases of falling spheroids, the density ratio $\rho/\rho_s < 1$ has been used. The ratio ρ/ρ_s thus represents a more or less significant correction of the gravity. The fluid is assumed to adhere perfectly to the solid body surface. The fluid medium is considered infinite and quiescent

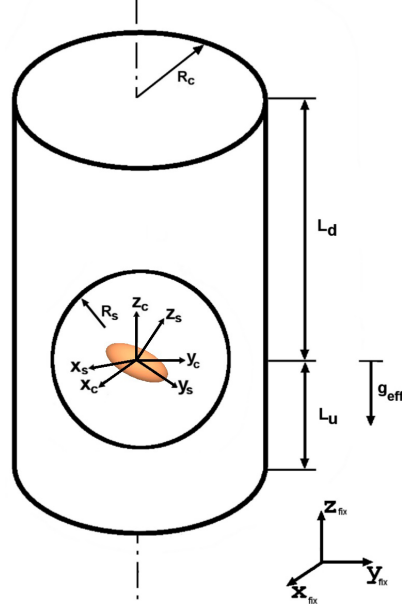


Figure 3.1: Geometry of the problem. g_{eff} : vertical vector of effective gravity oriented downward or upward for falling or ascending bodies, $(x_{fix}, y_{fix}, z_{fix})$: fixed reference frame, (x_c, y_c, z_c) : vertically translated frame, and (x_s, y_s, z_s) : frame of the spherical sub-domain rotating with the body. Numerical parameters: radius of the spherical sub-domain $R_s = d$, $R_c = 8d$, $L_u = 12d$, $L_d = 25d$.

far from the moving body.

The velocity vector is considered with respect to a fixed reference frame. The axes of the cylindrical sub-domain remain parallel to this fixed frame while those of the spherical sub-domain rotate, in which the velocity field is described by its projection onto the local rotating frame. The outer boundary conditions are a Dirichlet (zero velocity) condition at the inflow boundary (bottom basis in Figure 3.1) and zero Neumann boundary conditions simulating no-stress conditions at the outflow (on top basis) and on the cylindrical surface.

The non-dimensionalization is based on the scale of the force resulting from the weight and buoyancy $(m - \rho V) \mathbf{g}$, where m is the mass and V the volume of the body. This force defines the velocity scale

$$U_{ref} = \sqrt{|m^* - V^*|gd} \quad (3.2)$$

where m^* and V^* stand for the non-dimensionalized mass and volume of the body

$$m^* = \frac{m}{\rho d^3}, \quad V^* = \frac{V}{d^3}. \quad (3.3)$$

In that case, the fluid equations write

$$\frac{\partial \mathbf{v}}{\partial t} + [(\mathbf{v} - \mathbf{u} - \boldsymbol{\omega} \times \mathbf{r}) \cdot \nabla] \mathbf{v} + \boldsymbol{\omega} \times \mathbf{v} = -\nabla p + \frac{1}{G} \nabla^2 \mathbf{v} \quad (3.4)$$

and

$$\nabla \cdot \mathbf{v} = 0 \quad (3.5)$$

where \mathbf{u} is the translation velocity of the body center, $\boldsymbol{\omega}$ is the angular velocity of the rotating spherical sub-domain. The Galileo number G appearing in Eq. 3.4 is given by

$$G = \frac{U_{ref}d}{\nu} = \frac{\sqrt{|m^* - V^*| \mathbf{g}d^3}}{\nu} = \frac{\sqrt{m^* \mathbf{g}_{eff}d^3}}{\nu} \quad (3.6)$$

The solid body equations then write the non-dimensionalized movement equations:

$$m^* \left(\frac{d\mathbf{u}}{dt} + \boldsymbol{\omega} \times \mathbf{u} \right) = \mathbf{F}_{fl}(\mathbf{v}, p) + \mathbf{k}_{fix} \quad (3.7)$$

$$\alpha I^* \frac{d\Omega_3}{dt} = M_{fl_z} \quad (3.8)$$

$$I^* \left(\frac{d\Omega_+}{dt} - i\alpha\Omega_+\Omega_3 \right) = M_{fl_+} \quad (3.9)$$

where \mathbf{k}_{fix} is the vertical unit vector pointing upward or downward for falling or ascending bodies, respectively. Eqs. 3.8 and 3.9 are written for complex ($U(1)$, see e.g. Jenny & Dušek (2004)) coordinates of angular velocity $\Omega_+ = \Omega_x + i\Omega_y$ and torque $M_{fl_+} = M_{fl_x} + iM_{fl_y}$. The angular velocity vector of the spherical sub-domain has the components $\boldsymbol{\omega} = (\Omega_x, \Omega_y, 0)$. Due to the axisymmetry of spheroid, the body fitted mesh is not required to follow the rotation about its axis. The non-dimensionalized moment of inertia is defined as

$$I^* = m^* \left(\frac{1}{\chi^2} + 1 \right) / 20. \quad (3.10)$$

where the aspect ratio $\chi = d/a$ defined earlier. The full system of Navier-Stokes equations 3.4 and 3.5 and of motion equations 3.7 through 3.9 depends on three dimensionless parameters: the Galileo number G , dimensionless mass m^* and aspect ratio χ .

As described in Chapter 4 of Chrust (2012), the meshes tested and used for spheroids were adapted for the implementation of the spherical interface. The radius of the interface was close to be $1d$ for all simulations, they were run with the azimuthal Fourier decomposition and the spherical function expansion truncated at $M = 15$ and $\ell_{max} = 15$, respectively. The detailed explanation of the numerical method is provided in Chapter 3 of Chrust (2012).

3.3 Results

The transition scenario of freely falling or ascending spheroids can be characterized by a set of bifurcating asymptotic states. They correspond to stable asymptotic regimes reached in an infinite time horizon by the solid-fluid system for a fixed set of state parameters. In practical situations “infinite” means extremely diverse time scales given by the stability of the state. The latter decreases dramatically close to bifurcations and at the onset of chaos, not all bifurcating states are really observable in laboratory experiments. Given the objective to detect asymptotic states, the initial conditions of the simulations are chosen using already

symbol	description
+	Steady vertical
	States of the scenario of a perfect sphere (see Ch. 2)
▷	Steady oblique
▷	Low frequency oblique oscillating
▷	High frequency oblique oscillating
○	Perfect or slightly oblique zigzag
●	Zigzag 3D
	States of the scenario of a disk (Chrust <i>et al.</i> , 2013))
○	Flutter Planar “zigzagging” motion accompanied by fast oscillations with significant inclination angles (ϕ) typically larger than 30° .
●	Helical Purely helical or bi-periodic states resulting from a slow rotation of the symmetry plane (typical for large Galileo numbers at small dimensionless masses.)
□	Intermittent See section 1.7.
▽	Tumbling See section 1.7.
▽	Spiral tumbling See Figure 1.15.
•	Vertical periodic of small amplitude (Replace the magenta asterisks of Figure 1.16.) Fluid modes with very small amplitudes of the solid body oscillations.
◇	Chaotic Denotes all 3D trajectories with more complicated than bi-periodic dynamics.
	States of spheroids of intermediate aspect ratio
▷	Switching of oblique oscillating and vertical periodic in perpendicular directions (see sections 3.3.6 and 3.3.7)
○	Vertical periodic of intermediate amplitude Periodic fluid modes separated from the flutter by a jump of amplitude and frequency for high aspect ratio. At intermediate aspect ratio, the transition between both is progressive and an arbitrary criterion based on the amplitude of inclination angle (ϕ) is used.
*	Planar, quasi-periodic All planar aperiodic states, vertical in the average or oblique.
▷	Oblique periodic Planar, periodic, only slightly drifting in the horizontal direction in contrast with oblique oscillating states for which the mean horizontal velocity dominates.

Table 3.1: Description of symbols presented in the state diagrams of various aspect ratios.

known results. This allows us not only to save CPU time but is the only practical way how to track branches of coexisting solutions in the many cases of subcritical bifurcation that occur in our study.

This section is organized in eight subsections corresponding to each aspect ratio studied varying from infinity to 1.1 to establish a link between transition scenario of a freely falling or ascending thin disk and that of a sphere. For each subsection, we provide a state diagram in the two-parameter $G - m^*$ plane. The used symbols are listed in Table 3.1. Their choice respects the symbols used in chapter 2 and in the Physics of Fluids paper by Chrust *et al.* (2013). Figures illustrating the trajectory styles of Table 3.1 will be presented in the following sections.

3.3.1 $\chi = \infty$

As can be expected, the transition scenario of a spheroid of aspect ratio $\chi = \infty$ resembles strongly to that of an infinitely thin disk. As already stated, this is due to the slightly smaller moment of inertia $I^* = m^*/20$ instead of $m^*/16$. For $m^* = 0$ this makes no difference and the lowest line of states in Figure 3.2 is directly reproduced from Figure 1.16. Progressively, as the non-dimensionalized mass (i.e. the inertial effects) increases, the difference between the disk and infinitely flat spheroid becomes more apparent but, qualitatively, the state diagram (Figure 3.2) contains the same four distinctive dominant regimes: vertical, fluttering (zigzagging), intermittent and tumbling, plus three oscillating states of small amplitude: vertical quasi-periodic, vertical periodic and chaotic. We shall call the latter fluid modes in agreement with the discussion of Chapter 2.

The symbols and colors used in Figure 3.2 correspond to those of Chrust *et al.* (2013) except for the stars denoting vertical trajectories periodically oscillating with very small amplitudes (quasi-vertical periodic trajectories) in the paper by Chrust *et al.* (2013), which have been replaced by magenta dots. The state diagram is dominated by the region of flutter, i.e. of states with planar oscillating trajectories distinctive by significant oscillations of the body axis. The minimal amplitude of these oscillations measured by the sine of the inclination angle is 0.22 at $m^* = 5$ and $G = 37$ so that there is no ambiguity with periodic “fluid modes” having amplitudes of at most 0.05. A typical example is the case $m^* = 0.025$, $G = 100$ where both states co-exist. The flutter has an amplitude of the sine of inclination angle of 0.46 whereas the fluid mode oscillates with an amplitude of only 0.054. As mentioned by Chrust *et al.* (2013), the fluid modes become chaotic at higher Galileo numbers. The amplitude of oscillations of the body axis remains, however, small. E.g. at $m^* = 0$, $G = 150$, the r.m.s. is 0.039. The tumbling and the intermittent states do not require any additional comment to what was stated by Chrust *et al.* (2013). The overlapping of the flutter and tumbling extends farther towards higher Galileo numbers for $m^* = 5$, which is obviously due to the lower moment of inertia allowing the flutter to keep a stability before switching to tumbling.

The primary bifurcation (the threshold is represented by the solid black line) was found always of Hopf type and subcritical for $m^* \geq 0.05$ in the same way as for disks. The subcritical nature of the bifurcation explains the bi-stability band of the flutter and of vertical states. The band seems to disappear for $m^* > 1$ but it can be assumed that the bifurcation

is still subcritical because we were unable to find saturated states with small amplitude at $m^* = 2$ and 5. E.g., at $m^* = 2$, the threshold of the bifurcation lies at $G_{crit} = 35.3$ and at $G = 36$ the saturated state is already a flutter with amplitude of the sine of inclination angle of 0.25. In contrast, the bifurcation is supercritical when it gives rise to fluid modes at very small m^* . Interestingly enough, the small amplitude of motion of the body is practically equivalent to a steady state and results in an inertia independent critical Galileo number.

The most salient specificity of the infinitely flat spheroid is the coexistence of vertical, relatively weakly oscillating trajectories with the tumbling regime. In spite of the obvious differences as compared to fluid modes at very small non-dimensionalized masses that can be seen in Figure 3.3 consisting in a larger amplitude of oscillation of the body axis and the fact that we did not evidence any periodic trajectory for these new states, we consider they can be qualified as fluid modes as well. To mark the difference, we denote the planar quasi-periodic states by an asterisk. More detailed quantitative information is presented in Table 3.2. Similarly as for very light bodies, the trajectories become three-dimensional and chaotic at higher Galileo numbers. To check that this co-existence was not missed when studying the disks, we tested whether these fluid modes resist if I^* is set equal to that of a homogenous disk. A result of such a test can be seen in Figure 3.4. The initially quasi-periodic oscillations give clearly the way to tumbling (angular velocity keeping the same sign).

The mentioned differences between the behavior of an infinitely flat spheroid and of a disk are, nevertheless, relatively minor. The scenario of infinitely flat spheroid can thus be considered as a good starting for the investigation of the effect of the shape variation between a disk and a sphere.

A remarkable feature common to disks and spheroids of high to moderate aspect ratio is the independence of the scenario on the Galileo number starting from a relatively moderate value of about 100. This relative independence on G was already noticed by Field *et al.* (1997), it is clearly demonstrated in Figure 1.16 reproduced from Chrust *et al.* (2013). In the same way, the lines separating different regimes tend to be horizontal in Figure 3.2 in the right of the diagram.

(m^*, G)	\bar{u}_z	A_{u_z}	A_{u_h}	St	$\phi_{max}(^\circ)$
(0, 100)	-1.446	0.004	0.050	0.102	1.598
(2, 100)	-1.376	0.020	0.123	0.119*	26.25
(5, 100)	-1.437	0.008	0.010	0.119*	3.963

Table 3.2: Quantitative data for vertical periodic and quasi-periodic states. Meaning of symbols: \bar{u}_z – mean vertical velocity; A_{u_z} , A_{u_h} – amplitude of oscillations of the vertical and horizontal velocity; St – the Strouhal number; ϕ_{max} – the maximum inclination angle with respect to the vertical direction. The values marked by * are dominant frequencies of quasi-periodic states.

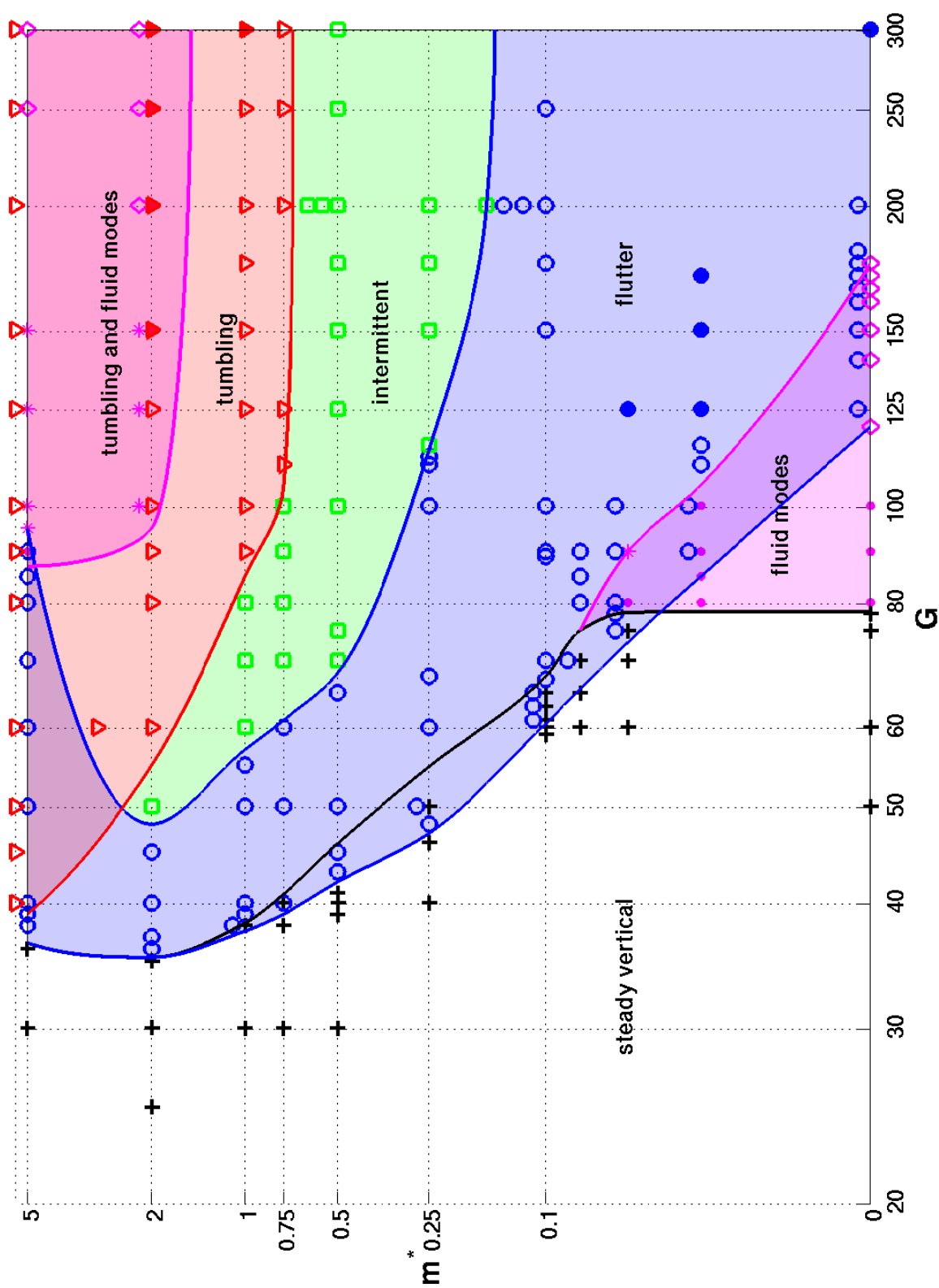


Figure 3.2: The state diagram for $\chi = \infty$ in the $G - m^*$ plane. The symbols denote the regimes investigated by simulations. The full lines delimit the stability domains of regimes of the corresponding color.

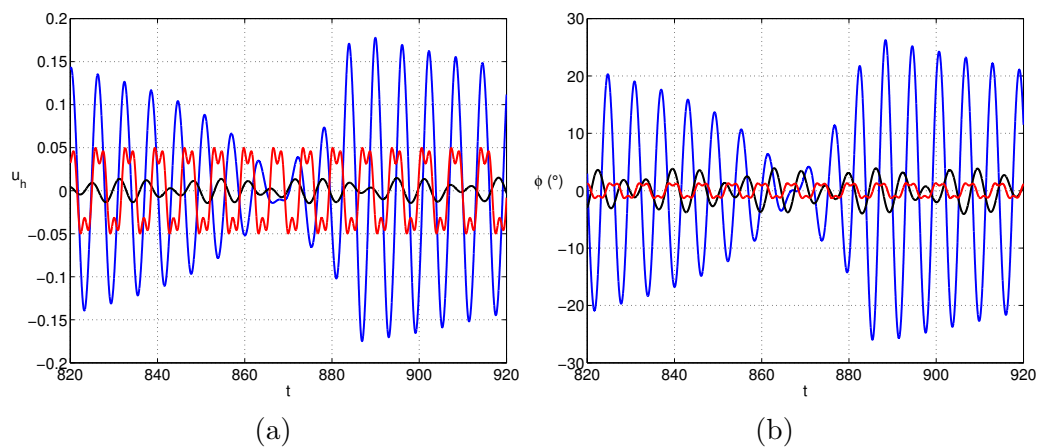


Figure 3.3: The comparisons of the horizontal velocity (figure (a)) and inclination angle (b) for the vertical quasi-periodic and vertical periodic states. Red: $m^* = 0, G = 100$, blue: $m^* = 2, G = 100$, black: $m^* = 5, G = 100$.

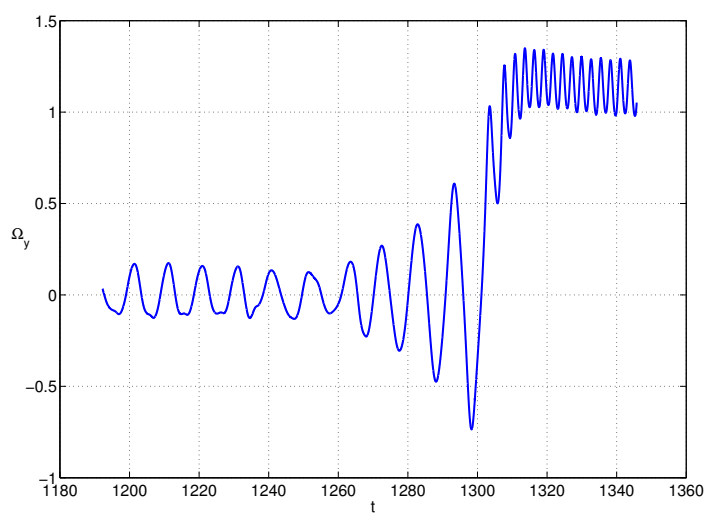


Figure 3.4: Angular velocity of the rotation of homogeneous disk at $m^* = 5, G = 150$. Simulation restarted from the fluid mode of an infinitely flat spheroid at the same point of the parameter plane.

3.3.2 $\chi = 10$

The effect of body shape on the characteristics of a freely moving spheroid is already significant for as flat a spheroid as that of aspect ratio 10 as can be seen in Figure 3.6. In the lower part of the figure ($m^* < 0.3$) we observe an upward shift of the primary bifurcation threshold to $G_{crit} = 91.0$. More importantly, the primary bifurcation is regular, i.e. the real eigenvalue has become more unstable than the complex eigenpair. This explains why exactly the same critical Galileo number was found for $m^* = 0, 0.1$ and 0.25 . The secondary Hopf bifurcation follows at a critical Galileo slightly above 92. We evidenced also two oblique oscillating states at $m^* = 0.1, 0.25$ and at $G = 96, 98$) for both m^* values. Figure 3.5 sheds some light on the sequence of instabilities. It represents the evolution of inclination of the body axis as a function of time starting from a vertical state. The faster growth of the primary instability (exponential growth) and the slower growth of oscillations can be easily seen in the initial stage of the simulation. The primary instability saturates at $\sin(\psi) \approx 0.066$ (less than 4°). Subsequently only the amplitude of oscillations (of the secondary instability) goes on growing. During this stage, the mean value decreases. It may be expected to ultimately disappear to yield a vertical periodic state. In the case of Figure 3.5), the steady mean value is, however, only partially absorbed by non-linear effects and an oblique oscillating asymptotic state is reached. By restarting using as initial state at $G = 100$ we verified that at this Galileo number ($G = 96$) the vertical periodic state is not stable. However, at $G = 98$ we found a co-existence of both, a vertical and an oblique oscillating state. The same holds for $m^* = 0.25$. For this higher non-dimensionalized mass, the steady oblique state (at $G = 94$) and oblique oscillating states (at $G = 96, 98, 100$ and 105) were found to co-exist with the vertical periodic one (at $G = 98, 100$ and 105 they are quasi-periodic). This means that there is no progressive evolution from the steady oblique to vertical periodic regime via an oblique oscillating state, the mean value of which would tend to vanish progressively. Instead a subcritical bifurcation is at the origin of the vertical periodic state.

It may be objected that such a detailed investigation might lack physical relevance. However, the steady oblique primary bifurcation states, together with oblique oscillating one, represent something like an embryonic sphere-like scenario. This brings the explanation of the inertia independent primary bifurcation threshold and shows that even for a very flat spheroid there is a link, albeit very weak, with the dynamics of a perfect sphere. It is to be noted that the frequency of asymptotic oscillations in Figure 3.5 is 0.17. Given the different non-dimensionalization accounting for the body shape, it is preferable to convert this value to Strouhal number based on the average vertical velocity which is 1.53 in this case. This results in a Strouhal number of 0.11, corresponding rather to that of fluid modes ($St = 0.13$) than solid-fluid modes ($St = 0.05$) of the sphere. This justifies not only the choice of the yellow symbols but, more generally, the label “fluid modes” for the entire lower magenta sub-domain of the diagram.

A next striking feature of the diagram is the extent of the sub-domain of the flutter. This is due essentially to the very significant shift of the primary bifurcation threshold to higher Galileo numbers. The lowest threshold, $G_{crit} = 78.0$, was found at $m^* = 1.5$, whereas for infinitely flat spheroid the lowest critical Galileo number was $G_{crit} = 35.3$ (at $m^* = 2$). In contrast the domain of existence of the flutter did not shrink so much which results in

the large bi-stability domain. The extent of the bi-stability domain of the flutter and of the steady vertical states is impressive. The stability domain of the flutter overlaps also with the intermittent and tumbling subdomains, which results into three co-existing states for some problem parameters. Also the tumbling (and partly intermittent) domain extends far downward (for G) and overlaps with the domain of vertical states. It can be conjectured that the better aerodynamic shape than that of an infinitely thin spheroid might explain why the two unsteady regimes are sustained when the Galileo number is reduced (i.e, the viscous effects increase).

Three different symbols for seemingly qualitatively the same regimes, in which the center of the spheroid describes an oscillating, in the average vertical, trajectory, appear in the state diagram 3.6. An example of “vertical periodic” state is given in Figure 3.7. Its specificity consists in very small angles of inclination of the body axis (less than 6° in the figure). Similarly as for the infinitely flat spheroid, the flutter can be unambiguously distinguished from vertical periodic fluid modes by the much larger amplitude of the inclination of the body axis (see Figures 3.8 and 3.9). The maximal sine of inclination in Fig. 3.9 is 0.19 to be compared with a flutter for the same m^* at $G = 65$ having an amplitude of 0.77 which is also close to that of Fig. 3.8. In contrast, the periods of both the flutter and of the fluid mode are not very different for the same inertia (see Table 3.3). The comparison of Figures 3.7 and 3.9 explains why we use the same denomination for weakly oscillating states in the lower part of the diagram and in the co-existence domain for high m^* . The primary bifurcation becomes manifestly subcritical for $m^* \geq 0.5$. In the domain of flutter we evidenced, in some cases, a destabilization of the planar trajectories for higher Galileo numbers. The states where this destabilization was positively evidenced are represented as helical and marked by filled blue circles in the diagram 3.6. The observed trajectories are, however not mono-periodic and purely helical like in the paper by Chrust *et al.* (2013), but their projection onto the horizontal plane is rather represented by a turning flat ellipse. As the result, such dynamics is, strictly speaking, quasi-periodic. An example is represented in Figure 3.12. The kino-gram of the motion shows that the trajectory remains actually very close to that of a flutter.

At the interface between the domain of flutter and of tumbling (Figure 3.10) states typical for their mostly irregular switching between a zigzagging (fluttering) stage and tumbling were evidenced in the same way as by Field *et al.* (1997) and Chrust *et al.* (2013) and in Section 3.3.1 (see Figure 3.11 a)). Chrust *et al.* (2013) already noted that in numerical simulations the intermittency becomes periodic with a given number of tumbings alternating in each direction. An example is given in Figure 3.11 b) where the body tumbles five times over edge before changing the rotation direction.

(m^*, G)	\bar{u}_z	A_{u_z}	\bar{u}_h	A_{u_h}	$\phi_{max}(^\circ)$	period
(0.25, 100)	-1.54	0.005	0	0.078	6.1	4.07
(0.25, 115)	-1.38	0.37	0	0.770	49	3.11
(0.75, 200)	-1.33	0.45	0.97	0.32	90	2.18
(2, 65)*	-1.41	0.09	0	0.24	50	5.76
(2, 100)**	-1.420	0.005	0	0.061	11.1	5.30

Table 3.3: Quantitative data characterizing selected periodic states for aspect ratio $\chi = 10$. Same meaning of symbols as in Table 3.2. *: flutter, **: fluid mode.

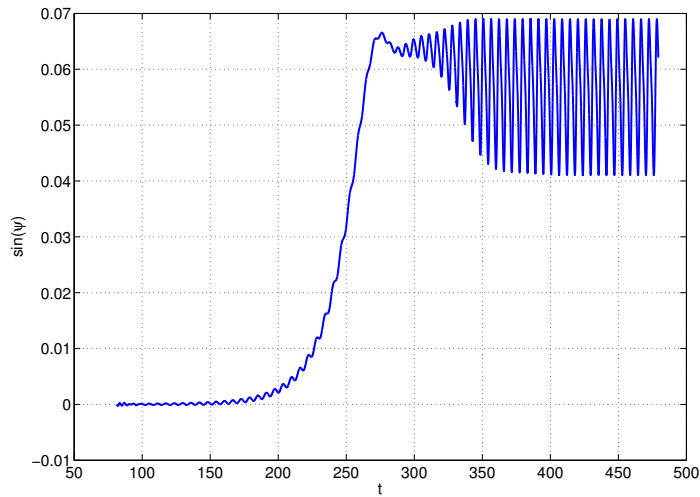


Figure 3.5: Evolution to the oblique oscillating regime for $\chi = 10$, $m^* = 0.1$ and $G = 96$.

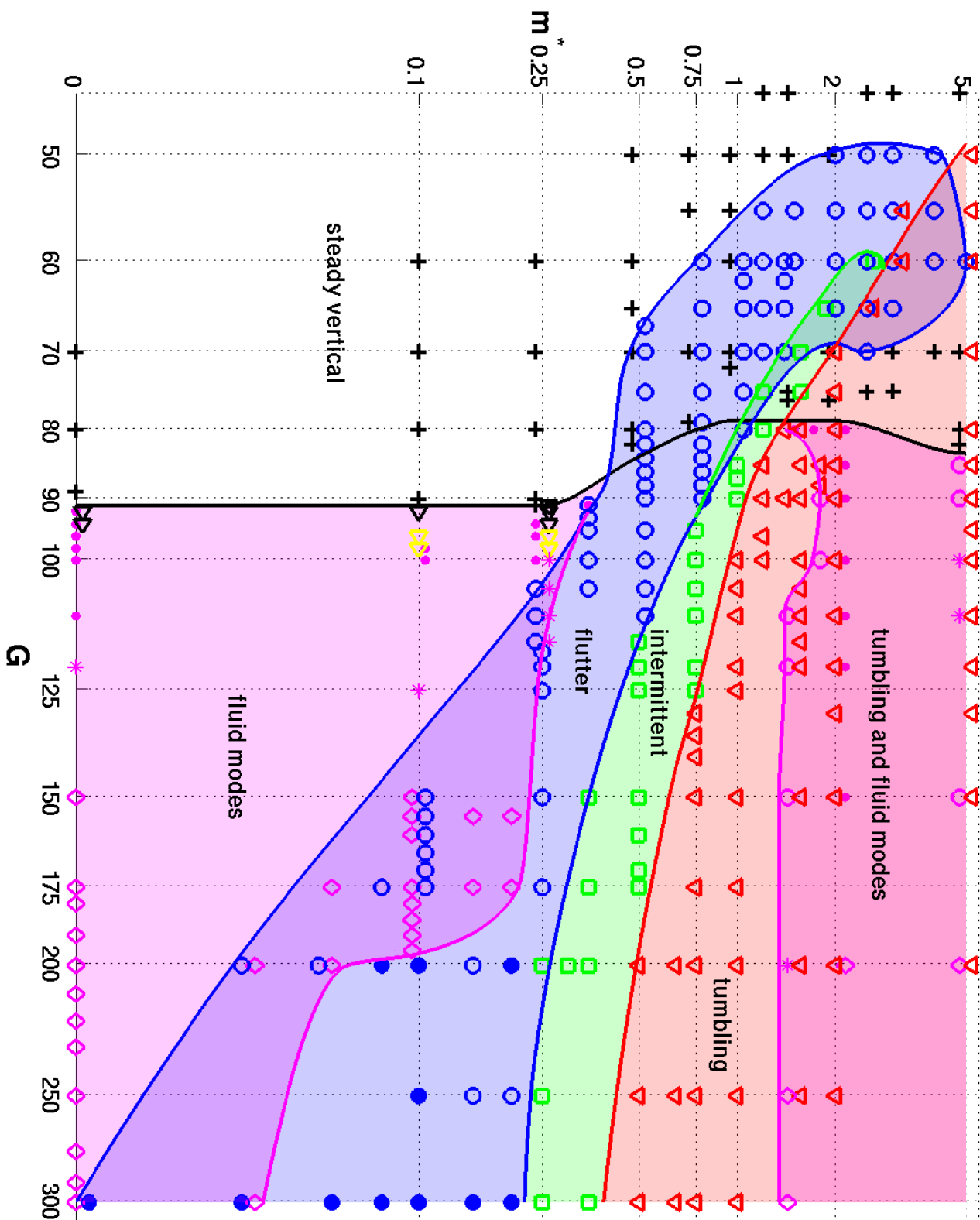


Figure 3.6: The state diagram for spheroids of $\chi = 10$.

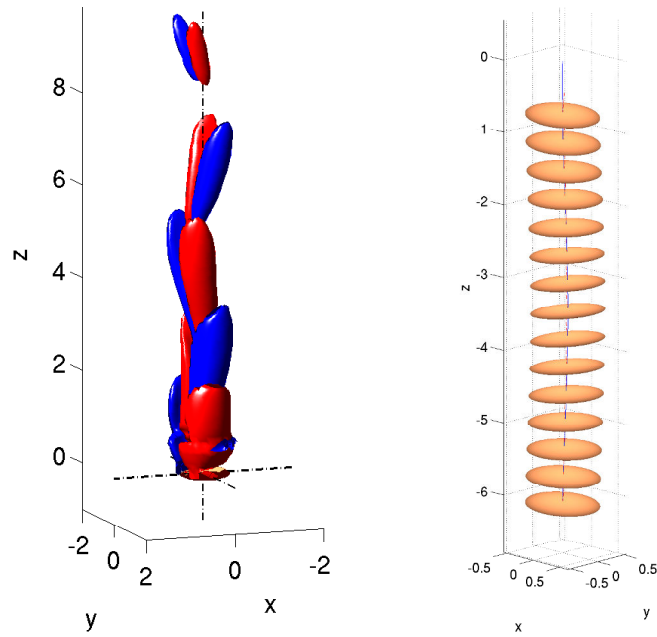


Figure 3.7: Vorticity structures and trajectory of vertical periodic state of spheroid of aspect ratio 10 at $m^* = 0.25$, $G = 100$ ($\sin \psi_{max} = 0.1$, vorticity level: $\omega_z = \pm 0.4$).

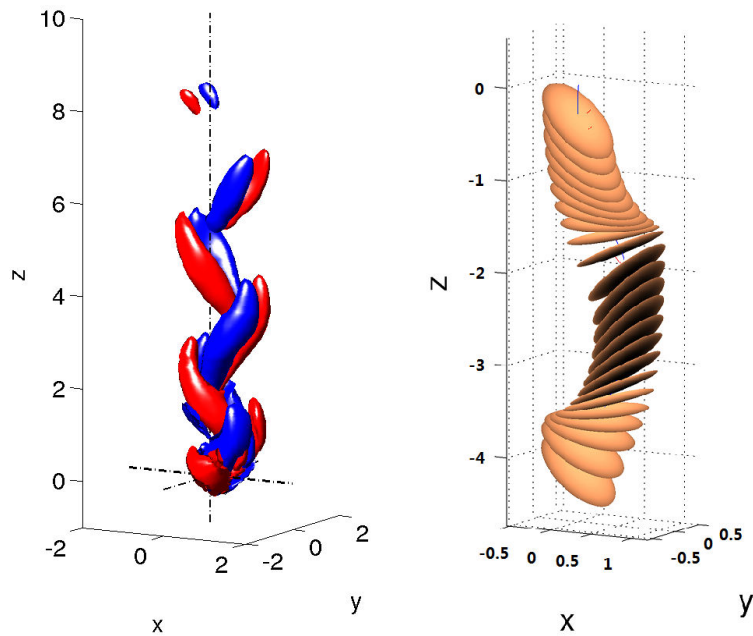


Figure 3.8: Vorticity structures and trajectory of a flutter of spheroid of aspect ratio 10 at $m^* = 0.25$, $G = 115$; $\sin \psi_{max} = 0.75$, vorticity level $\omega_z = \pm 0.8$.

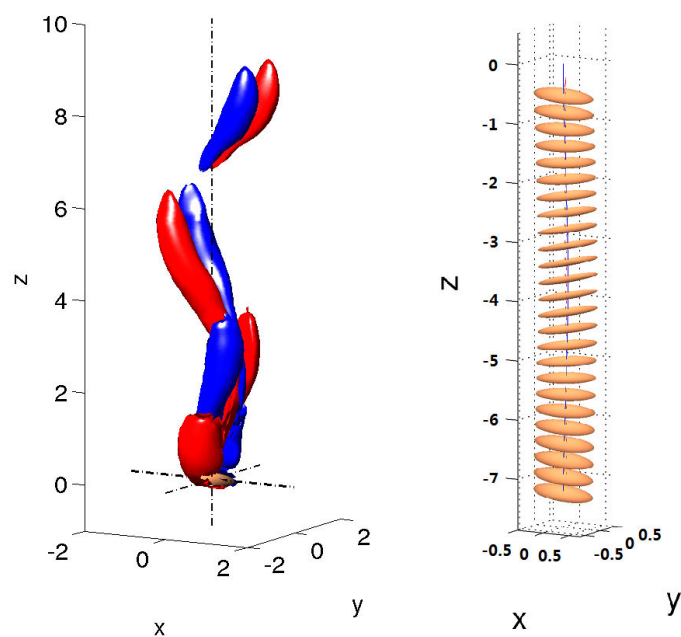


Figure 3.9: Vorticity structures and trajectory of a fluid mode of spheroid of aspect ratio 10 at $m^* = 2$, $G = 100$ ($\sin \psi_{max} = 0.19$, vorticity level $\omega_z = \pm 0.8$).

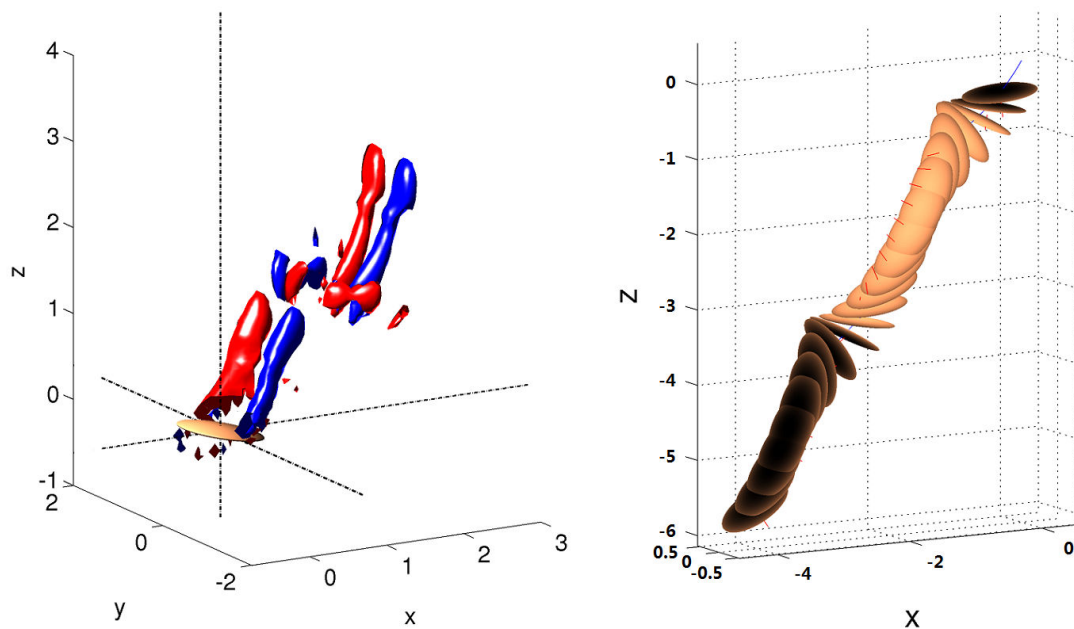


Figure 3.10: Vorticity structures and trajectory of a tumbling state of spheroid of aspect ratio 10 at $m^* = 0.75$, $G = 200$ (vorticity level: $\omega_z = \pm 2$).

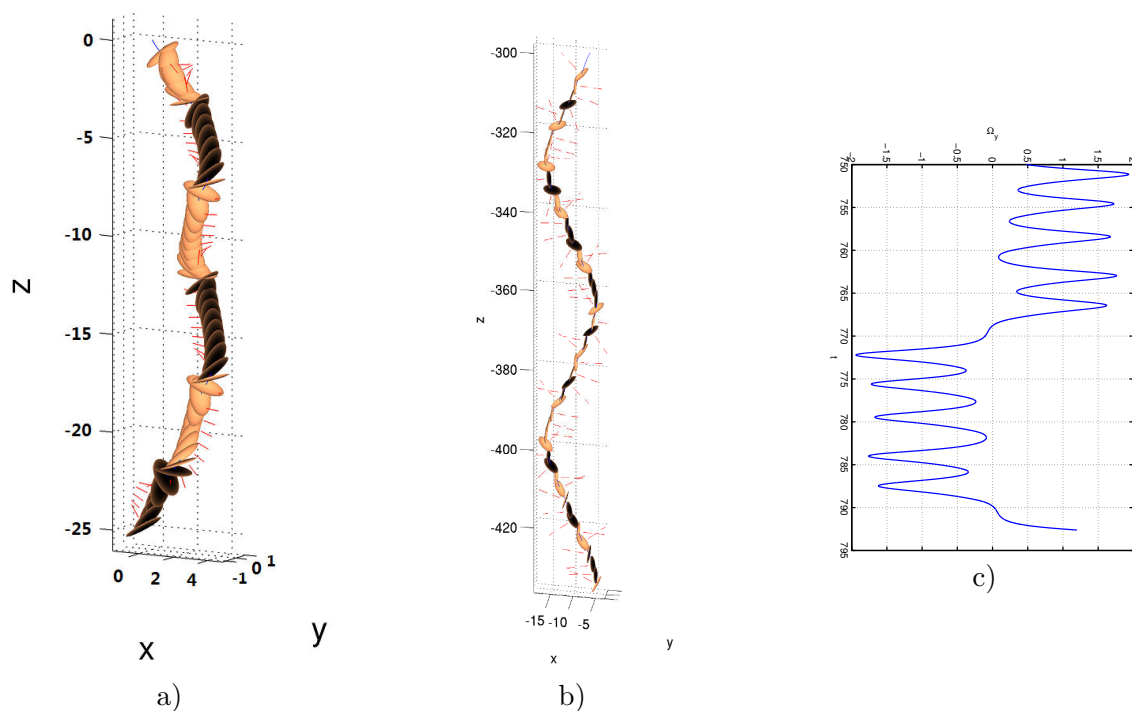


Figure 3.11: “Intermittent” trajectories of spheroid of aspect ratio 10. a) At $m^* = 0.75$ and $G = 100$, b) and c) $m^* = 2$ and $G = 65$. a) and b) Kino-gram, c) angular velocity of the body rotation.

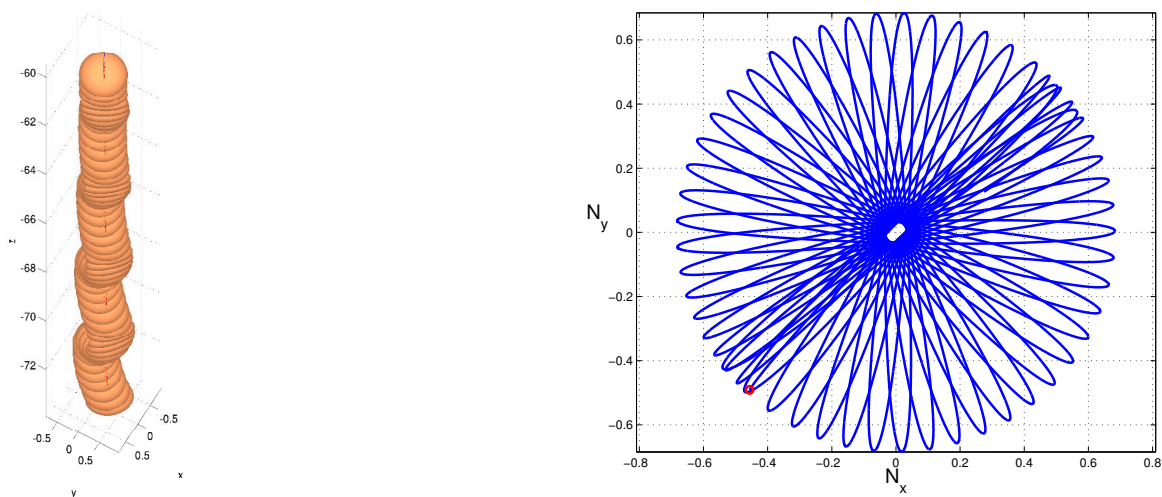


Figure 3.12: Kino-gram (left) and projection of unit vector of the body axis \mathbf{N} on the horizontal plane of a trajectory with non zero helicity for $\chi = 10$ and at $m^* = 0.1$, $G = 250$. Red circle indicates the location of the end of time series.

A little exploration in the domain of vertical falls reveals an interesting analogy of infinitesimal perturbations of vertical trajectories. The various falling styles observed for spheroids of high and low non-dimensionalized masses illustrated in Figures 3.13 through 3.15 demonstrate that the same linear modes appearing as unstable above the instability threshold are also the most receptive to numerical disturbances (of the order of the double precision machine accuracy). It may be expected that stronger and realistic disturbances may have a similar effect. The problem of receptivity of linearly stable flows was addressed e.g. in the paper by Saïdi *et al.* (2011). Quantitative data of the periods of horizontal oscillations and vertical velocities confirm the close relation between the excited states and the instabilities (Table 3.4).

(m^*, G)	T	u_z	regime
(0, 70)	1.7647	-1.4236	vertical
(0, 300)	1.5484	-1.4914	helical
(0.1, 70)	2.7212	-1.4236	vertical
(0.1, 300)	2.3035	-1.4003	helical
(0.25, 50)	3.4587	-1.3006	vertical
(0.25, 175)	3.4270	-1.3829	flutter
(0.5, 40)	3.8087	-1.2204	vertical
(0.5, 78)	3.8257	-1.2200	flutter
(0.75, 50)	4.2642	-1.2204	vertical
(0.75, 250)	4.2100	-1.2714	tumbling
(1.5, 75)	5.1816	-1.4507	vertical
(1.5, 105)	5.1386	-1.4408	flutter
(2, 70)	5.9887	-1.4236	vertical
(2, 100)	6.0208	-1.4620	tumbling

Table 3.4: Comparison of period of horizontal oscillations T (half period for tumbling) and vertical velocity u_z for spheroids of “steady vertical” falls and states at higher Galileo numbers for various non-dimensionalized masses.

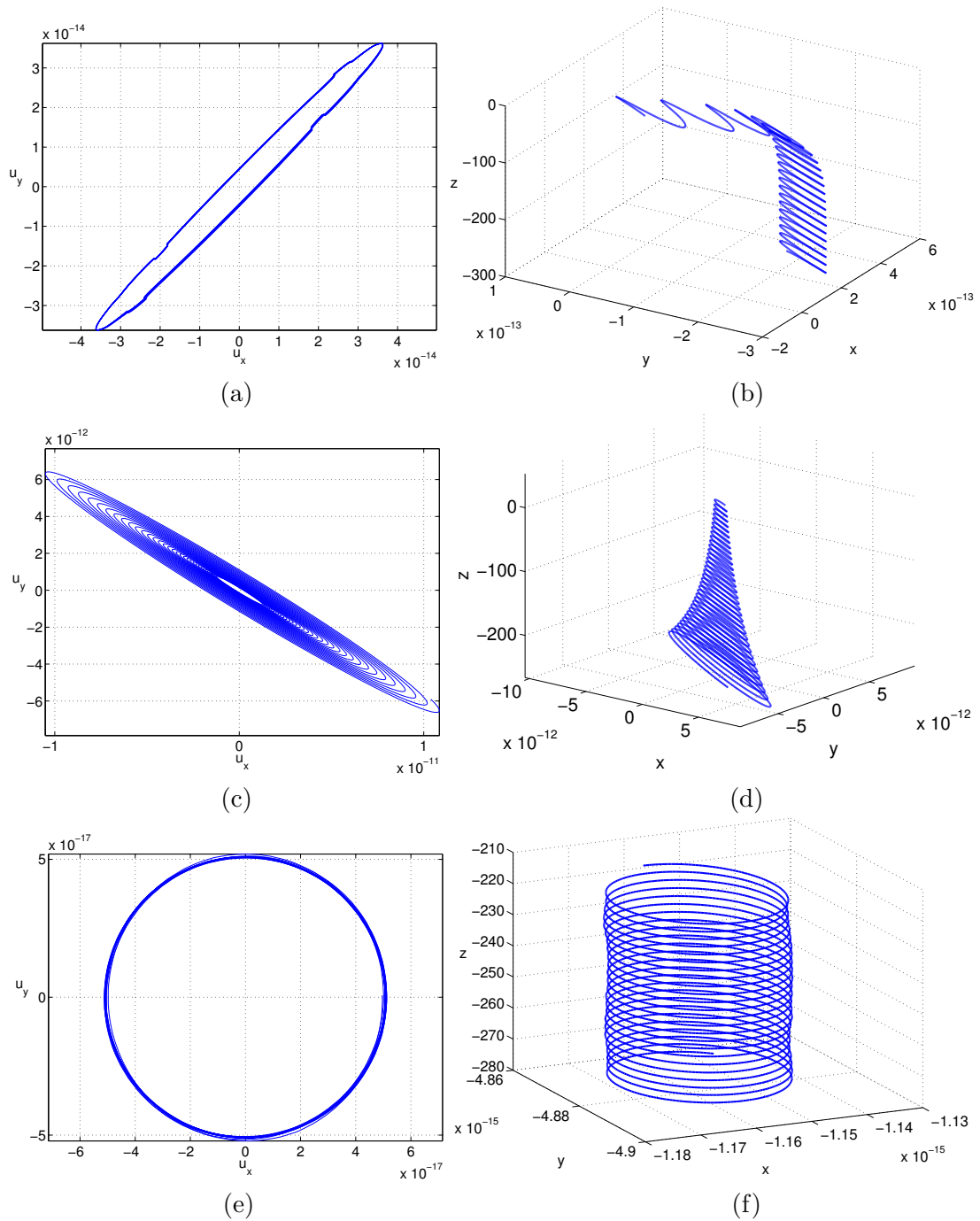


Figure 3.13: Various styles of “steady vertical” fall for spheroids. Projection of velocity vectors onto a horizontal plane and trajectory of spheroids at $m^* = 5, G = 80$ (figure (a,b)), $m^* = 2, G = 80$ (c,d) and $m^* = 0, G = 70$ (e,f).

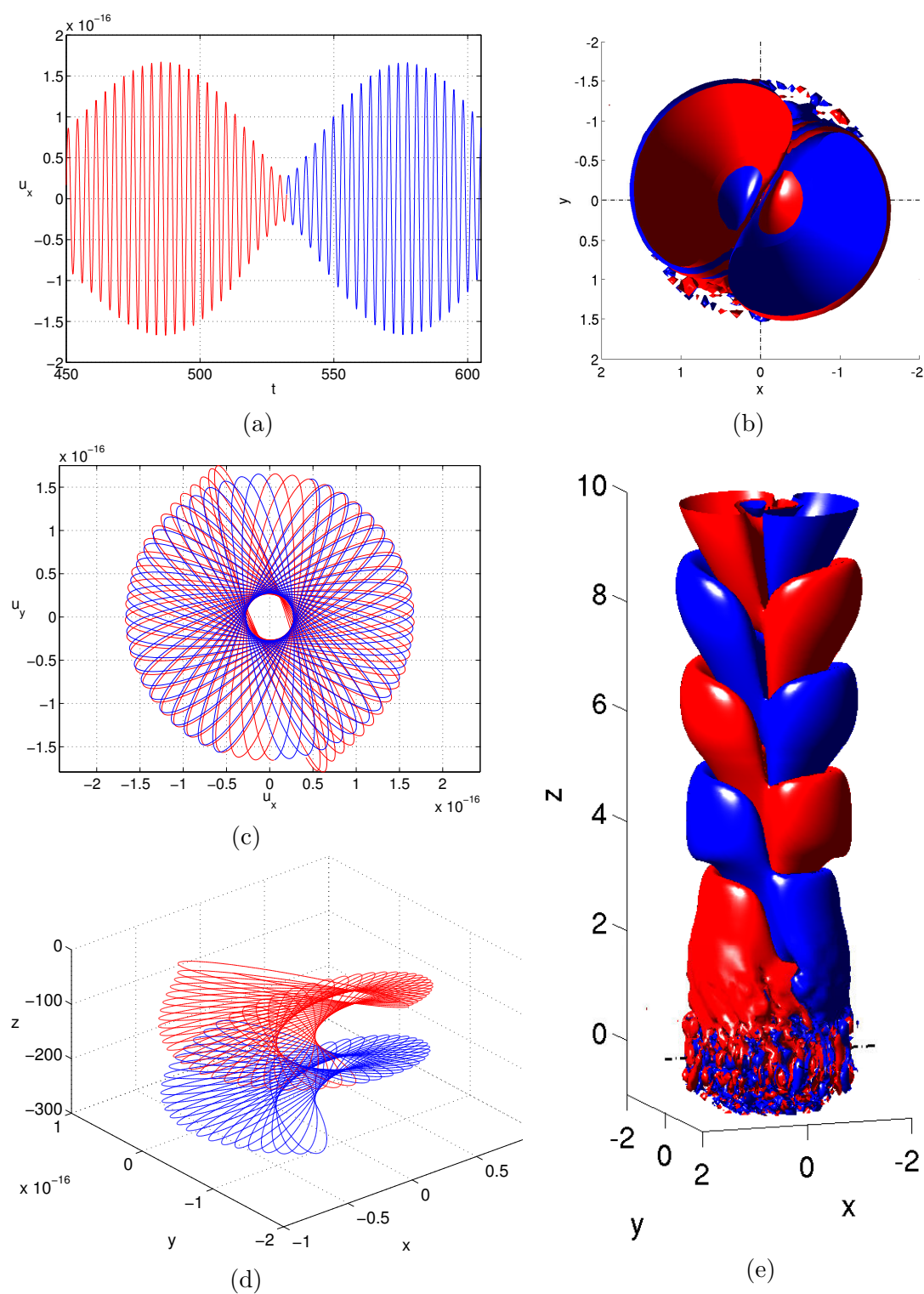


Figure 3.14: Horizontal velocity as a function of time (figure (a)), projection of velocity vectors onto a horizontal plane (c), trajectory (d), top and side views (b,e) of vorticity structures (vorticity level: $\pm 1.5 \times 10^{-17}$) for spheroids of $m^* = 0.25$, $G = 50$.

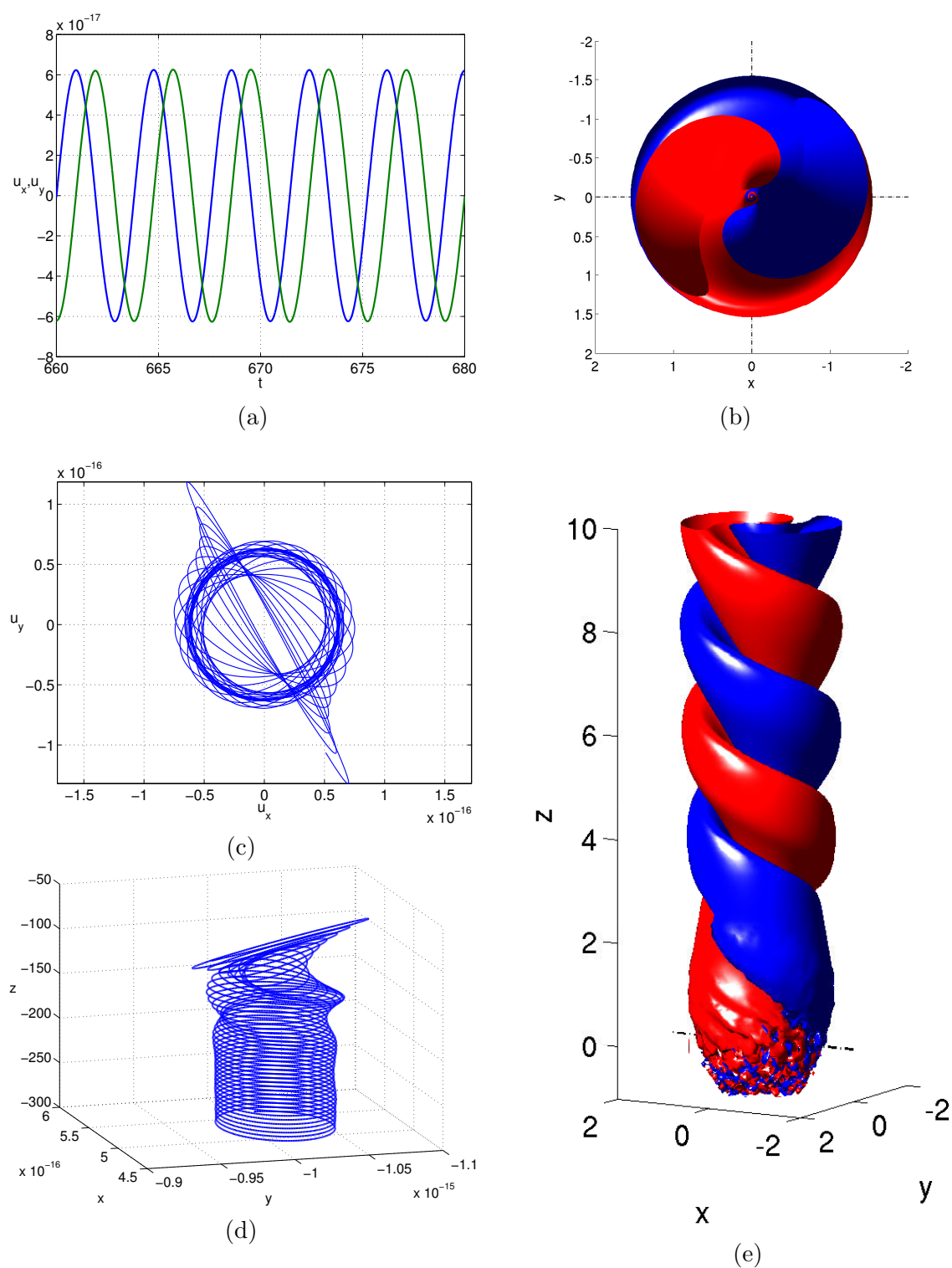


Figure 3.15: Horizontal velocities as a function of time (figure (a)), projection of velocity vectors onto a horizontal plane (c), trajectory (d), top and side views (b,e) of vorticity structures (vorticity level: $\pm 10^{-17}$) for spheroids of $m^* = 0.5$, $G = 40$.

3.3.3 $\chi = 6$

At the primary bifurcation, the state diagram 3.16 hints to a similar situation as at $\chi = 10$: the primary bifurcation is regular at $m^* \leq 0.25$. However, for this smaller aspect ratio, the transition from the steady oblique to vertical periodic state is progressive. This is illustrated, at $m^* = 0.1$, in Figure 3.17). The threshold of the primary, regular bifurcation is 90.1 independently of m^* (provided $m^* \leq 0.25$). For $G = 92$ we find an exponentially increasing inclination reaching a steady asymptotic value of about 3° (0.058 rad). The inset demonstrates the stage of linear growth. At $G = 94$ we are above the Hopf bifurcation threshold. The oscillation appears after the saturation of the primary instability is reached. Its effect consists in a reduction of the mean value similarly as in Figure 3.5. The decrease stops, however, before the mean value completely disappears. The asymptotic state is clearly characterized by a mean inclination of about 0.05 radians and an amplitude of oscillation of about 0.02. The same holds (qualitatively) for the horizontal velocity which results in an oblique oscillating regime. With growing Galileo number, the mean value ends up vanishing. This is the case at $G = 96$. A doubt may subsist if the asymptotic state has an exactly zero value. For this purpose the dependence of the mean value on time is represented in the inset. It clearly shows an exponential convergence to zero. At $m^* = 0$ the oblique oscillating state loses its mean value at $G = 98$, while, at $m^* = 0.25$, we observe an oblique oscillating regime at $G = 92$ and a vertical periodic one at $G = 94$ already. It means that the thresholds shift downward to the critical Galileo number of the primary bifurcation. This is coherent with the fact that this scenario is no longer observed at $m^* = 0.5$.

Unlike for a disk and very flat spheroids of aspect ratios larger or equal than 10, the primary bifurcation is not subcritical at higher non-dimensionalized masses. It continues to be supercritical but of Hopf type giving rise directly to vertical periodic fluid states. In the interval $0.25 \leq m^* < 1.8$, the vertical periodic fluid modes undergo a next bifurcation yielding states with a significant flutter or directly intermittent or tumbling trajectories. As a result, even in the interval $0.5 \leq m^* \leq 1.2$ a narrow “channel” of fluid modes connects the lower area to the upper one, which co-exists with tumbling states. This may be considered as an additional confirmation of the conjecture formulated in the previous sub-section consisting in establishing an analogy between fluid states at small and high inertia. The second bifurcation threshold is marked by the solid magenta line delimiting the fluid modes from higher Galileo numbers. This bifurcation is subcritical and the branch of fluttering states extends toward low Galileo numbers and the bi-stability domain overlaps, albeit less than for $\chi = 10$, with the domain of steady vertical trajectories. The progressive transition from a steady vertical regime to flutter with increasing Galileo number is illustrated in Figure 3.18 for $m^* = 1$. The exponential decay of small oscillations of the sine of the inclination angle of body axis at $G = 80$ proves the linear stability of the steady vertical mode. At $G = 85$, the Hopf bifurcation sets in and saturates at an amplitude less than 0.05 typically for the vertical periodic fluid mode. At $G = 90$ this mode becomes unstable. The new bifurcation is subcritical as can be seen from the super-exponential growth of the amplitude (Figure 3.18, graph of the logarithm of amplitude at $G = 90$). The last plot (e) shows the stability of the flutter (sine of inclination of 0.8) at the same Galileo number as that of the fluid mode (b) at $G = 85$.

For higher Galileo numbers, we observe the trend of the intermittent domain to disappear with decreasing aspect ratio. While the overlapping of flutter with vertical regime gets significantly reduced, there is practically no change in the extent of the stability domain of tumbling towards small Galileo numbers.

(m^*, G)	\bar{u}_z	A_{u_z}	\bar{u}_h	A_{u_h}	$\phi_{max}(^\circ)$	period
(0.1, 100)	-1.56	0.002	0	0.03	3.96	4.88
(0.25, 110)	-1.52	0.003	0	0.05	5.93	4.48
(0.25, 115)	-1.42	0.088	0	0.31	34.92	3.46
(1, 75)	-1.39	0.091	0	0.24	41.96	4.58
(1.5, 150)	-1.47	0.008	0	0.087	18.71	4.51
(2, 150)*	-1.39	0.18	0.80	0.12	90	5.26
(2, 150)**	-1.48	0.002	0	0.052	11.0	4.60

Table 3.5: Quantitative data characterizing selected periodic states for aspect ratio $\chi = 6$. Same meaning of symbols as in Table 3.2. *: tumbling (period corresponding to a full rotation by 2π), **: fluid mode.

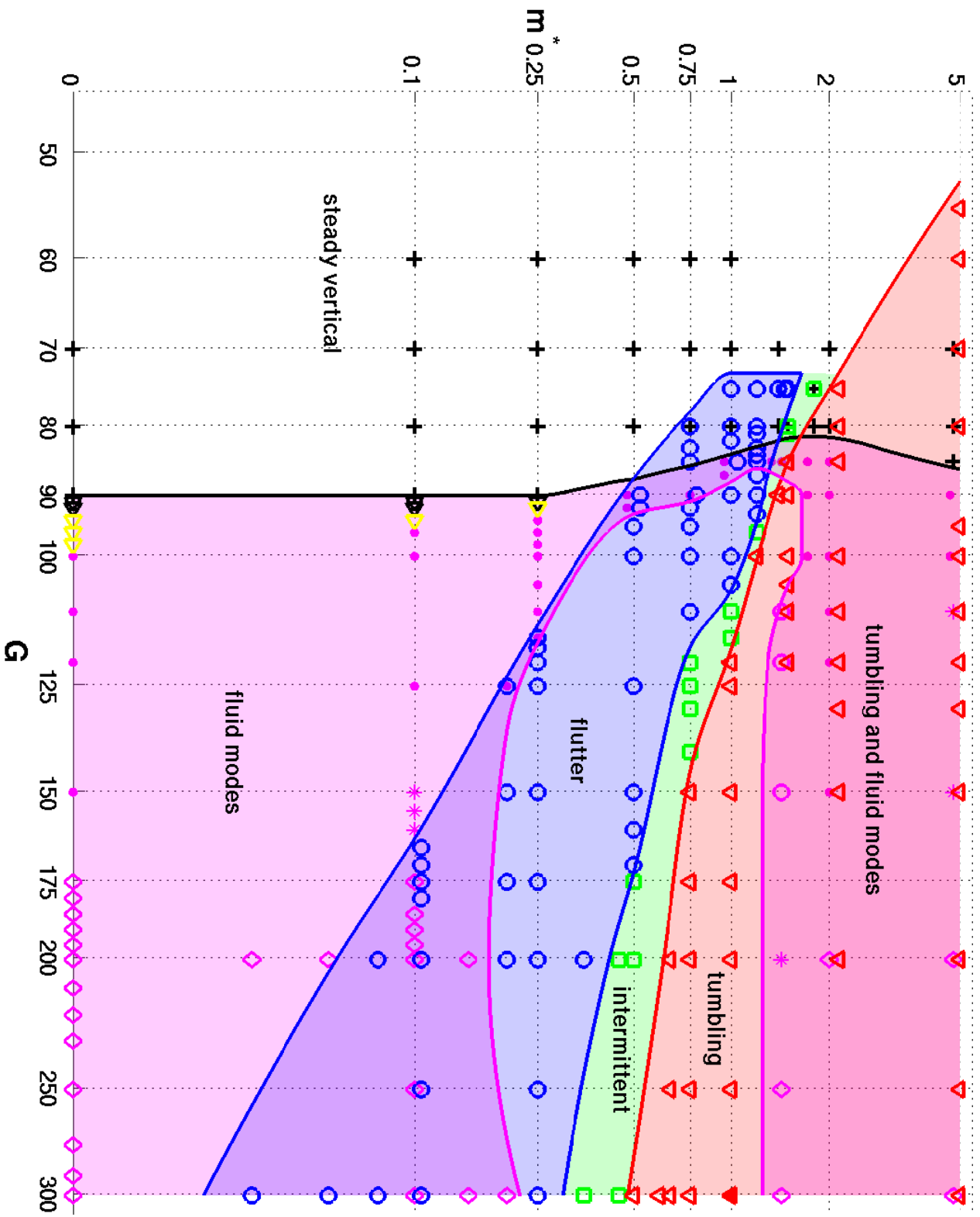


Figure 3.16: The state diagram for spheroids of $\chi = 6$.

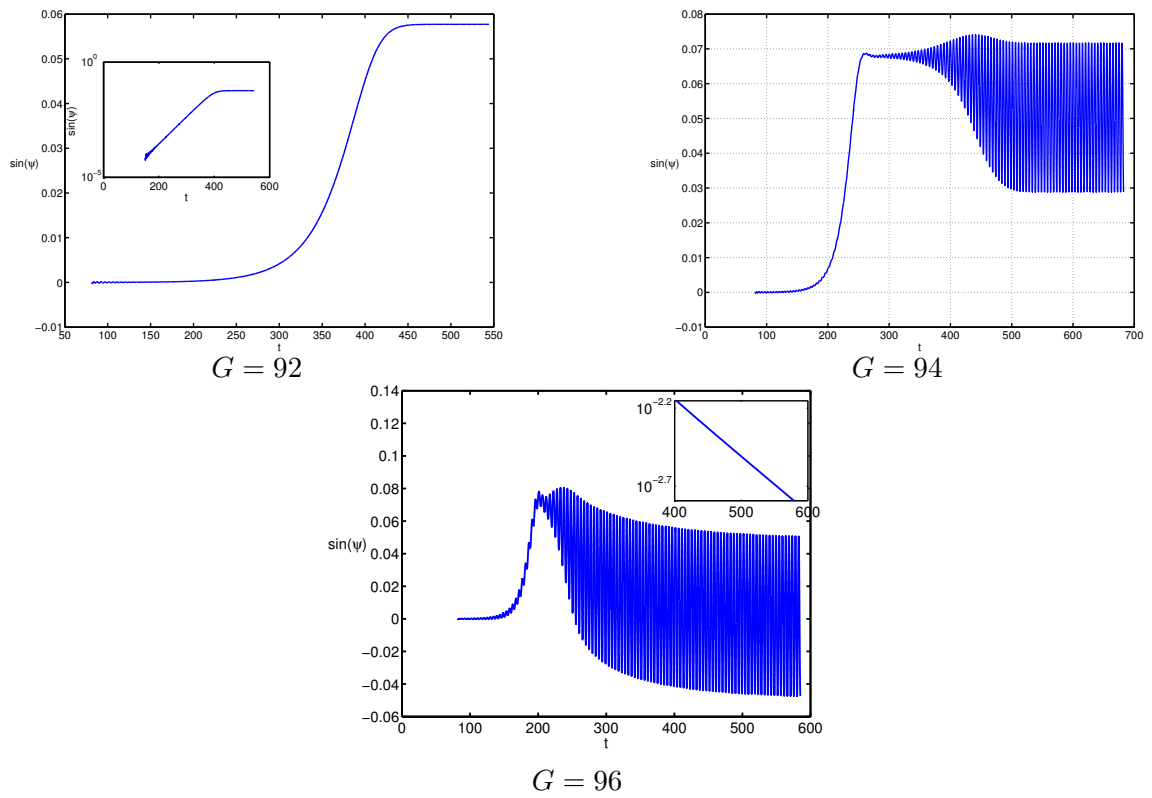


Figure 3.17: Evolution of the inclination of the axis of spheroid starting from a steady vertical state at $m^* = 0.1$ and $G = 92, 94$ and 96 . Inset of the figure at $G = 96$: horizontal axis: time, logarithmic vertical axis: mean value of $\sin \psi$ per oscillation.

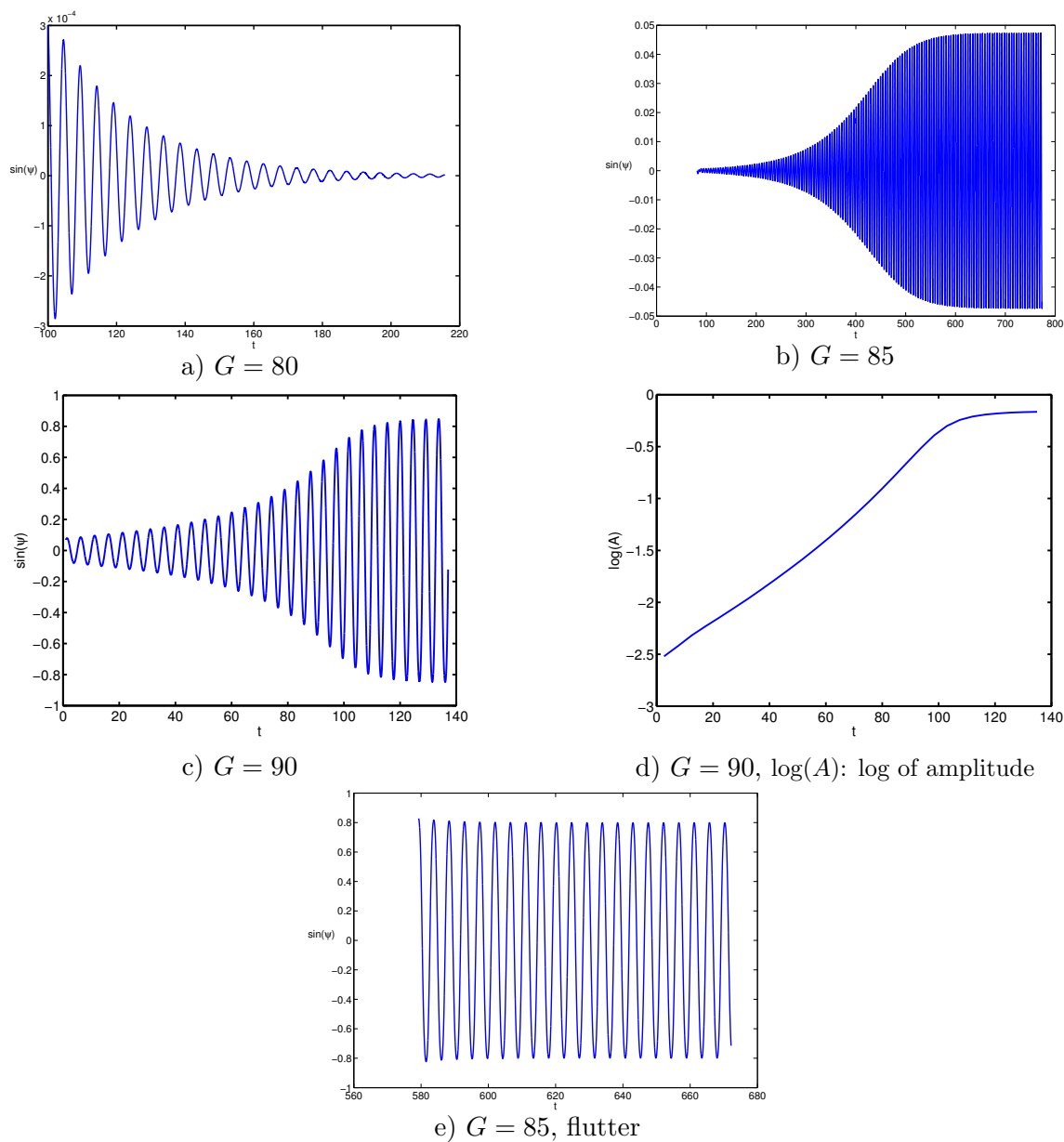


Figure 3.18: Evolution of the inclination of the axis of spheroid starting from a steady vertical state at $m^* = 1$. $G = 80$: stability of the steady vertical state. $G = 85$: convergence to vertical periodic state with small amplitude of oscillation (fluid mode). $G = 90$: secondary Hopf bifurcation saturating in the flutter. The $G = 90$, log of amplitude plot (figure d) demonstrates the sub-criticality. $G = 85$ flutter: coexisting flutter at $G = 85$.

3.3.4 $\chi = 5$

The specificities of the scenario for $\chi = 5$ as compared to $\chi = 6$ are the following (see top Figure 3.20):

- The regular bifurcation for small m^* is no longer present. The primary bifurcation is a Hopf one for all non-dimensionalized masses.
- The subcritical bifurcation, accompanied by a jump in amplitude of oscillation and by bi-stability, between the flutter and fluid modes is limited only to $m^* \geq 0.5$ and Galileo numbers smaller than 110. This is illustrated by Figure 3.19 showing that at $m^* = 0.75$ there is a bi-stability between large amplitude (flutter) and small one (fluid mode), at $m^* = 0.5$ there is still a jump, while at $m^* = 0.25$ the amplitude grows continuously with Galileo number. The flutter overlaps only very little with the vertical states.
- The domain of intermittence becomes very narrow and close to vanishing.

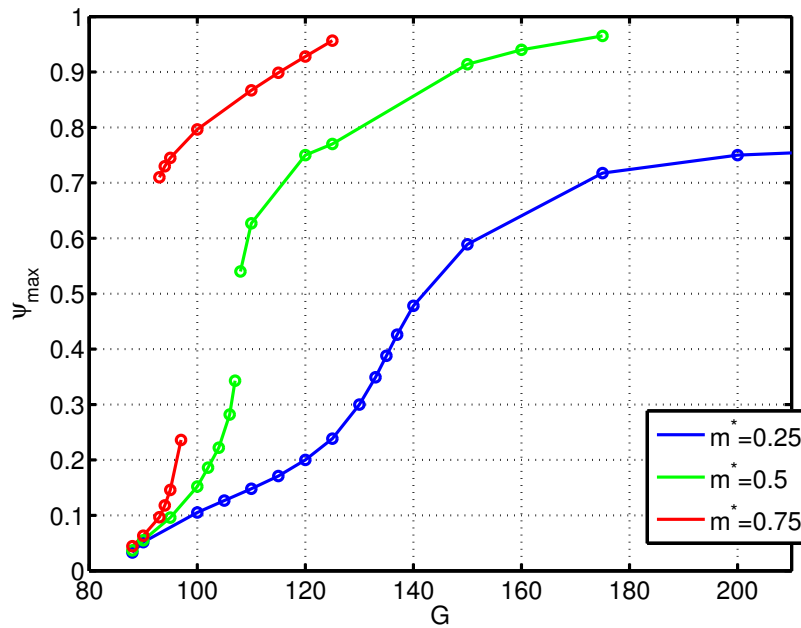
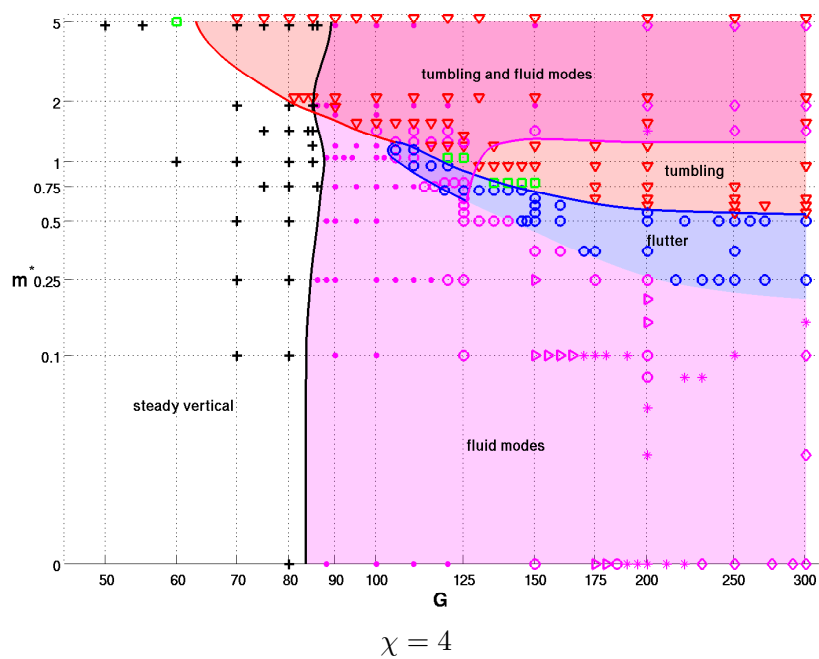
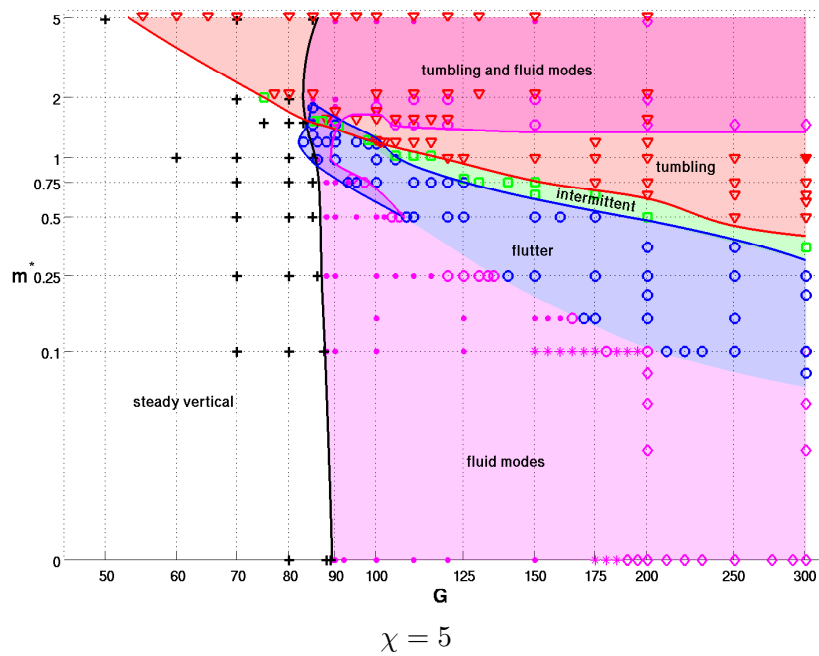


Figure 3.19: Sine of the inclination angles (ψ) as a function of Galileo number for spheroids of $m^* = 0.25, 0.5$ and 0.75 .

Figure 3.20: State diagrams for spheroids of $\chi = 5$ and 4.

3.3.5 $\chi = 4$

At aspect ratio $\chi = 4$ (bottom Figure 3.20), only a few intermittent states bordering the tumbling domain were evidenced. The flutter still arises via subcritical bifurcation from fluid modes, but only at $m = 0.75$, and its bi-stability domain with fluid modes is largely reduced.

3.3.6 $\chi = 3$

The most remarkable feature of the aspect ratio 3 is the reappearance of the regular primary bifurcation. In contrast with very flat spheroids, it sets in for high inertia $m^* = 3, 4, 5$. The m^* independent critical Galileo number is then 90.6. The specificity of the secondary bifurcation (at $\chi = 3$ and also $\chi = 2$) consists in the instability of the oblique oscillating state. (See Figure 3.21). Instead of saturating to yield a constant mean value and amplitude, it grows until the mean value vanishes and a vertical periodic state appears. The latter is not stable either. A steady oblique state in the perpendicular direction arises and the selection of the new symmetry plane of the wake makes the oscillation in the previous direction vanish. The steady oblique state grows until oblique oscillations appear and the cycle repeats regularly. It can be expected that in presence of sufficient random noise the repetition would not be periodic but rather intermittent. In the example of Figure 3.21, it can also be seen that the direction of the steady oblique growth in the perpendicular plane is selected arbitrarily. The frequency of oscillation only slightly varies (by less than 10%) over the whole cycle. The typical Strouhal is 0.11, i.e. the same as for the oblique oscillating state existing for small inertia at aspect ratios $\chi \geq 6$.

Next, we remark the complete disappearing of the flutter, which could be distinguished, at least partially, by a discontinuity from fluid modes at higher aspect ratios. As can be seen in Table 3.7 no vertical periodic state has an amplitude of inclination of the body axis exceeding 30° (sine larger than 0.5). There is thus no longer a continuous transition to the tumbling state. For a constant aspect ratio the tumbling regime can be reached by selecting m^* and Galileo number in the small subdomain where tumbling does not co-exist with fluid modes and then vary the parameters on the tumbling branch.

Table 3.6 provides quantitative data on some selected periodic states.

(m^*, G)	\bar{u}_z	A_{u_z}	\bar{u}_h	A_{u_h}	$\phi_{max}(^\circ)$	period
(0, 100)	-1.48	0.007	0	0.14	13.08	4.45
(1, 100)	-1.57	0.0009	0	0.024	4.85	5.03
(1, 125)	-1.56	0.005	0	0.056	11.94	4.57
(1, 150)*	-1.67	0.3	0.85	0.16	90	5.6
(1, 150)**	-1.56	0.012	0	0.084	17.1	4.38
(5, 70)*	-1.79	0.12	0.45	0.07	90	12.3

Table 3.6: Quantitative data characterizing selected periodic states for aspect ratio $\chi = 3$. Same meaning of symbols as in Table 3.2. *: Tumbling, **: fluid mode.

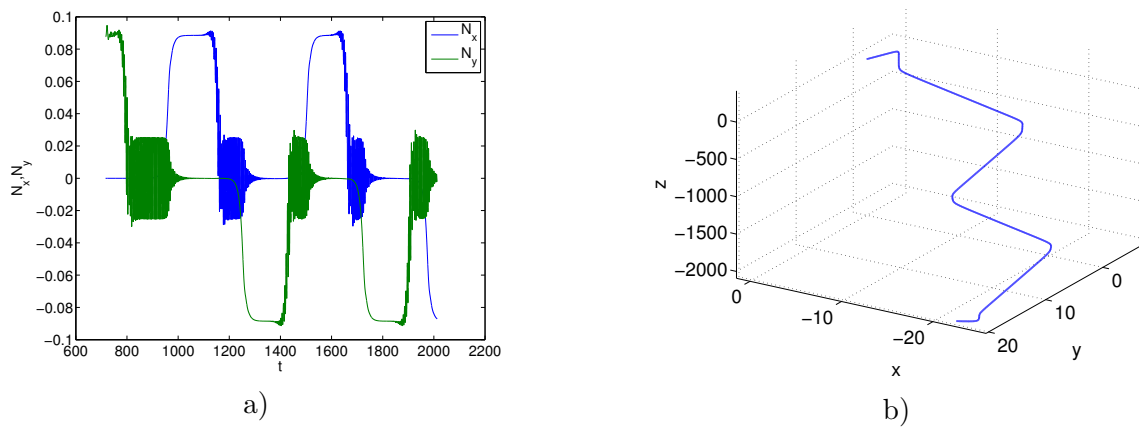


Figure 3.21: $\chi = 3, m^* = 5, G = 105$: Example of a trajectory switching periodically from a vertical periodic to steady oblique and oblique oscillating state. a) Horizontal projections N_x, N_y of the unit vector of the body axis as function of time, b) trajectory.

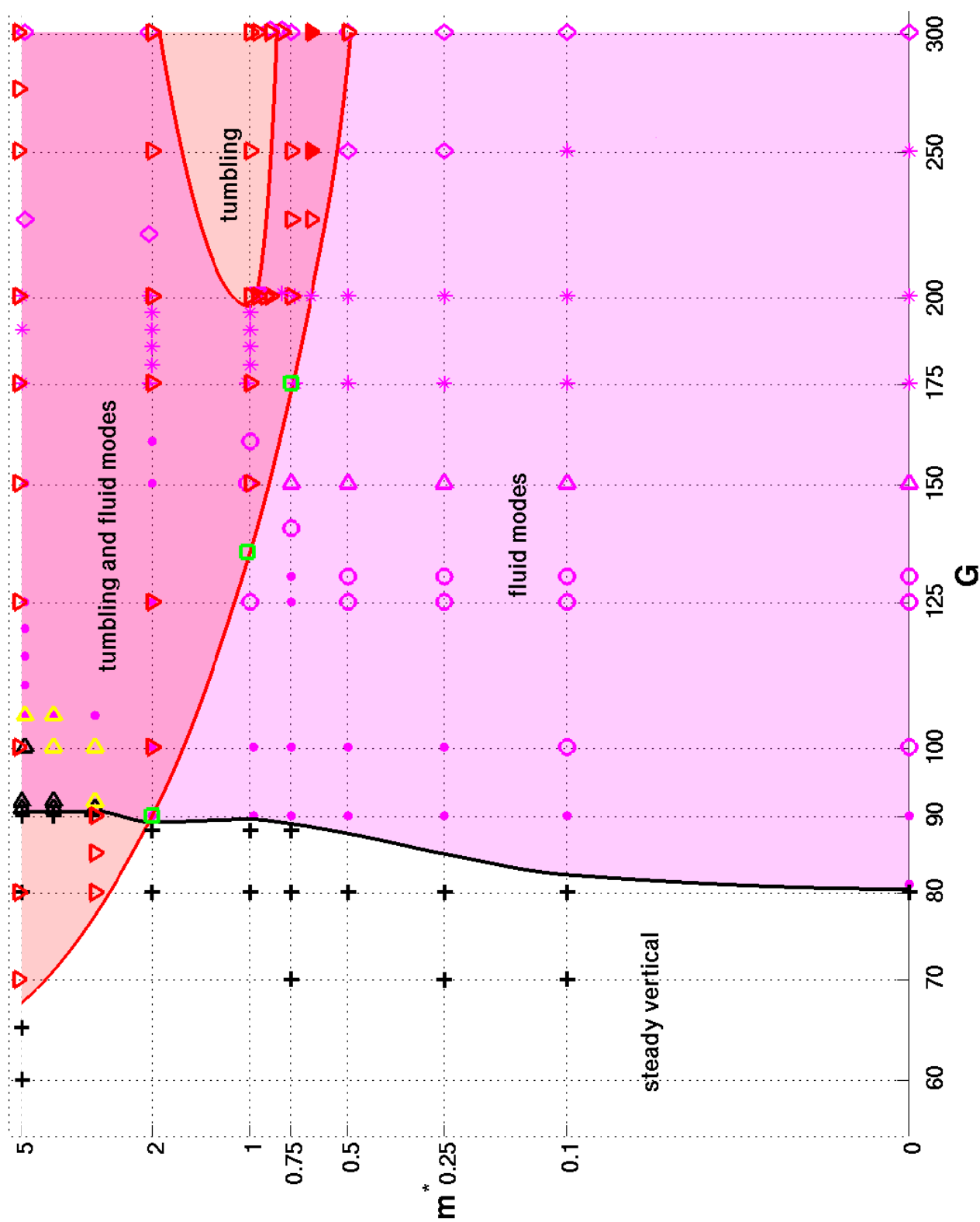


Figure 3.22: The state diagram for spheroids of $\chi = 3$.

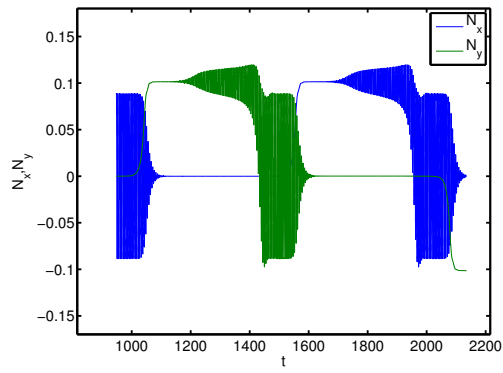
3.3.7 $\chi = 2$

The primary supercritical Hopf bifurcation was evidenced only up to $m^* \leq 0.25$ for this aspect ratio. For $m^* \geq 0.5$, the primary bifurcation is already regular and the sphere-like scenario sets in at first two bifurcations. The m^* independent critical Galileo number is 94.3. The secondary, Hopf bifurcation leads, again, to a switching between steady oblique, oblique oscillating and vertical periodic states. The period of this switching varies significantly depending on the parameters but is remarkably regular (see Figure 3.23), which can be explained by the absence of random noise.

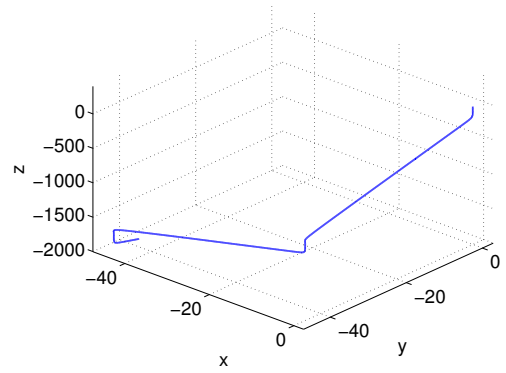
We evidenced no mono-stable tumbling sub-domain for the aspect ratio 2. Table 3.7 shows that, again, **no vertical periodic state has an amplitude of inclination of the body axis exceeding 30°** . There is thus no longer any direct transition to tumbling possible for bodies of this aspect ratio just by changing their Galileo number. This might mean that a simple acceleration from the rest will not yield a tumbling unless the rotation is externally triggered. Then, however, it will remain self-sustained in the parameter domain represented in the diagram 3.24. At the edge of the domain of stability of the tumbling mode we still evidenced several cases of intermittent behavior (green squares). Table 3.7 shows also that the oblique oscillations have a frequency close to that of fluid modes of the sphere.

(m^*, G)	\bar{u}_z	A_{u_z}	\bar{u}_h	A_{u_h}	$\phi_{max}(^\circ)$	period
(0.1, 100)	-1.53	0.017	0	0.23	16.48	5.28
(0.5, 150)	-1.65	0	0	0.13	12.07	4.73
(1, 150)	-1.68	0	0	0.072	46.73	4.64
(2, 150)*	-1.75	0.13	0.77	0.053	90	3.71
(2, 150)**	-1.72	0	0	0.046	12.75	4.72

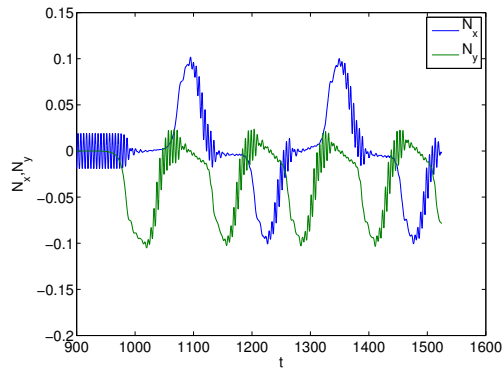
Table 3.7: Quantitative data characterizing selected periodic states for aspect ratio $\chi = 2$. Same meaning of symbols as in Table 3.2. *: Tumbling, **: fluid mode.



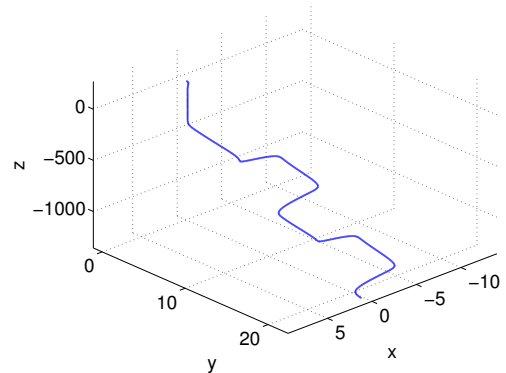
a)



b)

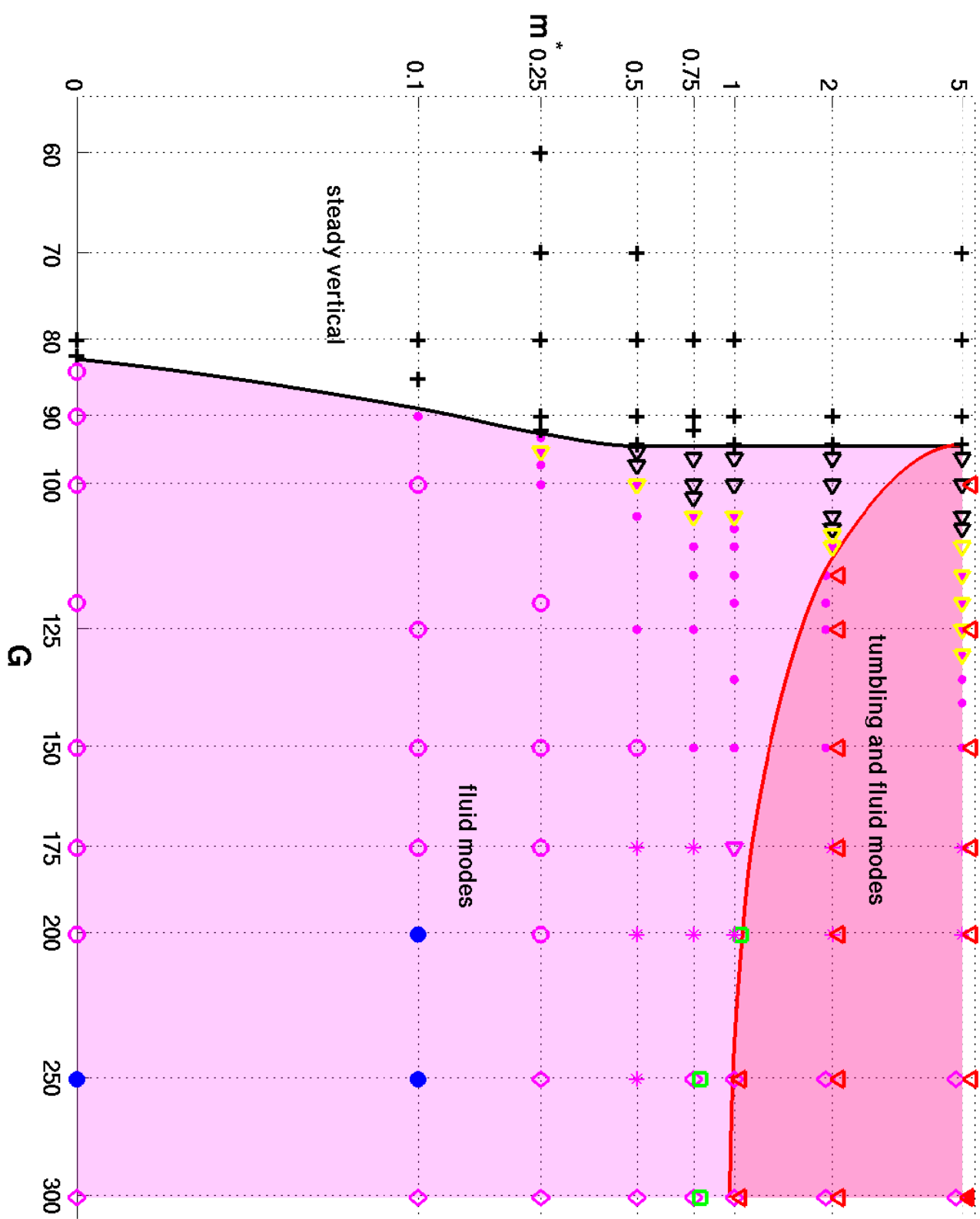


c)



d)

Figure 3.23: $\chi = 2, m^* = 2, G = 110$: a) Horizontal projections N_x, N_y of the unit vector of the body axis as function of time, b) trajectory. c),d) $m^* = 5, G = 120$.

Figure 3.24: The state diagram for spheroids of $\chi = 2$.

3.3.8 $\chi = 1.1$

The transition scenario of a spheroid of aspect ratio $\chi = 1.1$ is close to that of a sphere for sufficiently dense spheroids. The symbols and colors used in Figure 3.25 correspond to those in Figure 2.7 of the previous chapter. The present case of almost spherical body can be quantitatively compared to a perfect sphere by converting the non-dimensionalization. If we neglect the small difference of aspect ratio, the present reference velocity (3.2) and that used for the perfect sphere (2.3) differ by the factor $\sqrt{\pi/6}$ (i.e. $U_{ref} = \sqrt{\pi/6} U_{ref,sphere}$). As the result, the Galileo number defined by Eq. (3.6) is smaller by this factor and the velocities and frequencies are larger by its inverse. The primary bifurcation threshold (that of the steady oblique regime) found to be $G_{crit}^* = 155.8$ (independently of the density ratio) becomes $G_{crit} = 112.7$ in terms of the definition (3.6). For an almost spherical spheroid of aspect ratio $\chi = 1.1$ this threshold lies at $G_{crit} = 110.8$ and is represented by the black vertical line separating the domain of steady vertical trajectories (black crosses) from that of steady oblique regimes (rightward pointing black triangles). The horizontal velocity does not exceed 10% of the vertical one, similarly as for the perfect sphere. It is to be noted that, unlike the perfect sphere, the spheroid does not rotate. This fact has, however, a very limited impact on the onset of the primary instability.

The secondary Hopf bifurcation leads to two different oblique oscillating regimes with two different frequencies as already stated for the sphere by Jenny *et al.* (2004). The more accurate recent investigation of chapter 2 evidenced the high frequency at as low a density ratio as 1.7. In the present context, the density ratio is replaced by the non-dimensionalized mass whose value differs by the factor $\pi/6$ from the density ratio in the case of a perfect sphere, i.e. the limit between buoyant and falling spheres corresponds to $m^* = 0.52$ and the density ratio 1.7 corresponds to $m^* = 0.9$. The slightly aspherical shape is enough to shift the threshold between the low and high frequency states to about $m^* = 2$ (i.e. about twice as high). As already mentioned, the present definition of reference velocity (3.2) implies that non-dimensionalized frequencies should be larger by the factor $\sqrt{6/\pi}$ than those found for a perfect sphere. The non-dimensionalized frequency of the low frequency regimes of a sphere was found to be slightly less than 0.07 (see Jenny *et al.*, 2004) at the Hopf bifurcation threshold whereas that of the high frequency was slightly less than 0.18 which was shown to correspond to the vortex shedding frequency of the fixed sphere wake in chapter 2. In terms of the present non-dimensionalization, these values are equivalent to 0.097 and 0.249, respectively. This agrees very well with those obtained for the spheroid of aspect ratio 1.1 in the green (low frequency) and yellow (high frequency) filled domains in Figure 3.25. The low frequency varies from 0.09 (at $m^* = 2$) to 0.11 (at $m^* = 0$) whereas the high frequency is practically constant and equal to 0.25. A small domain of “zigzagging” regimes was also evidenced (cyan domain). These regimes were shown by Jenny *et al.* (2004) to result from the oblique oscillating regime by toggling to the opposite side of the vertical when the oscillation amplitude is large enough to make the horizontal velocity momentarily vanish. In Chapter 2, they were shown to be only exceptionally perfectly periodic and planar. For the spheroid of aspect ratio 1.1, the trajectories are also more often rather three-dimensional and irregular on large time scales with very low characteristic frequencies (0.03 - 0.04, i.e. about 2.5 to 3 times smaller than the low frequency oblique oscillating regime. They represent a

transition between periodic oblique oscillation regimes and chaotic regimes (represented by magenta symbols in Figure 3.25). Table 3.8 confirms a satisfactory quantitative agreement between dynamical characteristics of regimes of an almost spherical spheroid and of a perfect sphere for comparable non-dimensionalized masses and Galileo numbers.

In spite of this close similarity to the scenario of a perfect sphere, the diagram of Figure 3.25 still presents features typically for flat bodies for very small inertia (m^* roughly smaller than 0.25). We evidenced a bounded area of linear instability below the threshold of the steady oblique regime for $m^* < 0.1$. In Figure 3.25 the area is delimited by a solid blue line from lower Galileo numbers and by a dashed blue line from higher Galileo numbers, corresponding, for increasing Galileo numbers at constant m^* , respectively, to a destabilization and re-stabilization of the vertical trajectory. The lines determine the threshold of the Hopf bifurcation yielding a planar oscillating trajectory, vertical in the average. The frequency is slightly higher than in the oblique oscillating regime: 0.12 to 0.14 as compared to 0.10. At saturation, the oscillations of the body are (unlike the fluid modes discussed elsewhere) significant - about 20 degrees for the oscillating states evidenced at $G = 90$ and correspond thus to the “flutter” of flat bodies. The bifurcation corresponding to the re-stabilization, i.e. setting in for decreasing Galileo numbers, is subcritical. As a result the flutter remains stable outside the described small subdomain of linear instability of the vertical ascension. The domain of stability of this regime is delimited by the solid blue line and is filled in blue. It partially coexists with the states characteristic for a spherical body.

Perfect spheres with little inertia have been shown to describe mostly chaotic trajectories for higher Galileo numbers except for an “island” of vertical oscillating trajectories situated around the parameter point (in present non-dimensionalization) $m^* = 0.5$, $G = 200$. The frequency of oscillation at this point was found to be 0.2 (again in the present non-dimensionalization). The spatial amplitude of oscillation about the vertical direction is very small for this state - about 0.1 of the sphere diameter so that these trajectories may be appropriately called “quasi-vertical”. At a close point $m^* = 0.25$, $G = 200$, the trajectory of the spheroid of aspect ratio 1.1 presents completely different characteristics. The oscillation frequency is 0.125 (instead of 0.2) and the amplitude of excursions with respect to the vertical direction is equal to 1 d . This shows that the flutter of the spheroid has nothing to do with the periodic quasi-vertical regime of a perfect sphere. The motion of the spheroid is also marked by a very large amplitude of oscillations of the spheroid axis (70 degrees) indicating that the aspherical shape, albeit only slightly flattened, has a decisive impact on the dynamics of rising bodies with small solid/fluid density ratio.

spheroid of aspect ratio $\chi = 1.1$ and sphere								
(m^*, G)	u_z	u_h	A_{u_h}	$\sin \psi$	$A_{\sin \psi}$	f	Ω_h	A_{Ω_h}
(0.25,115)	1.81	0.098	0	0.078	0	steady		
(0.26, 116)	1.83	0.088	0			steady	0.016	0
(0.25,120) (oo)	1.83	0.12	0.046	0.090	0.042	0.096		
(0.26, 126)	1.86	0.15	0.043			0.087	0.020	0.013
(0.5,130) (zz)	1.86	0	0.25	0	0.21	0.043		
(0.26,130)	1.86	0	0.27			0.033	0.054	
(1,120)	1.83	0.133	0	0.101	steady			
(1.05,123)	1.85	0.146	0			steady	0.015	0
(2.5,140) (oohf)	1.89	0.185	0.0029	0.122	0.0007	0.24		
(2.1,145)	1.92	0.196	0.0026			0.25	0.010	0.0006
(2,300)*	2.15	0.03	0.14	0.01	0.10	0.08		
(2.1,270)*	2.16	0.03	0.11			0.09	0.006	0.018

vertical oscillating states of spheroid $\chi = 1.1$							
(m^*, G)	u_z	u_h	A_{u_h}	$\sin \psi$	$A_{\sin \psi}$	f	
(0.025, 90)	1.62	0	0.31	0	0.34	0.13	
(0.025, 110)	1.61	0	0.49	0	0.56	0.14	
(0.35,175)	1.76	0	0.60	0	0.78	0.124	
(0.35,175)*	1.95	0	0.19	0	0.19	0.095	

Table 3.8: Top: comparison of some characteristic regimes of a spheroid of aspect ratio $\chi = 1.1$ (upper lines) and of a sphere (lower lines). oo - oblique oscillating, zz - low frequency periodic zigzagging, oohf - oblique oscillating, high frequency. (Parameters relevant for the sphere are converted to the non-dimensionalization of the present chapter). u_h : (average) horizontal velocity, A_{u_h} : horizontal velocity amplitude, $\sin \psi$: (average) sine of inclination, $A_{\sin \psi}$: amplitude of oscillations of the body axis in terms of the sine of inclination, f : frequency, Ω_h : (average) horizontal projection of angular velocity, A_{Ω_h} : amplitude of Ω_h . *: non-periodic states - amplitudes replaced by r.m.s. and frequency by the peak of power spectrum corresponding to the most visible oscillations. Bottom: characteristics of some vertical oscillating states of spheroid of $\chi = 1.1$.

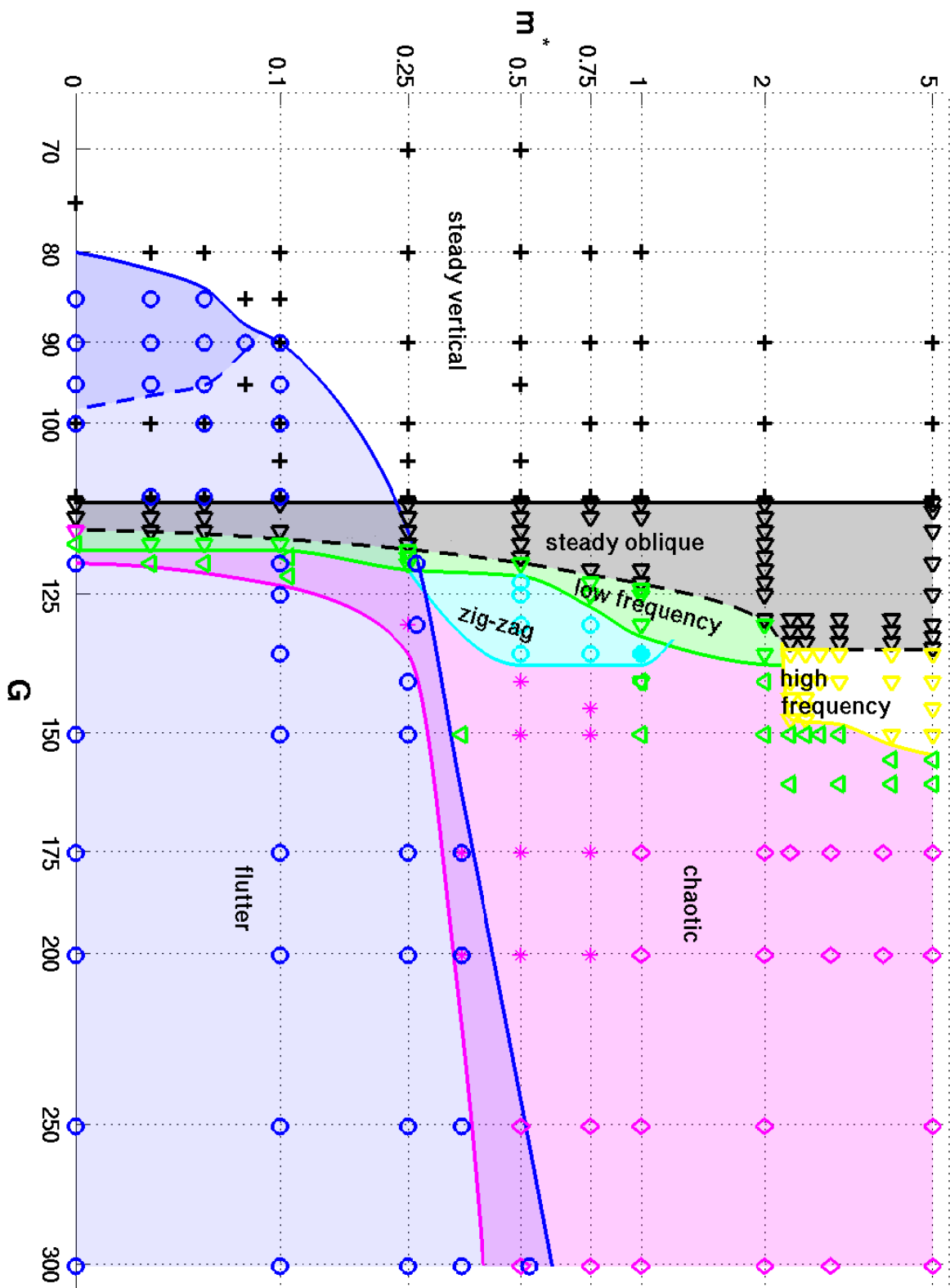


Figure 3.25: The state diagram for spheroids of $\chi = 1.1$.

3.3.9 Conclusion

The investigation of the three-parameter space was conducted in parameter planes of constant aspect ratio. This choice is, of course, arbitrary and the parameter space might be swept differently depending on the application. E.g., for spheroids manufactured of the same material and investigated in the same fluid, a $\rho_s/\rho = \text{const}$ subset of parameters would be of interest. This surface does not correspond to any of the three parameters of our study taken as constant. (The non-dimensionalized mass involves the aspect ratio in its definition.) In spite of that, we hope that not only the investigation of individual $\chi = \text{const}$ planes was carried sufficiently into detail but that the spacing between the aspect ratios is not too coarse to prevent a potential user of our results from a reliable interpolation. Since our results might be of use for various benchmarking purposes, the generated time series will be made available in the form of matlab files.

The primary instability threshold can be represented as a function of two variables in the $\chi - m^*$ plane. We present this comprehensive information in Figure 3.26.

The scenario is strongly marked by subcritical effects making sometimes several totally different regimes co-exist for the same set of parameters. This opens the problem of receptivity in experimental application where noise is never absent. The numerical reproductivity of results might depend on the choice of initial conditions. The evolution from very thin to almost spherical spheroids involves an intriguing presence of a regular primary bifurcation not only for small aspect ratios when the body shape is close to that of a sphere but also for very flat spheroids provided their inertia is small enough. The two basic regimes of falling disks: the flutter and the tumbling remain of importance throughout the whole scenario. Especially the robustness of the tumbling, evidenced down to the aspect ratio of 2, is remarkable.

The investigation of the spheroid of aspect ratio 1.1 indicates the case of a perfect sphere cannot be obtained as a simple mathematical limit extrapolating the dynamics of spheroids. The behavior of the spheroid of aspect ratio 1.1 shows the existence of very significant oscillations of the body axis for ascending bodies of very low solid/fluid density ratio making almost spherical spheroids very different from perfect spheres. This might be a hint for the explanation of the zigzagging trajectories observed by Horowitz & Williamson (2010) that we failed to explain using the results of simulations of freely moving perfect spheres. In contrast, the agreement of simulations and experiments carried out with flat bodies is very satisfactory (see e.g. Chrust *et al.*, 2014). More broadly, an ideal spherical body is perhaps not an ideal prototype representing solid bodies of arbitrary shapes.

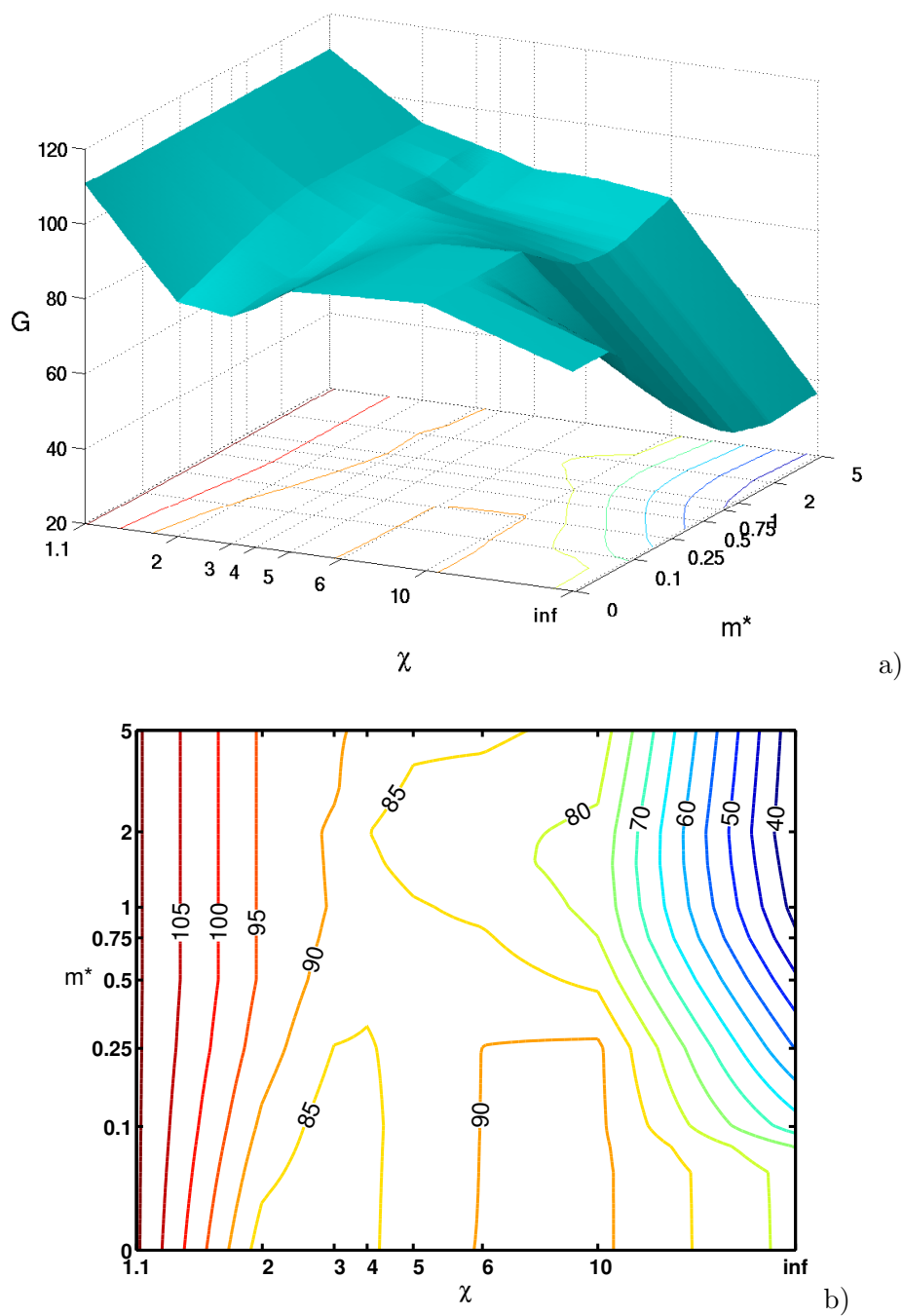


Figure 3.26: Critical Galileo number of the primary instability as a function of the aspect ratio and non-dimensionalized mass. a) 3D surface, b) iso-contours. The actual variables of the axes are $\xi = 1/(1 + \chi)$ and $\mu = \log_{10}(m^* + 0.05)$.

Chapter 4

Bubble rising in a quiescent liquid

4.1 Introduction

The knowledge of the behavior of a single bubble is fundamental for understanding bubble flows present in many practical applications. The collective effects in these flows can be strongly affected by path instabilities enhancing horizontal dispersion and flow turbulence. Though, in agreement with expectations, very small bubbles follow straight vertical trajectories, experimental observations evidenced either zigzagging or spiral trajectories (Lunde & Perkins, 1998; Brücker, 1999) of millimetric bubbles in water. The prediction of the onset of non straight trajectories and of their form was identified as a basic issue. Experimental observations encountered several difficulties due to the small size of bubbles and due to the effect of contamination of bubbles in water (Duineveld, 1995) on the bubble shape and on their motion. This, in its turn, motivated an effort to bring answers by numerical means.

The simplest mathematical description of a gas bubble in a liquid consists in ignoring the gas motion in the limit of zero density and viscosity (see e.g. Batchelor, 1967, ch. 4.9) by considering it as a constant volume enclosed by a variable free surface. In this approximation, the mathematical problem depends only on two independent parameters. In this chapter we choose the Galileo number $Ga = \sqrt{gd^3}/\nu$ and the Bond number $Bo = \rho gd^2/\sigma$ where g stands for the gravity, d for the equivalent diameter, ν and ρ the kinematic viscosity and the density of the fluid and σ for the surface tension.

Many experimentally observed regimes were at too high Galileo numbers to provide information on the instability onset (at $Ga = 390$ and $Bo = 0.85$ in Ellingsen & Risso (2001) and for $Ga > 500$ in Veldhuis *et al.* (2008)). Only relatively few observations provide data allowing the estimation of the likely loss of stability of straight vertical trajectories. Oscillating trajectories of bubbles in pure water were observed starting from the size given by equivalent radius of 0.81 mm, which corresponds to $Ga = 200$ and $Bo = 0.35$, by de Vries *et al.* (2002a). Zenit & Magnaudet (2008) and Zenit & Magnaudet (2009) (using silicon oil) have evidenced an onset of zigzagging trajectory between regimes given by $Bo = 2, Ga = 150$ and $Bo = 2.5, Ga = 176$ in the first cited paper and between $Bo = 3.2, Ga = 85$ and $Bo = 3.9, Ga = 99$ in the second one.

Facing the numerical difficulties, much numerical work tried to introduce simplifications

to bring the problem within the scope of available numerical tools. The experimental observation of relatively invariable ellipsoidal shapes by Ellingsen & Risso (2001) (bubbles in water, $Ga = 390$, $Bo = 0.8$) led to a series of numerical investigations (Mougin & Magnaudet, 2002a; Magnaudet & Mougin, 2007a; Tchoufag *et al.*, 2013) of free or fixed bubbles having a fixed ellipsoidal shape, the aspect ratio χ of which replaced the role of the Bond number in the parametric study. The common feature of the obtained results consists in predicting a minimal aspect ratio $\chi > 2.2$ for the instability to be possible at all. Fully three-dimensional simulations involving a dynamically varying 3D bubble shape are within the possibilities of present day methods, namely involving immersed boundary and level set methods (see e.g. Koebe *et al.*, 2003; Gaudlitz & Adams, 2009). This type of simulation remained, however, until recently, too costly for parametric studies and the work was mostly presented rather as numerical achievement than serious physical investigation (see also Tuković & Jasak, 2012).

An interesting compromise was recently considered by Cano-Lozano *et al.* (2013) who used fixed but realistic shapes of axisymmetric bubbles to predict a marginal stability curve of their vertical paths assuming that they behave as undeformable objects at the onset of instability. This assumption might still be unrealistic since the only force opposed to the deformation is the surface tension allowing a high flexibility of the free surface and rich dynamics including surface waves. Nevertheless, the obtained results show that an instability exists down to a Bond number of 0.2 when, at the obtained onset, the bubble aspect ratio is only 1.5. A parametric study of the behavior of fully three-dimensional bubbles was recently published by Tripathi *et al.* (2015). The used VOF method allowed them to account even for the bubble breakup at highly supercritical regimes. At the onset of non axisymmetry, two regimes - the already well documented, zigzagging one and a new steady one reported to appear at $Bo > 40$ - have been evidenced. The focus of the paper being set on spectacular cases of bubble breakup at very high Bond numbers (up to 500) there are only a few of points close to the separation line between the vertical and oscillatory regime, corresponding to experimental observations (called II). An accurate investigation of the very onset of instability is thus still missing.

In this chapter, we mainly concentrate on the linear analysis of stability of steady vertical trajectories of bubbles, similarly as Cano-Lozano *et al.* (2013) have done, but without the restrictive assumption of fixed bubble shape. I.e. the degrees of freedom of the deformable bubble surface are allowed to participate in the loss of axisymmetry and in the loss of steadiness of the flow. In the case of free sphere (Jenny *et al.*, 2003), the additional degrees of freedom due to the sphere free motion changed the threshold of the primary bifurcation but not very significantly because the arising non-axisymmetric state was steady. For the bubble, the linear analysis confirms the expectations that the instability is due to a Hopf bifurcation triggering oscillations in the whole investigated range of Bond numbers. It appears, however, that the instability is accompanied with a deformation of the axisymmetric form of the bubble and that the latter is far from behaving like a rigid body. As remarked in the conclusion, the results are to be understood as a lower bound for the critical Galileo numbers at which easily observable oscillations are to be expected.

4.2 Mathematical formulation and numerical method

Unlike for previous chapters, the problem of the rising bubble required a significant effort of algorithmic development. This was due to the expected dynamically varying three-dimensional shape of the bubble and by the necessity to account for the stress boundary condition at the bubble surface. Neither of these features could be directly accommodated in the existing versions of the numerical code mentioned in previous chapters. For this reason, we initially considered the possibility of using another existing code. A finite volume and a finite element code were taken under consideration, however, none of them provided readily available accurate treatment of the free surface. Moreover, similarly as in the case of the sphere and spheroids, the expected three-dimensionality is the result of axisymmetry breaking of an originally axisymmetric flow so that the use of the spectral azimuthal decomposition remains indicated as the most efficient approach. As a result, an adaptation of the spectral – spectral-element code was undertaken. The description of the technical details does not fit the result oriented scheme of the previous chapters. For this reason, it has been relegated to the appendix (Appendix 6.1 and 6.2). It will serve as reference for future work consisting in further optimization of the new code and its exploiting above the primary instability threshold, which is the main topic of the present chapter.

4.2.1 Governing equations

Taking the bubble as a void of constant volume V , we solve the flow only in the liquid phase. Newtonian liquid of density ρ and kinematic viscosity ν delimited by a free surface with constant surface tension σ is considered. The flow in the liquid obeys the usual set of incompressible Navier-Stokes equations. For the purpose of numerical simulations, the latter will be non-dimensionalized using the equivalent diameter d ($V = \pi d^3/6$) as length scale, the gravitational acceleration to define the velocity scale as $U_g = \sqrt{gd}$ and the density ρ to define the pressure scale ρU_g^2 . The non-dimensionalized Navier-Stokes equations are written in the frame translated with the velocity \mathbf{u}_b of the bubble center while the velocity field is expressed in a fixed frame. This results in equations

$$\frac{\partial \mathbf{v}}{\partial t} + [(\mathbf{v} - \mathbf{u}) \cdot \nabla] \mathbf{v} + \nabla p - \nabla \cdot \left(\frac{2}{Ga} \boldsymbol{\tau} \right) = 0 \quad (4.1)$$

and

$$\nabla \cdot \mathbf{v} = 0 \quad (4.2)$$

where \mathbf{v} stands for the flow velocity, $\boldsymbol{\tau} = 1/2 (\nabla \mathbf{v} + \nabla \mathbf{v}^T)$ for the strain rate tensor, p for the dynamic pressure and the Galileo number Ga has been introduced in Sec. 3.1. \mathbf{u} is the mesh velocity with respect to the fixed frame composed of the translation velocity of the bubble center \mathbf{u}_b and the velocity field of the mesh deformation \mathbf{u}_{def} ($\mathbf{u} = \mathbf{u}_b + \mathbf{u}_{def}$). The non-dimensionalized form of the dynamic boundary condition at the bubble surface S_b can be written as

$$-p \mathbf{n} + \frac{2}{Ga} \boldsymbol{\tau} \cdot \mathbf{n} - \frac{1}{Bo} \kappa \mathbf{n} = -(p_b - z) \mathbf{n} \quad (4.3)$$

with \mathbf{n} the unit normal vector (pointing inside the bubble), p_b the pressure inside the bubble due to surface tension and bubble motion and z the vertical Cartesian coordinate along a

downward pointing axis. This term appears after extraction of the hydrostatic pressure in Eq. (4.1). The pressure component proportional to $-z$ clearly drives the bubble motion. κ stands for the curvature and the Bond number Bo was also introduced in Sec. 3.1. The kinematic equation at the bubble surface consists in propagating the bubble surface along its normal with velocity equal to the normal projection of the velocity field:

$$\frac{\partial \mathbf{x}_b}{\partial t} = [(\mathbf{v} - \mathbf{u}_b) \cdot \mathbf{n}] \mathbf{n}. \quad (4.4)$$

The bubble incompressibility is equivalent to the zero volume flux through the bubble surface

$$\int_{S_b} \mathbf{v} \cdot \mathbf{n} dS = 0. \quad (4.5)$$

Finally, the bubble velocity \mathbf{u}_b is given by the requirement that the velocity of the geometrical center of the bubble surface propagated according to Eq. (4.4) be zero:

$$\int_{S_b} [(\mathbf{v} - \mathbf{u}_b) \cdot \mathbf{n}] \mathbf{n} dS = 0. \quad (4.6)$$

4.2.2 Numerical method

Eqs. (4.1) through (4.6) are solved in a vertically oriented cylindrical domain with a Cartesian frame $Oxyz$, the origin O of which coincides with the bubble center similarly as depicted in Jenny & Dušek (2004) (see also Figure 6.1 in Appendix 6.2). The points at the bubble surface keep their polar and azimuthal angles ψ, θ they had initially when the bubble shape was spherical. This yields a parametrization $\mathbf{x} = \mathbf{x}(\psi, \theta) \equiv \mathbf{x}(\xi)$ ($\xi = \xi_1, \xi_2 \equiv \psi, \theta$). The differentiation of the parametrization yields tangent vectors $\mathbf{x}_\psi, \mathbf{x}_\theta$, the normal vector $\mathbf{N} = \mathbf{x}_\psi \times \mathbf{x}_\theta$, the covariant metric tensor $g_{\alpha,\beta} = \mathbf{x}_\alpha \cdot \mathbf{x}_\beta$, ($\alpha, \beta = 1, 2$) and the surface element $dS = \sqrt{g} d\cos(\psi)d\theta$ where $g = \det\{g_{\alpha,\beta}\}$. The normalized normal vector (pointing inside the bubble) in Eqs. (6.28) and (4.4) is obtained as $\mathbf{n} = -\mathbf{N}/\sqrt{g}$. For the curvature we use the formula:

$$\kappa \mathbf{n} = \frac{1}{\sqrt{g}} \sum_{\alpha,\beta} \frac{\partial}{\partial \xi^\alpha} \left(\sqrt{g} g^{\alpha,\beta} \frac{\partial \mathbf{x}}{\partial \xi^\beta} \right). \quad (4.7)$$

with $g^{\alpha,\beta}$ standing for the contravariant metric tensor. To keep the bubble at the origin of the computational domain, we require that $\int_{S_b} [(\mathbf{v} - \mathbf{u}_b) \cdot \mathbf{n}] \mathbf{n} dS = 0$, which provides the bubble velocity \mathbf{u}_b . The boundary conditions at the outer domain boundary intended to simulate an unconfined quiescent fluid consist in setting a zero flow velocity at the upper (upstream) cylinder basis and at the lateral boundary and in a zero stress outflow boundary condition at the bottom (downstream) cylinder basis.

The spatial discretization follows the lines described by Ghidersa & Dušek (2000) who showed that the azimuthal Fourier decomposition is an optimal choice of extending an axisymmetric discretization to represent a 3D flow appearing at the onset of axisymmetry-breaking. The axial-radial plane is broken up into spectral elements (Patera, 1984). The configuration of the deformable bubble requires to account for a non-axisymmetric and moving boundary. This is done in physical space (i.e. on a 3D mesh after summing the azimuthal

modes) by an ALE approach consisting in propagating the bubble deformation within a sphere of radius R_s (chosen as $R_s = d$) by a linear interpolation. The transformation $\mathbf{x}(R, \psi, \theta)$ between the axisymmetric spherical mesh and the deformed one is also decomposed using the combination of azimuthal Fourier and spectral element decompositions. The principle of the deformation of the radial-axial mesh is illustrated in Figure 4.1. For a 3D bubble, the mesh deformation represented on the right of Figure 4.1 varies in the azimuthal direction. All discretized variables are stored in the form of azimuthal modes parametrized on the undeformed mesh. Inside the deformed spherical sub-domain, the parametrization is equivalent to that of spherical coordinates R, ψ, θ where R is the distance from the origin in the undeformed mesh $R = \sqrt{r^2 + z^2}$ where r and z are the radial and axial coordinates. A scalar variable $f(R, \psi, \theta)$ is represented as

$$f(R, \psi, \theta) = \sum_{m=-M}^M f_m(R, \psi) e^{-im\theta}, \quad (4.8)$$

the truncation M being one of the numerical parameters of the method. Horizontal projections of vectorial variables are treated as complex numbers in the complex plane spanned by the horizontal axes and are stored as coefficients of expansion:

$$v_+ = v_x + i v_y = e^{i\theta} \sum_{m=-M}^M v_{+,m}(R, \psi) e^{-im\theta}. \quad (4.9)$$

The degree of non-orthogonality is measured by the smallest sine of angle of coordinate lines. In Figure 4.1 this value is 0.88 and it remains larger than 0.7 even for the most deformed shapes (at $Bo = 20$). This is achieved by keeping a uniform discretization in the polar direction when the bubble deforms. (I.e., denoting s the arc-length of the meridian of the average axisymmetric bubble, we require that $ds/d\psi$ remains independent of ψ .) It can be concluded that the non-orthogonality of the mesh deformation does not reduce the numerical accuracy.

The time-discretization is based on the time-splitting approach (see also Patera, 1984) yielding a globally only first order accuracy with an error proportional to $\Delta t/G$. In spite of that, combined with a third order explicit (Adams-Bashforth) treatment of advective terms setting a considerable restriction on the time step, the time-splitting method proved to provide a very satisfactory accuracy (see Uhlmann & Dušek, 2014) in the past. The underlying idea of the time-splitting formulation consists in assuming that viscous effects are small as compared to the pressure ones. This assumption amounts to splitting the boundary condition (4.3) into a Dirichlet pressure boundary condition neglecting the viscous stress and a Neumann boundary condition for the viscous stress when solving for velocity. An essential ingredient is an implicit treatment of the curvature allowing us to obtain numerical stability by letting the surface waves to decay. The deformable bubble boundary requires, especially for small Bond numbers leading to very stiff dynamics, an additional time-step restriction.

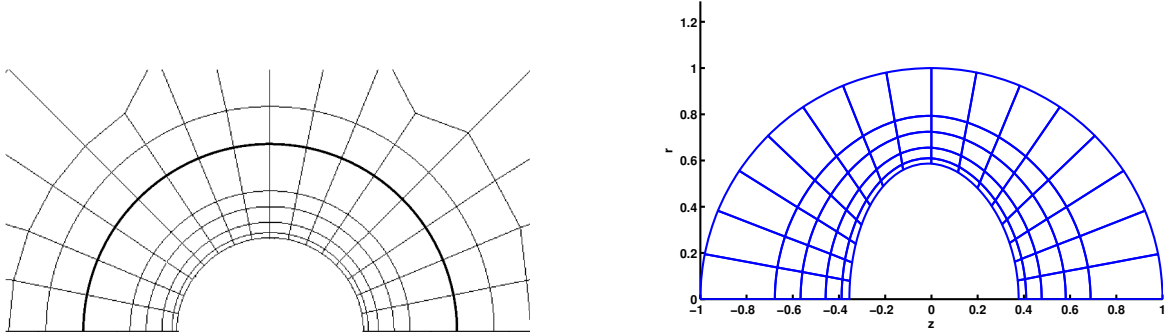


Figure 4.1: Left: undeformed spectral element mesh (mesh0), right: 2D mesh deformation around an axisymmetric bubble at $Ga = 100$ and $Bo = 1$.

4.3 Numerical validation

The numerical implementation has many numerical parameters. By taking up the same domain extent as in previous work we rely upon the tests carried out by Chrust (2012) and Kotouč (2008). It appears that, actually, the size of domain could even be reduced because the free surface generates much less vorticity than solid bodies. Next, the decomposition of the axial-radial plane of the mesh0 was also thoroughly tested in previous work. Given the fact that curvature plays a central role in dynamics of the free surface we, nonetheless, test the effect of mesh refinement at the bubble equator where the curvature is the largest and varies the most rapidly. We also test the effect of internal refinement of elements by increasing the number of collocation points of the spectral element discretization to track possibly insufficient spatial resolution of the bubble surface. The spatial discretization depends also on the truncation of the azimuthal Fourier expansion. However, the present work focuses essentially on linear analysis for which only modes 0 and 1 are sufficient. The time discretization is tested by varying the time step. Finally, the comparison with available axisymmetric data by Cano-Lozano *et al.* (2013) is presented.

4.3.1 Mesh refinement

The effect of mesh refinement was tested in two ways. A global mesh refinement is easily obtained by increasing the number of collocation points. We considered 6, 8 and 10 collocation points per spatial direction of spectral elements. The relative difference of amplitudes was less than 0.001 on a time interval of 7 periods (for a test at $Bo = 1$ and $Ga = 100$). Such a difference corresponds to an error of less than 10^{-4} in the determination of the growth rate. The observed variation of the growth rate as a function of Galileo number being $d\gamma/dGa = 0.011$ at $Bo = 1$, an increase of the number of collocation points cannot improve the obtained critical Galileo numbers by more than 10^{-3} . Three different meshes locally refined at the bubble surface, with 16, 20 and 30 elements (96, 120 and 180 collocation points)

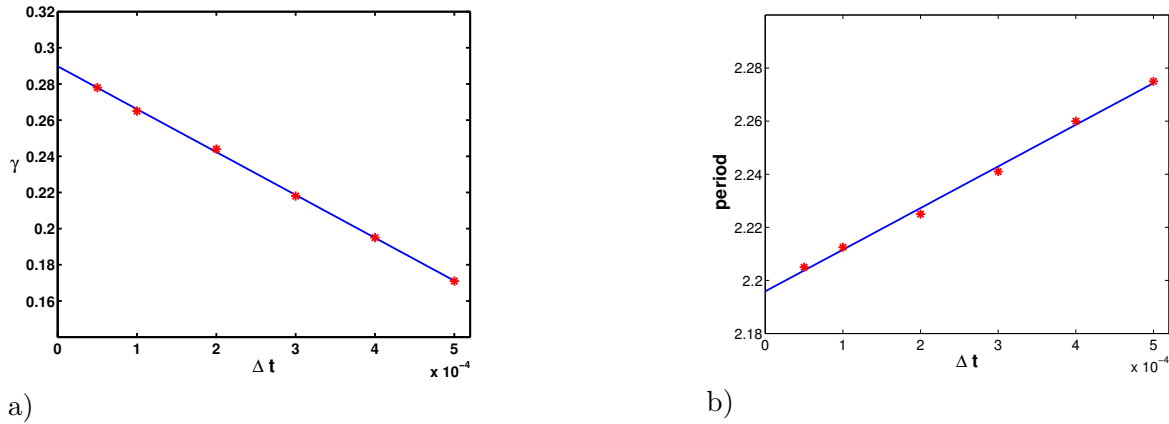


Figure 4.2: a): Amplification rate, b): period as a function of the time step for $Bo = 1$ and $Ga = 110$. (Solid line: linear regression)

along the bubble surface, were also developed and their effect on the instability investigated. The meshes are referred to as mesh0, mesh1 and mesh2, respectively. Their total number of spectral elements is 245, 277 and 387. We found a 5×10^{-4} difference of amplification rate between mesh0 and mesh1 at $Bo = 1, Ga = 100$ and 3×10^{-4} difference between mesh1 and mesh2 at $Bo = 10, Ga = 120$, where we expected the effect of spatial resolution to be more significant due to the sharp peak of curvature arising along the bubble equator. In conclusion, the spatial resolution is sufficient in order not to influence the results. For Bond numbers smaller or equal to 1, mesh0 was used, for Bo larger or equal to 2 we preferred mesh1 to capture the curvature in reliable manner. At least one simulation for each Bond number was also checked on mesh2.

4.3.2 Time step

In contrast with the spatial discretization, the time step dependence appeared to be non-negligible. The time step convergence of the amplification rate and of the period of oscillation of the perturbation is clearly of first order as expected (see Figure 4.2) due to the first order accuracy of the time-splitting method. Figure 4.2 a) shows that a larger time-step leads to a smaller amplification rate, i.e. to an overestimation of the critical Galileo number. The very accurately linear dependence of amplification rates on the time step allowed us to eliminate this effect by extrapolating to $\Delta t = 0$ using systematically two different time steps. (The first results were obtained with some sufficiently small time-step and then they were improved using a halved step.)

4.3.3 Validation

The used code represents a relatively limited evolution of the code used extensively for exploring the path instabilities of disks and flat cylinders (Chrust *et al.*, 2013, 2014). This previous version was validated by comparison to results obtained by by Auguste (2010)

and Auguste *et al.* (2013) using a completely different code. A very similar version of the code was also validated by comparison with an IBM code (Uhlmann & Dušek, 2014). The most significant modifications consisted in implementing (i) a stress formulation (ii) the dynamic boundary condition (4.3) combined with the three-dimensional deformation of the spherical subdomain. The validation of the stress formulation is easily obtained by checking that it does not modify the results for solid bodies. As for the point (ii), there is no difference in the treatment of axisymmetric and non-axisymmetric bubbles. The whole code is written with an arbitrary truncation of the azimuthal Fourier expansions (4.8) and (4.9). The mesh deformation is implemented in the physical space in which there is technically no difference between an axisymmetric and non-axisymmetric solution. The truncation of the azimuthal expansion, hence the number of discretization points in the azimuthal direction of the physical space, is variable and the (absence of) effect of its variation was tested. In absence of comparable three-dimensional data, the axisymmetric results by Cano-Lozano *et al.* (2013) provide a good test.

The investigation of the marginal stability curve leads us to focus on regimes close to $Ga = 100$. There is a graphic table of axisymmetric bubble shapes in Figure 3 of the paper by Cano-Lozano *et al.* (2013) mentioning the aspect ratios at different Bond and Galileo numbers. We superimposed the shapes of the second line of their Figure with our bubble shapes in Figure 4.3. The agreement is very good but it might be objected that the resolution of the shapes reproduced from Cano-Lozano *et al.* (2013) is insufficient. Table 4.1 reproducing the available quantitative data is more convincing. A special attention should be paid to the excellent agreement of the upstream and downstream curvatures, showing that the computed shapes are very accurately identical. (The only possible objection might concern a lack of agreement between the aspect ratios at $Bo = 20$. At this Bond number, the aspect ratio, defined as the ratio of the diameter of the horizontal projection and of the length measured along the symmetry axis, becomes large because of the upstream dimple. The very good agreement in the upstream curvature shows that very likely the actual shapes are the same.) The agreement of our data and of the axisymmetric data obtained by a totally different code (Gerris - based on the VOF method) confirms the soundness of the treatment of the deformable bubble surface. The only new feature is that this treatment is not limited to axisymmetry.

4.4 Linearly unstable mode

In this chapter we focus on the linear regime and the linear perturbation mode. It is one of the advantages of the spectral azimuthal expansion to enable such an investigation in an efficient manner. On the other hand, the development of the code has not yet advanced sufficiently to allow for a large scale investigation of the non-linear phenomena.

Limiting the description of the results to the bubble shape, let us express the shape of the bubble as a sum of axisymmetric shape $\mathbf{x}_{b,axi}$ and of a linear perturbation \mathbf{x}'_b as $\mathbf{x}_b = \mathbf{x}_{b,axi} + \mathbf{x}'_b$. (The velocity and pressure fields decompose in the same way.) In Ghidersa & Dušek (2000) it is shown that axisymmetry breaking can occur potentially in any azimuthal subspace $m > 0$. Though the expected zigzagging trajectory indicates that the most unstable

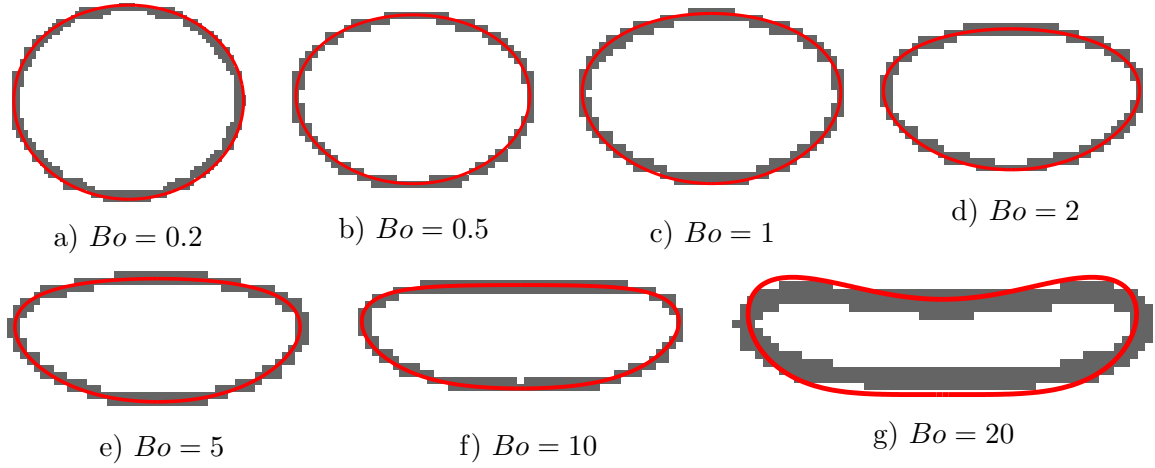


Figure 4.3: Computed axisymmetric shapes at $Ga = 100$ and at Bond numbers indicated in the figure (red lines) compared to shapes of Fig. 3 Cano-Lozano *et al.* (2013) (gray).

Bo	0.1	0.2	0.5	1	2	5	10	20
AR	1.11	1.20	1.39	1.60	1.88	2.43	3.20	6.15
	<i>1.09</i>	<i>1.19</i>	<i>1.38</i>	<i>1.59</i>	<i>1.86</i>	<i>2.40</i>	<i>3.19</i>	<i>5.22</i>
u_z	2.80	2.55	2.11	1.73	1.42	1.09	0.90	0.72
	<i>2.64</i>	<i>2.51</i>	<i>2.03</i>	<i>1.74</i>	<i>1.42</i>	<i>1.09</i>	<i>0.92</i>	<i>0.74</i>
κ_{front}	0.86	0.76	0.61	0.46	0.32	0.16	0.03	-0.29
	<i>0.86</i>	<i>0.76</i>	<i>0.60</i>	<i>0.46</i>	<i>0.33</i>	<i>0.16</i>	<i>0.03</i>	<i>-0.27</i>
κ_{back}	0.90	0.84	0.74	0.65	0.56	0.39	0.19	0.01
	<i>0.94</i>	<i>0.84</i>	<i>0.74</i>	<i>0.65</i>	<i>0.55</i>	<i>0.38</i>	<i>0.17</i>	<i>-0.01</i>

Table 4.1: Comparison of our axisymmetric data (upper lines) with those by Cano-Lozano *et al.* (2013) (lower lines in italics) at $Ga = 100$.

is the $m = 1$ space we did not truncate our decomposition to $M = 1$ and investigated the amplification of modes $m \leq 7$ at $Bo = 1$. In agreement with expectation, the instability arises in the $m = 1$ subspace. Due to the switching between the spectral and physical space implemented to account for a possible three-dimensional geometry, the $m > 0$ azimuthal modes are not exactly zero even if the solution is axisymmetric unlike it was the case in Ghidersa & Dušek (2000). As the result, the instability emerges naturally from numerical noise without any additional perturbation. It is easy to see that the $m = 1$ mode emerges as the first. Higher modes emerge only later, their amplitude is proportional to the m -th power of the amplitude of the linearly unstable mode and their amplification rates are multiples of the linear amplification rates which is typical for non-linear slave modes associated to the linear mode. As long as the linearly unstable mode remains small (we limit ourselves to amplitudes not exceeding 10^{-6}), the solution behaves like a superposition of the base flow (axisymmetric solution) and of a linear perturbation even if the coupling between different modes is not inhibited.

The linear perturbation is thus obtained directly as the $m = \pm 1$ terms of expansions (4.8) and (4.9) used for the spatial discretization, the $m = 0$ term standing for the axisymmetric solution.

$$\begin{aligned} z'_b &= \left(c_{z,1}(\psi, t) e^{-i\theta} + c.c. \right) \\ x'_{b,+} &= \left(c_{+,1}(\psi, t) e^{-i\theta} + c_{+,-1}(\psi, t) e^{i\theta} \right) e^{i\theta}. \end{aligned} \quad (4.10)$$

where $c.c.$ denotes the complex conjugate term. The horizontal projection of the shape deformation is expressed as $x'_+ = x' + iy'$ in the complex plane.

Unless non-linear effects set in, the two helical modes $c_{+,1}(\psi, t) e^{-i\theta}$ and $c_{+,-1}(\psi, t) e^{i\theta}$ can have arbitrary amplitudes. It appears that they arise with equal amplitudes which makes the trajectory planar and the solution to have a planar symmetry starting from the linear regime. Since this is the most widely observed form of bubble trajectories we shall limit the description of the linear mode to this case. The orientation of the symmetry plane is determined arbitrarily by initial conditions. Denoting α its angle of rotation w.r.t. xOz plane, it appears that the complex coefficients in Eqs. (4.10) can be expressed in terms of only two real functions a_z, a_+ .

$$c_{z,\pm} = a_z(\psi, t) e^{i\alpha}; \quad c_{+,\pm 1} = a_+(\psi, t) e^{\pm i\alpha}. \quad (4.11)$$

The time dependence is driven by the eigenvalues $\lambda_{\pm} = \gamma \pm i\omega$ characteristic for a Hopf bifurcation. They can be obtained, e.g., from the time series of horizontal velocities in the linear regime (see the left half of Figure 4.6 b) as their period $T = 2\pi/\omega$ and amplification rate γ . Integrating over an oscillation period:

$$C_{z,\pm}(\psi) = \frac{1}{T} \int_{t_0}^{t_0+T} a_z(\psi, t) e^{-\lambda_{\pm}(t-t_0)} dt, \quad (4.12)$$

$$C_{+,\pm}(\psi) = \frac{1}{T} \int_{t_0}^{t_0+T} a_+(\psi, t) e^{-\lambda_{\pm}(t-t_0)} dt, \quad (4.13)$$

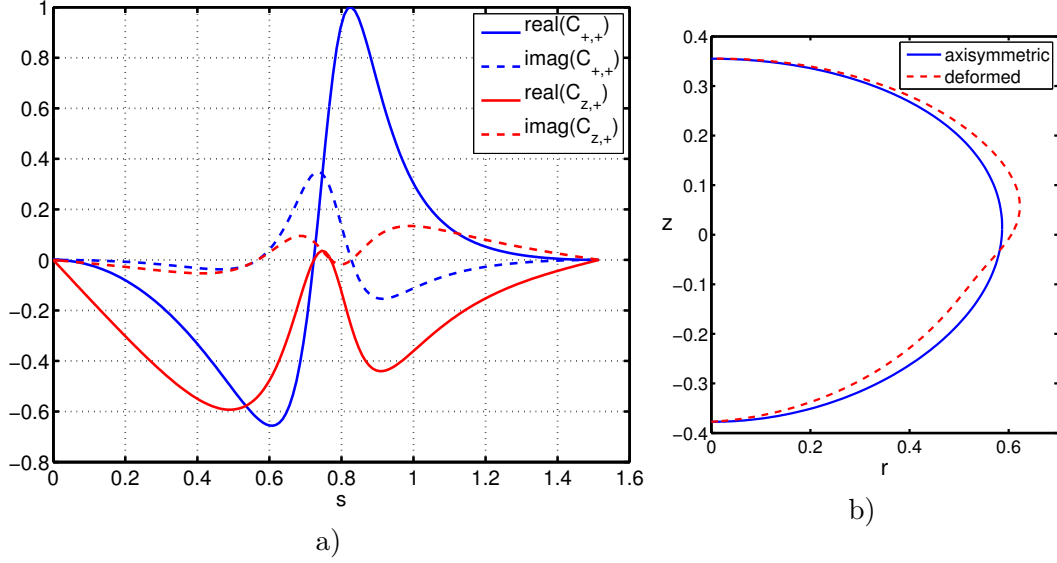


Figure 4.4: a): Linear mode of the shape perturbation expressed in terms of two complex coefficients (4.14) and (4.15) at $Bo = 1$ and $Ga = 100$, represented as functions of arc length of the axisymmetric shape illustrated by the solid blue line of figure b). (The z axis points upward, $s = 0$ corresponds to the bottom point.) The coefficients are normalized so that $C_{+,+} = 1$ at the maximum of its absolute value. The red dotted line in figure b) shows the effect of perturbation by 1% of the unstable mode of figure a).

we get the part of eigenfunctions describing the shape deformation. Replacing, further, $a_z = C_{z,+} e^{\lambda+t} + c.c$ and similarly for a_+ , in Eq. (4.11), we arrive at the expression of the shape perturbation in terms of unstable eigenfunctions in the form:

$$z'_b = 2C_{z,+}(\psi) \cos(\theta - \alpha) e^{\lambda+t} + c.c. \quad (4.14)$$

and

$$x'_{b,+} = \left[2C_{+,+}(\psi) \cos(\theta - \alpha) e^{\lambda+t} + c.c. \right] e^{i\theta} \quad (4.15)$$

The coefficients $C_{z,\pm}$ and $C_{+,\pm}$ are genuine complex functions expressing the fact that the bubble surface, as a soft object, does not oscillate in phase. To represent them independently of the (arbitrary) parametrization by ψ , we introduce the parameter s as the arc-length of the curve defining the axisymmetric shape, $ds = \sqrt{dz_{b,axi}^2 + dr_{b,axi}^2}$, measured from the rear (bottom) intersection with symmetry axis. The resulting functions are represented in Figure 4.4. To illustrate the effect on the bubble shape, we represent the superposition of the axisymmetric shape and $0.01 \times$ the perturbation (4.14) and (4.15) in the trajectory plane ($\theta = \alpha$) and at $t = 0$ (i.e. the moment corresponding to the phase for which the Figure 4.4 a) is represented). The red dotted line in Figure 4.4 b) shows that the instability yields a horizontal shear at the equator. This shear is obviously related to the fact that the vertical

velocity component $C_{z,+}$ is almost zero at the equator while, if the bubble oscillated without deformation, there should be a maximum of amplitude.

4.5 Marginal stability curve

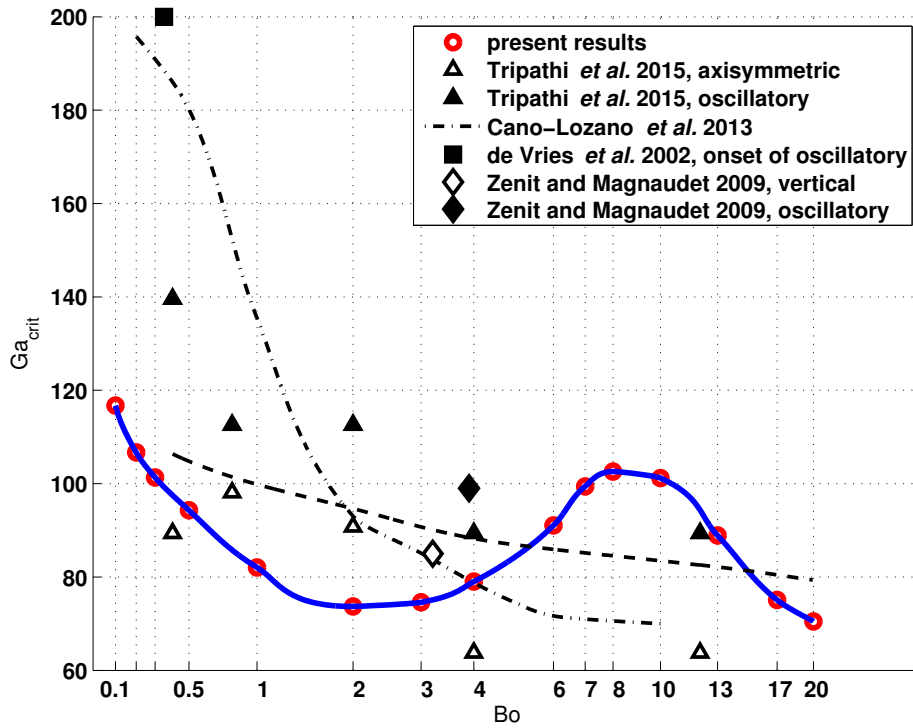
In previous work (e.g. Mougin & Magnaudet, 2002a; Tchoufag *et al.*, 2013; Cano-Lozano *et al.*, 2013) the thresholds of path instabilities of rising bubbles were estimated under the assumption of various but un-deformable shapes. It is not surprising to find different instability thresholds if the shape deformation is accounted for. In Figure 4.5 we represent the threshold of the zigzagging motion in the Bond – Galileo number parameter plane obtained by the linear stability analysis described above in the interval of Bond numbers going from 0.1 to 20. In the same graph we reported the curve obtained by Cano-Lozano *et al.* (2013) and that drawn in the state diagram of Tripathi *et al.* (2015). We also reported the states actually simulated by Tripathi *et al.* (2015) situated close to our marginal stability curve. Three experimental results are also represented.

For $Bo > 1$ there is a qualitative agreement between all results including the experimental data by Zenit & Magnaudet (2009). For small Bond numbers, the marginal stability curve of Cano-Lozano *et al.* (2013) rises almost twice as high as our curve. However, the (approximately drawn) curve of Tripathi *et al.* (2015) follows relatively well the mean trend of our data. The data of Tripathi *et al.* (2015) seem to place the critical Galileo number between 80 and 100, close to $Bo = 4$ the experimental data by Zenit & Magnaudet (2009) let us conclude to a threshold at about 90. The most striking feature of the marginal stability curve we present in Figure 4.5 is its non monotonous trend. However, globally, our curve does not depart very far from $Ga = 100$. It reaches a minimal critical Galileo number of about 73 between $Bo = 2$ and 3. For higher Bond numbers the curve starts to rise and reaches a maximum of slightly more than $Ga = 100$ at $Bo = 8$ before dropping to less than 70 at $Bo = 20$.

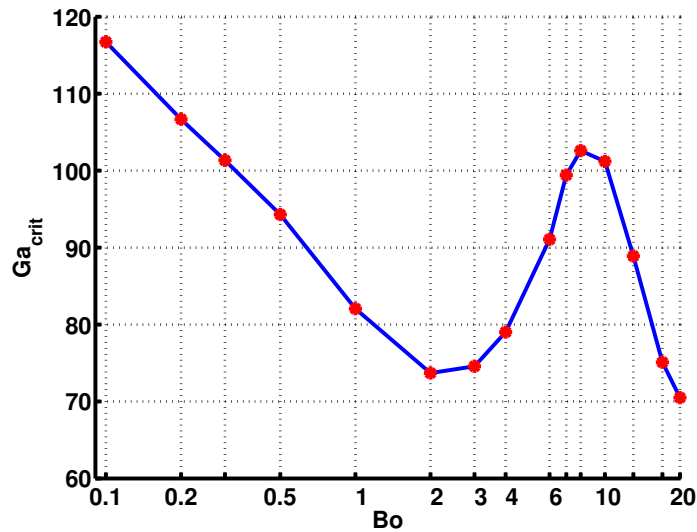
Exhaustive information on the bubble aspect ratio, terminal rising velocity, internal pressure, period of oscillation and maximal curvature is provided in Table 4.2.

4.6 Some preliminary non-linear results

As widely accepted, the instability leads to a planar zigzagging trajectory. This cannot be shown by linear analysis but the trajectory of a bubble reaching the saturation of the instability represented in Figure 4.6 does not depart from planarity and confirms this observation. Before the non-linear effects, leading to instability saturation, set in, the vertical velocity, the aspect ratio and the bubble pressure remain constant while the horizontal velocities and the non-axisymmetric perturbation of the bubble shape grow exponentially. The bubble shape deforms significantly when the instability saturates (see Figure 4.7). Though the investigation of saturated trajectories goes beyond the scope of this chapter, three conclusions can be drawn from Figure 4.7: i) the bubble remains essentially horizontal, ii) the shape significantly deforms at the equator, iii) the oscillation of the trajectory has a very small amplitude and is mainly to be put on account of the shape oscillation. All these features



a) horizontal scale: $\log(Bo + 2)$.



b) logarithmic scale of Bo

Figure 4.5: Critical Galileo number Ga_{crit} of the onset of linear instability as a function of the Bond number. Full blue lines: interpolation of results from Table 4.2, dashed line: reproduced from Tripathi *et al.* (2015).

Bo	Ga_{crit}	AR	u_z	p_b	T	κ_{max}
0.1	116.7	1.14	3.09	37.6	1.29	4.43
0.2	106.7	1.22	2.64	18.21	1.54	4.70
0.3	101.3	1.28	2.38	11.87	1.71	4.90
0.5	94.3	1.37	2.07	6.86	1.97	5.27
1.0	82.1	1.49	1.66	3.27	2.48	5.76
2.0	73.7	1.68	1.34	1.54	3.22	6.57
3.0	74.6	1.88	1.20	0.98	3.80	7.41
4.0	79.0	2.08	1.12	0.70	4.33	8.27
6.0	91.1	2.49	1.02	0.44	5.40	9.92
7.0	99.4	2.72	0.99	0.41	5.42	10.76
8.0	102.6	2.90	0.96	0.36	5.65	11.31
10	101.2	3.22	0.90	0.30	5.83	11.98
13	88.9	3.53	0.82	0.24	5.80	12.31
17	75.1	3.81	0.75	0.19	5.86	12.80
20	70.5	4.02	0.71	0.17	6.05	13.35

Table 4.2: Critical Galileo numbers Ga_{crit} and values of aspect ratio (AR), rising velocity u_z , bubble pressure p_b , period of oscillation T and maximum curvature κ_{max} at the onset of instability.

contradict the experimentally observed trajectories like those of Veldhuis *et al.* (2008) where very large oscillation amplitudes are reported, the bubble does not necessarily present shape oscillations (Figure 1 (a) of the cited paper) but significantly tilts. The regimes of these bubbles correspond, however, to Reynolds numbers of the order of 1000. At smaller Reynolds (Galileo) numbers, the experimentally observed amplitude is much smaller. Zenit & Magnaudet (2009) report amplitudes of only about two tenth of equivalent bubble diameter. As for the shape of axisymmetric bubbles there is a good agreement between the experimental observation of Zenit & Magnaudet (2008) and the numerical data but experimental 3D shapes are not available. The simulations of Tripathi *et al.* (2015) indicate strong 3D deformations, however, the figures are available only at high Galileo numbers. The link of the linear analysis with the experimentally observed trajectories may also be complicated by the existence of a weakly oscillating regime or by a subcritical nature of the primary bifurcation as it is the case for disks and thin cylinders.

4.7 Conclusions

In this chapter, we presented the marginal stability curve of the path instability of gas bubbles rising in a quiescent Newtonian liquid. The mathematical model makes a full abstraction of the dynamics of gas inside the bubble but the bubble surface is realistically modeled by standard free-surface boundary conditions and no limits are set to its deformation. The corresponding mathematical formulation is in agreement with what is considered as an ideal

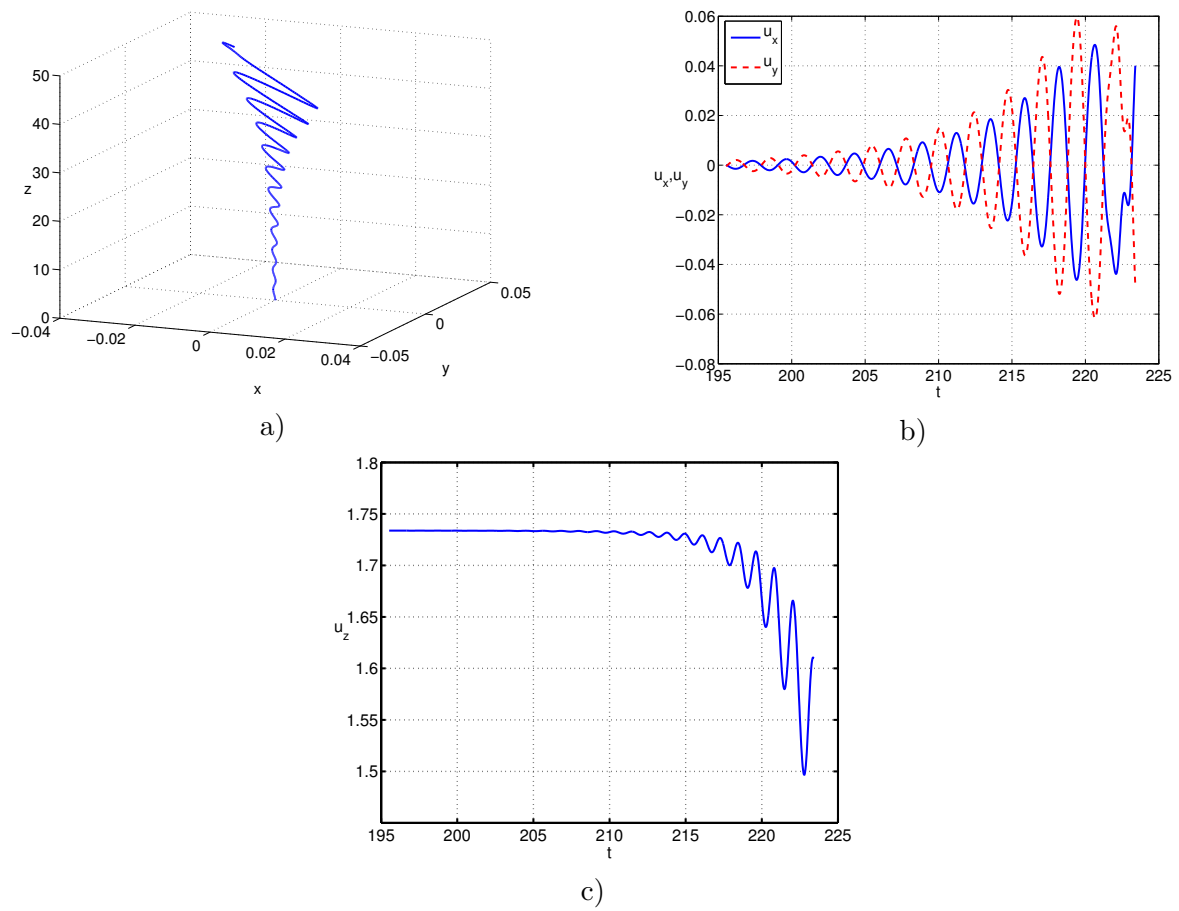


Figure 4.6: Saturating trajectory at $Bo = 1$ and $Ga = 100$. a) Trajectory. b) Horizontal velocity as a function of time. c) Vertical velocity.

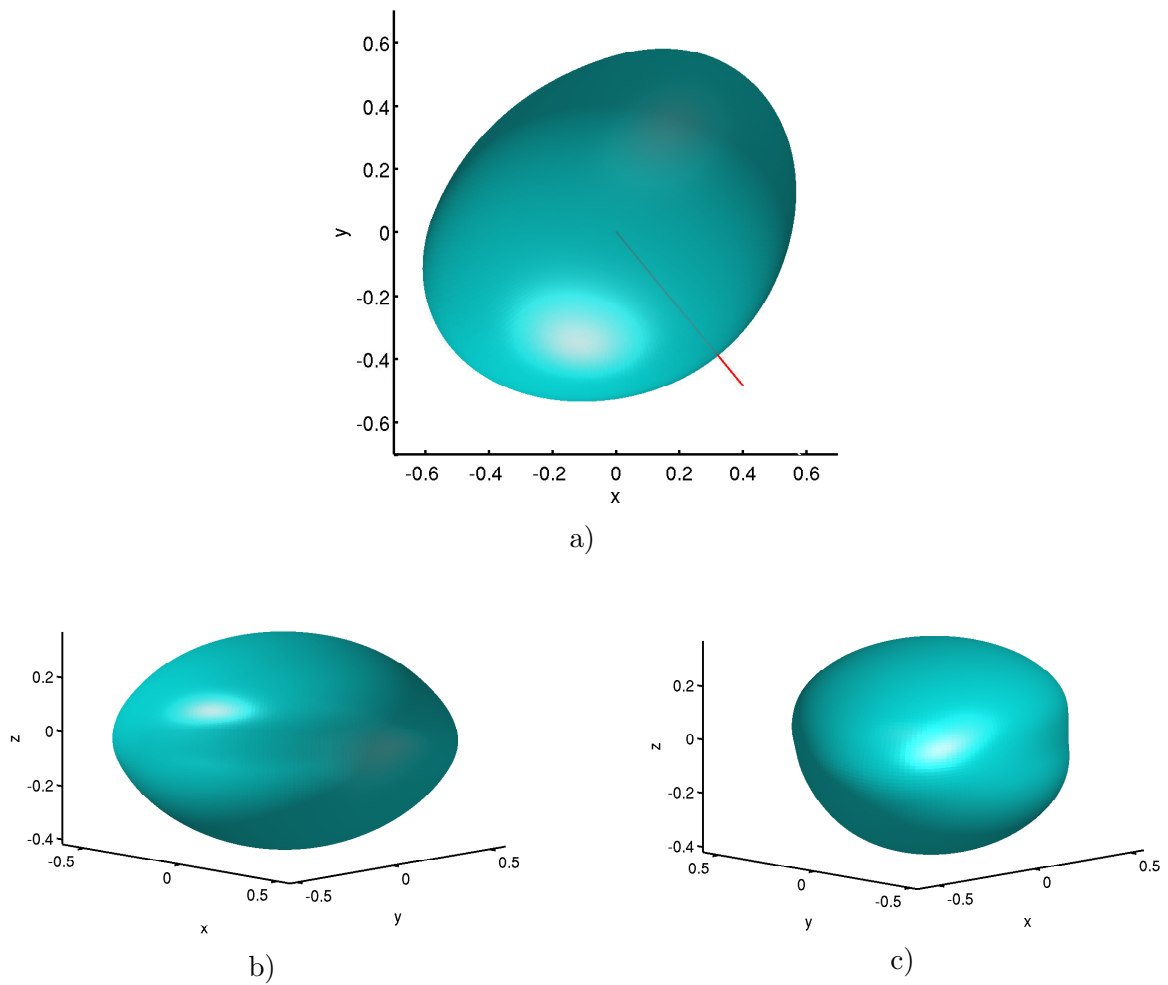


Figure 4.7: Deformed bubble in the (almost saturated) non-linear regime at $Bo = 1$ and $Ga = 100$. a) View from above. The horizontal drift direction is represented by the red (dark) line. b) Almost horizontal view along the trajectory plane. The bubble moves towards the reader. c) Almost horizontal view perpendicular to the trajectory plane. The bubble moves to the right.

bubble in the literature. The investigation is carried out in the Bond – Galileo number two-parameter plane and the obtained thresholds, guaranteed within less than one Galileo number unit, are results of a linear analysis. A relatively good agreement with recent comparable results by Tripathi *et al.* (2015) is obtained and, while the scope of investigation in the $Bo - Ga$ is much less ambitious, a significantly more accurate information on the instability onset is provided. Investigation of non-linear effects at Galileo numbers above the marginal stability curve of Figure 4.5 goes beyond the scope of the present work but, as shown in Figure 4.7, rises some questions concerning the most often reported observations at high Galileo number. A significant effort to simulate strongly non-linear regimes has to be developed in further work. If the supercritical nature of the Hopf bifurcation is confirmed, the present data may serve as a lower bound for Galileo numbers at which oscillating trajectories can be expected to appear. While not much of surprise is to be expected at Bond numbers smaller than 0.1 where the trend of the critical Galileo number is very clearly exponential if represented in a purely logarithmic scale, very large Bond numbers remain a numerical challenge because of the large bubble deformation. The presented linear analysis can, nonetheless be pushed to $Bo \sim 50$ without too much difficulty, however, the physical sense of such exploration becomes questionable because the dimple of the bubble deepens until reaching a toroidal shape. This not only sets a limit to the ALE method (though this stage can be circumvented by letting the surface tension progressively decrease starting from an already obtained asymptotic state) and may result in a bubble breakup well before reaching the asymptotic regime.

Chapter 5

Conclusions and perspectives

The understanding of the transition of motion of isolated bodies is essential for understanding multi particle flows. The present thesis studies the characteristics of various transition scenarios of freely moving bodies under the effect of gravity, buoyancy and hydrodynamic forces. The numerical results reveal the multiformity and beauty of motions of solid bodies of variable shapes and give some preliminary idea on the behavior of bubbles.

As a perfect body, sphere has a completely singular scenario compared to that of a disk and oblate spheroids. High and low frequency oblique oscillating regimes are identified as fluid modes and solid modes with dominant solid-fluid interaction. The separation between them is accurately identified and is shown to depend on both the density ratio and the Galileo number. For dense spheres, the transition to chaos is shown to be accompanied by an intriguing coexistence between planar and rotating oscillations which are evidenced just after spheres lose their steady oblique motion and oscillate with a high frequency. In contrast, oblique oscillating trajectories of light spheres become chaotic due to the increase of their amplitude of oscillations making them start to rise vertically for short moments. At these vertical stages, the trajectories end up by losing their planarity and become chaotic. The region of chaotic regimes is, however, not homogeneous. Several cases of “order in chaos” are evidenced. The most prominent are vertical periodic trajectories with fast oscillations. Several isolated perfect zigzagging and zigzagging – rotating trajectories mark the transition of light spheres. Very regular helical regimes are found for high Galileo numbers and very light spheres. The challenge of a quantitative characterization of the chaotic domain is raised by suggesting several possibilities of relevant statistical post-treatment of simulated data.

The significant difference between scenarios of a sphere and that of a disk motivates the study of freely moving oblate spheroids of intermediate aspect ratio. The attempt to provide a link is based on the variation of aspect ratios of spheroids from infinity to 1.1 which corresponds, respectively, to an infinitely thin (inhomogeneous) disk and an almost spherical body. Parameter planes for 8 aspect ratios are studied and results are presented in the form of 8 state diagrams. Impressive subcritical effects responsible for several regions of coexistence of very different regimes are evidenced. The most present regimes, known from previous work, are the “flutter” and the “tumbling” states. These states characteristic of a strong solid-fluid interaction are accompanied by a variety of less spectacular fluid modes,

which are equally important for the understanding of the scenario. A fascinating analogy of infinitesimal oscillations of vertical trajectories sustained only by numerical noise and fully non linear supercritical trajectory patterns indicate hint to the relevance of linear modes far above the primary instability thresholds. The correspondence and similarity between spheroids of aspect ratio $\chi = 1.1$ and spheres is far less satisfactory than that of flat spheroids and infinitely thin disks, which shows the specificity of perfectly spherical bodies.

The investigation of the marginal stability curve for a deformable gas bubble in this thesis provides the critical parameters of the onset of instability in the Bond - Galileo number two parameter plane. The results present a big discrepancy compared to older theory based on a prescribed ellipsoidal bubble shape, which is not surprising since bubbles always vary the shape. The bubble shape oscillates strongly in the stage of acceleration and very quickly settles to an asymptotic asymmetric shape which is far from ellipsoidal. A better agreement is obtained with theory assuming fixed realistic axisymmetric shapes. The remaining difference is to put on account of the shape variation accompanying the instability. A significant effort to simulate strongly non-linear regimes is still to be developed in further work.

The use of theoretically idealized results in understanding the real world is always interesting in spite of the fact that real situations are not always ideal. More complex situations make, however, the use of such results tricky. Suppose that, one day, a consensus establishes for precise critical values of the onset and loss for every certain regime of bodies of every different shape, will it be easy to predict multiphase flows under complicated disturbances of infinite variety of real world situations? Sometimes astounding predictions are formulated. Astrophysicists claim that if there had not been one more electron in one billion electron-positron pairs on Earth 10 billion years ago, we would not have been existed. The study of the transition of a single particle has certainly a less accurate link with large scale properties of multi particle flows but represents its cornerstone. It shows how fast the high regularity of space and time can be disturbed to lead to very complex local space-time behaviors.

Chapter 6

Appendix

6.1 Mathematical formulation of the problem of a rising bubble

6.1.1 Freely moving fluid inclusion

The bubble is a special case of fluid inclusion. Typically, a fluid inclusion is formed by a small amount of liquid immersed in another liquid with which it does not mix like a drop of oil in water, a bubble of gas in a liquid or a drop of liquid in a gas. The ambient fluid will be considered unconfined and quiescent except for the motion induced by the moving inclusion. For the purpose of numerical treatment the domain of ambient fluid will be finite but the so induced confinement will be checked to have no effect on the simulated dynamics. Our computational domain Ω is a vertical cylinder of height $L = L_{in} + L_{out}$ and radius R_c translated with the inclusion with its axis kept vertical (see figure 6.1). The boundary conditions at the cylinder surface simulates a quiescent fluid at the inflow cylinder basis and on lateral cylindrical surface and a no stress condition at the outflow. While the computational domain accompanies the motion of the inclusion, the flow velocity is defined with respect to a fixed frame. The domain Ω breaks up into the subdomains :

$$\Omega = \Omega_i \cup \Omega_e \quad (6.1)$$

the index i referring to the volume occupied by the inclusion and e to the external fluid. The interface $\partial\Omega_i$ is denoted S .

The following Navier Stokes equations hold within each subdomain ($j = 1, 2; \quad 1 \equiv i, 2 \equiv e$):

$$\nabla \cdot \mathbf{v} = 0 \quad (6.2)$$

$$\frac{\partial \mathbf{v}}{\partial t} + [(\mathbf{v} - \mathbf{u}) \cdot \nabla] \mathbf{v} + \nabla \frac{p}{\rho_j} - \nabla \cdot [(\mu_j / \rho_j) \boldsymbol{\tau}] = \mathbf{g} \quad (6.3)$$

the densities ρ_j and dynamic viscosities μ_j being considered constant both in time and space. The pressure includes the hydrostatic pressure of the external fluid $\nabla p_s = \rho_e \mathbf{g}$ which can be

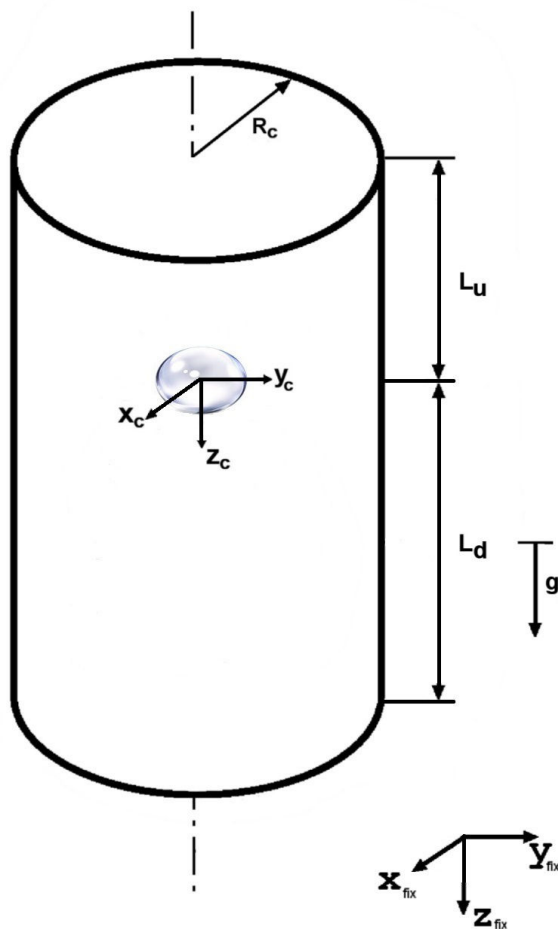


Figure 6.1: Computational domain represented for a rising bubble

extracted for a bubble. $\boldsymbol{\tau}$ stands for twice the strain rate tensor:

$$\boldsymbol{\tau} = \nabla \mathbf{v} + (\nabla \mathbf{v})^T \quad (6.4)$$

and \mathbf{u} is the velocity of the center of the inclusion. At the interface, the following conditions are satisfied:

$$\mathbf{v}_i = \mathbf{v}_e \quad \text{on } S \quad (6.5)$$

$$\boldsymbol{\sigma}_i \cdot \mathbf{n} = \boldsymbol{\sigma}_e \cdot \mathbf{n} - \eta \kappa \mathbf{n} \quad \text{on } S \quad (6.6)$$

where κ is the curvature of S , \mathbf{n} is the unit normal vector to S and $\boldsymbol{\sigma}_i$ stands for the stress tensor the Cartesian components of which are defined as

$$\sigma_{k,\ell} = -p\delta_{k,\ell} + \mu \left(\frac{\partial v_k}{\partial x_\ell} + \frac{\partial v_\ell}{\partial x_k} \right). \quad (6.7)$$

The interface moves with respect to the reference frame proportionally to the normal projection of the relative velocity

$$\frac{\partial \mathbf{x}_S}{\partial t} = [(\mathbf{v} - \mathbf{u}) \cdot \mathbf{n}] \mathbf{n}. \quad (6.8)$$

where \mathbf{x}_S denotes a position vector at the interface. The center of the inclusion will be required to coincide with the origin of the frame. For this reason, its relative velocity must be zero, which defines the constraint

$$\int_{S_b} [(\mathbf{v} - \mathbf{u}) \cdot \mathbf{n}] \mathbf{n} dS = 0 \quad (6.9)$$

allowing the computation of \mathbf{u} . The z axis of the local frame (O, x, y, z) is oriented opposite to the inclusion motion, i.e. downward for a rising bubble. As a consequence, the inflow cylinder basis has a negative coordinate $z = -L_u$, the outflow basis is defined by $z = L_d$ where L_u and L_d denote the upstream and downstream domain lengths ($L_u + L_d = L$). The following boundary conditions hold at the cylinder surface:

$$\mathbf{v}|_{z=-L_u, r=R} = 0 \quad (6.10)$$

$$(p + \boldsymbol{\tau} \cdot \mathbf{n})|_{z=L_d} = 0. \quad (6.11)$$

Extraction of hydrostatic pressure of the external domain

The hydrostatic pressure of the external liquid

$$p_s = \rho_e \mathbf{g} \cdot \mathbf{x} = \text{sign}(\rho_e - \rho_i) \rho_e g z \quad (6.12)$$

can be extracted by writing

$$p = \tilde{p} + \rho_e \mathbf{g} \cdot \mathbf{x}. \quad (6.13)$$

As a consequence $\nabla \frac{p}{\rho_e} = \nabla \frac{\tilde{p}}{\rho_e} + \mathbf{g}$, $\nabla \frac{p}{\rho_i} = \nabla \frac{\tilde{p}}{\rho_i} + \frac{\rho_e}{\rho_i} \mathbf{g}$ and equation (6.3) becomes

$$\frac{\partial \mathbf{v}}{\partial t} + [(\mathbf{v} - \mathbf{u}) \cdot \nabla] \mathbf{v} + \nabla \frac{\tilde{p}}{\rho_j} - \nabla \cdot ((\mu_j / \rho_j) \boldsymbol{\tau}) = \mathbf{g}_j \quad (6.14)$$

where

$$\mathbf{g}_e = 0; \quad \mathbf{g}_i = (1 - \rho_e / \rho_i) \mathbf{g} \quad (6.15)$$

In what follows, we focus on ascending inclusions and bubbles $\rho_e > \rho_i$. In this case we write the equations in the internal domain rather

$$\frac{\rho_i}{\rho_e} \left[\frac{\partial \mathbf{v}}{\partial t} + [(\mathbf{v} - \mathbf{u}) \cdot \nabla] \mathbf{v} \right] + \nabla \frac{\tilde{p}}{\rho_e} - \nabla \cdot [(\mu_i / \rho_e) \boldsymbol{\tau}] = -(1 - \rho_i / \rho_e) \mathbf{g}, \quad (6.16)$$

which makes it possible to take the limit $\rho_i / \rho_e \rightarrow 0$.

Nondimensionalized equations

The non-dimensionalization will be carried out with respect to the properties of the external fluid. The viscosity and density of the inclusion is then described by the ratios: μ_i/μ_e and ρ_i/ρ_e . The length scale is defined by the effective diameter of the inclusion

$$d = (6V_i/\pi)^{1/3} \quad (6.17)$$

equal to its diameter when at rest in the absence of gravity. The non-dimensionalized position vector is

$$\mathbf{x}^* = \mathbf{x}/d. \quad (6.18)$$

The ratio of apparent weight of the inclusion and of the mass of the displaced external fluid defines the acceleration scale: $|1 - \rho_i/\rho_e|g$. This yields the velocity scale $\sqrt{|1 - \rho_i/\rho_e|gd}$ used to non-dimensionalize of the velocity and pressure fields:

$$\mathbf{v}^* = \frac{\mathbf{v}}{\sqrt{|1 - \rho_i/\rho_e|gd}}. \quad (6.19)$$

$$p^* = \frac{\tilde{p}}{|\rho_e - \rho_i|gd} \quad (6.20)$$

If we omit the “*”, the non-dimensionalized equations write as follows. In the external sub-domain Ω_e :

$$\frac{\partial \mathbf{v}}{\partial t} + [(\mathbf{v} - \mathbf{u}) \cdot \nabla] \mathbf{v} + \nabla p - \nabla \cdot \left[\frac{1}{G} \boldsymbol{\tau} \right] = 0; \quad \text{on } \Omega_e \quad (6.21)$$

and inside the inclusion:

$$\frac{\rho_i}{\rho_e} \left[\frac{\partial \mathbf{v}}{\partial t} + [(\mathbf{v} - \mathbf{u}) \cdot \nabla] \mathbf{v} \right] - \nabla \cdot \left(\frac{\mu_i}{\mu_e} \frac{1}{G} \boldsymbol{\tau} \right) + \nabla p = -\mathbf{k}; \quad \text{on } \Omega_i. \quad (6.22)$$

Eq. (6.2) still holds everywhere. \mathbf{k} is the unit vector in the direction of the z -axis and G is the Galileo number

$$G = \frac{\sqrt{|1 - \rho_i/\rho_e|gd^3}}{\nu_e}. \quad (6.23)$$

The conditions at interface remain given by Eqs. (6.5,6.6,6.9) with the stress tensor given by Eq. (6.7) with ρ and μ replaced, respectively, by 1 and $1/G$ in the external sub-domain and by ρ_i/ρ_e and $\mu_i/(\mu_e G)$ inside the inclusion. The stress discontinuity condition (6.6) writes:

$$\boldsymbol{\sigma}_i \cdot \mathbf{n} = \boldsymbol{\sigma}_e \cdot \mathbf{n} - \frac{1}{Bo} \kappa \mathbf{n} \quad \text{on } S \quad (6.24)$$

where the modified Bond number is defined as

$$Bo = \frac{|\rho_e - \rho_i|gd^2}{\sigma} \quad (6.25)$$

and σ is the interfacial tension.

The problem of an inclusion depends on four physical parameters: G , Bo , ρ_i/ρ_e and μ_i/μ_e .

Case of a bubble

In the external domain, Eq. (6.21) holds as it is. For an air bubble, at normal conditions $\rho_i/\rho_e \approx 0.0013$ and $\mu_i/\mu_e \approx 0.018$. Eq. (6.22) then reduces, with a good approximation, to

$$\nabla p = -\mathbf{k}; \quad \Leftrightarrow \quad p = -z + p_b \quad (6.26)$$

where p_b is a uniform pressure inside the bubble due to capillarity and external dynamic pressure. The capillary pressure inside a spherical air bubble of 1 mm diameter in water represents less than 0.003 of normal atmospheric pressure so that the volume of the bubble remains very accurately constant for dynamic pressure variations. As a result, a gas bubble can be considered as a void of constant volume in a liquid. The constant volume can be expressed as the constraint of zero volume flux at the bubble surface S_b :

$$\int_{S_b} \mathbf{v} \cdot \mathbf{n} dS = 0. \quad (6.27)$$

The dynamic condition (6.24) at interface becomes a boundary condition:

$$-p\mathbf{n} + \frac{1}{G}\boldsymbol{\tau} \cdot \mathbf{n} - \frac{1}{Bo}\kappa\mathbf{n} = -(p_b - z)\mathbf{n}. \quad (6.28)$$

The Galileo and Bond numbers simplify to:

$$G = \frac{\sqrt{gd^3}}{\nu}; \quad Bo = \frac{\rho gd^2}{\sigma} \quad (6.29)$$

where ρ stands for the liquid density and σ for the surface tension and ν for the kinematic viscosity. Physically, the role of the bubble pressure p_b is to maintain the constant volume, mathematically it's a Lagrangian multiplier enabling the constraint (6.27). The bubble surface will be described by the position vector \mathbf{x}_b obeying the equation:

$$\frac{\partial \mathbf{x}_b}{\partial t} = [(\mathbf{v} - \mathbf{u}_b) \cdot \mathbf{n}] \mathbf{n} \quad (6.30)$$

where \mathbf{u}_b stands for the bubble velocity satisfying

$$\int_{S_b} [(\mathbf{v} - \mathbf{u}_b) \cdot \mathbf{n}] \mathbf{n} dS = 0. \quad (6.31)$$

6.1.2 Semi-discrete equations and weak formulation

In what follows, the case of the bubble will be considered. For a better readability, we assemble the system of equations to be solved. It is given by Eqs. (6.2,6.21) with boundary conditions (6.10,6.11) at the outer computational domain boundaries and the condition (6.28) at bubble surface. In addition, the equation of propagation of the bubble surface (6.30) with the incompressibility constraint (6.27) and with the condition defining the bubble velocity with respect to the fixed frame (6.31) are to be accounted for. This yields the following system of equations:

$$\frac{\partial \mathbf{v}}{\partial t} + [(\mathbf{v} - \mathbf{u}_b) \cdot \nabla] \mathbf{v} + \nabla p - \nabla \cdot \left[\frac{1}{G} \boldsymbol{\tau} \right] = 0; \quad (6.32)$$

$$\nabla \cdot \mathbf{v} = 0; \quad (6.33)$$

with outer boundary conditions

$$\mathbf{v}|_{z=-L_u, r=R} = 0, \quad (6.34)$$

$$p|_{z=L_d} = 0; \quad \boldsymbol{\tau} \cdot \mathbf{n}|_{z=L_{out}} = 0, \quad (6.35)$$

and constraints and boundary conditions at the bubble surface S_b :

$$\int_{S_b} \mathbf{v} \cdot \mathbf{n} dS = 0, \quad (6.36)$$

$$-p\mathbf{n} + \frac{1}{G} \boldsymbol{\tau} \cdot \mathbf{n} - \frac{1}{Bo} \kappa \mathbf{n} = -(p_b - z) \cdot \mathbf{n}, \quad (6.37)$$

$$\frac{\partial \mathbf{x}_b}{\partial t} = [(\mathbf{v} - \mathbf{u}_b) \cdot \mathbf{n}] \mathbf{n}, \quad (6.38)$$

$$\int_{S_b} [(\mathbf{v} - \mathbf{u}_b) \cdot \mathbf{n}] \mathbf{n} dS = 0. \quad (6.39)$$

The normal vector \mathbf{n} will be oriented outward of the computational domain according to the standard convention.

Considering the advective terms to be treated explicitly (the third order Adams-Bashforth extrapolation will be used), we choose the time discretization of Eqs. (6.32,6.33) written in the form:

$$\frac{\mathbf{v}^{(n+1)} - \mathbf{v}^{(n)}}{\Delta t} + [(\mathbf{v} - \mathbf{u}) \cdot \nabla] \mathbf{v}^{(n)} + \nabla p^{(n+1)} - \nabla \cdot \left(\frac{1}{G} \boldsymbol{\tau}^{(n+1)} \right) = 0 \quad (6.40)$$

$$\nabla \cdot \mathbf{v}^{(n+1)} = 0 \quad (6.41)$$

(n) denoting known values at the previous step and ($n + 1$) values to be computed at the current step.

In the weak formulation, the term $\nabla p^{(n+1)} - \nabla \cdot \left(\frac{1}{G} \boldsymbol{\tau}^{(n+1)} \right)$ yields:

$$\begin{aligned} & \int_{\Omega} \mathbf{w} [\nabla p^{(n+1)} - \nabla \cdot \left(\frac{1}{G} \boldsymbol{\tau}^{(n+1)} \right)] d\Omega = \\ & \int_{\Omega} \left[-(\nabla \cdot \mathbf{w}) p^{(n+1)} + \nabla \mathbf{w} \cdot \frac{1}{G} \boldsymbol{\tau}^{(n+1)} \right] + \int_{S_b} \mathbf{w} (p\mathbf{n} - \frac{1}{G} \boldsymbol{\tau}^{(n+1)} \cdot \mathbf{n}) dS \end{aligned} \quad (6.42)$$

where \mathbf{w} is a test vector field. The boundary condition (6.35) amounts to considering the surface term equal to zero at the outflow of the domain and the condition (6.37) at the bubble surface is accommodated by setting:

$$\int_{S_b} \mathbf{w} (p\mathbf{n} - \frac{1}{G} \boldsymbol{\tau}^{(n+1)} \cdot \mathbf{n}) dS = \int_{S_b} \mathbf{w} \cdot \mathbf{n} (p_b^{(n+1)} - z - \frac{1}{Bo} \kappa^{(n+1)}) dS \quad (6.43)$$

Two additional quantities to be solved for at the time step $n + 1$ appear: the bubble pressure $p_b^{(n+1)}$ and the curvature $\kappa^{(n+1)}$. The internal bubble pressure p_b is a Lagrange multiplier making the flow field satisfy the volume conservation constraint (6.36)

$$\int_{S_b} \mathbf{v}^{(n+1)} \cdot \mathbf{n} dS = 0. \quad (6.44)$$

The bubble surface propagates with the velocity $[(\mathbf{v} - \mathbf{u}) \cdot \mathbf{n}] \mathbf{n}$ with respect to the mesh assumed to move with the translation velocity \mathbf{u}_b with respect to the fixed frame. The center of the bubble will be related to the new velocity $\mathbf{v}^{(n+1)}$ by the relation

$$\int_S [(\mathbf{v}^{(n+1)} - \mathbf{u}_b) \cdot \mathbf{n}] \mathbf{n} dS = 0 \quad (6.45)$$

where \mathbf{n} is the normal vector of the geometry determined at the previous time-step. Written equivalently in coordinates:

$$\left(\int_S n_i n_j dS \right) u_{b,j} = \int_S (\mathbf{v}^{(n+1)} \cdot \mathbf{n}) n_i. \quad (6.46)$$

the relation (6.45) amounts to solving a linear system of three equations.

Implicit treatment of the curvature

Special care is necessary to the treatment of the curvature in order to avoid numerical instability due to capillarity waves. The bubble surface will be parametrized by the polar and azimuthal angles (ψ and θ , respectively) of its initially spherical shape. In what follows, we use the formula determining the curvature and the normal vector of a surface $\mathbf{x}_b(\xi)$ parametrized by two parameters ξ^α , $\alpha = 1, 2$, ($\xi^1 = \psi$ and $\xi^2 = \theta$):

$$\kappa n_i = -\frac{1}{\sqrt{g}} \sum_{\alpha,\beta} \frac{\partial}{\partial \xi^\alpha} \left(g^{\alpha,\beta} \sqrt{g} \frac{\partial x_b^i}{\partial \xi^\beta} \right) \quad (6.47)$$

where $i = 1, 2, 3$ are the Cartesian components. The metric tensor $g_{\alpha,\beta}$ is

$$g_{\alpha,\beta} = \frac{\partial \mathbf{x}}{\partial \xi^\alpha} \cdot \frac{\partial \mathbf{x}}{\partial \xi^\beta}, \quad (6.48)$$

g stands for its determinant and $g^{\alpha,\beta}$ is its contravariant counterpart (inverse matrix of $\{g_{\alpha,\beta}\}$).

In appendix 6.3 we show that in the approximation of irrotational flow of an inviscid fluid the problem reduces to a set of uncoupled equations for undamped linear oscillators:

$$\frac{d^2 B_{\ell,m}}{dt^2} + \frac{\sigma \ell(\ell+1)^2}{\rho R^3} B_{\ell,m} = 0. \quad (6.49)$$

From the numerical view-point, an explicit time-discretization of Eqs. (6.49) is numerically unstable. Indeed, an equation of undamped oscillator $\ddot{x} + \omega^2 x = 0$, transforms to a first

order complex equation $\dot{z} = i\omega z$ by setting $z = x - \frac{i}{\omega}\dot{x}$. An explicit time discretization with time step Δt amounts to iterations $z^{(n+1)} = (1 + i\omega\Delta t)z^{(n)}$ with a factor larger than 1 in absolute value. A sufficient damping may compensate the growth but, in our case, we need an algorithm assuring the decay of surface waves whatever the damping. The semi-implicit formula brings about neither amplification nor damping and the implicit one yields a factor of absolute value $1/\sqrt{1 + i\omega\Delta t} \approx 1 - \frac{1}{2}(\omega\Delta t)^2$ smaller than one. The implicit formula is thus to be preferred.

Our problem (Eqs. (6.32) through (6.39)) can be modeled as a damped oscillator written in the form

$$\frac{dv}{dt} + bv + \omega^2 x = 0, \quad (6.50)$$

$$\frac{dx}{dt} = v, \quad (6.51)$$

the first equation modeling the flow equations and the second one the bubble surface propagation. The elastic term $\omega^2 x$ in Eq. (6.50) plays the role of the curvature in Eq. (6.37). The explicit treatment of this term leads to the time-stepping algorithm

$$(1 + b\Delta t)v^{(n+1)} = v^{(n)} - \omega^2\Delta t x^{(n)} \quad (6.52)$$

$$x^{(n+1)} - \Delta t v^{(n+1)} = x^{(n)} \quad (6.53)$$

while the implicit approach with $x^{(n)}$ replaced by $x^{(n+1)} = x^{(n)} + \Delta t v^{(n+1)}$ in Eq. (6.52) yields

$$((1 + b\Delta t + \omega^2(\Delta t)^2)v^{(n+1)} = v^{(n)} - \omega^2\Delta t x^{(n)} \quad (6.54)$$

$$x^{(n+1)} - \Delta t v^{(n+1)} = x^{(n)}. \quad (6.55)$$

A simple calculation shows that, for zero damping $b = 0$, algorithm (6.52,6.53) behaves like the semi-implicit formula applied to the undamped complex oscillator while algorithm (6.54,6.55) yields (up to terms of order $O((\Delta t)^2)$) the factor $1 - \frac{1}{2}(\omega\Delta t)^2$ characteristic of the implicit formula.

It is easily seen that, in spite of all the effort aiming at a better numerical stability, the non-linearities make the implicitation only partial which results in a destabilizing effect, if the curvature in Eq. (6.37) is simply replaced by its value obtained from the geometry at previous time-step. The viscosity is insufficient to ensure the stability as soon as the Galileo number exceeds the value of about 10 (for $\text{Bo}=1$).

Following the considerations of the model problem, Eq. (6.38) will be used to propagate the bubble surface once the new velocity field has been obtained, i.e., in the first order version,

$$\mathbf{x}_b^{(n+1)} = \mathbf{x}_b^{(n)} + \Delta t \left[(\mathbf{v}^{(n+1)} - \mathbf{u}_b^{(n+1)}) \cdot \mathbf{n} \right] \mathbf{n}. \quad (6.56)$$

(Actually the third order Adams-Bashforth extrapolation has been used, nevertheless, the more accurate formula brings no visible additional improvement.) Upon substitution to Eq.

(6.47), the curvature term can be written as

$$\kappa^{(n+1)} \mathbf{n} = -\frac{1}{\sqrt{g}} \sum_{\alpha, \beta} \frac{\partial}{\partial \xi^\alpha} \left(g^{\alpha, \beta} \sqrt{g} \frac{\partial \mathbf{x}_b^{(n)}}{\partial \xi^\beta} \right) - \Delta \kappa \mathbf{n}, \quad (6.57)$$

$$\Delta \kappa \mathbf{n} = -\Delta t \frac{1}{\sqrt{g}} \sum_{\alpha, \beta} \frac{\partial}{\partial \xi^\alpha} \left[g^{\alpha, \beta} \sqrt{g} \frac{\partial}{\partial \xi^\beta} \left((\mathbf{v}^{(n+1)} - \mathbf{u}_b^{(n+1)}) \cdot \mathbf{n} \right) \mathbf{n} \right]. \quad (6.58)$$

In weak formulation

$$-\int_{S_b} (\mathbf{w} \cdot \mathbf{n}) \kappa dS = \int_{S_b} \frac{\partial \mathbf{w}}{\partial \xi^\alpha} \cdot \left(g^{\alpha, \beta} \frac{\partial \mathbf{x}}{\partial \xi^\beta} \right) dS. \quad (6.59)$$

This results in the weak formulation of the boundary condition (6.43)

$$\begin{aligned} \int_{S_b} \mathbf{w} (p \mathbf{n} - \frac{1}{G} \boldsymbol{\tau}^{(n+1)} \mathbf{n}) dS &= \int_{S_b} \mathbf{w} \cdot \mathbf{n} p_b^{(n+1)} dS + \frac{\Delta t}{B_o} \int_{S_b} \frac{\partial (\mathbf{w} \cdot \mathbf{n})}{\partial \xi^\alpha} \cdot \left(g^{\alpha, \beta} \frac{\partial (\mathbf{v}^{(n+1)} \cdot \mathbf{n})}{\partial \xi^\beta} \right) dS \\ &\quad - \int_{S_b} (\mathbf{w} \cdot \mathbf{n}) \left(z + \frac{1}{B_o} \kappa^{(n)} \right) dS \end{aligned} \quad (6.60)$$

where the first two terms on the RHS containing the unknowns p_b and $\mathbf{v}^{(n+1)}$ contribute to the problem matrix and the last term contributes to the RHS term.

Weak formulation of the linear problem at step $n + 1$

The considerations described above result in the following weak formulation of the linear problem to be solved at each time-step:

$$\begin{aligned} &\int_{\Omega} \left[\frac{1}{\Delta t} \mathbf{w} \cdot \mathbf{v}^{(n+1)} + \nabla \mathbf{w} \cdot \frac{1}{G} \boldsymbol{\tau}^{(n+1)} - (\nabla \cdot \mathbf{w}) p^{(n+1)} - \Phi \nabla \cdot \mathbf{v}^{(n+1)} \right. \\ &\quad \left. - \mathbf{w} \cdot \left[\frac{1}{\Delta t} \mathbf{v}^{(n)} - ((\mathbf{v} - \mathbf{u}_b) \cdot \nabla \mathbf{v})^{(n)} \right] \right] d\Omega + \\ &p_b^{(n+1)} \int_{S_b} \mathbf{w} \cdot \mathbf{n} dS + \frac{\Delta t}{B_o} \int_{S_b} \frac{\partial (\mathbf{w} \cdot \mathbf{n})}{\partial \xi^\alpha} \cdot \left(g^{\alpha, \beta} \frac{\partial (\mathbf{v}^{(n+1)} \cdot \mathbf{n})}{\partial \xi^\beta} \right) dS \\ &a \int_{S_b} (\mathbf{v}^{(n+1)} \cdot \mathbf{n}) dS - \int_{S_b} (\mathbf{w} \cdot \mathbf{n}) \left(z + \frac{1}{B_o} \kappa^{(n)} \right) dS \\ &\mathbf{v}^{(n+1)} = 0 \quad \text{on inflow}; \quad p^{(n+1)} = 0 \quad \text{on outflow.} \end{aligned} \quad (6.61)$$

where \mathbf{w} is a vectorial test function, Φ a scalar test function and a a scalar test variable. Once solved, the resulting velocity field $\mathbf{v}^{(n+1)}$ is used to calculate the bubble velocity (Eqs. (6.45,6.46)) and the bubble surface is moved using Eq. (6.56).

6.1.3 Time splitting formulation

The weak formulation (6.61) provides, after appropriate discretization and by variation with respect to discretized test functions and the variable a , a single linear problem to be solved, yielding directly the new velocity and pressure fields as well as the bubble pressure $p_b^{(n+1)}$. The obtained ‘augmented’ matrix is, however, badly conditioned and the code ought to

have been significantly reformulated for the purpose while, in its previous versions, the time splitting formulation gave entire satisfaction for flows of fluids having low viscosity. It involves significantly simplified matrix inversions resulting in reduced computing costs. Its implementation required some additional tradeoffs discussed in this section.

The time splitting formulation consists in separating the computation of velocity and pressure updates by splitting the velocity increment $\mathbf{v}^{(n+1)} - \mathbf{v}^{(n)}$ into two terms

$$\mathbf{v}^{(n+1)} - \mathbf{v}^{(n)} = (\mathbf{v}^{(n+1)} - \hat{\mathbf{v}}) + (\hat{\mathbf{v}} - \mathbf{v}^{(n)}) \quad (6.62)$$

and by approximating the coupled system of equations (6.32, 6.33) in the following manner:

$$\frac{\hat{\mathbf{v}} - \mathbf{v}^{(n)}}{\Delta t} + ([(\mathbf{v} - \mathbf{u}) \cdot \nabla] \mathbf{v})^{(n)} + \nabla p^{(n+1)} = 0, \quad (6.63)$$

$$\nabla \cdot \hat{\mathbf{v}} = 0, \quad (6.64)$$

$$\frac{\mathbf{v}^{(n+1)} - \hat{\mathbf{v}}}{\Delta t} - \nabla \cdot \left(\frac{1}{G} \boldsymbol{\tau}^{(n+1)} \right) = 0. \quad (6.65)$$

The inaccuracy of the formulation, due to the not exactly zero divergence of velocity, is proportional to $\Delta t/G$ so that, for short time step and sufficiently large Galileo number, it can be expected to be acceptable. Eqs. (6.63, 6.64) yield a Poisson problem for the pressure:

$$\nabla^2 p^{(n+1)} = \nabla \cdot \left(\frac{\mathbf{v}^{(n)}}{\Delta t} - ([(\mathbf{v} - \mathbf{u}) \cdot \nabla] \mathbf{v})^{(n)} \right) \quad (6.66)$$

for which it is necessary to define boundary conditions compatible with the condition (6.37) at the bubble surface. The idea of Eqs. (6.63) and (6.64) consists in ignoring the viscosity effects in the computation of the pressure. Continuing along the same line, we can reduce the boundary condition (6.37) by discarding the viscous term and set a Dirichlet pressure boundary condition at the bubble surface:

$$p^{(n+1)}|_{S_b} = \left(p_b^{(n)} - z - \frac{1}{Bo} \kappa^{(n)} \right). \quad (6.67)$$

assuming the bubble pressure p_b to be known.

At the inflow no modification of the boundary conditions used for simulating solid bodies is required and is described in previous work (Christ, 2012). A Dirichlet boundary condition defining the velocity results in a Neumann condition for the pressure

$$\left. \frac{\partial p^{(n+1)}}{\partial \mathbf{n}} \right|_{S_{inflow}} = \left(\frac{\mathbf{v}^{(n)}}{\Delta t} - ([(\mathbf{v} - \mathbf{u}) \cdot \nabla] \mathbf{v})^{(n)} \right) \cdot \mathbf{n} - \frac{\mathbf{v}|_{S_{inflow}} \cdot \mathbf{n}}{\Delta t}. \quad (6.68)$$

The velocity field at the next step $\mathbf{v}^{(n+1)}$ is obtained by solving the Helmholtz problem (6.65) completed by standard Dirichlet and Neumann conditions $\mathbf{v} = 0$ and $\boldsymbol{\tau} \cdot \mathbf{n} = 0$, set, respectively, at the inflow and outflow of the domain (see Eqs. (6.34) and (6.35)).

At the bubble surface we require the implicit treatment of the curvature. The pressure boundary condition (6.67) combined with the dynamic boundary condition (6.43) yields:

$$\left. \frac{1}{G} \boldsymbol{\tau}^{(n+1)} \cdot \mathbf{n} \right|_{S_b} = + \frac{1}{Bo} \Delta \kappa \mathbf{n} \quad (6.69)$$

where $\Delta \kappa$ is the curvature correction (6.58). Physically, this condition assumes that surface waves are dissipated by viscosity. This results in the weak formulation of the velocity problem

$$\int_{\Omega} \left[\frac{1}{\Delta t} \mathbf{w} \cdot \mathbf{v}^{(n+1)} + \nabla \mathbf{w} \cdot \frac{1}{G} \boldsymbol{\tau}^{(n+1)} \right] d\Omega + \Delta t \frac{1}{Bo} \int_{S_b} g^{(n), \alpha, \beta} \frac{\partial(\mathbf{n} \cdot \mathbf{w}) \mathbf{n}}{\partial \xi^\alpha} \frac{\partial(\mathbf{n} \cdot \mathbf{v}^{(n+1)}) \mathbf{n}}{\partial \xi^\beta} \sqrt{g^{(n)}} d^2 \xi - \int_{\Omega} \frac{1}{\Delta t} \mathbf{w} \cdot \hat{\mathbf{v}} d\Omega = 0. \quad (6.70)$$

The bubble pressure $p_b^{(n+1)}$ is obtained by requiring the volume flux through the bubble surface to be zero. This is done in the following way. After updating the deformable mesh (see the next section), the effect of a unit pressure variation at the bubble surface on the velocity field is computed by setting all variables to zero and by solving first the pressure equation for a unit pressure boundary condition and by computing the corresponding flow field afterward. This yields the corresponding volume flux. The solved problem being linear, the obtained information is then used to adjust the bubble pressure and update the velocity field to respect the zero volume flux condition. If the mesh were fixed, this solution would be needed only once at the beginning of the computation. However, the mesh deforms slightly at each time step which makes the solution of the pressure and velocity equations depend on the mesh deformation. The procedure must thus be done at each time step. The solver being iterative, the accuracy of resolution can be adjusted to the global accuracy required at a time step for the velocity and pressure fields. Since the mesh deforms only a little at a single time-step, the computing costs can be made much smaller than those of the pressure and velocity computation itself.

6.2 Bubble: numerical method of solution

The cylindrical domain of figure 6.1 around an undeformed spherical bubble is discretized using a Fourier decomposition in the azimuthal direction and a spectral element decomposition in the radial-axial plane. An example of the mesh in the radial axial plane is given in figure 6.2. Three meshes with 16, 20 and 30 elements along the bubble surface (245, 277 and 387 elements totally, named mesh0, mesh1 and mesh2) were created. They differ only in a close neighborhood of the bubble as seen in the details represented in figure 6.3.

If the bubble is spherical, the 3D mesh is obtained by revolution of radial-axial plane about the axis. The idea of capturing the bubble deformation is based on the ALE approach consisting in following the bubble deformation by the mesh. Since the size of the bubble is small compared to the size of the whole computational domain, it is not necessary to propagate its deformation everywhere. It is sufficient to deform the mesh only inside a sphere of radius large enough to contain the bubble after it has deformed. It appeared that

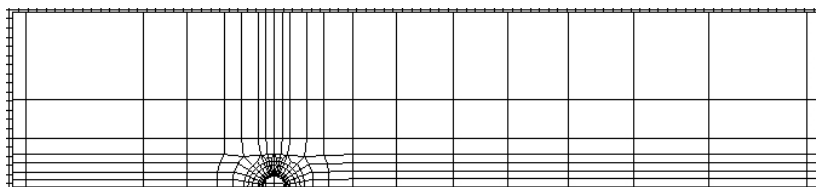


Figure 6.2: Spectral element mesh in the radial-axial plane

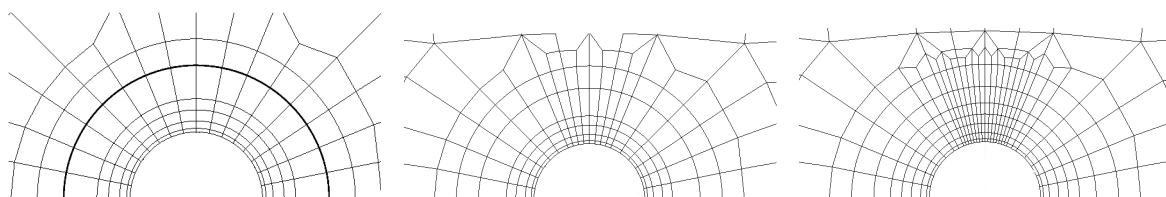
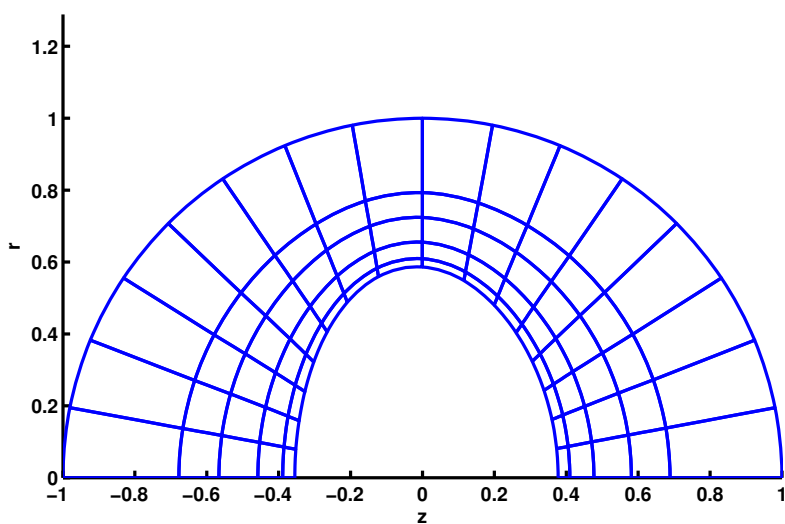


Figure 6.3: From left to right: detail of mesh16, mesh20 and mesh30.

a radius R_s equal to the diameter of the spherical bubble was sufficient for all considered Bond numbers. The intersection of this sphere with the axial-radial plane is represented by the thick half circle in the left figure 6.3. An idea of the deformed mesh is provided in figure 6.4. The figure 6.4 was obtained for an axisymmetric bubble but a similar mesh arises in

Figure 6.4: Deformed mesh around an axisymmetric bubble at $Bo = 1$ and $G = 100$.

different azimuthal directions also if the bubble is non-axisymmetric. The difference between non-axisymmetric and axisymmetric shape consists in variable deformation depending on the azimuthal angle. The deformed mesh is parametrized by keeping track of the positions of the moving meshpoints as functions of their position on the undeformed mesh (see section 6.2.3 for more details), i.e. the undeformed mesh is maintained as reference and the mesh deformation is represented as additional vector field on the undeformed cylindrical mesh. The same cylindrical mesh is used for describing the pressure and velocity fields, which reduces the necessary modification of the code used in the previous PhD thesis by Chrust (2012).

Outside the deformed spherical sub-domain, the principles of the discretization are the same as described in the PhD thesis by Chrust (2012). The stress boundary condition at the bubble surface required, however, a stress formulation (involving the deformation velocity tensor) of the Navier-Stokes equations. We describe the way how the variables are stored in sub-section 6.2.1 and the implementation of differential operators in sub-section 6.2.2. The mesh deformation is addressed in sub-section 6.2.3.

6.2.1 Storage of variables

To explain the representation of vectors, we shall focus on the velocity field. The Cartesian coordinates (with origin at the center of the spherical sub-domain) will be named z for the projection onto the cylinder axis and x, y for the projection onto the normal plane. The cylindrical coordinates are obtained by parametrizing the xOy plane by polar coordinates r, θ so that $x = r \cos \theta$ and $y = r \sin \theta$. In cylindrical coordinates, vectors are expressed by their axial, radial and azimuthal projections, e.g. v_z, v_r, v_θ instead of v_z, v_x, v_y . The periodicity of all variables with respect to θ allows the use of Fourier expansion (shown by Ghidersa & Dušek (2000) to be optimal for the description of axisymmetry breaking in flows as already mentioned in the Introduction.) An old numerical paper by Orszag (1974) shows that the Fourier expansion is not to be applied to the radial and azimuthal components but to their complex combination $v_r + i v_\theta$. The complex representation is also more convenient for the description of rotations about the symmetry (z) axis. Mathematically, it amounts to switching from an $O(2)$ representation (by 2×2 real matrices) of the rotation group to the $U(1)$ representation in the complex plane where rotations are simply given by multiplications by complex units (see Jenny & Dušek, 2004). The $U(1)$ representation is used in the transverse xOy plane. The projection z being invariant with respect to rotations about the axis, it behaves in the same way as a scalar (like the pressure).

In $U(1)$ representation, the transverse velocity components are replaced complex combinations in the following way:

$$v_{\pm} = v_x \pm i v_y; \quad \tilde{v}_{\pm} = v_r \pm i v_\theta. \quad (6.71)$$

The $-$ component is redundant but useful after decomposition into complex Fourier modes.

The cylindrical version is denoted by tilde. The transformation is defined by the matrix

$$\mathbf{L} = \begin{bmatrix} 1 & 0 & 0 \\ 0 & 1 & -i \\ 0 & 1 & i \end{bmatrix}$$

$$\mathbf{v}_{U(1)} = \mathbf{L}\mathbf{v}_{O(2)}.$$

The U(1) representation yields a simple transformation:

$$v_{\pm} = e^{\pm i\theta} \tilde{v}_{\pm}. \quad (6.72)$$

To write the transformation of the whole velocity vector in a compact way, define

$$d(\theta) = \text{diag}(1, e^{-i\theta}, e^{i\theta}).$$

Then

$$\mathbf{v} = d(\theta)\tilde{\mathbf{v}} \quad (6.73)$$

where

$$\mathbf{v} = \begin{pmatrix} v_z \\ v_- \\ v_+ \end{pmatrix}; \quad \tilde{\mathbf{v}} = \begin{pmatrix} v_z \\ \tilde{v}_- \\ \tilde{v}_+ \end{pmatrix}.$$

In our discretization we work with Fourier modes of truncated Fourier expansions:

$$v_z = \sum_{m=-M}^M c_{z,m}(z, r) e^{-im\theta} \quad (6.74)$$

$$\tilde{v}_- = \sum_{m=-M}^M c_{-,m}(z, r) e^{-im\theta} \quad (6.75)$$

$$\tilde{v}_+ = \sum_{m=-M}^M c_{+,m}(z, r) e^{-im\theta} \quad (6.76)$$

M being the largest Fourier mode taken into account. The following redundancies make it possible to reduce the storage to positive indexes only:

$$c_{z,-m}(z, r) = \overline{c_{z,m}(z, r)}; \quad c_{\pm,-m}(z, r) = \overline{c_{\mp,m}(z, r)}.$$

The scalars (e.g. pressure) are stored in the same way as v_z . We store $c_{z,m}$, $c_{-,m}$ and $c_{+,m}$ for $0 \leq m \leq M$.

6.2.2 Differential operators on undeformed mesh

The spectral accuracy of the code is obtained by taking the θ derivatives in spectral space. Their implementation is described in previous work (e.g. Jenny & Dušek, 2004) except for the stress formulation required in the present case.

The gradient of the velocity vector defined in Cartesian coordinates and $U(1)$ representation is expressed as:

$$\nabla \mathbf{v} = \begin{pmatrix} \frac{\partial v_z}{\partial z} & \frac{\partial v_-}{\partial z} & \frac{\partial v_+}{\partial z} \\ \nabla_- v_z & \nabla_- v_- & \nabla_- v_+ \\ \nabla_+ v_z & \nabla_+ v_- & \nabla_+ v_+ \end{pmatrix}. \quad (6.77)$$

In Eq. (6.77), ∇_{\pm} stand for

$$\nabla_{\pm} = \frac{\partial}{\partial x} \pm i \frac{\partial}{\partial y}. \quad (6.78)$$

The transformation to $O(2)$ representation is obtained by a simple matrix multiplication

$$[\nabla \mathbf{v}]_{O(2)} = \mathbf{L}^{-1} \nabla \mathbf{v} \mathbf{L}^{T-1}; \quad \mathbf{L}^{-1} = \begin{bmatrix} 1 & 0 & 0 \\ 0 & \frac{1}{2} & \frac{1}{2} \\ 0 & \frac{i}{2} & \frac{i}{2} \end{bmatrix}. \quad (6.79)$$

The transformation of the gradient of the axial component of velocity to cylindrical coordinates is the same as for a scalar:

$$\nabla v_z = d(\theta) \tilde{\nabla} v_z \quad (6.80)$$

where ∇ and $\tilde{\nabla}$ are the gradient in Cartesian coordinates and cylindrical coordinates, respectively, both in $U(1)$ representation:

$$\nabla = \begin{pmatrix} \frac{\partial}{\partial z} \\ \nabla_- \\ \nabla_+ \end{pmatrix}; \quad \tilde{\nabla} = \begin{pmatrix} \frac{\partial}{\partial z} \\ \tilde{\nabla}_- \\ \tilde{\nabla}_+ \end{pmatrix}; \quad \tilde{\nabla}_{\pm} = \frac{\partial}{\partial r} \pm i \frac{\partial}{\partial \theta}. \quad (6.81)$$

For the $+$ and $-$ transverse $U(1)$ components we get (see also Eq. (6.72):

$$\nabla_{\pm} v_{\pm} = e^{\pm i\theta} \tilde{\nabla}_{\pm} \left(e^{i\theta} \tilde{v}_{\pm} \right) = e^{\pm i\theta} e^{i\theta} \left(\tilde{\nabla}_{\pm} \mp \frac{1}{r} \right) \tilde{v}_{\pm} \quad (6.82)$$

and

$$\nabla_{\pm} v_{\mp} = e^{\pm i\theta} \tilde{\nabla}_{\pm} \left(e^{-i\theta} \tilde{v}_{\mp} \right) = e^{\pm i\theta} e^{-i\theta} \left(\tilde{\nabla}_{\pm} \pm \frac{1}{r} \right) \tilde{v}_{\mp}. \quad (6.83)$$

This yields the transformation

$$\nabla \mathbf{v} = d(\theta) \tilde{\nabla} \tilde{\mathbf{v}} d(\theta) \quad (6.84)$$

where

$$\tilde{\nabla} \tilde{\mathbf{v}} = \begin{bmatrix} \frac{\partial v_z}{\partial z} & \frac{\partial \tilde{v}_-}{\partial z} & \frac{\partial \tilde{v}_+}{\partial z} \\ \tilde{\nabla}_- v_z & \left(\tilde{\nabla}_- - \frac{1}{r} \right) \tilde{v}_- & \left(\tilde{\nabla}_- + \frac{1}{r} \right) \tilde{v}_+ \\ \tilde{\nabla}_+ v_z & \left(\tilde{\nabla}_+ + \frac{1}{r} \right) \tilde{v}_- & \left(\tilde{\nabla}_+ - \frac{1}{r} \right) \tilde{v}_+ \end{bmatrix}. \quad (6.85)$$

The operations $\tilde{\nabla}_{\pm} \pm \frac{1}{r}$ are available in the code in the form of gradients which we denote as:

$$\tilde{\nabla} v_- = \begin{bmatrix} \frac{\partial \tilde{v}_-}{\partial z} \\ \left(\tilde{\nabla}_- - \frac{1}{r} \right) v_- \\ \left(\tilde{\nabla}_+ + \frac{1}{r} \right) v_- \end{bmatrix} \quad (6.86)$$

$$\tilde{\nabla} v_+ = \begin{bmatrix} \frac{\partial \tilde{v}_+}{\partial z} \\ \left(\tilde{\nabla}_- + \frac{1}{r} \right) v_+ \\ \left(\tilde{\nabla}_+ - \frac{1}{r} \right) v_+ \end{bmatrix}. \quad (6.87)$$

It is easily seen than the O(2) representation is

$$\mathbf{L}^{-1} \tilde{\nabla} \tilde{\mathbf{v}} \mathbf{L}^{T-1} = \begin{bmatrix} \frac{\partial v_z}{\partial z} & \frac{\partial v_r}{\partial z} & \frac{\partial v_\theta}{\partial z} \\ \frac{\partial v_z}{\partial r} & \frac{\partial v_r}{\partial r} & \frac{\partial v_\theta}{\partial r} \\ \frac{1}{r} \frac{\partial v_z}{\partial \theta} & \frac{1}{r} \frac{\partial v_r}{\partial \theta} - \frac{v_\theta}{r} & \frac{1}{r} \frac{\partial v_\theta}{\partial \theta} + \frac{v_r}{r} \end{bmatrix}$$

as expected.

The gradients are available in the code in terms of Fourier modes (in spectral representation). The $U(1)$ representation makes the singularity $1/r$ removable. The Fourier transformations (6.74, 6.75, 6.76) yield the gradients in physical space. Equations (6.79), (6.84) and (6.85) then provide the transformation from gradients in cylindrical coordinates transformed to physical space to Cartesian coordinates in usual O(2) formulation.

Stress formulation

To obtain the diffusion term of Navier-Stokes equations in the non-stress formulation it is sufficient to write a variation of the functional

$$a(\mathbf{w}, \mathbf{v}) = \int_{\Omega} \tilde{\nabla} \tilde{\mathbf{w}} \cdot \tilde{\nabla} \tilde{\mathbf{v}} \, dz r dr d\theta.$$

E.g. the \tilde{v}_+ equation results from variation with respect to \tilde{w}_+ i.e.:

$$\tilde{\nabla}^\dagger \cdot \tilde{\nabla} \tilde{v}_+ = \left[-\frac{\partial^2}{\partial z^2} + \frac{1}{2} \left(\tilde{\nabla}_-^\dagger + \frac{1}{r} \right) \left(\tilde{\nabla}_- + \frac{1}{r} \right) + \frac{1}{2} \left(\tilde{\nabla}_+^\dagger - \frac{1}{r} \right) \left(\tilde{\nabla}_+ - \frac{1}{r} \right) \right] \tilde{v}_+.$$

This yields the Laplacian operator

$$-\frac{\partial^2}{\partial z^2} - \frac{1}{r} \frac{\partial}{\partial r} r \frac{\partial}{\partial r} + \frac{1}{r^2} \left(i \frac{\partial}{\partial \theta} - 1 \right)^2$$

which is easily seen taking into account the formula:

$$\tilde{\nabla}_\pm^\dagger = -\frac{1}{r} \frac{\partial}{\partial r} r \pm i \frac{1}{r} \frac{\partial}{\partial \theta}. \quad (6.88)$$

The stress formulation consists in replacing $\tilde{\nabla} \tilde{\mathbf{v}}$ by $\tilde{\nabla} \tilde{\mathbf{v}} + \tilde{\nabla} \tilde{\mathbf{v}}^T$. I.e. the viscous term becomes:

$$\tilde{\nabla}^\dagger \cdot (\tilde{\nabla} \tilde{\mathbf{v}} + \tilde{\nabla} \tilde{\mathbf{v}}^T) \quad (6.89)$$

where $\tilde{\nabla}^\dagger$ stands alternatively for the adjoint operators in the columns of the expression for the velocity gradient (6.85).

In appendix 6.4, it is shown that

$$\tilde{\nabla}^\dagger \cdot \tilde{\nabla} \tilde{\mathbf{v}}^T$$

is zero due to the vanishing divergence.

The implementation in spectral representation is given in detail in appendix 6.5.

6.2.3 Description of bubble surface and domain deformation

The bubble surface can be described by the position vector parametrized by spherical coordinates

$$\mathbf{x}^{(b)} = \mathbf{x}_b(\psi, \theta) = \begin{pmatrix} z^{(b)} \\ \tilde{x}_-^{(b)} \\ \tilde{x}_+^{(b)} \end{pmatrix} \quad (6.90)$$

where ψ is the polar angle obtained on the undeformed mesh from the transformation:

$$\begin{aligned} z &= 0.5 \cos \psi, \\ r &= 0.5 \sin \psi. \end{aligned} \quad (6.91)$$

In the same way as the velocity vector (6.74, 6.75, 6.76), the position vector will be expanded into Fourier modes:

$$\tilde{\mathbf{x}}^{(b)} = \sum_{m=-M}^M \mathbf{c}_m^{(b)}(\psi) e^{-im\theta} \quad (6.92)$$

where

$$\mathbf{c}_m^{(b)} = \begin{pmatrix} z_{b,m} \\ x_{b,-,m} \\ x_{b,+,m} \end{pmatrix}. \quad (6.93)$$

With the help of a spherical function expansion used instead of the Fourier decomposition (6.92), it can be shown that the Fourier modes have the same behavior at the axis as that of velocity (see Ghidersa & Dušek, 2000), i.e.

$$\begin{aligned} z_{b,m} &\sim (\sin \psi)^m \\ x_{b,\pm,m}(\psi) &\sim (\sin \psi)^{|m \mp 1|}, \end{aligned} \quad (6.94)$$

$$(6.95)$$

which enables the removal of singularities at the axis.

The mesh will be deformed by interpolating between the bubble surface defined in the undeformed mesh by the radial spherical coordinate $\eta = \eta_1 = 0.5$ and a fixed spherical surface of radius η_2

$$\mathbf{x}^{(s)} = \eta_2 \mathbf{n}$$

where

$$\mathbf{n} = \begin{bmatrix} \cos \psi \\ \sin \psi \cos \theta \\ \sin \psi \sin \theta \end{bmatrix}.$$

A simple linear interpolation is used

$$\mathbf{x} = \frac{\eta_2 - \eta}{\eta_2 - \eta_1} \mathbf{x}^{(b)} + \frac{\eta - \eta_1}{\eta_2 - \eta_1} \mathbf{x}^{(s)} \quad (6.96)$$

resulting in the transformation

$$\mathbf{x} = \mathbf{x}(\eta, \psi, \theta).$$

To define the transformation of gradients, we need the Jacobian matrix :

$$\frac{\partial \mathbf{x}}{\partial \eta} = \mathbf{N}_\eta = \frac{1}{\eta_2 - \eta_1} (\mathbf{x}^{(s)} - \mathbf{x}^{(b)}); \quad (6.97)$$

$$\frac{\partial \mathbf{x}}{\partial \psi} = \eta \mathbf{N}_\psi = \frac{\eta_2 - \eta}{\eta_2 - \eta_1} \sum_m \frac{\partial \mathbf{c}_m^{(b)}}{\partial \psi} e^{-im\theta} + \frac{\eta - \eta_1}{\eta_2 - \eta_1} \eta_2 \mathbf{n}_\psi; \quad (6.98)$$

$$\frac{\partial \mathbf{x}}{\partial \theta} = \eta \sin \psi \mathbf{N}_\theta = \frac{\eta_2 - \eta}{\eta_2 - \eta_1} \sum_m (-im) \mathbf{c}_m^{(b)} e^{-im\theta} + \frac{\eta - \eta_1}{\eta_2 - \eta_1} \eta_2 \sin \psi \mathbf{n}_\theta \quad (6.99)$$

where

$$\mathbf{n}_\psi = \frac{\partial \mathbf{n}}{\partial \psi}; \quad \mathbf{n}_\theta = \frac{1}{\sin \psi} \frac{\partial \mathbf{n}}{\partial \theta}$$

and the vectors $\mathbf{N}_\eta, \mathbf{N}_\psi, \mathbf{N}_\theta$ are identical with the unit orthonormal vectors of spherical coordinates if the mesh is undeformed. They are obtained in cylindrical coordinates and transformed to Cartesian ones using Eq. (6.73). Eqs. (6.98) and (6.99), restricted to the bubble surface ($\eta = 0.5$), yield also the tangent vectors at the bubble surface and the metric tensor (6.48).

The inverse of the Jacobian matrix:

$$\mathbf{J}^T = \left[\frac{\partial \mathbf{x}}{\partial \eta}, \frac{\partial \mathbf{x}}{\partial \psi}, \frac{\partial \mathbf{x}}{\partial \theta} \right] \quad (6.100)$$

is

$$\mathbf{J}^{-1} = \frac{1}{\det(\tilde{\mathbf{J}})} \left[\mathbf{N}_\psi \times \mathbf{N}_\theta, \frac{1}{\eta} \left(\mathbf{N}_\theta \times \frac{\partial \mathbf{x}}{\partial \eta} \right), \frac{1}{\eta \sin \psi} \left(\frac{\partial \mathbf{x}}{\partial \eta} \times \mathbf{N}_\psi \right) \right]. \quad (6.101)$$

Gradients

A scalar gradient writes as:

$$\nabla f = \frac{1}{\det(\tilde{\mathbf{J}})} \left[(\mathbf{N}_\psi \times \mathbf{N}_\theta) \frac{\partial f}{\partial \eta} + \left(\mathbf{N}_\theta \times \frac{\partial \mathbf{x}}{\partial \eta} \right) \frac{1}{\eta} \frac{\partial f}{\partial \psi} + \left(\frac{\partial \mathbf{x}}{\partial \eta} \times \mathbf{N}_\psi \right) \frac{1}{\eta \sin \psi} \frac{\partial f}{\partial \theta} \right]. \quad (6.102)$$

Introducing the cylindrical coordinates $r = \eta \sin \psi, z = \eta \cos \psi$ we get:

$$\begin{aligned}\frac{\partial f}{\partial \eta} &= \cos \psi \frac{\partial f}{\partial z} + \sin \psi \frac{\partial f}{\partial r}, \\ \frac{1}{\eta} \frac{\partial f}{\partial \psi} &= -\sin \psi \frac{\partial f}{\partial z} + \cos \psi \frac{\partial f}{\partial r}.\end{aligned}$$

This results in the gradient in deformed cylindrical coordinates written as follows:

$$\nabla f = \tilde{\mathbf{J}}^{-1} \begin{bmatrix} \cos \psi & \sin \psi & 0 \\ -\sin \psi & \cos \psi & 0 \\ 0 & 0 & 1 \end{bmatrix} \begin{bmatrix} \frac{\partial f}{\partial z} \\ \frac{\partial f}{\partial r} \\ \frac{1}{r} \frac{\partial f}{\partial \theta} \end{bmatrix}. \quad (6.103)$$

where

$$\tilde{\mathbf{J}}^T = \left[\frac{\partial \mathbf{x}}{\partial \eta}, \mathbf{N}_\psi, \mathbf{N}_\theta \right]. \quad (6.104)$$

As already mentioned, the stored velocity field components are $\tilde{v}_\pm = e^{\mp i\theta} v_\pm$ where v_\pm are $U(1)$ Cartesian components. The velocity vector will be projected onto a fixed Cartesian basis. It will not be submitted to the coordinate deformation unlike the usual approach consisting in projecting onto the local basis of coordinate vectors (6.97,6.98,6.99). As the result, its components are differentiated like scalars.

In short-hand notation

$$\nabla f = \mathbf{K} \begin{bmatrix} \frac{\partial}{\partial z} \\ \tilde{\nabla}_- \\ \tilde{\nabla}_+ \end{bmatrix} f \equiv \mathbf{K} \tilde{\nabla} f \quad (6.105)$$

$$\nabla v_+ = e^{i\theta} \mathbf{K} \tilde{\nabla} \tilde{v}_+ \quad (6.106)$$

where

$$\mathbf{K} = \tilde{\mathbf{J}}^{-1} \begin{bmatrix} \cos \psi & \sin \psi & 0 \\ -\sin \psi & \cos \psi & 0 \\ 0 & 0 & 1 \end{bmatrix} \begin{bmatrix} 1 & 0 & 0 \\ 0 & \frac{1}{2} & \frac{1}{2} \\ 0 & \frac{i}{2} & -\frac{i}{2} \end{bmatrix}. \quad (6.107)$$

The matrix \mathbf{K} has the following form if no deformation is present:

$$\mathbf{K}_0 = \tilde{\mathbf{J}}_0^{-1} \begin{bmatrix} \cos \psi & \sin \psi & 0 \\ -\sin \psi & \cos \psi & 0 \\ 0 & 0 & 1 \end{bmatrix} \begin{bmatrix} 1 & 0 & 0 \\ 0 & \frac{1}{2} & \frac{1}{2} \\ 0 & \frac{i}{2} & -\frac{i}{2} \end{bmatrix} = \begin{bmatrix} 1 & 0 & 0 \\ 0 & \frac{1}{2} e^{-i\theta} & \frac{1}{2} e^{i\theta} \\ 0 & \frac{i}{2} e^{-i\theta} & -\frac{i}{2} e^{i\theta} \end{bmatrix} \quad (6.108)$$

where $\tilde{\mathbf{J}}_0^{-1}$ is the Jacobian matrix of undeformed spherical coordinates:

$$\tilde{\mathbf{J}}_0^{-1} = \begin{bmatrix} \cos \psi & -\sin \psi & 0 \\ \sin \psi \cos \theta & \cos \psi \cos \theta & -\sin \theta \\ \sin \psi \sin \theta & \cos \psi \sin \theta & \cos \theta \end{bmatrix}. \quad (6.109)$$

It is to be noted that

$$\mathbf{K}_0^\dagger \mathbf{K}_0 = \text{diag}(1, 1/2, 1/2). \quad (6.110)$$

The factors $1/2$ must be compensated since they are already included in the implemented divergence operator. The matrix (6.109) being orthogonal, the matrix elements of the Jacobian matrix of transformation from deformed to undeformed spherical coordinates:

$$\mathbf{J}_{def}^{-1} = \tilde{\mathbf{J}}^{-1} \tilde{\mathbf{J}}_0 \quad (6.111)$$

is identity for an undeformed mesh. The modification of the matrix \mathbf{K}_0 due to the mesh deformation writes then

$$\mathbf{K} = \mathbf{J}_{def}^{-1} \mathbf{K}_0, \quad (6.112)$$

i.e. the mesh deformation is totally accounted for by the matrix field (6.111). Alternatively to Cartesian coordinates, cylindrical coordinates can be used. In that case the matrix (6.108) is simply replaced by

$$\tilde{\mathbf{K}}_0 = \tilde{\mathbf{J}}_0^{-1} \begin{bmatrix} \cos \psi & \sin \psi & 0 \\ -\sin \psi & \cos \psi & 0 \\ 0 & 0 & 1 \end{bmatrix} \begin{bmatrix} 1 & 0 & 0 \\ 0 & \frac{1}{2} & \frac{1}{2} \\ 0 & \frac{i}{2} & -\frac{i}{2} \end{bmatrix} = \begin{bmatrix} 1 & 0 & 0 \\ 0 & \frac{1}{2} & \frac{1}{2} \\ 0 & \frac{i}{2} & -\frac{i}{2} \end{bmatrix}. \quad (6.113)$$

The matrix field \mathbf{K} defines the viscous term in the stress formulation in the way described in appendix 6.6.

6.3 Capillarity waves on a spherical free surface

To understand the origin of capillarity waves on a spherical surface, let us consider the standard approach of infinitesimal waves in the approximation of irrotational flow of an inviscid fluid. In 2D, this approach leads to the textbook description of capillarity waves. Be ϕ the velocity potential

$$\mathbf{v} = \nabla \phi. \quad (6.114)$$

The incompressibility condition (6.33) yields the Laplace-Poisson equation

$$\nabla^2 \phi = 0 \quad (6.115)$$

with boundary conditions $\mathbf{v} \rightarrow 0$, i.e. $\phi \rightarrow 0$ for $r \rightarrow \infty$ and the dynamic condition (Bernoulli equation)

$$\frac{\partial \phi}{\partial t} + \frac{p}{\rho} = const. \quad (6.116)$$

at the bubble surface. (In the Bernoulli equation (6.116) the non-linear term $(\nabla \phi)^2/2$ is dropped out at linearization and purely capillarity waves (without gravity effects) are considered. The pressure depends on the curvature:

$$p = p_0 - \sigma \kappa \quad (6.117)$$

p_0 being the static pressure inside the bubble. If differentiated with respect to time, Eq. (6.116) yields the wave equation

$$\frac{\partial^2 \phi}{\partial t^2} - \frac{\sigma}{\rho} \frac{\partial \kappa}{\partial t} = 0. \quad (6.118)$$

The velocity potential can be expanded into spherical functions

$$\phi = \sum_{\ell,m} \varphi_{\ell,m}(r,t) Y_{\ell,m}(\psi, \theta), \quad (6.119)$$

which reduces Eq. (6.115) to a set of ordinary differential equations

$$\left(\frac{1}{r^2} \frac{\partial}{\partial r} r^2 \frac{\partial}{\partial r} - \frac{\ell(\ell+1)}{r^2} \right) \varphi_{\ell,m} = 0 \quad (6.120)$$

with boundary condition at infinity:

$$\varphi_{\ell,m}(r,t) \rightarrow 0; \quad r \rightarrow \infty. \quad (6.121)$$

The solution is:

$$\varphi_{\ell,m}(r) = B_{\ell,m}(t) r^{-\ell-1}; \quad \ell > 0; \quad (6.122)$$

($\varphi_{0,0}(r) = 0$). The bubble surface will be parametrized

$$\mathbf{x}_b = r(\psi, \theta) \mathbf{u}_r(\psi, \theta) \quad (6.123)$$

where \mathbf{u}_r is the radial unit vector in spherical coordinates and $r = R + \Delta r(\psi, \theta)$ is a weakly perturbed sphere radius. Using the parametrization (6.123) in the formula for the curvature (6.47) and linearizing the result with respect to derivatives of Δr we get:

$$\kappa = \frac{2}{R} - \frac{1}{R^2} \left(\frac{1}{\sin \psi} \frac{\partial}{\partial \psi} \sin \psi \frac{\partial r}{\partial \psi} - \frac{1}{\sin^2 \psi} \frac{\partial^2 r}{\partial \theta^2} \right) + O((\Delta r)^2). \quad (6.124)$$

If differentiated with respect to time, the expression for κ depends on

$$\frac{dr}{dt} = v_r = \frac{\partial \phi}{\partial r}. \quad (6.125)$$

Eq. (6.118) becomes

$$\frac{\partial^2 \phi}{\partial t^2} + \frac{\sigma}{\rho} \frac{1}{R^2} \left(\frac{1}{\sin \psi} \frac{\partial}{\partial \psi} \sin \psi \frac{\partial}{\partial \psi} - \frac{1}{\sin^2 \psi} \frac{\partial^2}{\partial \theta^2} \right) \frac{\partial \phi}{\partial r} = 0 \quad (6.126)$$

and, with account of the decomposition (6.119,6.122), leads to the set of second order ordinary differential equations equivalent to undamped oscillators

$$\frac{d^2 B_{\ell,m}}{dt^2} + \frac{\sigma}{\rho} \frac{\ell(\ell+1)^2}{R^3} B_{\ell,m} = 0. \quad (6.127)$$

with the angular frequencies of oscillation of eigenmodes ℓ, m equal to

$$\omega_\ell = \left(\frac{\sigma \ell(\ell+1)^2}{\rho R^3} \right)^{1/2}. \quad (6.128)$$

6.4 Divergence of transposed velocity gradient

In the v_z equation the corresponding additional term is obtained by replacing the first column of the velocity gradient (6.85) by the first line (to account for the transposed):

$$\tilde{\nabla}^\dagger \cdot \frac{\partial}{\partial z} \tilde{\mathbf{v}}$$

where $\tilde{\nabla}$ is the scalar gradient operator. Since the z -derivative commutes with $\tilde{\nabla}^\dagger$ we get

$$\frac{\partial}{\partial z} \tilde{\nabla}^\dagger \cdot \tilde{\mathbf{v}} = 0$$

The situation is less straightforward for transverse components v_+ and v_- . Take

$$\tilde{\nabla}^\dagger \cdot \begin{bmatrix} \tilde{\nabla}_+ v_z \\ \left(\tilde{\nabla}_+ + \frac{1}{r}\right) \tilde{v}_- \\ \left(\tilde{\nabla}_+ - \frac{1}{r}\right) \tilde{v}_+ \end{bmatrix}. \quad (6.129)$$

The operator $\tilde{\nabla}$ is, this time, that acting on v_+ in the third column of velocity gradient (6.85). This allows us to write the expression (6.129) in more detail as:

$$-\frac{\partial}{\partial z} \tilde{\nabla}_+ v_z + \frac{1}{2} \left(\tilde{\nabla}_-^\dagger + \frac{1}{r}\right) \left(\tilde{\nabla}_+ + \frac{1}{r}\right) \tilde{v}_- + \frac{1}{2} \left(\tilde{\nabla}_+^\dagger - \frac{1}{r}\right) \left(\tilde{\nabla}_+ - \frac{1}{r}\right) \tilde{v}_+. \quad (6.130)$$

Using Eq. (6.88) it can be shown that:

$$\left(\tilde{\nabla}_-^\dagger + \frac{1}{r}\right) \left(\tilde{\nabla}_+ + \frac{1}{r}\right) = \tilde{\nabla}_+ \tilde{\nabla}_-^\dagger$$

and

$$\left(\tilde{\nabla}_+^\dagger - \frac{1}{r}\right) \left(\tilde{\nabla}_+ - \frac{1}{r}\right) = \tilde{\nabla}_+ \tilde{\nabla}_+^\dagger.$$

As the result, expression (6.130) becomes:

$$\tilde{\nabla}_+ \left[-\frac{\partial}{\partial z} v_z + \frac{1}{2} \tilde{\nabla}_-^\dagger \tilde{v}_- + \frac{1}{2} \tilde{\nabla}_+^\dagger \tilde{v}_+ \right] = 0$$

because the expression in the square brackets is the divergence of the velocity.

6.5 Stress formulation in spectral representation

Eq. (6.85) after decomposition into Fourier modes writes:

$$\tilde{\nabla} \tilde{\mathbf{v}}_m = \begin{bmatrix} \frac{\partial v_{z,m}}{\partial z} & \frac{\partial \tilde{v}_{-,m}}{\partial z} & \frac{\partial \tilde{v}_{+,m}}{\partial z} \\ \left(\frac{\partial}{\partial r} - \frac{m}{r}\right) v_{z,m} & \left(\frac{\partial}{\partial r} - \frac{m+1}{r}\right) \tilde{v}_{-,m} & \left(\frac{\partial}{\partial r} - \frac{m-1}{r}\right) \tilde{v}_{+,m} \\ \left(\frac{\partial}{\partial r} + \frac{m}{r}\right) v_{z,m} & \left(\frac{\partial}{\partial r} + \frac{m+1}{r}\right) \tilde{v}_{-,m} & \left(\frac{\partial}{\partial r} + \frac{m-1}{r}\right) \tilde{v}_{+,m} \end{bmatrix}. \quad (6.131)$$

and the symmetrized version is:

$$\left(\tilde{\nabla}_m \tilde{\mathbf{v}} + \tilde{\nabla}_m \tilde{\mathbf{v}}^T \right) = \begin{bmatrix} 2 \frac{\partial v_{z,m}}{\partial z} & \frac{\partial \tilde{v}_{-,m}}{\partial z} + \left(\frac{\partial}{\partial r} - \frac{m}{r} \right) v_{z,m} & \frac{\partial \tilde{v}_{+,m}}{\partial z} + \left(\frac{\partial}{\partial r} + \frac{m}{r} \right) v_{z,m} \\ \frac{\partial \tilde{v}_{-,m}}{\partial z} + \left(\frac{\partial}{\partial r} - \frac{m}{r} \right) v_{z,m} & 2 \left(\frac{\partial}{\partial r} - \frac{m+1}{r} \right) \tilde{v}_{-,m} & \left(\frac{\partial}{\partial r} - \frac{m-1}{r} \right) \tilde{v}_{+,m} + \left(\frac{\partial}{\partial r} + \frac{m+1}{r} \right) \tilde{v}_{-,m} \\ \frac{\partial \tilde{v}_{+,m}}{\partial z} + \left(\frac{\partial}{\partial r} + \frac{m}{r} \right) v_{z,m} & \left(\frac{\partial}{\partial r} - \frac{m-1}{r} \right) \tilde{v}_{+,m} + \left(\frac{\partial}{\partial r} + \frac{m+1}{r} \right) \tilde{v}_{-,m} & 2 \left(\frac{\partial}{\partial r} + \frac{m-1}{r} \right) \tilde{v}_{+,m} \end{bmatrix} \quad (6.132)$$

The storage of gradients avoiding redundancies consists in storing only positive modes for scalar quantities and positive and negative modes of of $\tilde{\nabla}_+$. I.e.:

$$S_{z,z,m} = 2 \frac{\partial v_{z,m}}{\partial z}; \quad m = 0 \dots M, \quad (6.133)$$

$$S_{z,+,m} = \frac{\partial \tilde{v}_{+,m}}{\partial z} + \left(\frac{\partial}{\partial r} + \frac{m}{r} \right) v_{z,m}; \quad m = -M \dots M, \quad (6.134)$$

$$S_{+,z,m} = \frac{\partial \tilde{v}_{+,m}}{\partial z} + \left(\frac{\partial}{\partial r} + \frac{m}{r} \right) v_{z,m}; \quad m = -M \dots M, \quad (6.135)$$

$$S_{+,-,m} = \left(\frac{\partial}{\partial r} - \frac{m-1}{r} \right) \tilde{v}_{+,m} + \left(\frac{\partial}{\partial r} + \frac{m+1}{r} \right) \tilde{v}_{-,m}; \quad m = -M \dots M, \quad (6.136)$$

$$S_{+,+,m} = 2 \left(\frac{\partial}{\partial r} + \frac{m-1}{r} \right) \tilde{v}_{+,m}; \quad m = -M \dots M. \quad (6.137)$$

6.6 Stress formulation on the deformed mesh

In Cartesian coordinates the functional of the weak formulation of the viscous term writes:

$$\begin{aligned} a(\mathbf{w}, \mathbf{v}) &= \int_{\Omega} \nabla \mathbf{w} \mu (\nabla \mathbf{v} + \nabla \mathbf{v}^T) d\Omega \\ &= \int_{\Omega} [\nabla w_z \mu \mathbf{S}_z + \overline{\nabla w_-} \mu \mathbf{S}_- + \overline{\nabla w_+} \mu \mathbf{S}_+] d\Omega \\ &= \int_{\Omega} [\mathbf{K} \tilde{\nabla} w_z \mu \mathbf{S}_z + e^{i\theta} \overline{\mathbf{K} \tilde{\nabla} w_-} \mu \mathbf{S}_- + e^{-i\theta} \overline{\mathbf{K} \tilde{\nabla} w_+} \mu \mathbf{S}_+] d\Omega \\ &= \int_{\Omega} [\tilde{\nabla} w_z \mathbf{K}^\dagger \mu \mathbf{S}_z + \tilde{\nabla} w_- \mathbf{K}^\dagger e^{i\theta} \mu \mathbf{S}_- + \tilde{\nabla} w_+ \mathbf{K}^\dagger e^{-i\theta} \mu \mathbf{S}_+] d\Omega \\ &= \int_{\Omega} [\tilde{\nabla} w_z \mathbf{K}^\dagger \mu \mathbf{S}_z + \overline{\tilde{\nabla} w_-} \mathbf{K}^\dagger e^{i\theta} \mu \mathbf{S}_- + \overline{\tilde{\nabla} w_+} \mathbf{K}^\dagger e^{-i\theta} \mu \mathbf{S}_+] \det(\tilde{\mathbf{J}}) r dr dz d\theta \\ &= \int_{\Omega} [\overline{w_z} \tilde{\nabla}^\dagger \mathbf{I} \mathbf{K}^\dagger \mu \mathbf{S}_z + \overline{\nabla w_-} \tilde{\nabla}^\dagger \mathbf{I} \mathbf{K}^\dagger e^{i\theta} \mu \mathbf{S}_- + \overline{w_+} \tilde{\nabla}^\dagger \mathbf{I} \mathbf{K}^\dagger e^{-i\theta} \mu \mathbf{S}_+] \det(\tilde{\mathbf{J}}) r dr dz d\theta \end{aligned}$$

where

$$\mathbf{I} = \text{diag}(1, 2, 2) \quad (6.138)$$

and μ stands for the viscosity. In the undeformed case

$$\text{diag}(1, 2, 2)\mathbf{K}_0^\dagger = \begin{bmatrix} 1 & 0 & 0 \\ 0 & e^{i\theta} & -ie^{i\theta} \\ 0 & e^{-i\theta} & ie^{-i\theta} \end{bmatrix} = \mathbf{K}_0^{-1}, \quad (6.139)$$

i.e.

$$\mathbf{IK}^\dagger = \mathbf{K}_0^{-1}(\mathbf{J}_{def}^{-1})^T. \quad (6.140)$$

This yields the following operators:

z-component operator:

$$\tilde{\nabla}^\dagger \mathbf{IK}^\dagger \mu \mathbf{MS}_z,$$

minus component operator:

$$\tilde{\nabla}^\dagger \mathbf{IK}^\dagger e^{i\theta} \mu \mathbf{MS}_-$$

and plus component operator:

$$\tilde{\nabla}^\dagger \mathbf{IK}^\dagger e^{-i\theta} \mu \mathbf{MS}_+$$

where $\tilde{\nabla}^\dagger$ are the divergence operators already implemented in cylindrical coordinates and \mathbf{M} is the mass matrix representing $d\Omega = \det(\tilde{\mathbf{J}})rdrdzd\theta$, i.e.

$$\mathbf{M} = \text{diag} \left(\frac{1}{n_\theta} \det(\tilde{\mathbf{J}}) B_{r,z} \right)$$

where $B_{r,z}$ are the integration weights in radial-axial plane and n_θ is the number of points on the circle of fft ($2M + 1$ or $2M + 2$).

Bibliography

- ACHENBACH, E. 1974 Vortex shedding from spheres. *J. Fluid Mech.* **66**, 209–221.
- ÅKERVIK, E., LUCA, B., HENNINGSON, D. S., HÖPPFNER, J., MARXEN, O. & SCHLATTER, P. 2006 Steady solutions of the navier-stokes equations by selective frequency damping. *Phys. Fluids* **18**, 068102.
- ANDERSON, A., PESAVENTO, U. & WANG, Z. J. 2005 Analysis of transitions between fluttering, tumbling and steady descent of falling cards. *J. Fluid Mech.* **541**, 91–104.
- AUGUSTE, F. 2010 Instabilités de sillage générées derrière un corps solide cylindrique, fixe ou mobile dans un fluide visqueux. PhD thesis, Université Paul Sabatier, Toulouse.
- AUGUSTE, F., FABRE, D. & MAGNAUDET, J. 2010 Bifurcations in the wake of thick circular disk. *Theor. Comput. Fluid Dyn.* **24**, 305–313.
- AUGUSTE, F., MAGNAUDET, J. & FABRE, D. 2013 Falling styles of discs. *J. Fluid Mech.* **719**, 388–405.
- AUTON, T. 1983 The dynamics of bubbles, drops and particles in motion in liquids. PhD thesis, Cambridge University.
- BASSET, A. B. 1888 *A Treatise on Hydrodynamics*. Cambridge University Press.
- BATCHELOR, G. K. 1967 *An introduction to fluid dynamics*. Cambridge at the university press.
- BERIS, A. & GIACOMIN, A. J. 2014 πάντα ρεῖ: Everything flows. *Appl. Rheol.* **24**, 52918.
- BHAGA, D. & WEBER, M. E. 1981 Bubbles in viscous liquids: shapes, wakes and velocities. *J. Fluid Mech.* **105**, 61–85.
- BOBINSKI, T., GOUJON-DURAND, S. & WESFREID, J. E. 2014 Instabilities in the wake of a circular disk. *Physical Review E* **89**, 053021.
- BÖNISCH, S. & HEUVELINE, V. 2007 On the numerical simulation of the unsteady free fall of a solid in a fluid: I. the newtonian case. *Comput. Fluids* **36**, 1434–1445.

- BOUCHET, G., MEBAREK, M. & DUŠEK, J. 2006 Hydrodynamic forces acting on a rigid fixed sphere in early transitional regimes. *European Journal of Mechanics, B/Fluids* **25**, 321–336.
- BOUSSINESQ, J. V. 1885 Sur la résistance qu’oppose un fluide indéfini au repos, sans pesanteur, au mouvement varié d’une sphère solide qu’il mouille sur toute sa surface, quand les vitesses restent bien continues et assez faibles pour que leurs carrés et produits soient négligeables. *Comptes Rendus de l’Académie des Sciences* **100**, 935–937.
- BRENNEN, C. E. 1995 *Cavitation and bubble dynamics*. Oxford University Press.
- BRÜCKER, C. 1999 Structure and dynamics of the wake of bubbles and its relevance for bubble interactions. *Physics of Fluids* **11**, 1781–1796.
- CABALLINA, O. 2002 Etude de l’instabilité d’un panache a bulles et comparaison avec les structures organisées d’un panache a masse volumique variable. PhD thesis, Université Louis Pasteur, Strasbourg.
- CANO-LOZANO, J. C., BOHORQUEZ, P. & MARTÍNEZ-BAZÁN, C. 2013 Wake instability of a fixed axisymmetric bubble of realistic shape. *Int. J. Multiphase Flow* **51**, 11–21.
- CHRUST, M. 2012 Etude numérique de la chute d’objets axisymétriques dans un fluide newtonien. PhD thesis, Université de Strasbourg.
- CHRUST, M., BOUCHET, G. & DUŠEK, J. 2010 Parametric study of the transition in the wake of oblate spheroids and flat cylinders. *J. Fluid Mech.* **665**, 199–208.
- CHRUST, M., BOUCHET, G. & DUŠEK, J. 2013 Numerical simulation of the dynamics of freely falling discs. *Physics of Fluids* **25**, 044102.
- CHRUST, M., BOUCHET, G. & DUŠEK, J. 2014 Effect of solid body degrees of freedom on the path instabilities of freely falling or rising flat cylinders. *J. Fluids and Structures* **47**, 55–70.
- CHRUST, M., DAUTEUILLE, C., BOBINSKI, T., ROKICKI, J., GOUJON-DURAND, S., WESFREID, J. E., BOUCHET, G. & DUŠEK, J. 2015 Effect of inclination on the transition scenario in the wake of fixed disks and flat cylinders. *J. Fluid Mech.* **770**, 189–209.
- DANAILA, I., DUŠEK, J. & ANSELMET, F. 1998 Nonlinear dynamics at a hopf bifurcation with axisymmetry breaking in a jet. *Physical Review E* **57**, 3695–3698.
- DUINEVELD, P.C. 1995 The rise velocity and shape of the bubbles in pure water at high reynolds number. *J. Fluid Mech.* **292**, 325–332.
- ELLINGSEN, K. & RISSO, F. 2001 On the rise of an ellipsoidal bubble in water: oscillatory paths and liquid-induced velocity. *J. Fluid Mech.* **440**, 235–268.
- ERN, P., RISSO, F., FABRE, D. & MAGNAUDET, J. 2011 Wake-induced oscillatory paths of bodies freely rising or falling in fluids. *Ann. Rev. of Fluid Mech.* **44**, 97–121.

- ESMAEELI, A. & TRYGGVASON, G. 1998 Direct numerical simulations of bubbly flows. part 1. low reynolds number arrays. *J. Fluid Mech.* **377**, 313–345.
- FABRE, D., AUGUSTE, F. & MAGNAUDET, J. 2008 Bifurcations and symmetry breaking in the wake of axisymmetric bodies. *Physics of Fluids* **20**, 051702.
- FABRE, D., TCHOUFAG, J. & MAGNAUDET, J. 2012 The steady oblique path of bouyancy-driven disks and spheres. *J. Fluid Mech.* **707**, 24–36.
- FERNANDES, P. C., RISSO, F., ERN, P. & MAGNAUDET, J. 2007 Oscillatory motion and wake instability of freely rising axisymmetric bodies. *J. Fluid Mech.* **573**, 479–502.
- FIELD, S. B., KLAUS, M. & MOORE, M. G. 1997 Chaotic dynamics of falling disks. *Nature* **388**, 252–254.
- FORTES, A. F., JOSEPH, D. D. & LUNDGREN, T. S. 1987 Nonlinear mechanics of fluidization of beds of spherical particles. *J. Fluid Mech.* **177**, 467–483.
- G. BOUCHET, M. MEBAREK & DUŠEK, J. 2006 Hydrodynamic forces acting on a rigid fixed sphere in early transitional regimes. *European Journal of Mechanics, B/Fluids* **25**, 321–336.
- GAUDLITZ, D. & ADAMS, N. A. 2009 Numerical investigation of rising bubble wake and shape variations. *Physics of Fluids* **21**, 122102.
- GHIDERSA, B. & DUŠEK, J. 2000 Breaking of axisymetry and onset of unsteadiness in the wake of a sphere. *J. Fluid Mech.* **423**, 33–69.
- GOLDBURG, A. & FLORSHEIM, B. H. 1966 Transition and strouhal number for the incompressible wake of various bodies. *Physics of Fluids* **9**, 45–50.
- GOVARDHAN, R. N. & WILLIAMSON, C. H. K. 2005 Vortex-induced vibrations of a sphere. *J. Fluid Mech.* **531**, 11–47.
- GUMOWSKI, K., MIEDZIK, J., GOUJON-DURAND, S., JENFFER, P. & WESFREID, J. E. 2008 Transition to a time-dependent state of fluid flow in the wake of a sphere. *Physical Review E* **77**.
- HAN, J. & TRYGGVASON, G. 1999 Secondary breakup of axisymmetric liquid drops acceleration by a constant body force. *Phys. Fluids A* **11**, 3650.
- HENDERSON, R. D. & BARKLEY, D. 1996 Secondary instability in the wake of a circular cylinder. *Physics of Fluids* **8**, 1683–1685.
- HOROWITZ, M. & WILLIAMSON, C. H. K. 2010 The effect of reynolds number on the dynamics and wakes of freely rising and falling spheres. *Journal of Fluid Mechanics* **651**, 251–294.
- HUA, J. & LOU, J. 2007 Numerical simulation of bubble rising in viscous liquid. *Journal of Computational Physics* **222**, 769–795.

- JALAAL, M. & MEHRAVARAN, K. 2012 Fragmentation of falling liquid droplets in bag breakup mode. *Int. J. Multiphase Flow* **47**, 115–132.
- JENNY, M., BOUCHET, G. & DUŠEK, J. 2003 Nonvertical ascension or fall of a free sphere in a Newtonian fluid. *Physics of Fluids* **15**, L9–L12.
- JENNY, M. & DUŠEK, J. 2004 Efficient numerical method for the direct numerical simulation of the flow past a single light moving spherical body in transitional regimes. *Journal of Computational Physics* **194**, 215–232.
- JENNY, M., DUŠEK, J. & BOUCHET, G. 2004 Instabilities and transition of a sphere falling or ascending freely in a Newtonian fluid. *J. Fluid Mech.* **508**, 201–239.
- JOHNSON, T. A. & PATEL, V. C. 1999 Flow past a sphere up to a Reynolds number of 300. *J. Fluid Mech.* **378**, 19–70.
- KAJISHIMA, T. & TAKIGUCHI, S. 2002 Interaction between particle clusters and particle-induced turbulence. *Int. J. Heat Fluid Flow* **23**, 639–646.
- KARAMANEV, D. G., CHAVARIE, C. & MAYER, R. C. 1996 Dynamics of the free rise of a light solid sphere in liquid. *AIChE Journal* **42** (6), 1789–1792.
- KARAMANEV, D. G. & NIKOLOV, L. N. 1992 Free rising spheres do not obey newton’s law for free settling. *AIChE Journal* **38** (11), 1843–1846.
- KIM, H. J. & DURBIN, P. A. 1988 Observations of the frequencies in a sphere wake and of drag increase by acoustic excitation. *Phys. Fluids* **31**, 3260.
- KLOTZ, L., GOUJON-DURAND, S., ROKICKI, J. & WESFREID, J. E. 2014 Experimental investigation of flow behind a cube for moderate reynolds numbers. *J. Fluid Mech.* **750**, 73–98.
- KOEBE, M., BOTHE, D. & WARNECKE, H.-J. 2003 Direct numerical simulation of air bubbles in water/glycerol mixtures: shapes and velocity fields. In *Proceedings of FEDSM 03: 4th ASME-JSME Joint Fluids Engineering Conference, Honolulu, Hawaii, USA, July 6-11*.
- KOMORI, S. & KUROSE, R. 1996 The effect of shear and spin on particle lift and drag in shear flow at high reynolds numbers. *Kluwer Academic Publishers, Advances in Turbulence VI*, 551–554.
- KOTOUČ, M. 2008 Transition à la turbulence du sillage d’une sphère fixe ou libre en convection mixte. PhD thesis, Université Louis Pasteur, Strasbourg I.
- KOTOUČ, M., BOUCHET, G. & DUŠEK, J. 2009 Transition to turbulence in the wake of a fixed sphere in mixed convection. *J. Fluid Mech.* **625**, 205–248.
- LALANNE, B., TANGUY, S. & RISSO, F. 2013 Effect of rising motion on the damped shape oscillations of drops and bubbles. *Physics of Fluids* **25**, 112107.

- LANDAU, L. D. & LIPSCHITZ, F.M. 1959 *Fluid Mechanics*, , vol. I. Pergamon.
- LEGENDRE, D. & MAGNAUDET, J. 1998 The lift force on a spherical bubble in a viscous linear shear flow. *J. Fluid Mech.* **368**, 81–126.
- LIENHARD, J. H. 1966 *Synopsis of lift, drag, and vortex frequency data for rigid circular cylinders*. Technical Extension Service.
- LUNDE, K & PERKINS, RJ 1998 Shape oscillations of rising bubbles. *Applied Scientific Research* **58** (1-4), 387–408.
- MAGARVEY, R. H. & BISHOP, R. L. 1961 Transition ranges for three-dimensional wakes. *Can. J. Phys.* **39**, 1418.
- MAGARVEY, R. H. & MACLATCHY, C. S. 1965 Vortices in sphere wakes. *Canadian Journal of Physics* **43** (9), 1649–1656.
- MAGNAUDET, J. 1997 The forces acting on bubbles and rigid particles. *ASME Fluids Engineering Division Summer meeting* pp. 1–9.
- MAGNAUDET, J. & MOUGIN, G. 2007a Wake instability of a fixed spheroidal bubble. *J. Fluid Mech.* **572**, 311–337.
- MAGNAUDET, J. & MOUGIN, G. 2007b Wake instability of a fixed spheroidal bubble. *J. Fluid Mech.* **572**, 311–337.
- MAGNAUDET, J., RIVERO, M. & FABRE, J. 1995 Accelerated flows past a rigid sphere or a spherical bubble. part 1. steady straining flow. *Journal of Fluid Mechanics* **284**, 97–135.
- MAHADEVAN, L., RYU, W. S. & SAMUEL, A. D. T. 1999 Tumbling cards. *Physics of Fluids* **11** (1), 1–3.
- MEI, R., KLAUSNER, J. & LAWRENCE, C. J. 1994 A note on the history force on a spherical bubble at finite reynolds number. *Phys. Fluids A* **6**, 418–20.
- MELIGA, P., CHOMAZ, J. M. & SIPP, D. 2009 Global mode interaction and pattern selection in the wake of a disk: a weakly nonlinear expansion. *J. Fluid Mech.* **633**, 159–189.
- MITTAL, R. 1999 Planar symmetry in the unsteady wake of a sphere. *AIAA Journal* **37**, 388–390.
- MITTAL, R. & WILSON, J. J. 1999 Symmetry properties of the transitional sphere wake. *AIAA Journal* **40**, 579–582.
- MOORE, D. W. 1963 The boundary layer on a spherical gas bubble. *J. Fluid Mech.* **16**, 161–176.
- MOUGIN, G. & MAGNAUDET, J. 2002a Path instability of a rising bubble. *Phys. Rev. Lett.* **88**, 014502–1.

- MOUGIN, G. & MAGNAUDET, J. 2002*b* Path instability of a rising bubble. *Phys. Rev. Lett.* **88**, 014502.
- MUCHA, P. J., TEE, S.-Y., WEITZ, D. A., SHRAIMAN, B. I. & BRENNER, M. P. 2004 A model for velocity fluctuations in sedimentation. *J. Fluid Mech.* **501**, 74–104.
- NAKAMURA, I. 1976 Steady wake behind a sphere. *Physics of Fluids* **19** (1), 5–8.
- NATARAJAN, R. & ACRIVOS, A. 1993 The instability of the steady flow past spheres and disks. *J. Fluid Mech.* **254**, 323–344.
- NGUYEN, N.-Q. & LADD, A. J. C. 2005 Sedimentation of hard-sphere suspensions at low reynolds number. *J. Fluid Mech.* **525**, 73–104.
- ORMIÈRES, D. 1999 Etude expérimentale et modélisation du sillage d'une sphère à bas nombre de Reynolds. PhD thesis, Université de Provence.
- ORMIÈRES, D. & PROVANSAL, M. 1999 Transition to turbulence in the wake of a sphere. *Phys. Rev. Lett.* **83**, 80–83.
- ORSZAG, S.A. 1974 Fourier series on spheres. *Mon. Weather Rev* **102**, 56–75.
- PATERA, A. 1984 A spectral element method for fluid dynamics: laminar flow in a channel expansion. *Journal of Computational Physics* **54** (3), 468–488.
- PIER, B. 2008 Local and global instabilities in the wake of a sphere. *J. Fluid Mech.* **603**, 39–61.
- PROSPERETTI, A. 2004 Bubbles. *Physics of Fluids* **16** (6), 1852–1865.
- PRZADKA, A., MIEDZIK, J., GUMOWSKI, K., GOUJON-DURAND, S. & WESFREID, J. E. 2008 The wake behind the sphere; analysis of vortices during transition from steadiness to unsteadiness. *Arch. of Mech.* **60** (6), 467–474.
- RIVERO, M, MAGNAUDET, J. & FABRE, J. 1991 Quelques résultats nouveaux concernant les forces exercées sur une inclusion sphérique par un écoulement accéléré = new results on the forces exerted on a spherical body by an accelerated flow. *Acad. Sci. Paris Serie II* **284** (312), 1499–1501.
- SAHA, A. K. 2004 Three-dimensional numerical simulations of the transition of flow past a cube. *Phys. Fluids A* **16**, 1630–1646.
- SAÏDI, A., DUŠEK, J. & DAVID, R. 2011 Receptivity of a spatially developing jet to stochastic perturbations. *Physics of Fluids* **23**, 024105.
- SAKAMOTO, H. & HANIU, H. 1990 A study on vortex shedding from spheres in a uniform flow. *Transactions of the ASME* **112**, 386–392.
- SAKAMOTO, H. & HANIU, H. 1995 The formation mechanism and shedding frequency of vortices from a sphere in uniform shear flow. *J. Fluid Mech.* **287**, 151–171.

- SHENOY, A. R. & KLEINSTREUER, C. 2008 Flow over a thin circular disk at low to moderate Reynolds number. *J. Fluid Mech.* **605**, 253–262.
- SHEW, W. L., PONCET, S. & PINTON, J. F. 2006 Force measurements on rising bubbles. *J. Fluid Mech.* **569**, 51.
- SQUIRES, V. R. 2007 *Physics, Mechanics and Processes of Dust and Sandstorms*. United Nations Convention to Combat Desertification.
- STRINGHAM, G.E., SIMONS, D.B. & GUY, H.P. 1969 *The Behavior of Large Particles Falling in Quiescent Liquids*. U.S. Government Printing Office.
- STROGATZ, S.H. 1994 *Nonlinear Dynamics and Chaos*. Addison-Wesley.
- TANABE, Y. & KANEKO, K. 1994 Behavior of a falling paper. *Phys. Rev. Lett.* **73**, 1372–1375.
- TANEDA, S. 1956 Experimental investigation of the wake behind a sphere at low Reynolds numbers. *Journal of the Physical Society of Japan* **11**, 1104.
- TCHOUFAG, J., FABRE, D. & MAGNAUDET, J. 2014 Global linear stability analysis of the wake and path of buoyancy-driven disks and thin cylinders. *J. Fluid Mech.* **740**, 278–311.
- TCHOUFAG, J., MAGNAUDET, J. & FABRE, D. 2013 Linear stability and sensitivity of the flow past a fixed oblate spheroidal bubble. *Physics of Fluids* **25**, 054108.
- TOMBOULIDES, A. G. & ORSZAG, S. A. 2000 Numerical investigation of transitional and weak turbulent flow past a sphere. *J. Fluid Mech.* **416**, 45–73.
- TOMBOULIDES, A. G., ORSZAG, S. A. & KARNIADAKIS, G. E. 1993 Direct and large-eddy simulation of axisymmetric wakes. In *31st Aerospace Sciences Meeting & Exhibit*.
- TRIPATHI, M. K., SAHU, K. C. & GOVINDARAJAN, R. 2014 Why a falling drop does not in general behave like a rising bubble. *Scientific Reports* **4**, 4771.
- TRIPATHI, M. K., SAHU, K. C. & GOVINDARAJAN, R. 2015 Dynamics of an initially spherical bubble rising in quiescent liquid. *Nature Communications* **6**:6268.
- TUKOVIĆ, Ž. & JASAK, H. 2012 A moving mesh finite volume interface tracking method for surface tension dominated interfacial fluid flow. *Comput. Fluids* **55**, 70–84.
- UHLMANN, M. & DOYCHEV, T. 2014 Sedimentation of a dilute suspension of rigid spheres at intermediate Galileo numbers: the effect of clustering upon the particle motion. *J. Fluid Mech.* **752**, 310–348.
- UHLMANN, M. & DUŠEK, J. 2014 The motion of a single heavy sphere in ambient fluid: A benchmark for interface-resolved particulate flow simulations with significant relative velocities. *Int. J. Multiphase Flow* **59**, 221–243.

- VARSHNEY, K., C., S. & WANG, Z. J. 2012 The kinematics of falling maple seeds and the initial transition to a helical motion. *Nonlinearity* **25**, C1–C8.
- VARSHNEY, K., CHANG, S. & WANG, Z. J. 2013 Unsteady aerodynamic forces and torques on falling parallelograms in coupled tumbling-helical motions. *Physical Review E* **87**, 053021.
- VELDHUIS, C.H.J. & BIESHEUVEL, A. 2007 An experimental study of the regimes of motion of spheres falling or ascending freely in a newtonian fluid. *International Journal of Multiphase Flow* **33** (10), 1074 – 1087.
- VELDHUIS, C., BISHEUVEL, A. & VAN WIJNGAARDEN, L. 2008 Shape oscillations on bubbles rising in clean and tap water. *Physics of Fluids* **20**, 040705.
- VILLERMAUX, E. & BOSSA, B. 2009 Single-drop fragmentation determines size distribution of raindrops. *Nature Physics* **5**, 697–702.
- DE VRIES, A.W.G., BIESHEUVEL, A. & VAN WIJNGAARDEN, L. 2002a Notes on the path and wake of a gas bubble rising in pure water. *Int. J. Multiphase Flow* **28**, 1823–1835.
- DE VRIES, A.W.G., BIESHEUVEL, A. & VAN WIJNGAARDEN, L. 2002b Notes on the path and wake of a gas bubble rising in pure water. *Int. J. Multiphase Flow* **28**, 823–1835.
- WILLMARTH, W. W., HAWK, N. E. & HARVEY, R. L. 1964 Steady and unsteady motions and wakes of freely falling disks. *Physics of Fluids* **7**, 197–208.
- WU, M. & GHARIB, M. 2002 Experimental studies on the shape and path of small air bubbles rising in clean water. *Physics of Fluids* **14** (7), L49–L52.
- ZENIT, R. & MAGNAUDET, J. 2008 Path instability of rising spheroidal air bubbles: A shape-controlled process. *Physics of Fluids* **20**, 061702.
- ZENIT, R. & MAGNAUDET, J. 2009 Measurements of the streamwise vorticity on the wake of an oscillating bubble. *Int. J. Multiphase Flow* **35**, 195–203.
- ZHONG, H., CHEN, S. & LEE, C. 2011 Experimental study of freely falling thin disks: Transition from planar zigzag to spiral. *Physics of Fluids* **23** (1), 011702.
- ZHOU, W. & DUŠEK, J. 2015 Chaotic states and order in the chaos of the paths of freely falling and ascending spheres. *Int. J. Multiphase Flow* **75**, 205–223.
- ZIELINSKA, B. J. A., GOUJON-DURAND, S., DUŠEK, J. & WESFREID, J. E. 1997 Strongly nonlinear effect in unstable wakes. *Phys. Rev. Lett.* **79**, 3893.

Published matter

Chapter 2 was published in *Int. J. Multiphase Flows* (see reprint enclosed).

Chapter 4 has been submitted to *Int. J. Multiphase Flows*.

Chapter 3 is in preparation for publication.